FUNDAMENTAL TOOL WEAR STUDY IN TURNING OF Ti-6Al-4V ALLOY (Ti64) AND NANO-ENHANCED MINIMUM QUANTITY LUBRICATION (MQL) MILLING

By

Trung Kien Nguyen

A DISSERTATION

Submitted to
Michigan State University
in partial fulfillment of the requirements
for the degree of

Mechanical Engineering - Doctor of Philosophy

2015

ABSTRACT

FUNDAMENTAL TOOL WEAR STUDY IN TURNING OF Ti-6Al-4V ALLOY (Ti64) AND NANO-ENHANCED MINIMUM QUANTITY LUBRICATION (MQL) MILLING

By

Trung Kien Nguyen

Titanium (Ti) alloy, in particular Ti-6Al-4V (Ti64), has been widely used in a variety of industries such as automobile, aerospace, chemistry, biomedicine and other manufacturing industries because of their desirable and unique mechanical properties. The well-known properties of Ti alloys include light-weight, excellent strength even at elevated temperatures, resistance to corrosion and biocompatibility, which cannot be collectively and comprehensively satisfied by any other alloys in some applications. In machining of Ti alloys, however, the low thermal conductivity and high hardness exposes cutting tools to high temperatures and cutting forces, which often fracture the cutting tools catastrophically. More importantly, the high chemical solubility of cutting tools causes the high chemical wear leading to accelerated wear on cutting tools, especially when cutting at high speeds. Polycrystalline diamond (PCD) and uncoated carbide tools are the most widely used tool materials for machining Ti alloys. In order to find the main reason for this puzzling behavior, this study revisits the fundamental wear mechanisms in rake and flank faces using PCD and carbide tools in dry turning of Ti64 alloy. The original microstructure of work material was characterized using Orientation Image Microscope (OIM) to explain the correlation of the wear pattern with the observed microstructure. Based on the microstructure and the tool wear patterns, this study

claims that wear damages are caused primarily by the heterogeneity coming from not only the presence of both α (hexagonal closed packed) and β (body centered cubic) phases but also the hard orientation of the α–phases. In addition to the heterogeneities, the adhesion layer detaching parts of the tool material also contributes to flank wear.

This thesis also considers improving tool life by adopting new lubrication techniques. In particular, Minimum Quantity Lubrication (MQL)-based machining process was chosen as it has many merits over not only conventional flood cooling machining but also dry machining. However, few disadvantages make the MQL-based machining process impractical to be adopted in many industrial production settings for more aggressive cutting conditions. At high cutting speeds, for example, a minute amount of oil used in MQL will simply evaporate or disintegrate as soon as the oil droplets strike the tools already heated to high temperatures. Lamellar structured solid lubricants (graphite and hexagonal boron nitride) in a platelet form have been mixed with a typical vegetable MQL oils to mitigate this major deficiency of MQL process. When the mixture of oil and these platelets are applied, the platelets are expected to provide additional lubricity even after the oil droplets have been disintegrated at high temperature. Thus, the enhancement achieved by adding these platelets allows us to expand the processing envelope of MQL. In this research project, a comprehensive study on the effect of the diameter and thickness of platelets was carried out. The results showed that the presence of nano-platelets in the MQL oil decreased the tool wear and improved the tool life compared to traditional MQL with pure oil as well as dry machining 1045 steel and Ti64 not only by providing lubricity at high temperature cutting condition but also by reducing the micro-chipping and tool fracture.

To my wife, Ha Dao,
my children, Chi Nguyen, and An Nguyen,
and my beloved family

ACKNOWLEDGMENTS

I would like to gratefully and sincerely thank my advisor, Dr. Patrick Kwon for his expertise, generous support, valuable encouragement, and excellent guidance for me to proceed through my doctoral studies and the completion of this dissertation. My deepest gratitude also goes for his patience, enlightening advice and help in improving my scientific and writing skills. I also wish to thank my committee members, Dr. Bieler, Dr. Feeny and Dr. Baek, for their support, valuable comments, and guidance to improve and complete this dissertation. My appreciation especially goes to Dr. Bieler for providing equipment for experiment that supported for analyzing data. A special thanks to Mr. Lars Haubold at Franhoufer CCL, USA for his generous help in doing the experiments and making equipment available for use. I would like to thank Brian Hoefler at Sandvik Coromant for providing tools for experiments. Many thanks go to Mr. Steve Allen at West Michigan Precision Machining for help in experiments.

A special acknowledgement goes to Dr. Tim K. Wong, and Dr. Kyung H. Park for their encouragement and instruction at the beginning of my graduate studies. Many thanks go to my colleagues, Xin Wang, Wang Mingang, David Schrock, Truong Do, Sirisak Tooptong, Dinh Nguyen for valuable discussion and general support as friends and co-workers. Furthermore, I am appreciative of my co-workers Di Kang for assistance with conducting some of the experiments contained in this work.

Most importantly, I wish to thank my wife, my children, my parents and my parents in law for their love, support and encouragement that provided my inspiration and was my driving force during my PhD study.

TABLE OF CONTENTS

LIST OF TABLES

LIST OF FIGURES

Chapter 1: Tool wear of carbide and PCD inserts in turning of Ti64

I.1 INTRODUCTION

I.1.1 Machining Titanium overview

Titanium (Ti) industry was established in 1950s mainly to make aerospace parts such as engine components, rockets, and spacecraft. Nowadays, Ti and its alloys have become the essential materials for aerospace and medical device industries due to its outstanding physical properties. The outstanding properties also make Ti alloys extremely difficult-to-machine materials. In particular, high speed cutting of Ti alloys is difficulty because of the extremely short tool life. For example, at the cutting speed of 122 m/min, polycrystalline diamond (PCD) cutting tools can last for 2-4 minutes and only about 1-2 minutes for uncoated carbide tools [Schrock, 2013]. The current recommended cutting speeds for Ti alloys are less than 30m/min with high speed steel (HSS) and 60m/min with carbide tools in dry machining [Rahman, 2003]. Overall the machinability of Ti alloys is considered to be poor in terms of many variables such as cutting forces, tool life, metal removal rate, and surface finish [Jaffery, 2008].

Ti alloys have the low density of around 4.5g/cm3, high hot strengths [Oosthuizen, 2010] and extremely low thermal conductivities, somewhere between 6.6 and 20W/m.K depending on the alloys. The phase transformation temperature (β-transus temperature or Ts) and the melting temperatures for pure titanium are around 882°C [Yang, 1999] and 1650°C [Oosthuizen, 2010], respectively. These temperatures vary depending on the content of alloy ingredients and pressure. For example, the beta

transus temperatures for Ti-5Al-2.5Sn, Ti-6Al-4V and Ti-5Al-2Sn-2Zr-4Cr-4Mo are 1040°C, 995°C, and 885°C, respectively [Semiatin, 1996]. The transus temperatures of pure titanium are 1055, 1013, and 873 °K for pressure of 0, 5 and 10 GPa, respectively [Velsavjevic, 2012]. Titanium is classified in two categories, commercially pure titanium (at least 99.67 wt% of Ti) and alloyed titanium (Ti alloys). Commercially pure titanium has low strength but outstanding corrosion resistance, which has very limited applications except in the chemical process industries. Ti alloys have higher strength and, thus, wider applications in aerospace and medical device industries. The allotropic nature makes the classification of Ti alloys into three categories, Alpha, Beta, and Alpha-Beta.

Alpha titanium alloys (Ti5Al2.5Sn, Ti8Al1Mo1V, etc.), hexagonal close packed microstructures, have the α-phase stabilizers such as Al, O, B, N, Sn that raise the β-transus temperature. Alpha and near-alpha alloys generally are not heat-treatable, brittle and have low to medium tensile strengths, high corrosion resistance, and good weldability. They are mainly used in corrosion resistance applications.

Beta alloys (Ti11.5Mo6Zr4.5Sn, Ti5553, etc.), body centered cubic microstructures, contain the β phase stabilizers such as V, Nb, Ta, and Mo that reduce the β-transus temperature. Alloys in this group are readily heat-treatable, ductile and exhibit high strengths and have slightly higher density [Machado, 1990]. The alloys in this group show higher hardenability.

Alpha-beta alloys (Ti6Al4V, Ti5Al4V, etc.) contain the combination of both α and β stabilizers. The mechanical properties of these alloys vary substantially depending on the heat treatment schedule, which can lead to high strength between room

temperature and moderately high temperatures. In general, the alloys in this group have higher strength than the alpha and near alpha alloys, and are widely used in the general purpose (strength applications) and aerospace industries as well. In the alpha-beta alloys group, Ti-6Al-4V is the most commonly used alloy (accounting for up to 60% of the titanium production [Boyer, 1996]).

The beta titanium alloys has much worse machinability than alpha and alpha-beta (α+β) titanium alloys [Arrazola, 2009; Machai, 2013].

Beside these alloys, there are two transition types of alloys, near alpha and near beta alloys. The near alpha alloys have up to 5% of beta stabilizers with the microstructure containing alpha phase and about 3-5% beta phase. The near beta alloys has the high fraction of metastable beta phase (βM) and the similar properties of α+β alloys [Maciej Motyka, 2012].

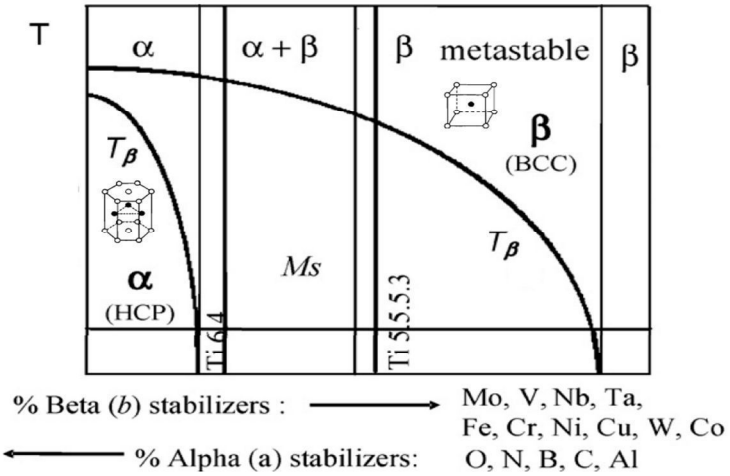

Figure 1: Phase diagram of the titanium alloys [E. Gautier and B. Appolaire, Ecole de Mines de Nancy, France]

In machining metal, approximately 90% of the heat generation come from plastic deformation [Boothroyd, 1975; Shahan, 1993]. However, the main distinction of Ti compared to other metallic alloys is its low thermal conductivities. They have the thermal conductivity around 6.6 W/m·K [Calamaz, 2008] compared to ferrous materials around 50.7W/m·K [Andriya, 2012; Nandy, 2008] and aluminum alloys around 200W/m·K [Toh, 2004] at room temperature. The thermal conductivity of titanium could reach 20W/mK at high temperature [Calamaz, 2008]. This makes the dissipation of the heat generated during machining extremely slow. Konig et al. [1979] stated that about 80% of heat generation is absorbed by the cutting tool in machining Ti alloys while only 50% for machining ferrous materials as shown in Figure 2. Therefore, most of the heat is concentrated on the cutting edge of the tool when machining Ti alloys. The effect of the low conductivity of Ti alloys can be evident by comparing the reported cutting temperatures; ~1000°C [Ezugwu, 1997; Hartung, 1982] when turning Ti alloys, 600°C when turning ferrous materials [Dhar, 2002; 2007] and 200°C when turning aluminum alloys [List, 2005]. The relatively small chip-tool contact area (typically three times less than that of steels [Ramesh, 2008]) leads to high stress and stress gradient on the tool. The high cutting temperature could be slightly relieved by reducing the cutting speed and using a large amount of coolant. High thermal stress and cutting force with the confined contact area result in extremely high stresses near the cutting edge (within 0.5mm [Ezugwu, 1997]) as well as excessive tool deformation and failure. In addition, the high temperature increases the wear rate of dissolution, diffusion, and chemical reaction of a tool material with Ti alloys, often beyond the transus temperature

(882°C for pure titanium [Yang, 1999]) where the drastic change in physical properties occurs .

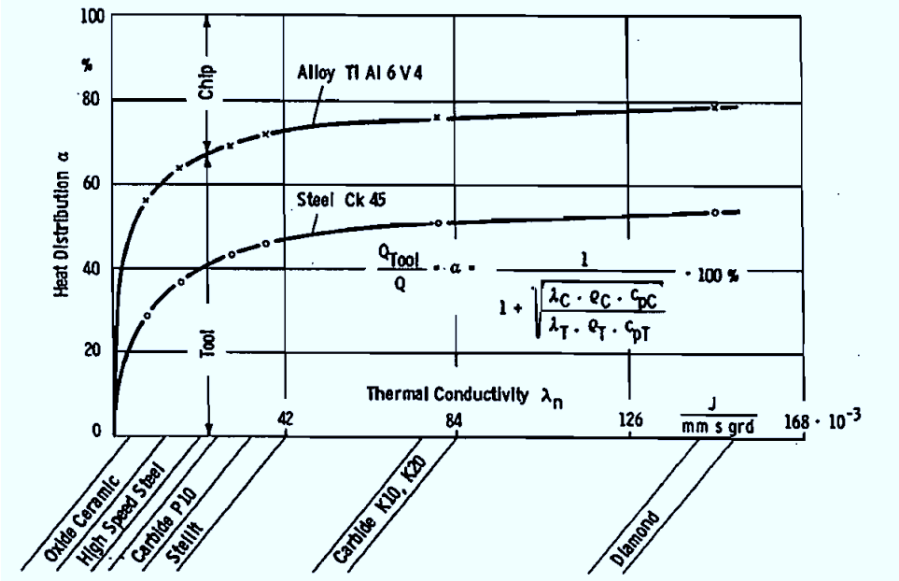

Figure 2: Heat distribution of thermal load on tool and chip in turning [Konig, 1979]

The surface integrity is another reason for reduction of tool life. It not only causes work hardening beneath the machined surface but also increases surface roughness. In particular, because of the high chemical affinity with a tool material, Ti alloys have a tendency to gall and weld to the tool, thus causing the fracture and tool geometry failure and resulting in premature tool failure. Applying coolant at high pressure helps overcome these problems. However, the high chemical reactivity of Ti with lubricants and additives creates other problems such as additional reaction possibilities [Andriya, 2012; Ezugwu, 1997; Rahman, 2003].

The low elastic modulus [Andriya, 2012; Machado, 1990] and high work hardenability of Ti alloys are additional obstacles in machining. The low elastic modulus of Ti alloys causes a higher deflection (twice as much as steels [Ezugwu, 1997; Machado, 1990]), which leads to chatter during machining.

Although most metals generates continuous chips in typical machining conditions, Ti alloys are notorious for segmented chips, experiencing plastic instability and discrete bursts of catastrophic thermoplastic shear in the primary shear zone. The frequency of the chip segmentation in α–β alloys is higher than those in α-alloys and β-alloys [Joshi, 2014]. Two shear bands was observed on each segmentation in □-alloys [Motonishi, 1987]. The chip morphology and serrated frequency of the chip also depends on cutting speed and microstructure [Gente, 2001; Joshi, 2014; Molinari, 2002; Rahim, 2008]. The lower chip segmentation frequency (larger spacing between segments) was found in a higher cutting speed [Bayoumi, 1995].

The challenges mentioned above are the principal problems associated with machining Ti alloys. When machining Ti alloys, the tool life dramatically decreases as the cutting speed increases. Thus, the tool materials should provide (1) high hot hardness, (2) good thermal resistance, (3) good thermal conductivity to reduce thermal gradient (4) good chemical inertness to minimize galling and welding, (5) high toughness to withstand vibration force, and localized stress and chip segmentation. The development of advanced coated tool materials has improved the machining productivity significantly in many materials such as ferrous and aluminum alloys but not for Ti alloys.

I.1.2 Motivation

In machining Ti alloys, beside PCD, the most successfully commercially available tool material for cutting titanium is straight grade (uncoated) carbide tools (WC-Co or WC). Even though many carbide tools with coatings are available in the market, the coated carbide tools are not effective in machining Ti alloys. The reason behind this

is not clearly discovered at the present time. Therefore, the selection of tool materials in machining Ti alloys is very difficult.

This thesis attempts to identify the wear mechanisms behind two main modes of tool wear, crater and flank wear, by understanding metallurgical structure of a selected Ti work material. This study can provide the fundamental knowledge in designing effective tool materials for machining Ti alloys.

I.1.3 Tool materials and tool wear mechanisms reported in literature

Over the past six decades, the production of Ti alloys has increased to meet the increased usage in aerospace applications. Many researchers have studied heavily the subject of machining Ti alloys to understand how to design effective tool materials and develop techniques to minimize machining cost. Numerous studies on the machinability of Ti alloys have been carried out. In fact, many hypotheses on tool wear mechanisms in machining Ti alloys have been introduced. Many researchers believe that both mechanical wear (abrasion, attrition) and chemical wear (dissolution, diffusion) are the main wear mechanisms in machining Ti alloys.

Tool materials for machining Ti alloys can be mainly classified in three groups:

- High speed steel tools (HSS)
- Coated and uncoated carbide tools
- Super hard tool materials: PCD and CBN

Narutaki et al. [1983] conducted turning experiment on both alpha (Ti-5Al-2.5Sn) and alpha-beta (Ti64) titanium alloys with straight carbide tools, CBN tools, cemented TiN tools, sintered Al_2O_3 tools, sintered and natural diamond tools, and TiC coated tools. He concluded that natural diamond tools offered excellent cutting performance

at the cutting speed of 1.67 m/s due to high thermal conductivity and low chemical reactivity in both dry and water based coolant conditions. The cutting speed for these diamond tools could go up to 3.33 m/s when applying sufficient coolant. Cemented TiN, TiC-coated, and CBN tools were not recommended. In addition, CBN tools caused very large and unusual groove marks on both the rake and flank faces. The sinter diamond tools exhibited similar performances as the carbide tools at high cutting speeds. Rahman et al. [2003] found that the binderless CBN tools without any cobalt binder yielded significant improvement in tool life compared to regular CBN tools, and even comparative to PCD tools at the cutting speed of 400m/min with high pressure coolant.

With the turning experiment of Ti64 with multilayer coated (TiN-Al_2O_3-TiCN-TiN) carbide tools, Ibrahim et al. [2009] stated that adhesive wear and welding were predominant wear mechanisms both in flank and the rake face. The adhesion wear took place after the coating had gone (worn out or flaked off). Corduan et al. [2003] conducted the machining experiment of Ti64 with PCD, CBN and TiB2 coated carbide. He recommended TiB2 coated carbide tools only for cutting speeds of less than 100 m/min. While PCD tools showed the lowest wear rate, CBN tools were only recommended for finishing cutting. He mentioned the delamination of TiB_2 coating is the main reason why the coated carbide tools did not work. Due to the mismatch in thermal expansions between coating and substrate, internal stress is generated as the temperature rises. The internal stress can intensify enough to break and flake off the coating.

I.1.3.1 *Dominant tool wear mechanisms*

In milling of Ti6246, Jawaid et al. [1999] claimed that the main wear mechanisms were dissolution/diffusion and attrition wear with PVD-TiN and CVD-TiCN+Al2O3 coated carbide tools which caused the carbide grain to pull out. Nabhani et al. [2001] conducted turning experiments of alpha-beta Ti48 with TiC/TiC-N/TiN coated WC, CBN (Cubic Boron Nitride) and PCD tools with “quick-stop” device to capture the in-situ tool condition during cutting process. By investigating tool wear appearance and coherent metallic layer, they concluded that diffusion/dissolution and attrition were the dominant tool wear mechanisms. The coating was not beneficial in resisting tool wear since these layers were rapidly worn off, leading to immediate exposure of the carbide substrate. The thickness of the protective adherent metal layer was strongly influenced by the balance between the diffusion rate of tool material through layer and the dissolution rate of the layer into work material.

I.1.3.2 *TiC protection layer*

Hartung and Kramer [1982] carried out a comprehensive study on turning Ti64 with various tool materials (WC, TiC, CBN, Al_2O_3, TiCN, PCD, etc.) and various coatings (HfO_2, HfC, TiC, HfN, TiN, etc.) on carbide inserts. They reported that Al_2O_3 had the highest tool wear and PCD was the best in terms of wear resistance. Uncoated carbide tools showed better performance than coated ones. A higher wear rate was recorded with all coated carbide tools. Furthermore, they claimed that the least soluble tool component controls the solubility of tool material. For example, the solubility of WC was not greater than that of C (0.6 at%) and less than that of W (100 at%). Thus, they concluded that dissolution and diffusion wear models of tool

constituents in titanium were not sufficient to describe the tool wear in machining of Ti alloys. They believed that, because of the high reactivity of Ti, the reaction layer, titanium carbide (TiC), is formed, which becomes the main factor to control tool wear. In the comparative research of turning Ti64 and Ti555.3 by Arrazola et al. [2009], the results supported the conclusion by Hartung and Kramer [1982]. He showed that the presence of TiC layer was less stable at the higher cutting speed (90m/min) which accelerated tool wear.

I.1.3.3 *Cobalt diffusion*

A cobalt-based diffusion tool wear model was introduced by Hua et al. [2005]. They carried out the turning experiment with Ti64 with uncoated carbide tools with two distinct cobalt contents (6wt% and 10wt%). In the model, the wear rate was calculated as the ratio of flux rate of diffused cobalt at tool-chip interface over density of cobalt. He found that the results of the model agreed well with the experimental data. Furthermore, the simulation indicated that the temperature increases with the increase in cutting speeds while the chip contact length decreases, which leads to rapid tool wear. The maximum depth of crater profile coincided with the peak temperature which moved closer to the tool nose as the cutting speed increased.

I.1.4 Phases and microstructure of Ti alloys

I.1.4.1 *Phases in Titanium alloys*

It is known that the cementite phase (Fe_3C) is present as the main abrasive contributing to the flank wear in machining ferrous materials. Titanium can exist in alpha, beta and rarely omega phases. Figure 3 shows the phase diagram as a

function of temperature and pressure. However, the phase diagram is strongly influenced by the alloying elements and their content as shown in Figure 4. The mechanical properties and hardness of Ti alloys influence the size, composition, and volumetric fraction of α, β and ω-precipitated phases. No significant hard phase exists in Ti alloys, which make hard to pinpoint the root cause of tool wear. In addition, the microstructural features, which are affected by heat treatment and alloying elements, also plays very important role in tool wear in machining Ti alloys.

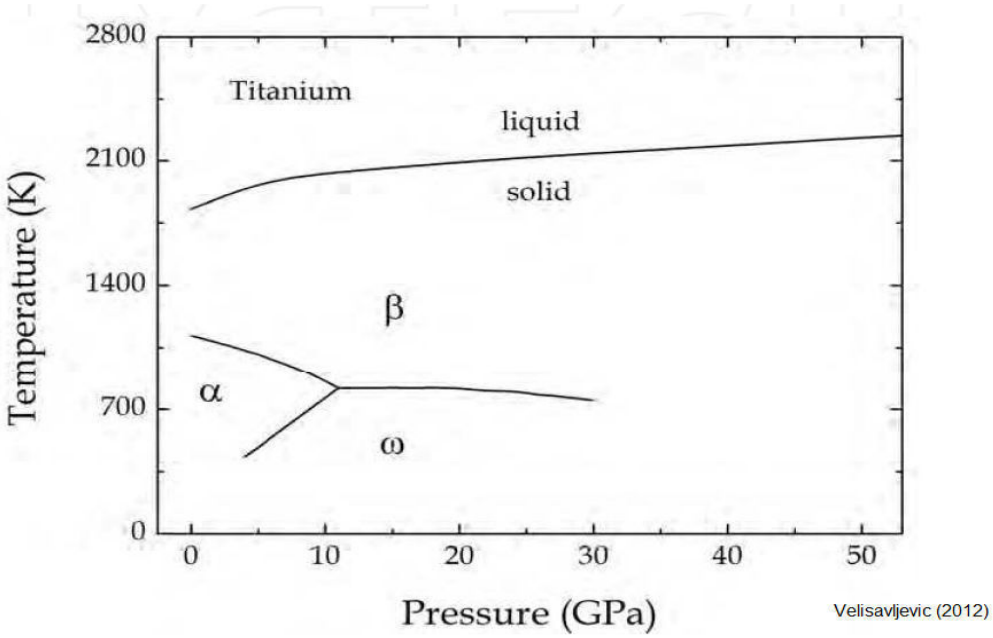

Figure 3: Phase diagram of titanium [Velsavjevic, 2012]

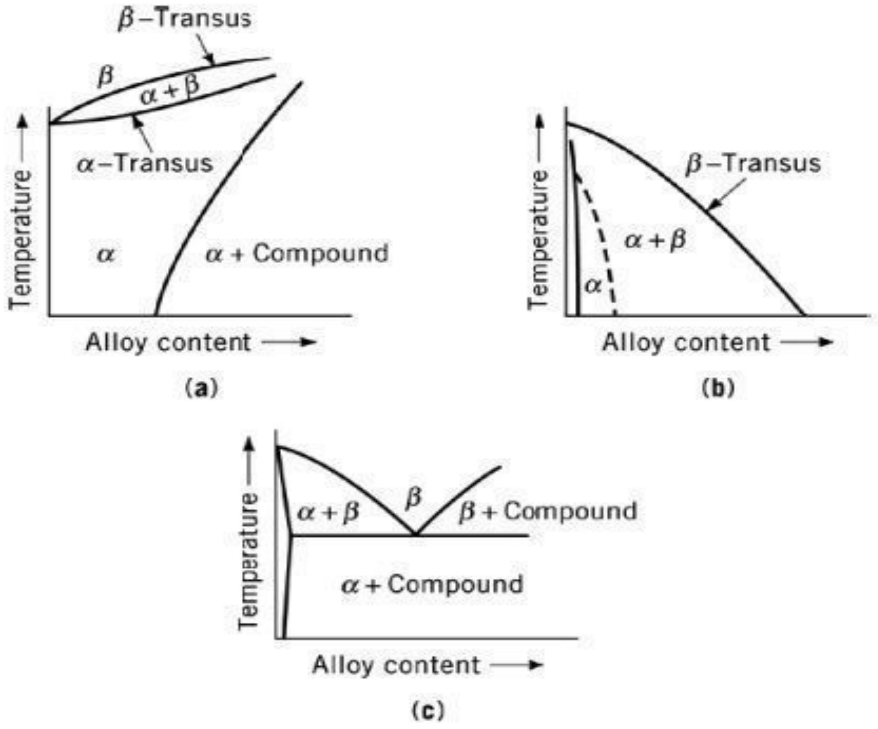

Figure 4: Typical phase diagram of Ti alloys: a) α-stabilized system, b) β-stabilized isomorphous system, c) β-stabilized eutectoid system [Frees, 2011]

Among the three phases of Ti, the α-phase with HCP structure is stable at room temperature and pressure without any alloy stabilizer. At room temperature, the hexagonal unit cell of the α-phase has the lattice parameters a (0.295 nm) and c (0.468 nm) as shown in Figure 5. The c/a ratio for pure α-phase (1.587) is smaller than the ideal ratio for the archetypal hexagonal crystal structure (1.633). Crystalline structures accommodate plastic deformation along certain planes and directions within the crystal lattice. As a general rule, the slip occurs in the densest packing crystal planes (number of atoms/area) along the directions of the highest linear density (atom/length). The α-phase has four slip planes, ({0001}, {$1\bar{1}00$}, {$1\bar{1}01$}, {$\bar{1}\,\bar{1}\,22$}, {$1\bar{1}01$}) and two slip directions (<$11\bar{2}0$>, <$11\ \bar{2}\,3$>) making to 24 possible slip systems as shown in Table 1. To determine which slip system is likely more active,

the critically resolved shear stress (CRSS) and the geometric relation between the slip plane and the applied stress are used. The CRSS shown in Figure 7 is the in-plane stress component required for dislocation movement as a function of temperature. The predominant slip mode in the α phase is in {$1\bar{1}00$}, {0001}, {$1\bar{1}01$} along <$11\bar{2}0$> direction. The highest CRSS is required for slip <11 $\bar{2}$ 3> direction. Because of the intrinsically anisotropic character, the α phase has pronounced variation of the elastic modulus (E) and hardness (H) as a function of the angle γ between the c-axis of the unit cell and load direction. The elastic modulus and hardness reach the highest values along the c-axis but the lowest in perpendicular direction to the c-axis as presented in Figure 8. Furthermore, the elastic and shear modulus and hardness decrease with the temperature as shown in Figure 9. The α-phase has two variational phases, martensite structure (α′) and orthorhombic martensite (α″).

The beta (β) phase is a metastable phase with body centered cubic (BCC) structure. It has more slip systems than the α-phase making it more ductile and easier to deform. The elastic modulus, shear modulus and hardness of the β phase are well below that of the α phase [Meier, 1992].

The omega (ω) phase only presents in metastable β-alloys. The isothermal ω particles have either an ellipsoidal or a cuboidal shape. It is well accepted that, the ω phase has the highest elastic modulus and hardness followed by the α and α′, phases [Zhou, 2004, 2008]. Many studies [Gabriel, 2013; Hickman B.S., 1969; Hsu, 2013; Jon, 1972; Jones, 2009] revealed that the ω (ellipsoidal) precipitates forms at the beginning of the aging treatments and quenching β alloys from the beta field.

Although the ω-phase cannot be identified with optical analysis or the X-ray diffraction (XRD) pattern, it can be investigated by the selected area diffraction (SAED) patterns and bright-field image with transmission electron microscopy (TEM) analysis.

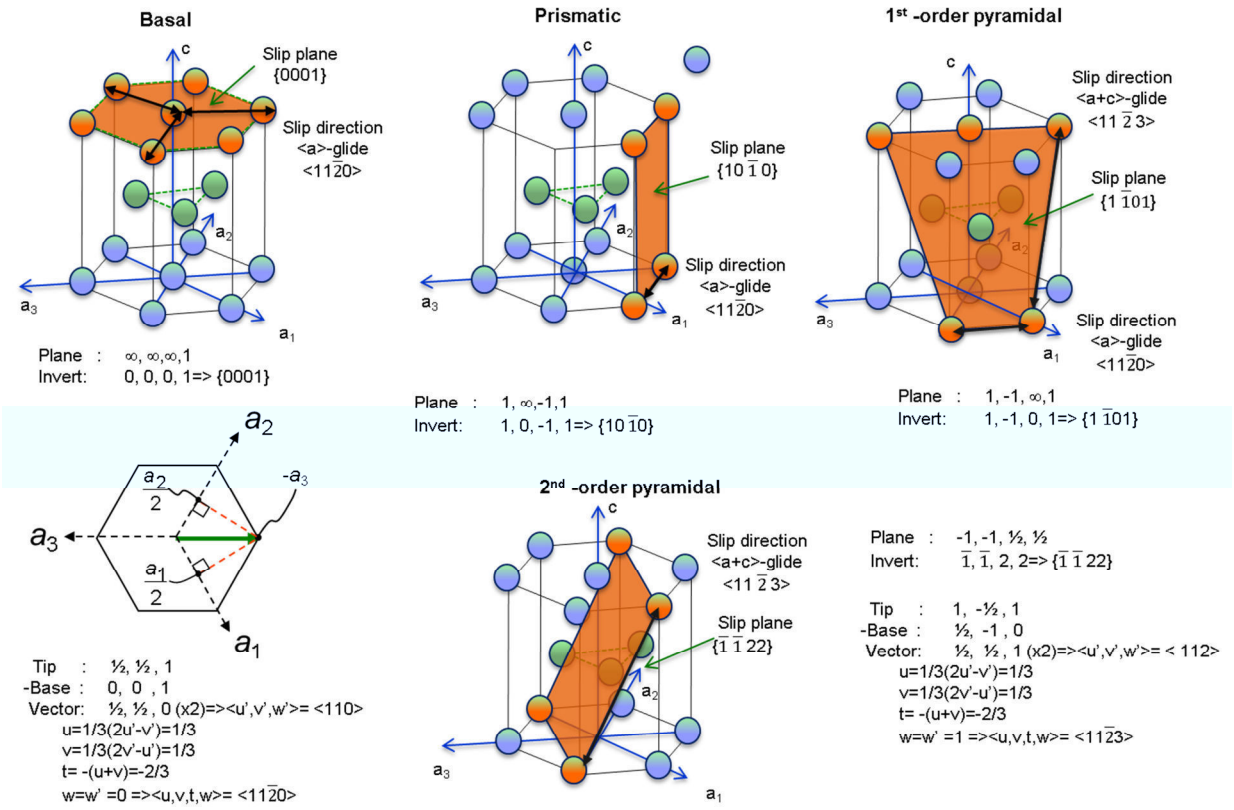

Figure 5: Alpha phase and its slip systems

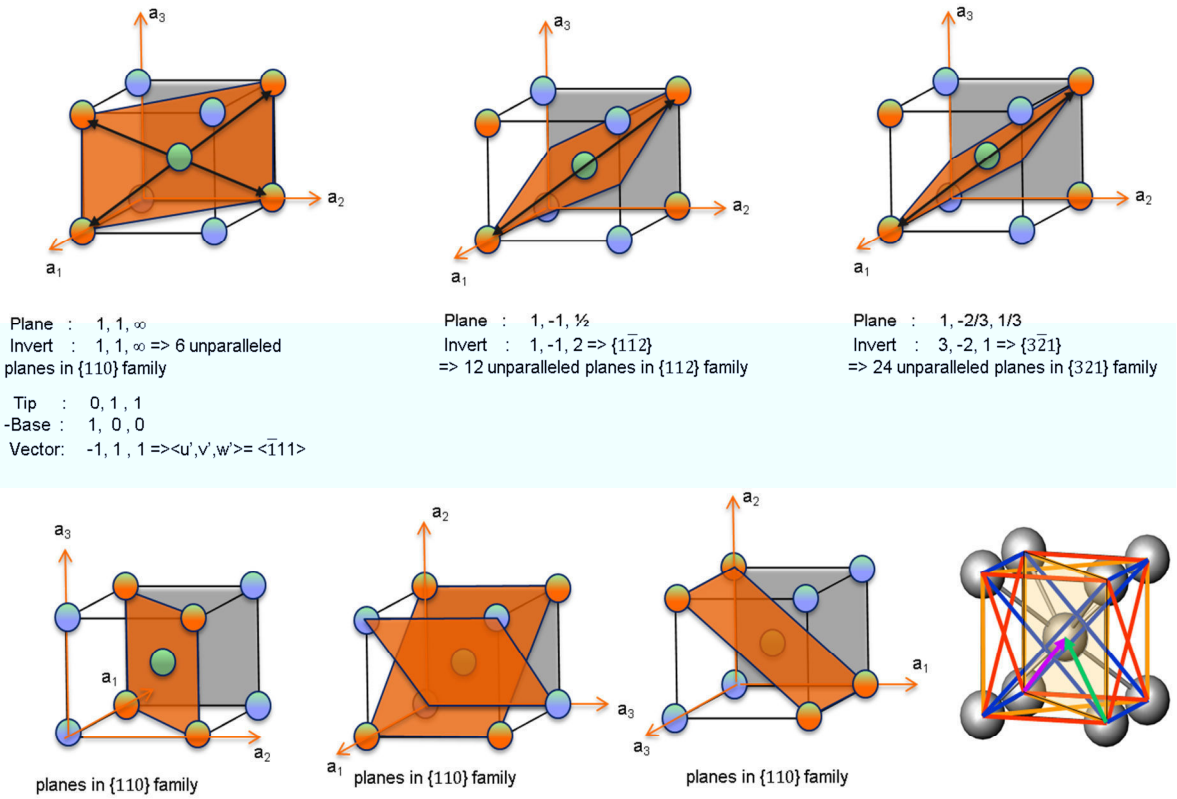

Figure 6: Beta phase and its slip systems

Table 1: Slip systems in alpha and beta phase

	Slip plane family No. of variants	Slip direction No. of variants	Total no of slip systems Designation
α phase	{0001}: 1	<a> or <11$\bar{2}$0>: 3	3 “Basal”
	{1$\bar{1}$00}: 3	<a> or <11$\bar{2}$0>: 1	3 “Prismatic”
	{1 $\bar{1}$01}: 6	<a+c> or <11$\bar{2}$3>: 1	6 “1st order Pyramidal”
	{1 $\bar{1}$01}: 6	<a> or <11$\bar{2}$0>: 1	6 “1st order Pyramidal”
	{$\bar{1}$ $\bar{1}$ 22}: 6	<a+c> or <11$\bar{2}$3>: 1	6 “2nd order Pyramidal”
β phase	{110}: 12	<$\bar{1}$11>: 1	12
	{112} : 12	<$\bar{1}$11>: 1	12
	{321}: 24	<$\bar{1}$11>: 1	24

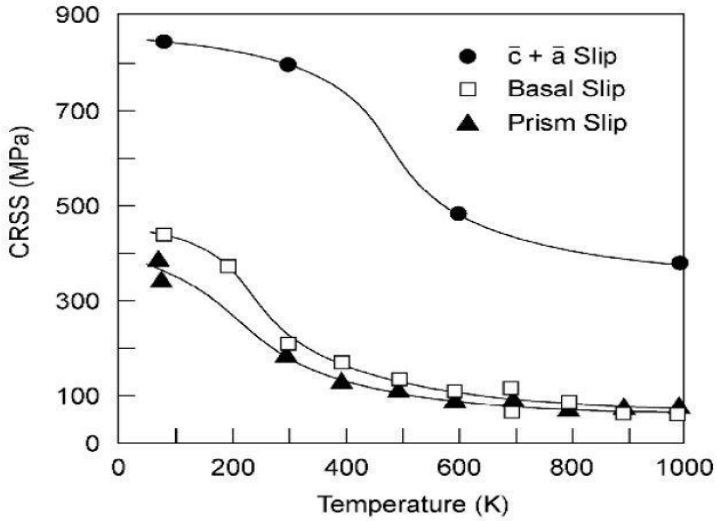

Figure 7: Critical resolved shear stresses (CRSS) as function of temperature for slip systems in α phase [Lütjering, 2003]

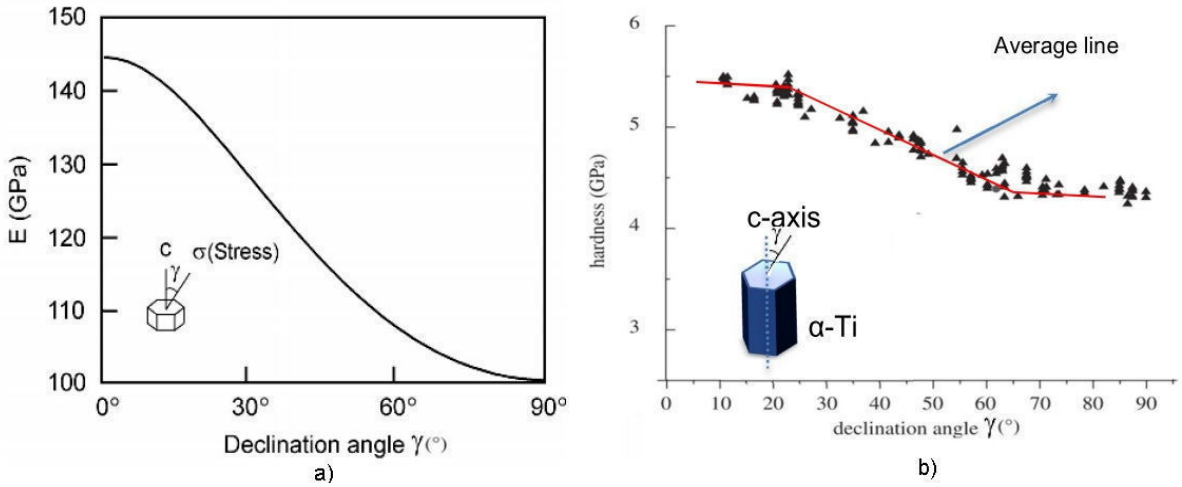

Figure 8: a) Elasticity (E) and b) hardness as a function of the angle γ between the c-axis of the unit cell and load direction [Lütjering, 2003; Britton, 2009]

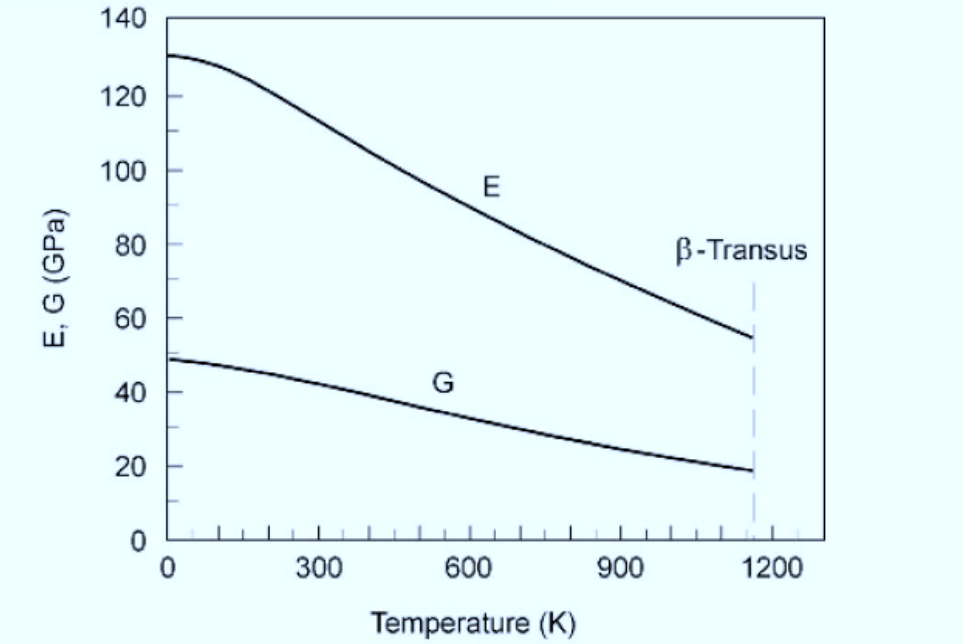

Figure 9: Elasticity (E) and shear (G) modulus of alpha phase as function of temperature [Lütjering, 2003]

I.1.4.2 *Phase transformation in Titanium alloys.*

The phase transformation happens with the transition metals in the group IVB such as Ti, Zr, Hf under applied pressure (p), temperature (T) or both (p, T). The α ⇔ β is more favorable with temperature while pressure is more critical for β ⇔ ω transformation.

The α → β transformation happens when the temperature reaches transus temperature (100% β phase). The transus temperature is strongly influenced by interstitial and substitutional alloy ingredients.

The β phase transforms to α phase during continuous cooling of the α-β Titanium alloys from above transus temperature. Depending on the cooling rate, the phase transformation mechanism could be β → α for slow cooling rate and diffusionless transformation β → α' for fast cooling rate at temperatures below 700-750 °C.

Quenching Ti64 alloy from the 750–900 °C temperature range produces an orthorhombic martensite (α″).

The β ⇔ ω transformation is reversible and diffussionless. The phase decomposition mechanism of the metastable beta phase in this material follows the classical behavior for this type of alloy: route 1 (β → β + ω + α → β + α) and route 2 (β → β + ω → β + ω +α → β + α) [Grabriel, 2013].

I.1.4.3 *Microstructure of α + β Ti alloys*

The properties, hardness and machinability of each Ti alloy are directly related to its microstructure. The dual phase (α + β) Ti alloys have different types of microstructure depending on the heat treatment (solution treated and aged temperatures; cooling rate and cooling rate. Four common microstructures are milled annealed, equiaxed structure, fully lamellar structure and bi-modal (or duplex) structure which is a combination of equiaxed and lamellar structure as shown in Figure 11. Equiaxed structure has good creep and crack growth resistance, but suffers from low tensile ductility and moderate fatigue properties. The bi-modal structure is characterized by high ductility and fatigue strength, high yield and tensile stress. High resistances to crack propagation and fracture toughness are the notable properties of a fully lamellar structure [Zhang, 2014]. The bi-modal microstructure is typical in the metallurgical processing of α + β alloys when heat-treated in the α + β field as shown in Figure 10 [Lütjering, 2003]. The fully lamellar structure can be achieved by heat treatment typically above beta-transus temperature (beta annealed) then slowly cooled in furnace or in the air. In this microstructure, the thickness of Widmanstätten α-laths, colony size, and prior grain size are important parameters

that can be controlled by the cooling rate. The fully lamellar structure is believed to be harder and more difficulty to machine than other microstructures.

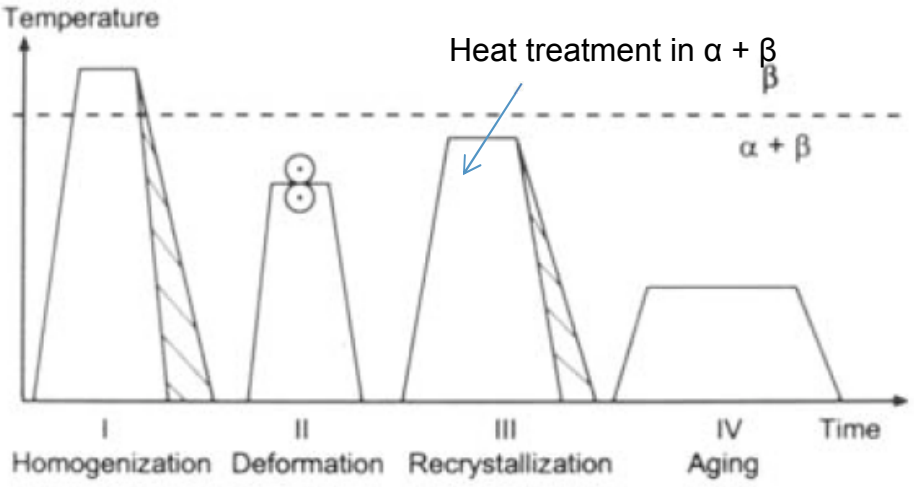

Figure 10: Schematically processing for bi-modal structure of two phase α + β Ti alloys[Lütjering, 2003].

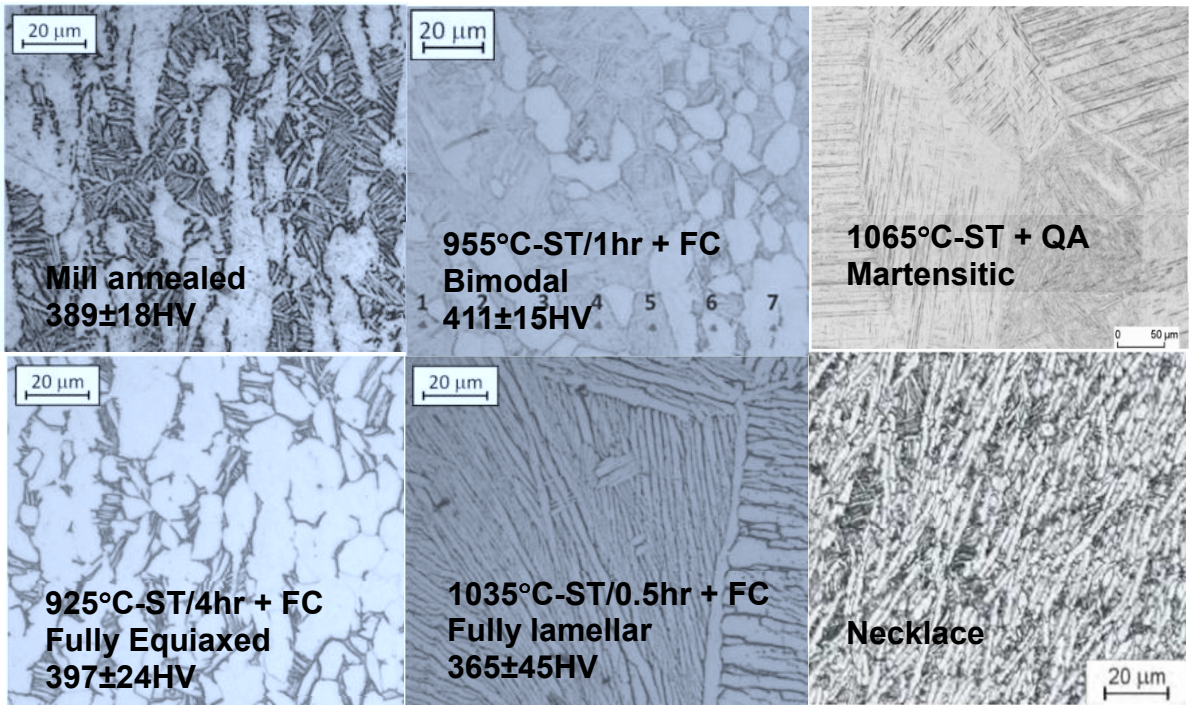

Figure 11: Various types of microstructure of Ti64 alloys [Attanasio, 2013; Maciej Motyka, 2012; Meyer, 2008]

I.2 EXPERIMENTAL SETUP AND PROCEDURES

I.2.1 Turning experiments of Ti64 alloy

The turning experiments were conducted with Ti-6Al-4V with the average hardness of 326HV on Yama Seiki GA-30 lathe using tungsten carbide (WC-6wt%Co) and PCD inserts. The tests were in dry condition to understand the wear mechanisms between Ti alloy and cutting tool. The tool insert geometry was ANSI designation CNMA-432.

To investigate wear evolutions in both the rake and flank faces, all the inserts were flat rake face without chip breaker. Two grades (YD101, YD201) of Zhuzhou Cemented Carbide Cutting Tools, Co, LTD, (ZCCCT, Zhuzhou, Hunan, China) brand uncoated carbide inserts were chosen for the test for their flat rake face. Grade YD201 was a straight grade carbide containing approximately 94% WC and 6% Co. The average grain size was 2μm. Carbide grade YD101 had a composition consisting of 93.6% WC, 0.15%NbC, 0.25%TaC, and 6%Co. The average grain size was 1μm.

Three PCD grades and two tungsten carbide grades were used as tool inserts in this study. The PCD tips were Compax® 1200 and 1500 grades, 92% diamond by volume, with average diamond grain size of 1.5 μm and 25 μm, respectively, manufactured by Diamond Innovation. Shape-Master Tool Company, Kirkland, IL, brazed each PCD tip onto an ISO CNMA120408 carbide base. The 1200 grade PCD inserts with 0° rake angle had an average grain size of 1.5μm. Two grades, 1210 and 1510, of PCD inserts with a 10° positive rake angle. The feed rate remained constant for all samples at 0.127 mm/rev (0.005 in/rev). Two sets of experiments with the

depth of cut (DOC) of 0.635 mm (low DOC) and 1.2 mm (high DOC), respectively, were conducted to see the effects of DOC to cutting process and tool wear. The information for tool grades and DOC was summarized in Table 2. The low DOC showed wear at the nose while the high DOC showed traditional flank wear. Lead angle refers to the angle between the imaginary line perpendicular to the direction of feed and the line parallel to the cutting edge of the insert. Rake angle in this context refers to the inclination angle in the tool holder that gives the insert its clearance with respect to the work piece. For consistency, both of the inserts were run with a -5° lead angle and a -5° rake angle with respect to the work material. The turning setup and the chip flow direction respect to tool were presented in Figure 12. Tables 1 and 2 below lists the cutting time used in the turning tests for carbide and PCD inserts at each cutting speeds.

Table 2: Tool grades and DOC used

Tool	Grade (Tool ID)	Rake angle	Grain size (μm)	Thermal conductivity (W/m·K)	DOC (mm)
Carbide	YD101	0°	1	65	0.635 & 1.2
Carbide	YD201	0°	2	75	0.635
PCD	PCD1200	0°	1.5	450	0.635
PCD	PCD1210	+10°	1.5	450	1.2
PCD	PCD1510	+10°	25	450	1.2

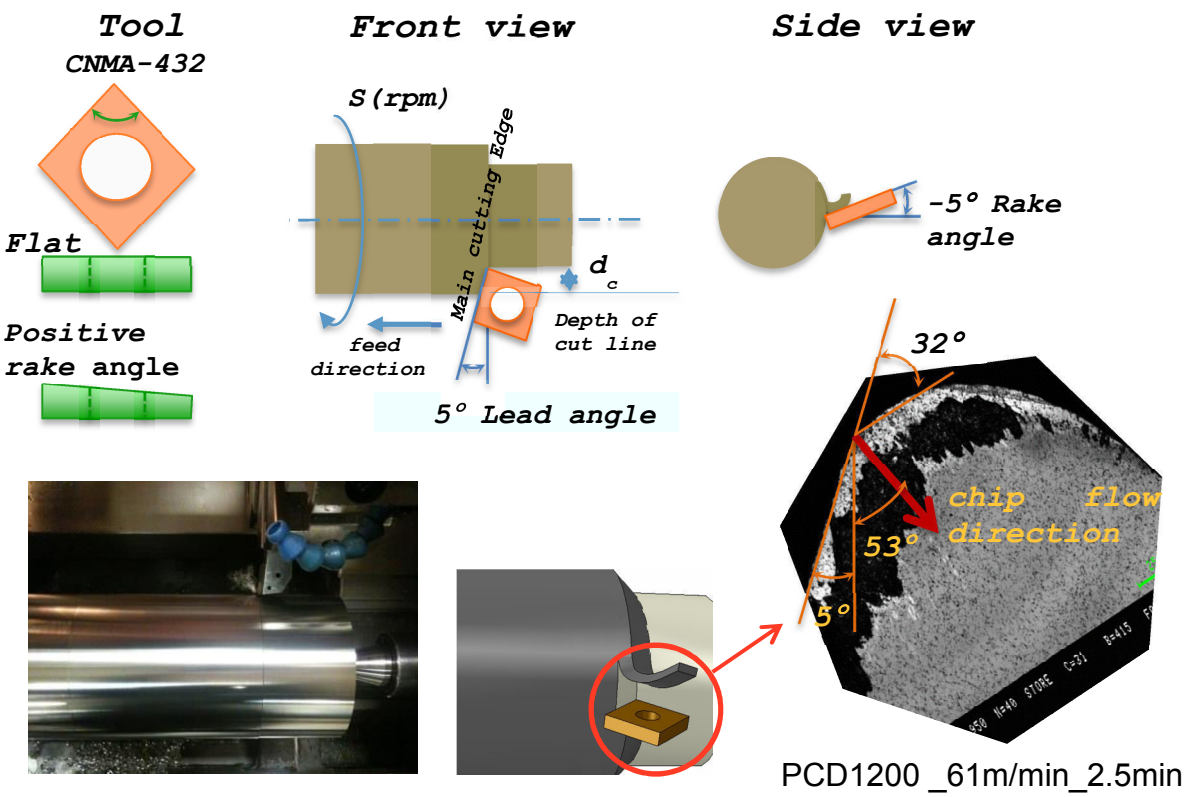

Figure 12: Ti64 alloy turning configuration and chip flow direction

Table 3: Cutting time for the second set of experiment at high DOC (d_c= 1.2 mm)

Cutting speed / Inserts	61m/min (200sfm)	91m/min (300sfm)	122m/min (400sfm)
YD101	2.4 min 5.2 min 6.8 min	1.6 min 3.5 min 4.5 min	0.6 min 1.1 min 1.8 min 1.9 min 2.2min 2.6 min (chipped) 2.7 min (chipped) 3.5 min (chipped)
PCD1510	2.5 min 5.4 min 6.8 min	1.6 min 3.5 min 5.4 min	1.2 min 2.7 min 3.5 min

Table 4: Cutting time for the first set of experiment at low DOC (d_c= 0.635 mm)

Cutting speed / Inserts	61m/min (200sfm)	91m/min (300sfm)	122m/min (400sfm)
YD101	3 min (chipped) 6 min (chipped) 9 min 12 min	1 min 2 min 3 min (chipped) 4 min	30 sec 1 min (chipped) 2 min (chipped)
YD201	3 min (chipped) 6 min 9 min (chipped) 12 min	All Inserts Chipped	30 sec 1 min (chipped) 2 min
PCD1200	6 min 12 min 18 min 24 min 30 min (chipped)	No Inserts Tested	1 min (chipped) 2 min 3 min 4 min
PCD1210	6 min 12 min 24 min	4 min 6 min 8 min	2 min 3 min 4 min

I.2.2 Confocal Microscopy

In this work, Ziess LSM 210 Confocal Laser Scanning Microscope (CSLM) was used to capture both 2-D and 3-D images of crater and flank wear. This particular confocal system can work in confocal, non-confocal and conventional optical modes.

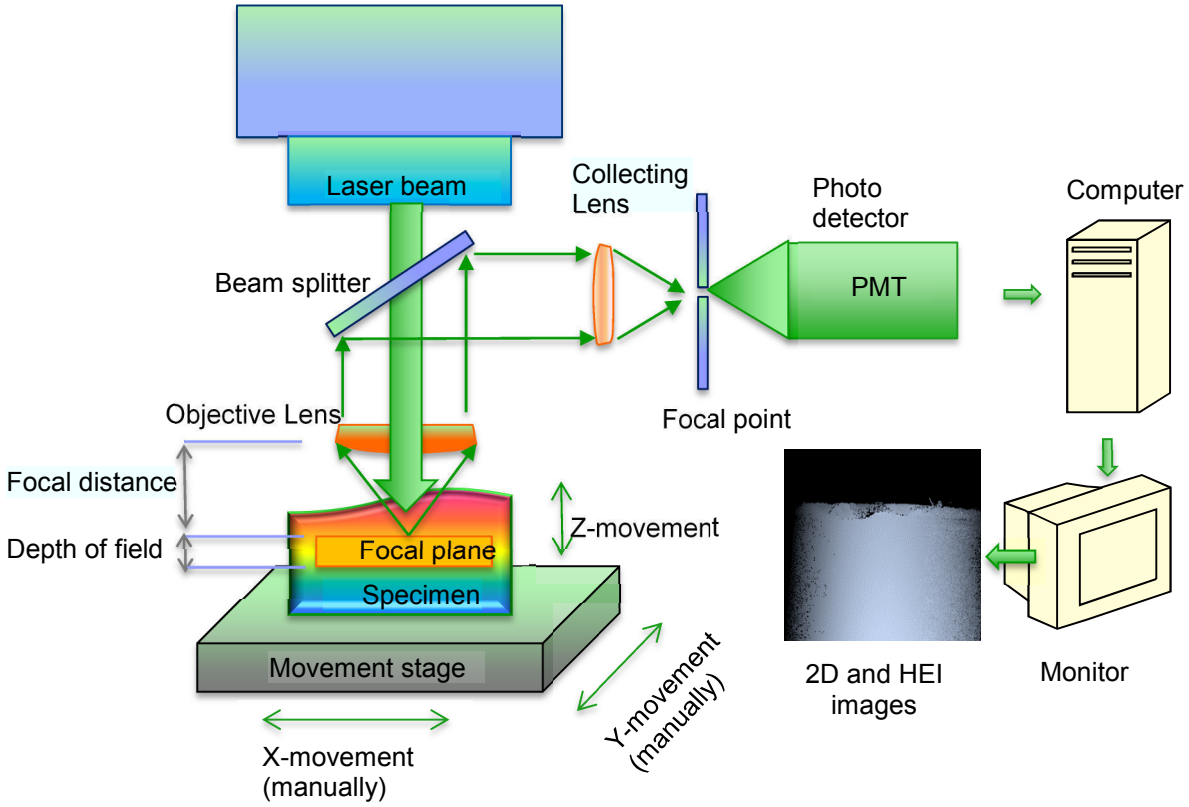

Figure 13: Operating principal of a confocal microscopy

Each 2-D picture was the overlapping image of 50 regular microscope pictures taken through the wear depth using Z-series function of CSLM. That revealed more information of the wear region at high to low points.

The CLSM is used to obtain the surface information from a very thin ‘‘optical slice’’ at a focal plane by eliminating the reflected light from above and below that plane. For this research, the number of optical slices (50-100), step size (500-3000nm) and objective (100X, 200X) were used to construct the comprehensive 3D wear surfaces. By manipulating a stack of optical slices, a grayscale encoded z-matrix [$z(x,y)$] that contained the height information of the worn surface was generated as an output image of the surface. The particular image is called a height encoded image (HEI). The 3D wear topographies as a three-dimensional mesh of (X, Y, Z) data of both the

rake and flank faces of the cutting tools were created from the HEI images. With the similar process, the 2D images are generated in a much higher quality, which have the detailed information to analyze the wear patterns on the inserts.

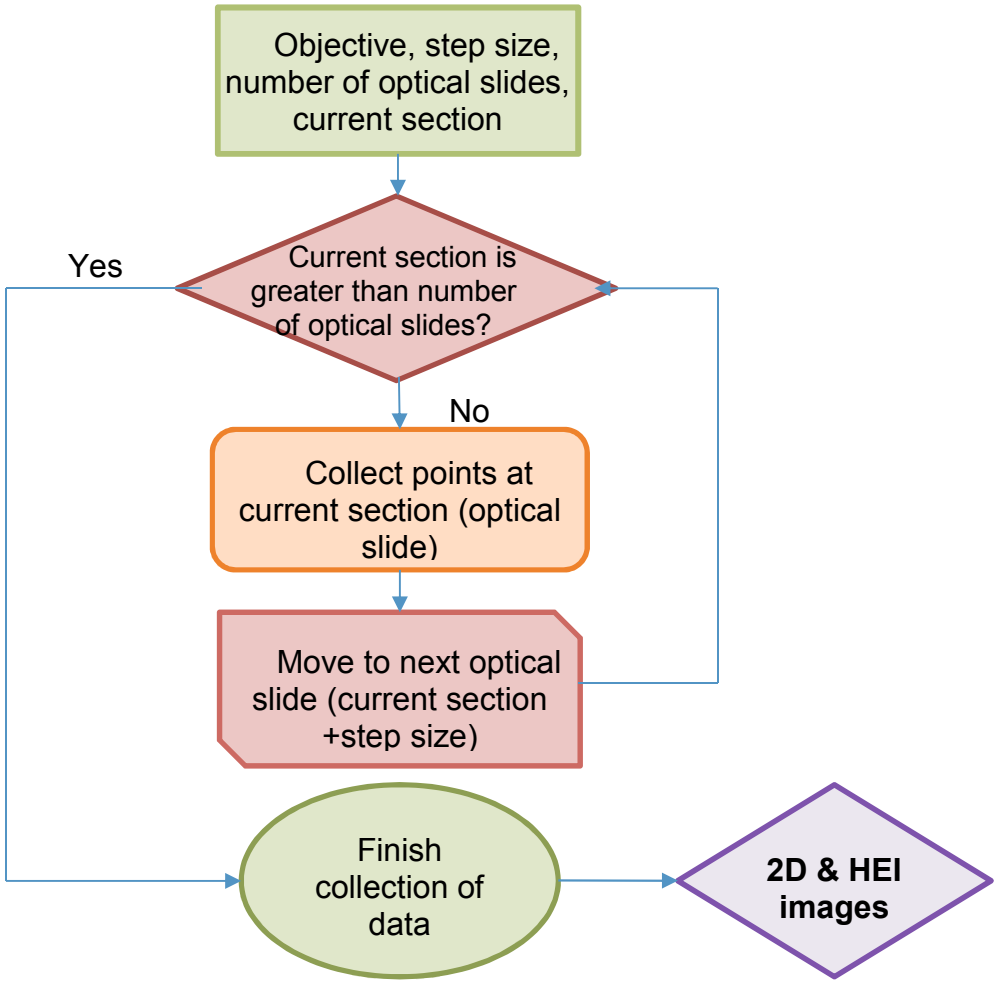

Figure 14: Flow chart of data collection with confocal microscopy

To reduce the noise in the capturing process, a wavelet filtering procedure described by Olortegui-Yume and Kwon [Olortegui-Yume, 2010; Park, 2011] was used to process the HEI images in Matlab. The main advantage of the wavelet transform for image processing is to extract the surface topography clearly from the raw image data without losing any surface details. In this work, the two-dimensional discrete wavelet transform (2D-DWT) was used in a multi-resolution scheme with a

two-channel filter bank, which consisted of a pair of filters, low-pass and high-pass, based on the chosen mother wavelets, Daubechies7 (db7) [Rioul, 1991].

Finally, the combination of multiple 2D wear profiles extracted from the 3D topographies for each cutting time provided the quantitative data on wear surfaces, which can be accumulated to construct the wear evolution as a function of time. For the crater wear on the rake face, the 2D crater wear profiles were taken in the direction of chip flow to insure maximum wear profiles. For nose and flank wear, 2D wear profiles were taken along the y direction at various x-positions (1^{st} to 256^{th} section) as shown in Figure 15. The PCD inserts with +10° rake angle inserts were placed on the 10° incline stage to measure them based on the horizontally flat plane.

The tool wear measurement was conducted both before and after an adhered layer (most likely Ti and TiC) was removed with a weak hydrofluoric acid solution (HF at 10 vol%).

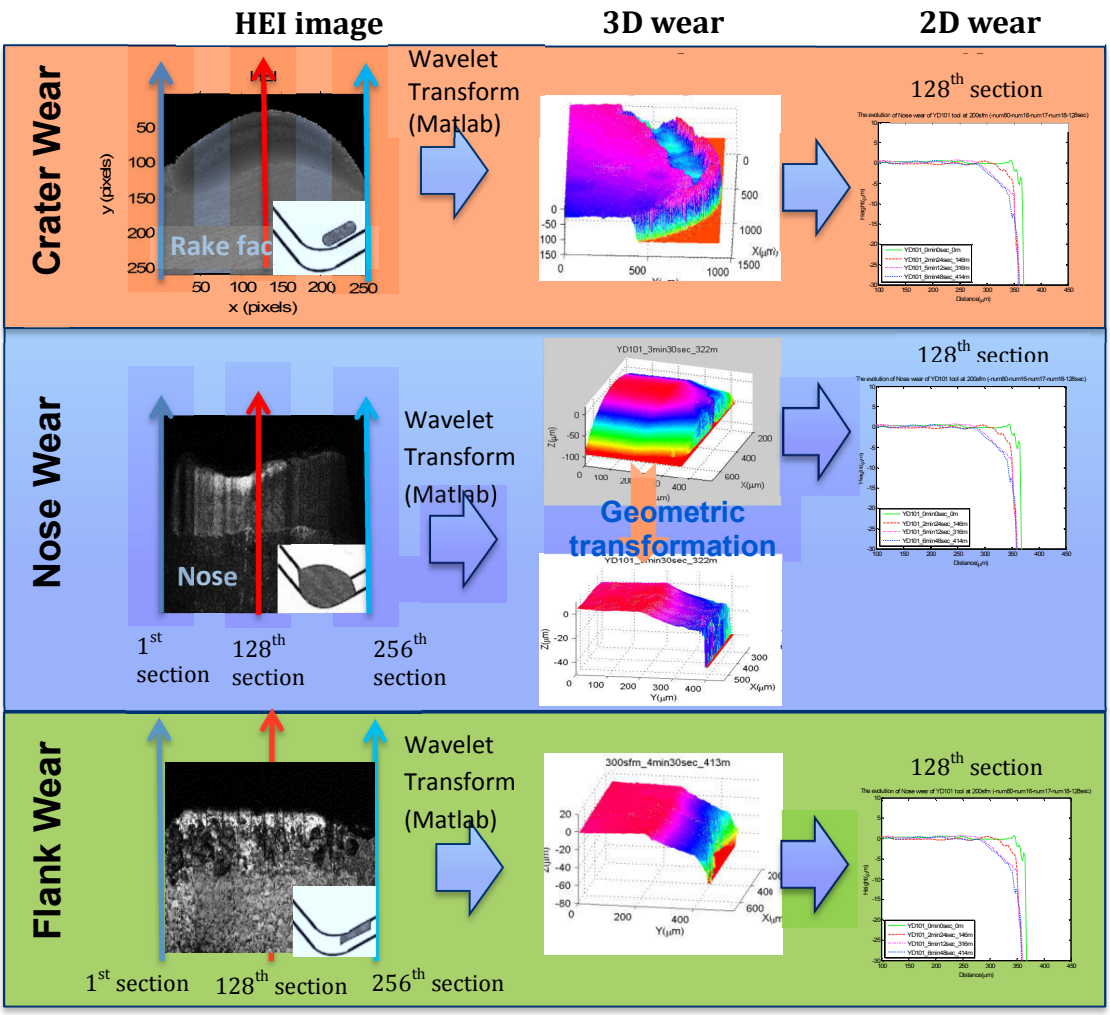

Figure 15: Measurements of tool wear at the rake face, nose and flank face

I.2.3 SEM picture and element mapping

The optical view and the element mapping of worn tools were captured and characterized before and after cleaning the adhesion layer using JEOL 6610LV Scanning Electron Microscope with Energy Dispersive X-ray Spectroscopy. The accelerating voltage and working distance were 20kV and 15mm, respectively.

I.3 EXPERIMENTAL RESULTS AND DISCUSSION

I.3.1 Wear Characteristics of tools inserts at low DOC

The machining experiments were divided into two sets based on the DOC. The crater wear characteristic of the first set with the low DOC was reported in detail elsewhere [Schrock, 2012; 2014]. In this thesis, the flank wear of the first set was studied and presented. Furthermore, the second set of the machining experiments with high DOC was conducted to study the wear characteristics of both flank ad crater wear. Figure 16 presents the definitions of crater and flank wear studied in this research.

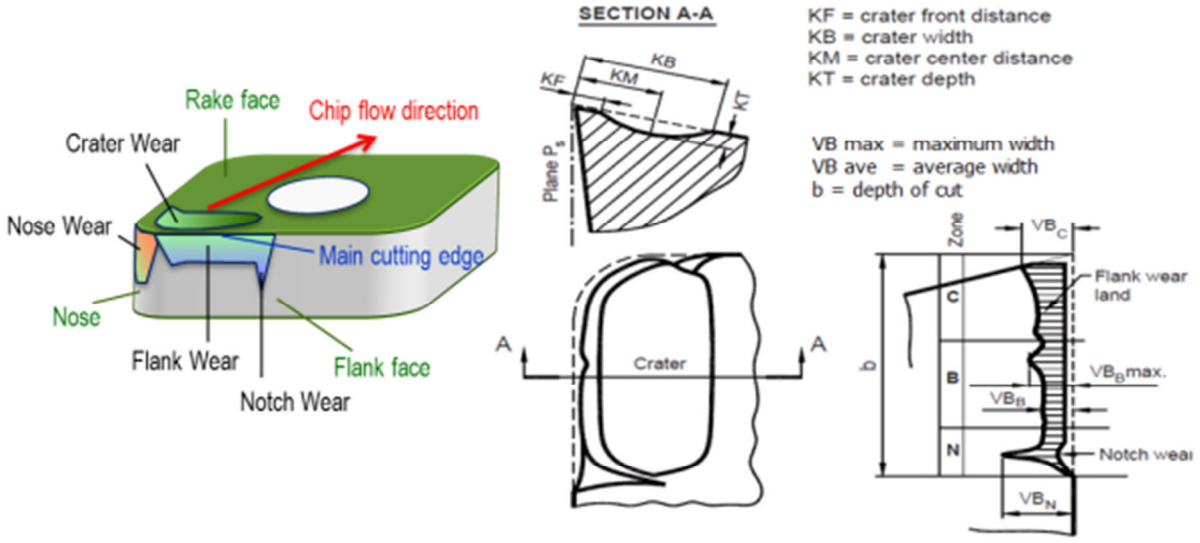

Figure 16: Types of tool wear according to standard ISO 3685:1993

I.3.1.1 *Crater wear at low DOC*

The maximum crater depths of carbide and PCD inserts from the first set of experiments are summarized in Table 5. The depths were calculated from the 2D-profiles of craters reported in [Schrock, 2012; 2014] after excluding the fractured and

chipped inserts. These data were used to compare those of high DOC presented in the next chapter.

Table 5: The maximum crater wear depth (μm) of the first turning tests with d_c=0.635 [Schrock, 2012; 2014]

Tool / Cutting time	YD101	YD201	PCD1200	PCD1210
	61 m/min (200sfm)			
3min	--	--	--	---
6min	17	24	--	--
9min	26	33	--	--
12min	45	42	--	--
	91 m/min (300sfm)			
1min	11	--	--	--
2min	35	--	--	--
3min	50	--	--	--
4min	64	--	--	--
5min	--	--	--	--
7min	--	--	--	--
	122 m/min (400sfm)			
1min	15	14	--	--
2min	62	--	--	--
3min	--	--	--	--

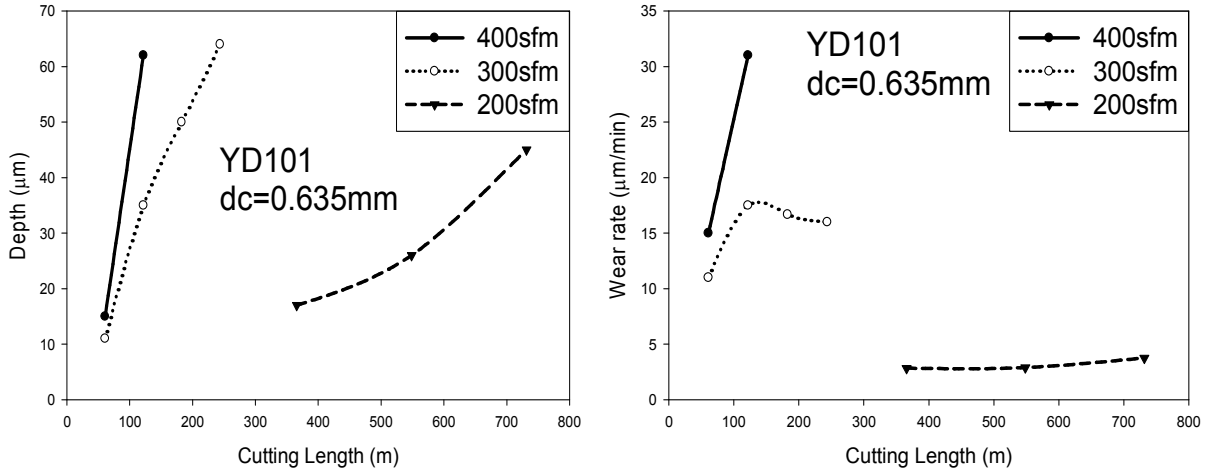

Figure 17: The maximum depth and wear rate of crater wear on carbide inserts (YD101) at low DOC

I.3.1.2 ***Nose wear at low DOC***

Nose wear and flank wear land were also analyzed at various cutting conditions (cutting speed and time). However, the first set generates notably the nose wear, which is slight different from traditional flank wear. It should be noted that the depths of nose wear along the tool curvature were much smaller than the tool radius. Therefore, the evolution of nose wear was not clearly represented in 3D topographies in its natural view. For a better representation, the 3D nose wear topographies are presented after the curved surface has been flattened by the geometric transformation as shown in Figure 18. In this transformation, the highest point for each profile along X-axis direction in the unworn area was determined based on the tool geometry. For each point along the X-profile, an addition in height (h) was calculated based on the tool radius (r) and the difference in x direction between this point and the highest point as shown in Figure 18. This transformation only affected the 3D view of the nose wear. The 2D wear profiles nose wear were plotted from initial data without any effect of geometric transformation.

The nose wear on carbide YD101 and PCD1200 inserts at various cutting speeds as a function of time were presented in Figures 19-23. Each figure consists of three sets of images from CLSM, (2D images, 3D images and 2D wear profiles at 128th location in X direction of the HEI images which consist 256 X-locations (or the crosstion at middle of measured wear region), see Figure 15). Each set contains from the fresh insert to the worn inserts after cutting for the longest time at each machining condition. The 3D images from CLSM show that the flank wear are characterised by two major damages, the scoring marks and the chipping in both macro- and micro-scales. For low and medium cutting speeds, the carbide inserts show smoother appearance on the wear land than PCD inserts. At the high cutting speed, as expected, both carbide and PCD inserts experienced more extensive chipping on the flank face. Figures 24 - 28 show the average nose wear land (V_{Bavg}) for both grades of carbide and PCD inserts. Despite of some missing data due to the macro chipping on most PCD1200 at 91m/min, the obtained data showed the general trend in flank wear. It should be pointed out that many smooth and wide scoring marks (width > 40μm) were obtained on the flank wear of the carbide inserts at medium and high cutting speeds. The scoring marks on the PCD inserts were much more narrow and much less in number.

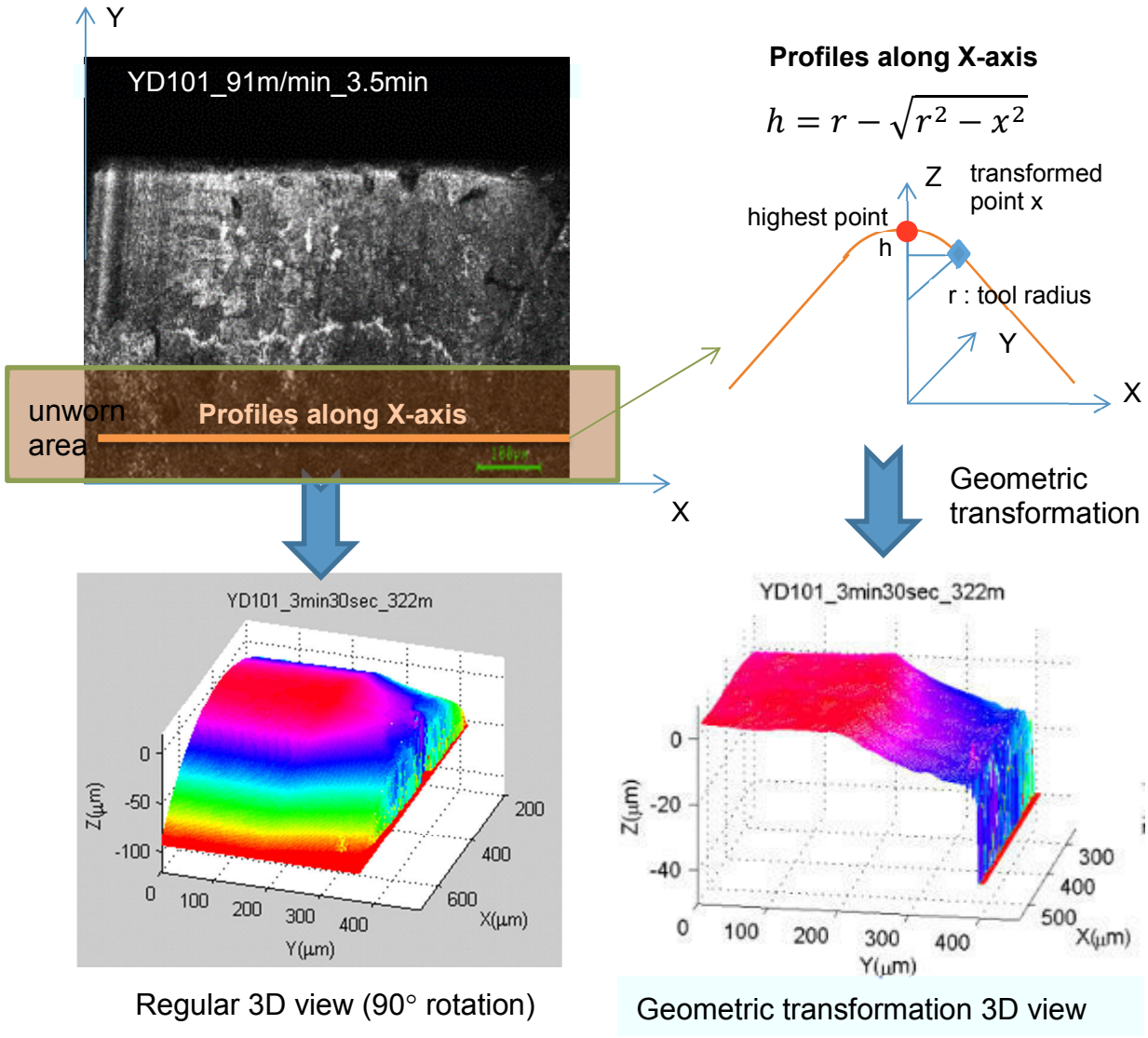

Regular 3D view (90° rotation)

Geometric transformation 3D view

Figure 18: The geometric transformation on the nose of tool inserts in 3D view.

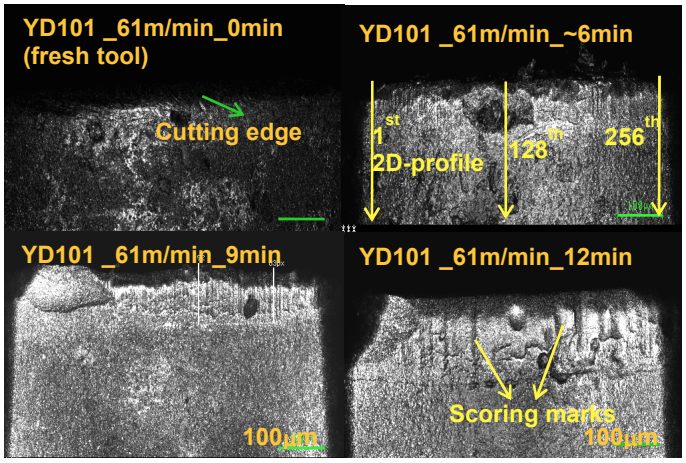

a) 2D image

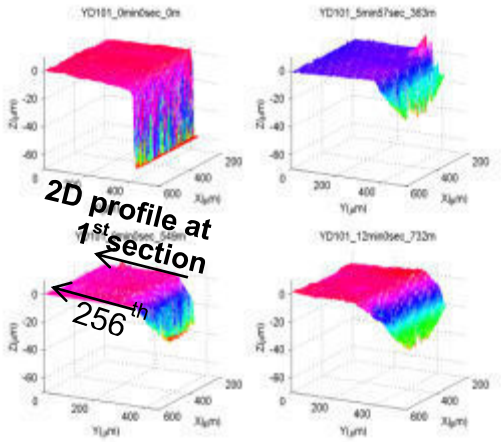

b) 3D image

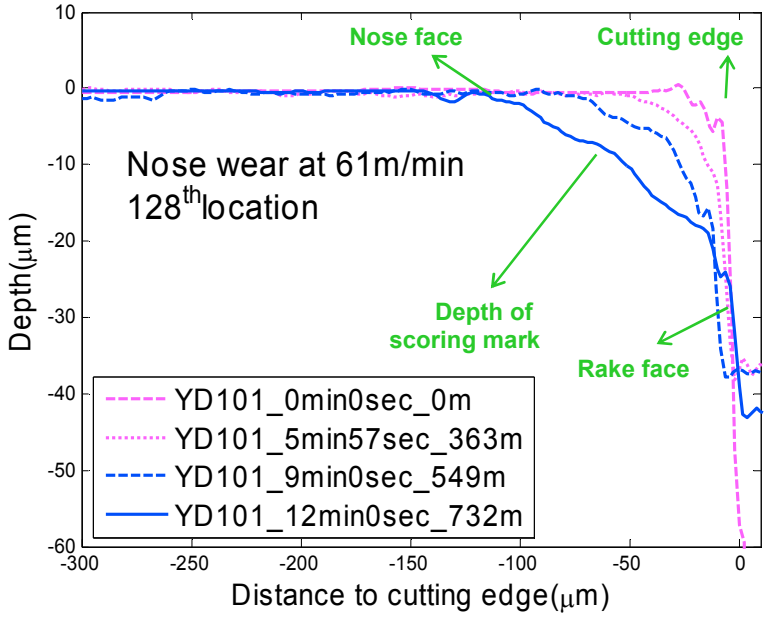

c) 2D profile of wear at 128th location

Figure 19: Nose wear evolution of carbide inserts (YD101) at the cutting speed of 61m/min.

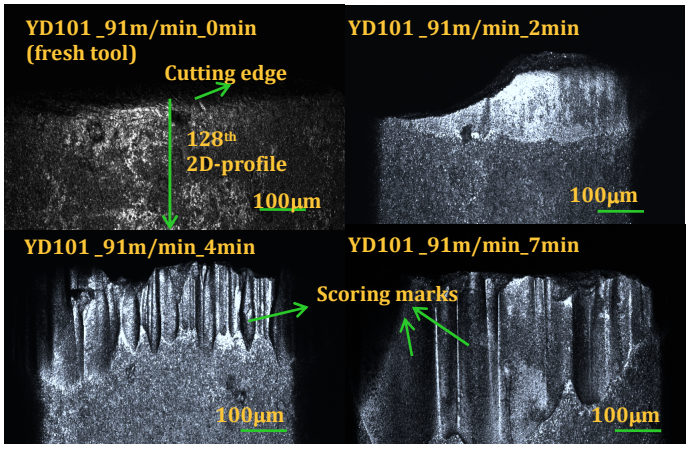

a) 2D image

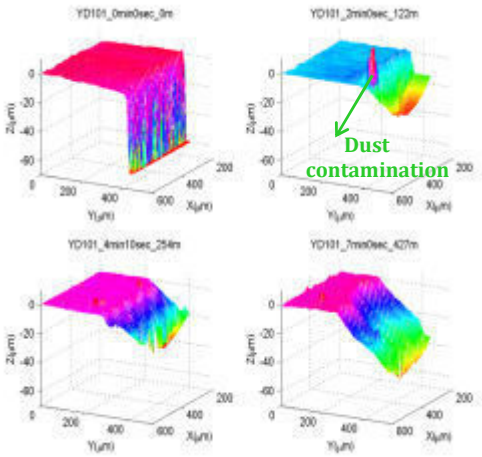

b) 3D image

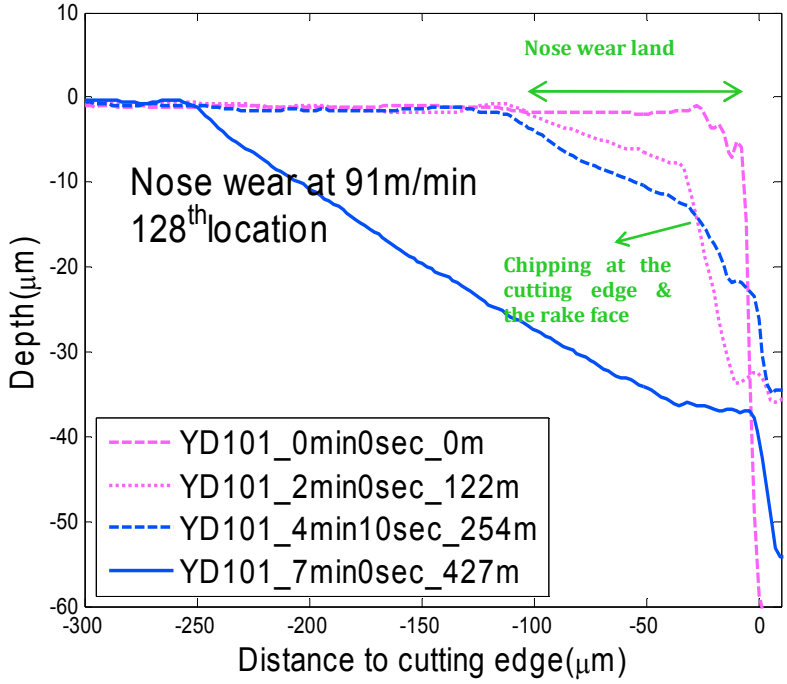

c) 2D profile of wear at 128th location

Figure 20: Nose wear evolution of carbide inserts (YD101) at 91m/min.

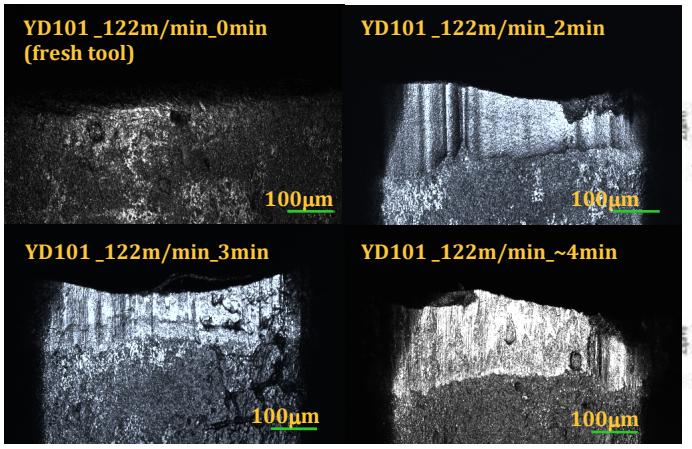

a) 2D image

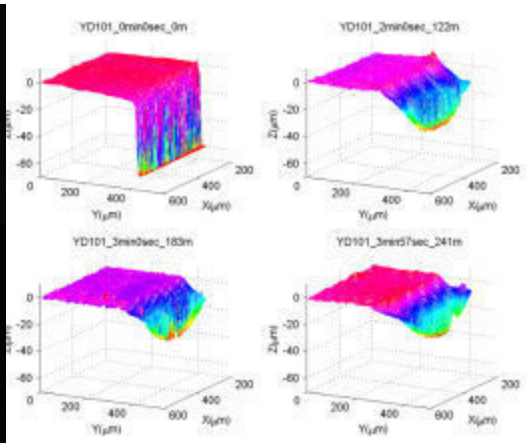

b) 3D image

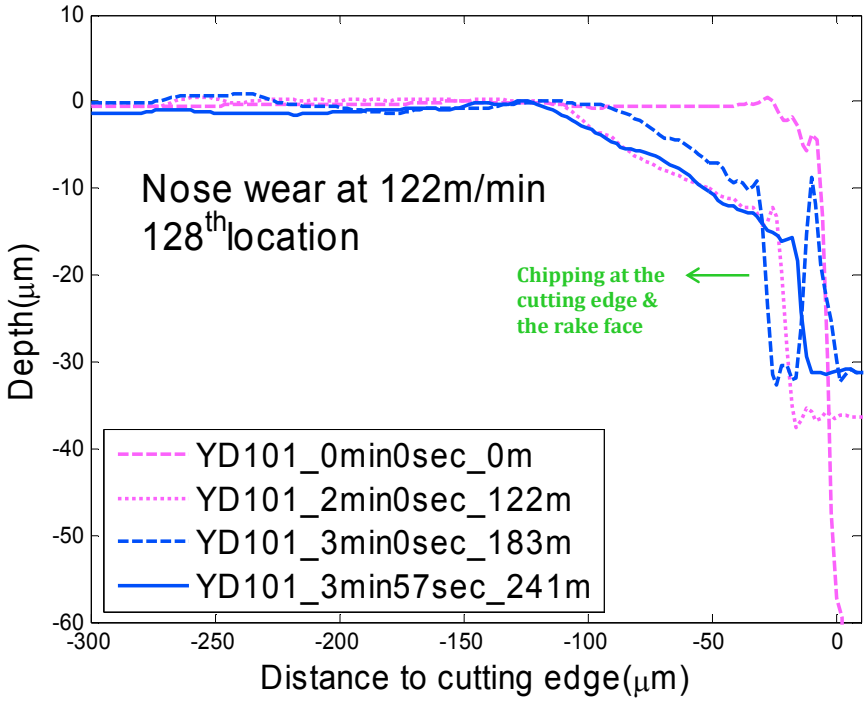

c) 2D profile of wear at 128th location

Figure 21: Nose wear evolution of carbide inserts (YD101) at cutting speed of 122m/min.

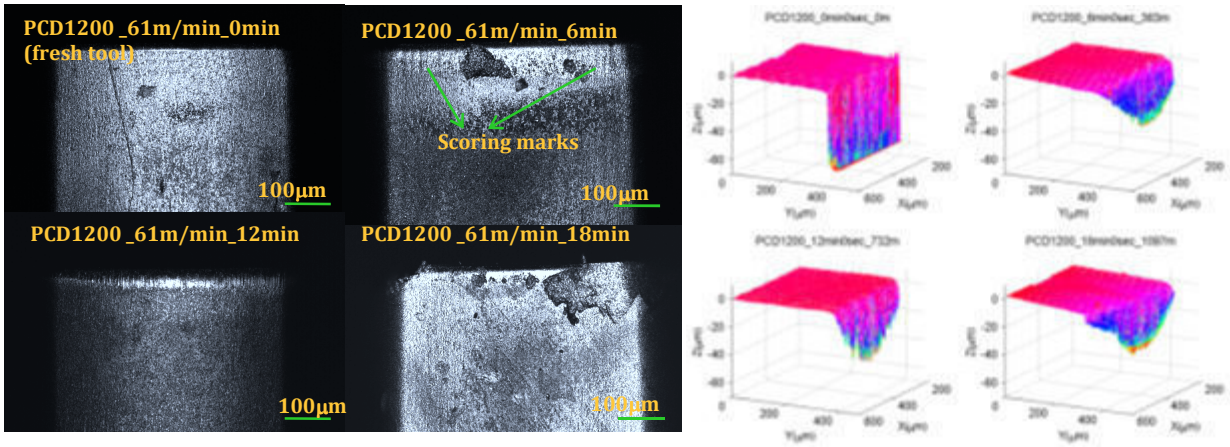

a) 2D image b) 3D image

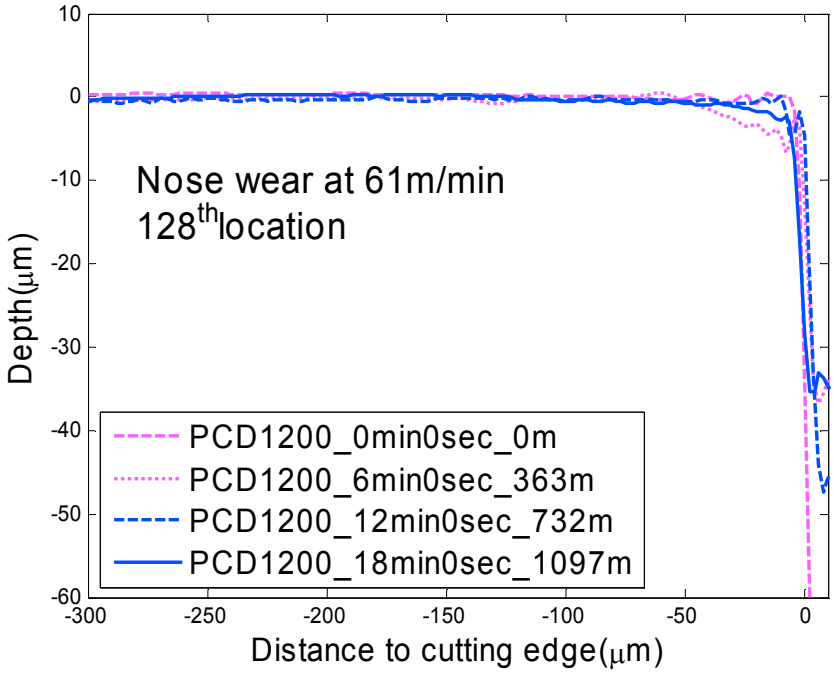

c) 2D profile of wear at 128th location

Figure 22: Nose wear evolution of PCD1200 inserts at cutting speed of 61m/min.

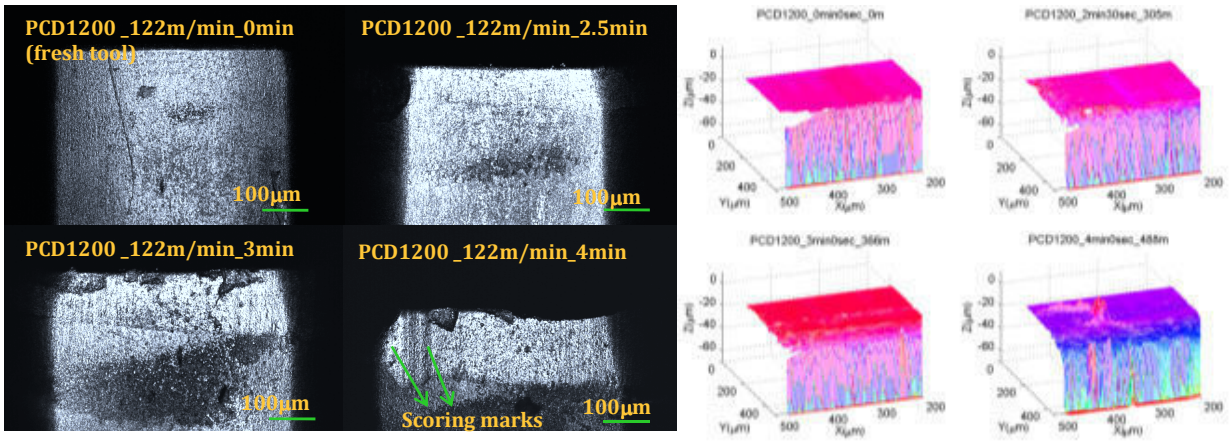

a) 2D image

b) 3D image

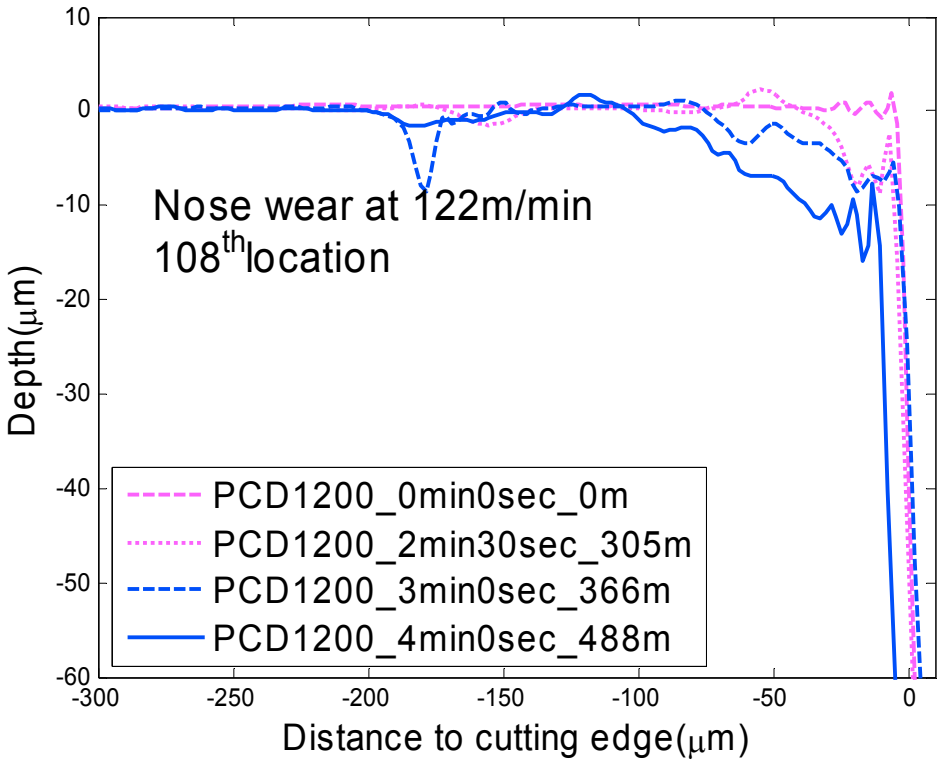

c) Wear profile at 128th location

Figure 23: Nose wear evolution of PCD1200 inserts at cutting speed of 122m/min.

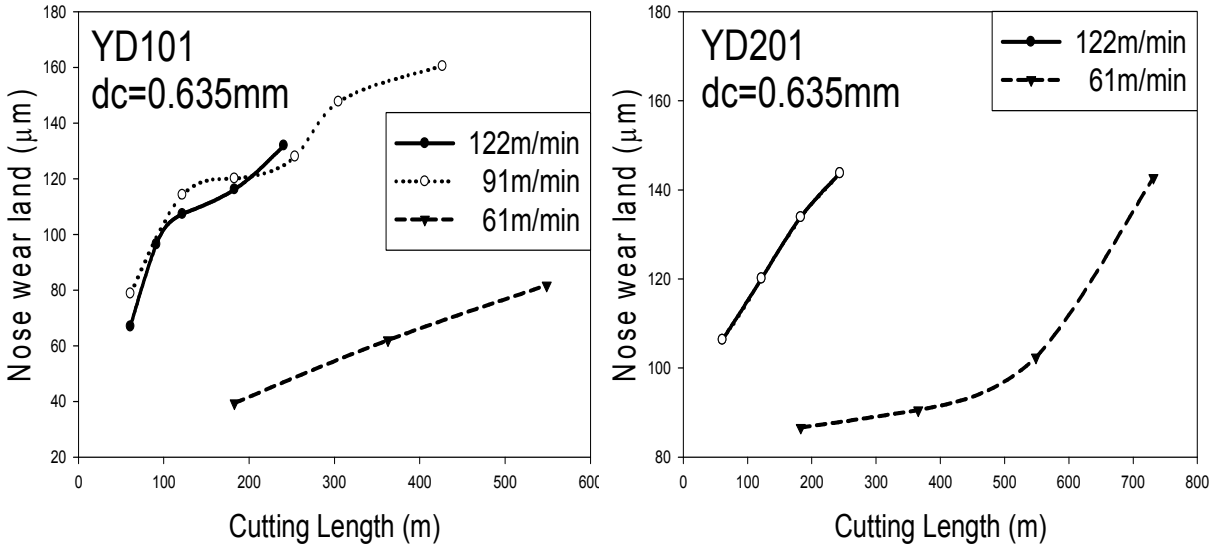

Figure 24: The average nose wear land of the carbide inserts at the low DOC.

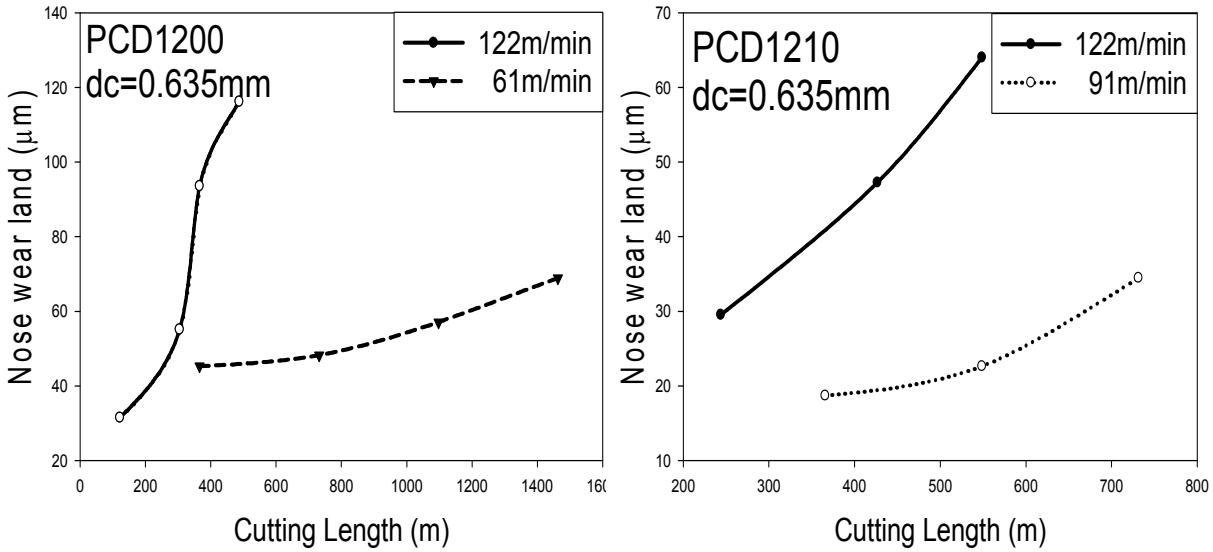

Figure 25: The average nose wear land of the PCD inserts at the low DOC.

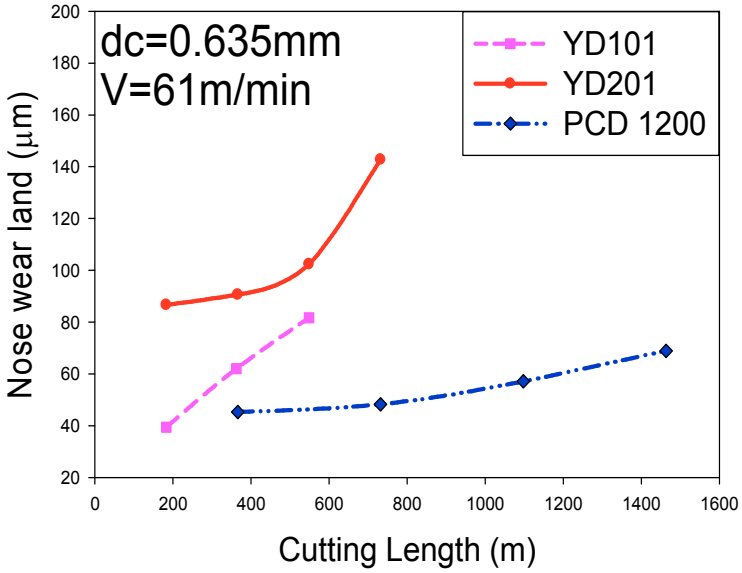

Figure 26: Comparison of nose wear land on carbide and PCD inserts at low cutting speed (61 m/min or 200sfm)

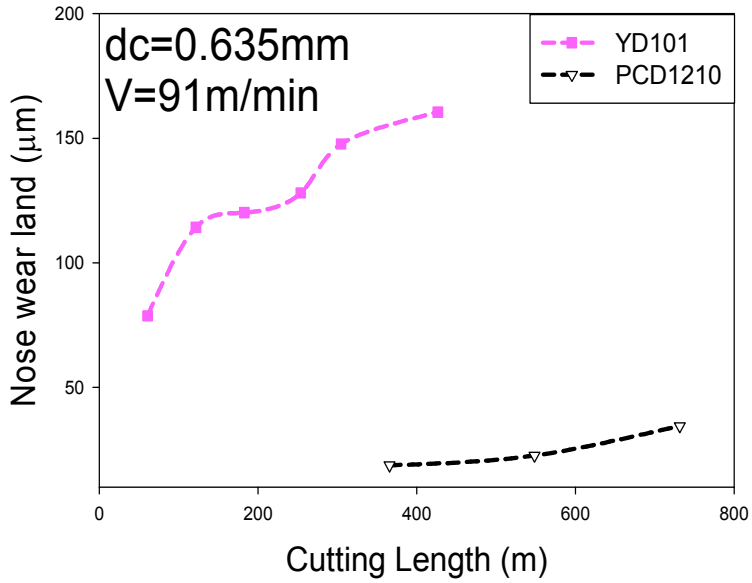

Figure 27: Comparison of nose wear land on carbide and PCD inserts at medium cutting speed (91 m/min)

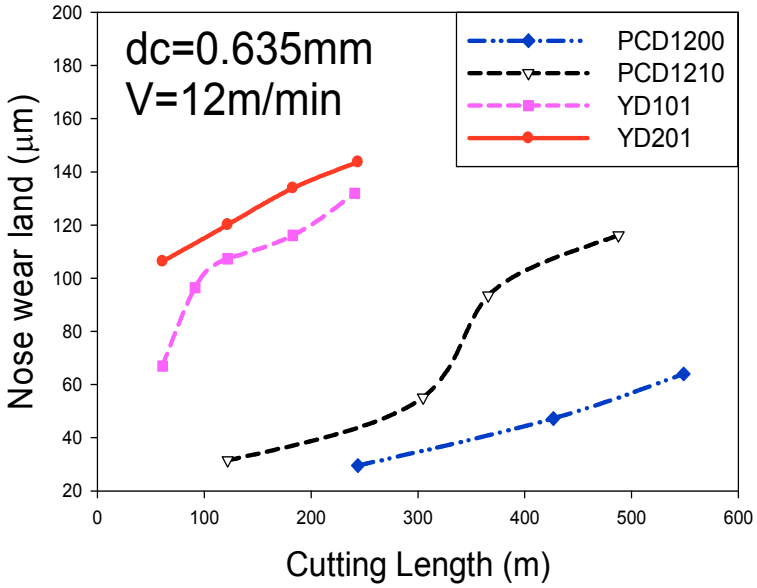

Figure 28: Comparison of nose wear land on carbide and PCD inserts at high cutting speed (122 m/min).

It should be pointed out that YD101 inserts at the medium cutting speed had larger scoring marks (>60µm) on the nose in comparison to low and high cutting speeds. In addition, all YD201 inserts at 91 m/min were fractured. The possible reason could be chatter and vibration at this cutting condition. There were less and smaller scoring marks observed on the nose of PCD inserts.

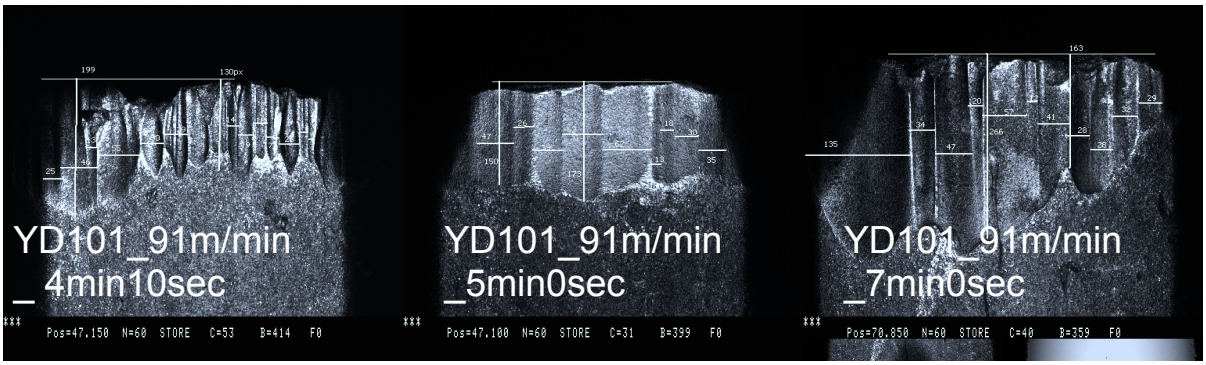

Figure 29: The scoring marks on the noses of YD101 inserts

I.3.2 Wear characteristics of tools inserts at high DOC

I.3.2.1 *Crater wear at high DOC*

It is interesting that the catastrophic failure from tool fracture of the cutting edge only happened after a cutting distance of more than 400m at high cutting speeds. At a low cutting speed, the chipping happened randomly on both carbide and PCD inserts of all grades at each cutting speed. Meanwhile, catastrophic fracture happened on most of the YD201 and PCD1210 rake inserts at 91 m/min and 61 m/min with low DOC, respectively. The possible cause for chipping and fracture with a low DOC was high temperature gradients and stress concentration along the short chip-tool contact lengths as evident in the study of temperature and stress distribution at the rake face of the tool using the FEM simulation to be discussed in the next section.

The 2D and 3D images of fresh and worn carbide inserts are presented in Figures 30-32 for all three cutting speeds. Interestingly, the results from the second set show smoother crater surface, a representative of thermochemical wear (dissolution and/or diffusion) on the carbide inserts. The smooth crater surfaces were seen on carbide inserts at even low cutting speed (200sfm) after cutting 5 min. The carbide inserts with the cutting time of less than 5 minutes at 200sfm showed a few abrasive marks but mainly dissolution/diffusion wear (insert after cutting 2.4min in Figure 30). The crater surfaces became more even and shinier as the cutting speed increases. The dissolution/diffusion may be more dominant at the medium and high cutting speed. As reported in the literature [Ezugwu, 1997; Hartung, 1982; Narutaki, 1983], the temperatures of medium and high cutting speeds with carbide tools were above the

transus temperature leading to acceleration of dissolution and diffusion rates. The crater wear developed closer to the cutting edge on the inserts at all cutting speeds. Therefore, the cutting edge of carbide inserts was weaken and chipped quickly. This phenomenon resulted from the high temperature near the cutting edge. The stable and sharp cutting edge was an important factor for long tool life in cutting Ti alloys. In machining Ti, not only were the cutting temperatures higher but also the crater wear occurred near the cutting edge alloys compared to machining ferrous materials [Ezugwu, 1997].

To represent the crater depth information, the 2D crater wear profiles along chip flow direction, where the maximum of crater was expected happen, were plotted various locations (88^{th}, 108^{th}, 128^{th} and 148^{th} sections in Figure 30). These maximum crater depths were obtained by taking the maximum depth value from the 2D wear profiles. The 2D crater profiles of the carbide inserts were presented in Figures 33 and Figure 34. Figures 33 showed the 2D crater wear profiles at 88^{th} and 108^{th} locations with the consistent depth of crater wear which presented the evidence of smooth crater wear on carbide inserts.

times higher than that of 61 m/min and two times higher than that of 91 m/min, respectively. Figure 43 compared the crater wear rate of carbide insets at low at high DOC. As expected, the wear rate at high DOC was much higher than that at low DOC at given cutting speed.

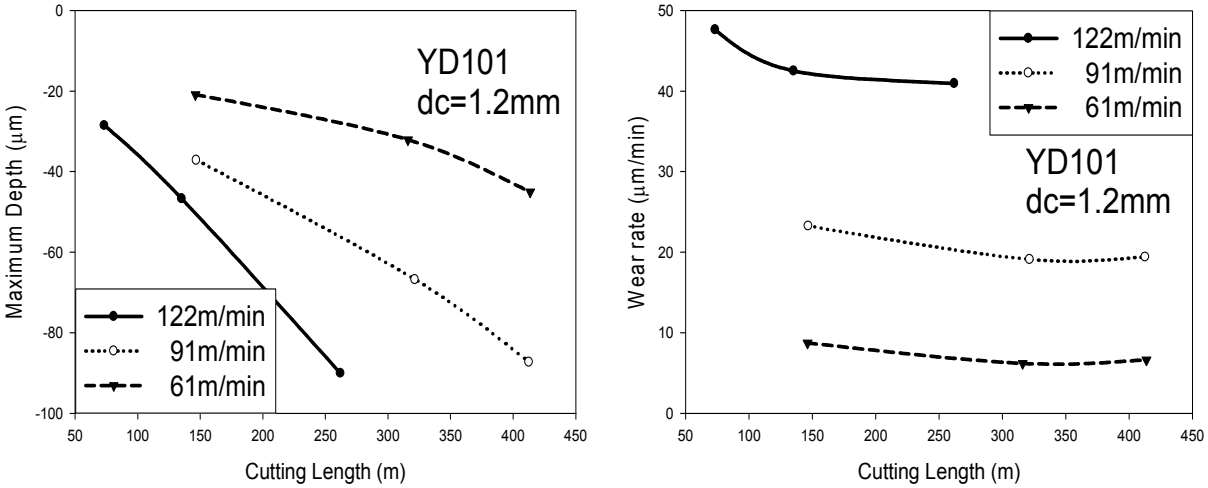

Figure 42: The maximum depth and wear rate of crater wear on carbide inserts (YD101) at high DOC

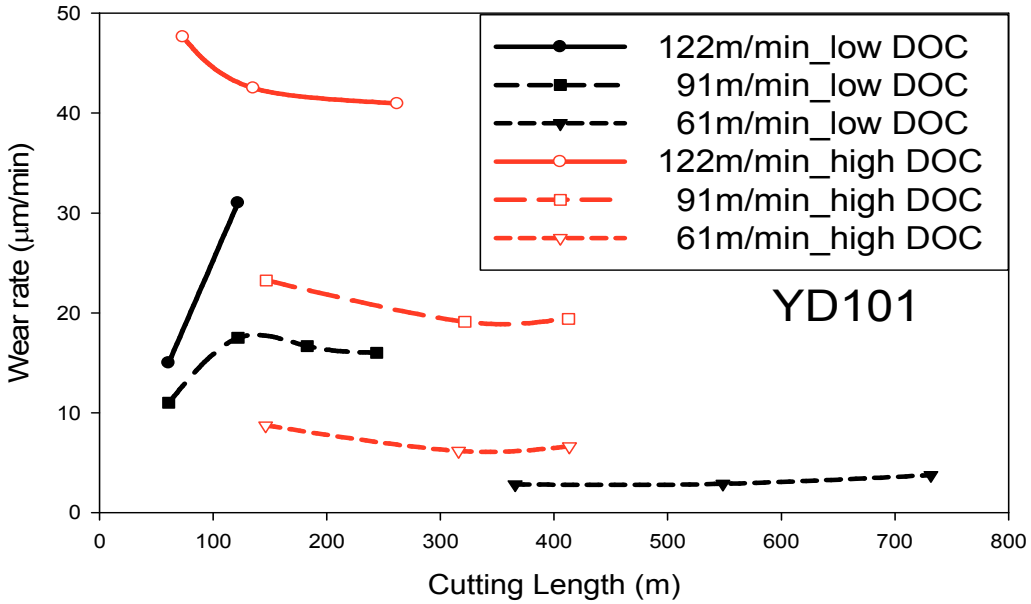

Figure 43: Comparison in wear rate of crater wear on carbide inserts (YD101) at low DOC and high DOC

I.3.2.2 ***Nose wear and flank wear at high DOC***

The nose and flank wear on the carbide and PCD1510 inserts at the longest cutting time of three cutting speeds were presented in Figures 44-47. In appareance, the carbide inserts showed even (in depth) nose and flank wear in appearance while uneven nose and flank were observed on PCD1510 inserts at the low and medium cutting speeds. In the literature, many researchers reported that titanium galls and welds to tool material lead to the chipping of the cutting edge. The welded or fractured chipping abraded the nose and flank face of tools causing scoring marks when the tool travels along the feed direction. The scoring marks were observed with both carbide and PCD1510 inserts. However, these scoring marks appeared more frequently with smooth and clearly appearance than those of PCD1510. Obviously, the temperatures at the flank face were much lower than those at the rake face. Therefore, the dissolution and diffusion mechanisms which cause smooth wear cannot be dominant in the flank face. Then, a question here is what causes these scoring marks on the flank faces of the carbide and PCD1510 inserts, respectively. The answer will be discussed in next section.

At the high cutting speed, as expected, with high temperature and less edge stability on the rake face, both carbide and PCD1510 inserts experienced catastrophic fracture. The inserts with a large fractured area suppressed the appearances of the steady-state wear patterns observed in nose wear, flank wear and crater wear. Figure 48 shows a very large damaged area on the carbide inserts resulted from a large fracture. For the cutting speed of 122 m/min, the carbide inserts last up to 2 minutes, and the PCD1510 tools withstand for up to 3.5 minutes.

Furthermore, the main failure of the carbide inserts was at the nose while the flank face of PCD1510 was more damaged. The failure of the PCD1510 inserts at all cutting speeds was affected by the notch wear as shown in Figure 47. The notch wear occurred at most cutting speeds and cutting times. It happened in the earlier stage of cutting and become more severe as the cutting speed increases.

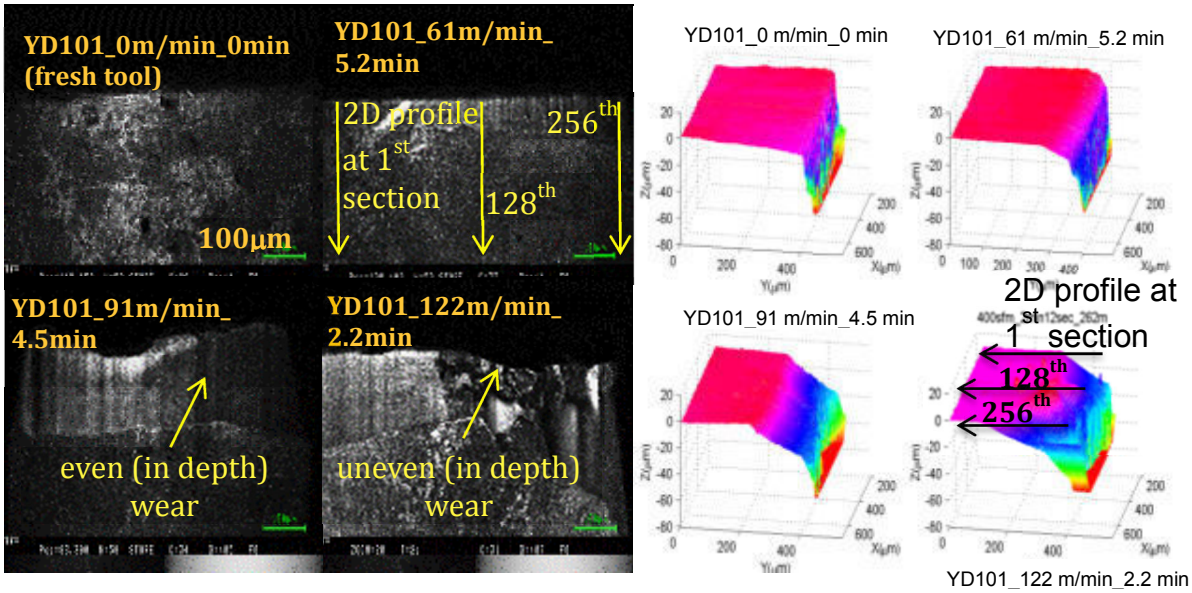

a) 2D images b) 3D images

Figure 44: Nose wear on carbide YD101 inserts at the longest cutting time of three cutting speeds.

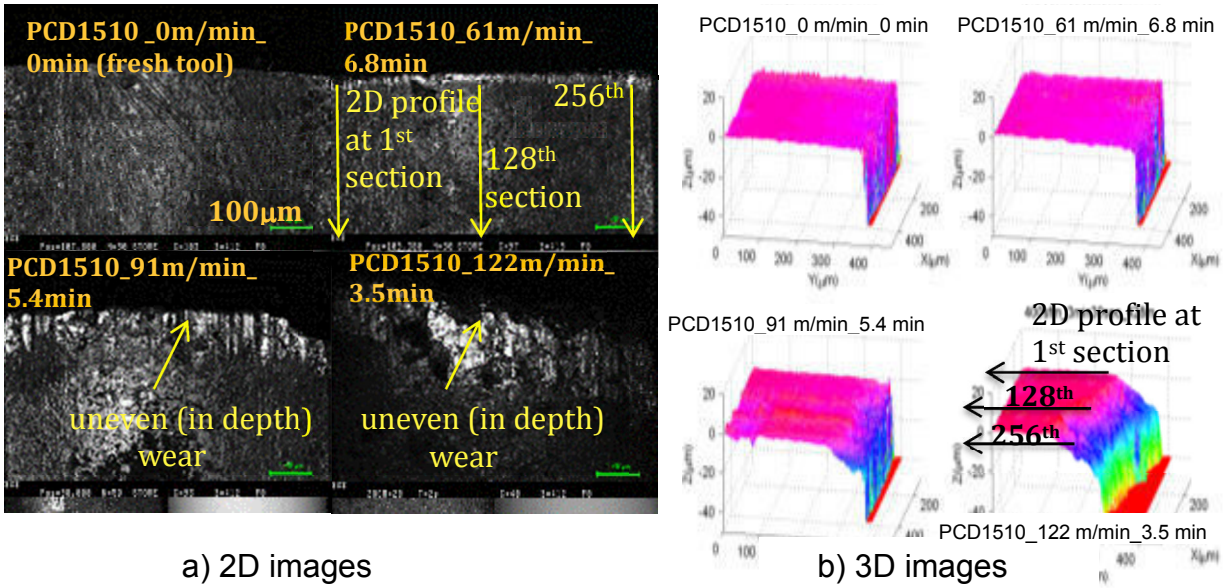

a) 2D images b) 3D images

Figure 45: Nose wear on the nose of PCD1510 inserts at the longest cutting time of three cutting speeds.

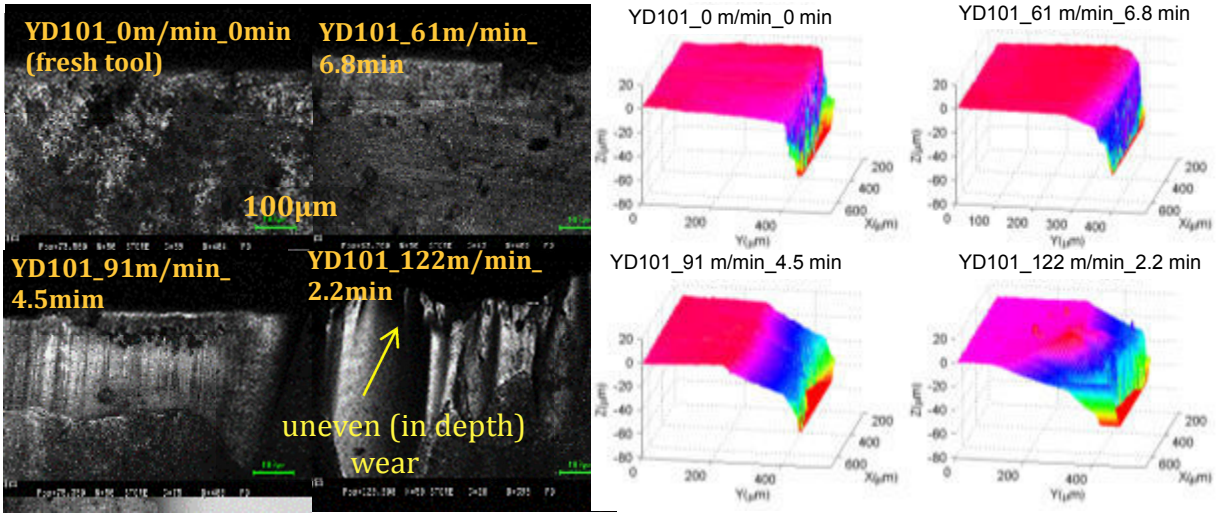

a) 2D images b) 3D images

Figure 46: The flank wear on carbide YD101 inserts at the longest cutting time of three cutting speeds.

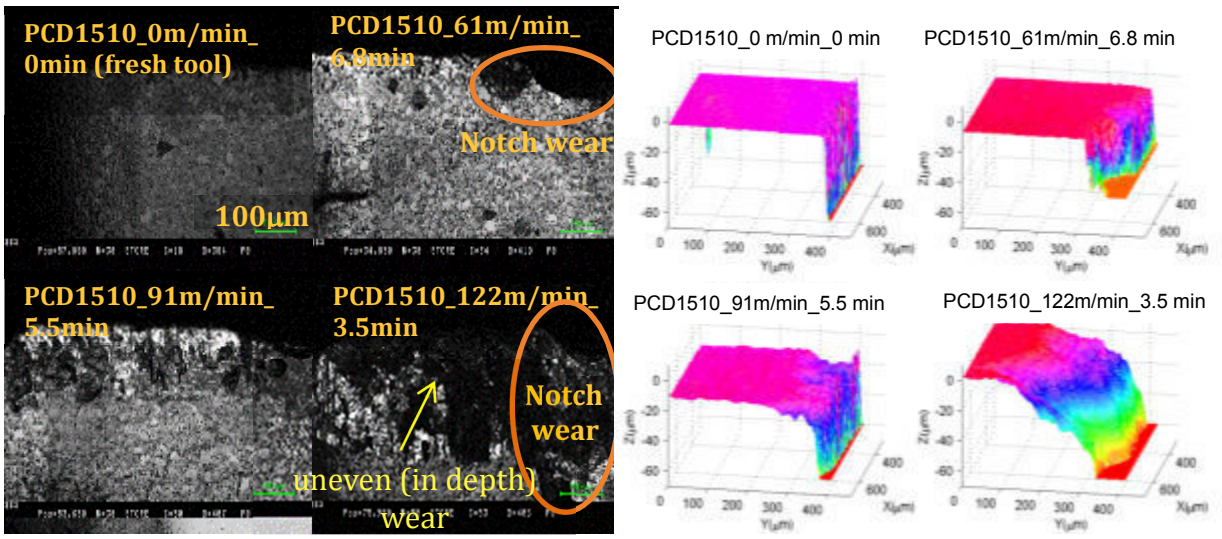

a) 2D images b) 3D images

Figure 47: The flank wear on PCD1510 inserts at the longest cutting time of three cutting speeds.

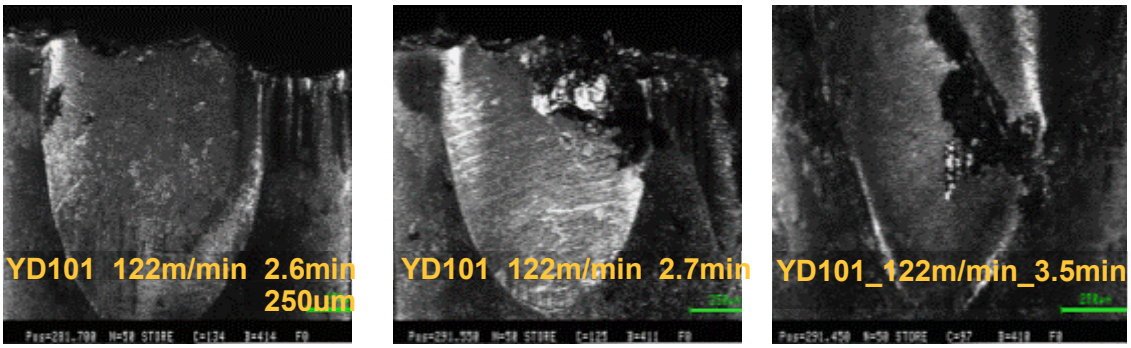

Figure 48: Nose damage of the carbide inserts (YD101)

The 2D nose and flank wear profiles were also plotted for each tool type as a function of cutting distances for three cutting speeds. The 2D wear profiles provide wear land as well as wear depth which was not determined with typical microscope and SEM images reported in literatures. The nose and flank wear profiles of the carbide and PCD1510 inserts can be compared in Figures 49-51. The 2D wear profiles provided consistent data of nose and flank wear land at four different locations (88th, 108th, 128th, 148th sections shown Figure 44). Because of the multiple

scoring marks, however, the 2D wear profiles was consistent in depth, especially for the carbide inserts at the medium and high cutting speed and the PCD1510 inserts in all cutting speeds. This happened in all cutting speeds with PCD1510 insert because of uneven wear which grain fractured out was also contributed to. Similar to crater wear, flank wear land at high DOC was much higher than low DOC as shown in Figure 54.

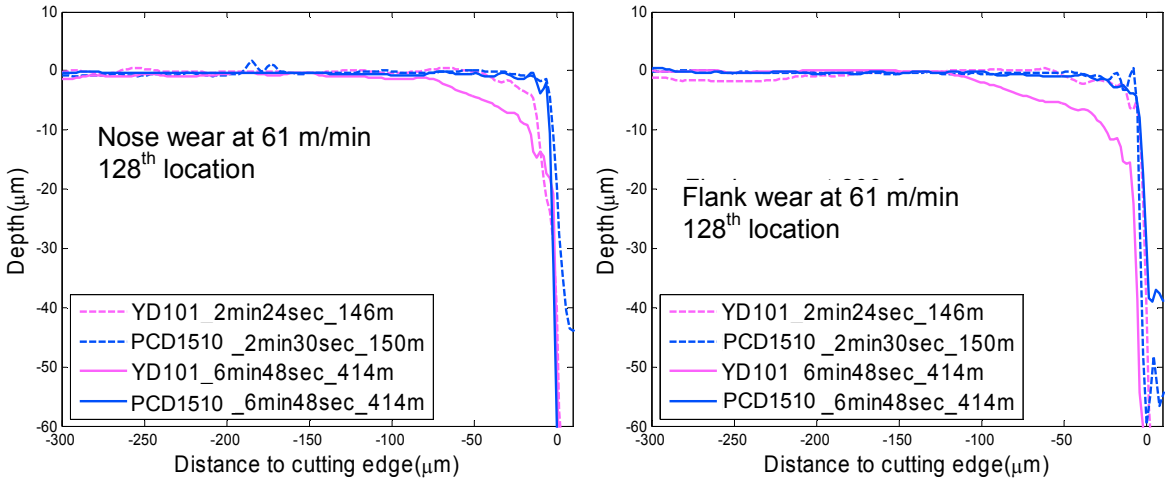

Figure 49: The 2D profiles of nose and flank wear at 128th section of carbide YD101 and PCD1510 inserts at 61m/min.

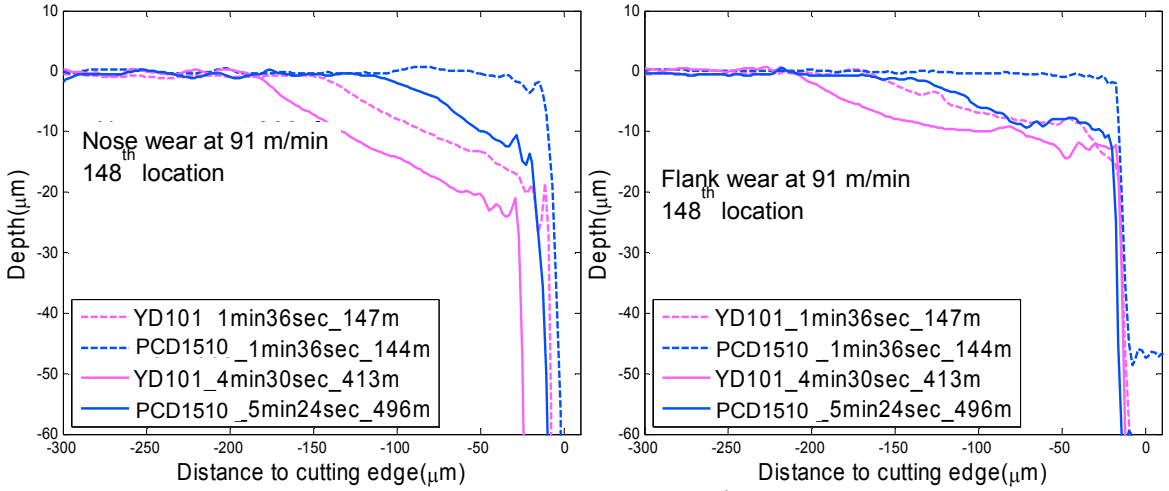

Figure 50: The 2D profiles of nose and flank at 148th section of carbide YD101 and PCD1510 inserts at 91m/min.

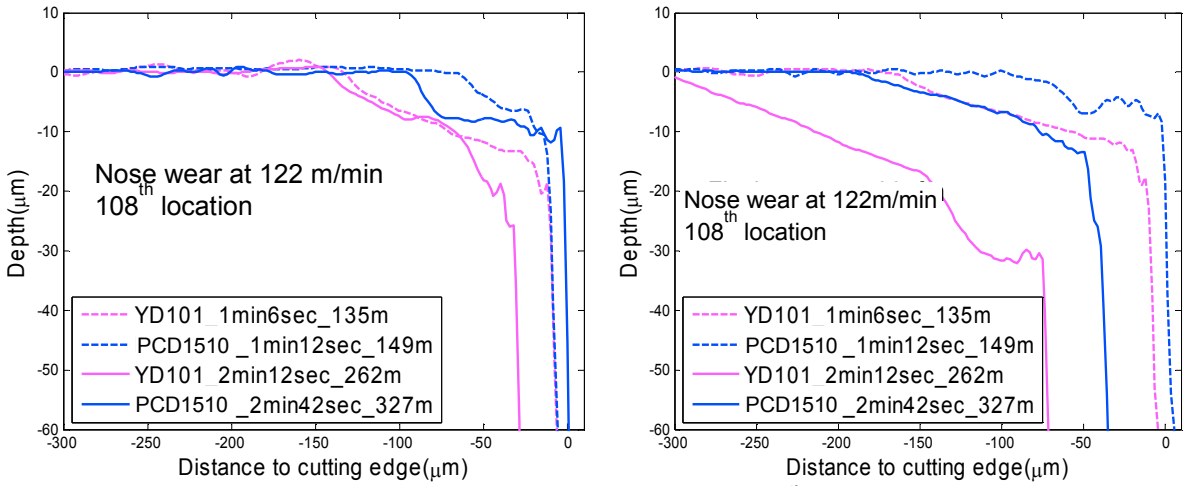

Figure 51: The 2D profiles of nose and flank wear at 108th section of carbide YD101 and PCD1510 inserts at 122m/min.

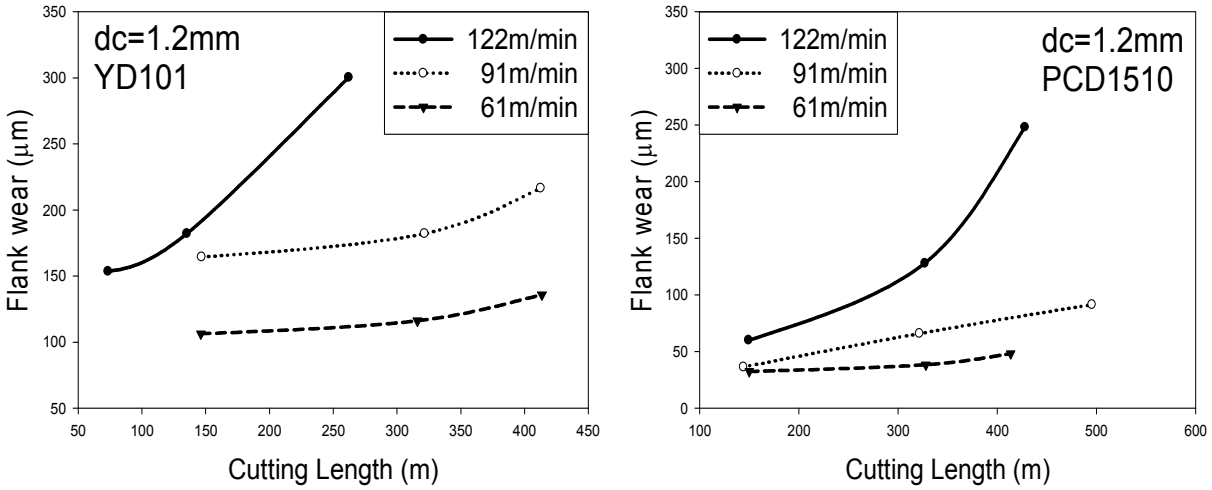

Figure 52: The evolution of flank wear land on the flank face of YD101 and PCD1510 inserts at various cutting speeds.

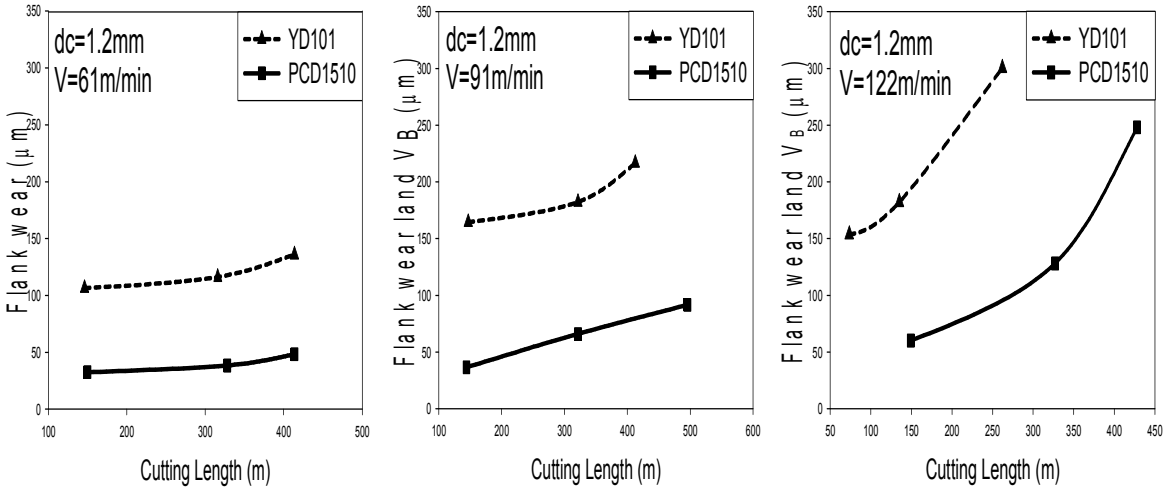

Figure 53: The comparison of flank wear land of carbide and PCD1510 inserts.

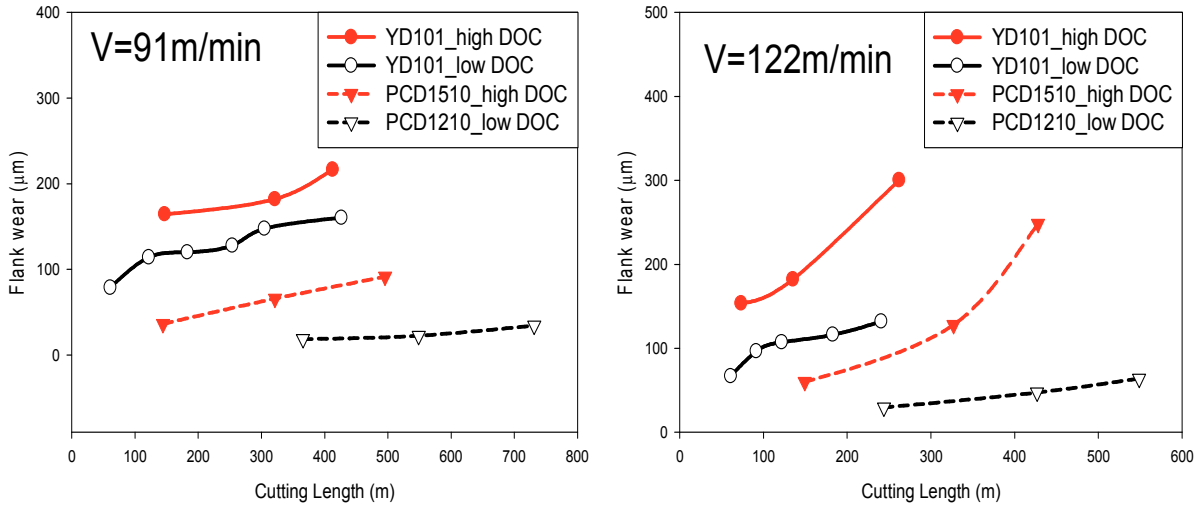

Figure 54: The comparison of flank wear land at low and high DOC.

I.3.3 SEM images and element mapping results

Figure 55 shows the adhesion layers on the PCD1510 and carbide inserts for all cutting speeds in the second set. Based on the images, the adhesion layers on PCD1510 inserts were more stable and uniform. These layers are known to protect the cutting edge during cutting process. Those layers strongly adhered to the rake face and cutting edge of the inserts. Because of this, the fragments of a tool material were pulled out when the layers were detached by the flowing chip. To determine the possible reaction between work and tool materials, the elemental mapping was conducted in the adhesion layers. Figures 56 and 57 represent the elemental composition of the adhesion layer represented by the white and dark areas (shown in Figure 55) for both PCD1510 and carbide inserts. Despite the deviation caused by the carbon contamination, the weight content of carbon increased and that of titanium decreased in the dark area as the cutting speed increased. The dark areas on the inserts from the low and medium cutting speeds could be a compound of Ti and C (TiC_x). The standard atomic weight ratio of C:Ti is 12u: 47.68u (about 1:4). Based on the weight content in the dark area, only adherent layer at low cutting speed with PCD1510 had the weight ratio of C:Ti at 4:1 which converted into 1:1 in atom ratio (or TiC). This result does not provide the definitive proof of the formation of TiC in the adhesion layer at the low cutting speed. However, the results provided the low possibility of the TiC formation at the medium and high cutting speeds because the weight ratio C:Ti was less than 4:1 (or 1:1 in atom ratio) at the medium and high cutting speed as shown in Figures 53 for PCD inserts and 54 for carbide inserts.

Hartung and Kramer [1982] and Arrazola et al. [2009] claimed that the TiC layer did not form at the high cutting speed.

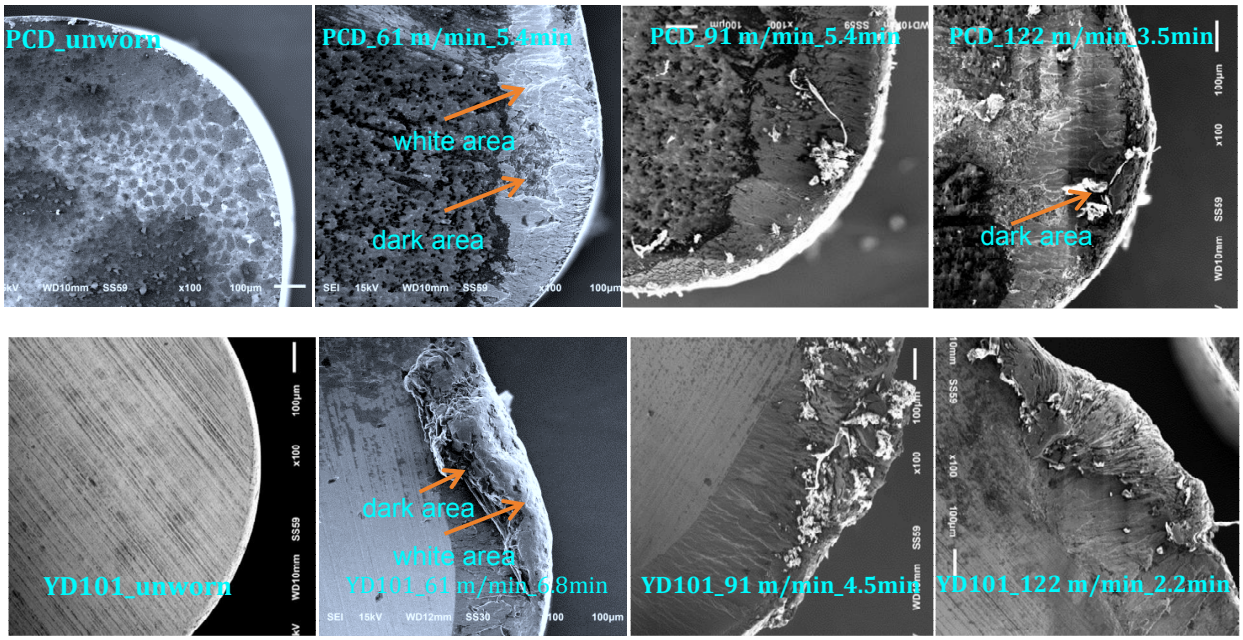

Figure 55: The SEM images of adhesion layer on the PCD1510 and carbide inserts in the second set (high DOC).

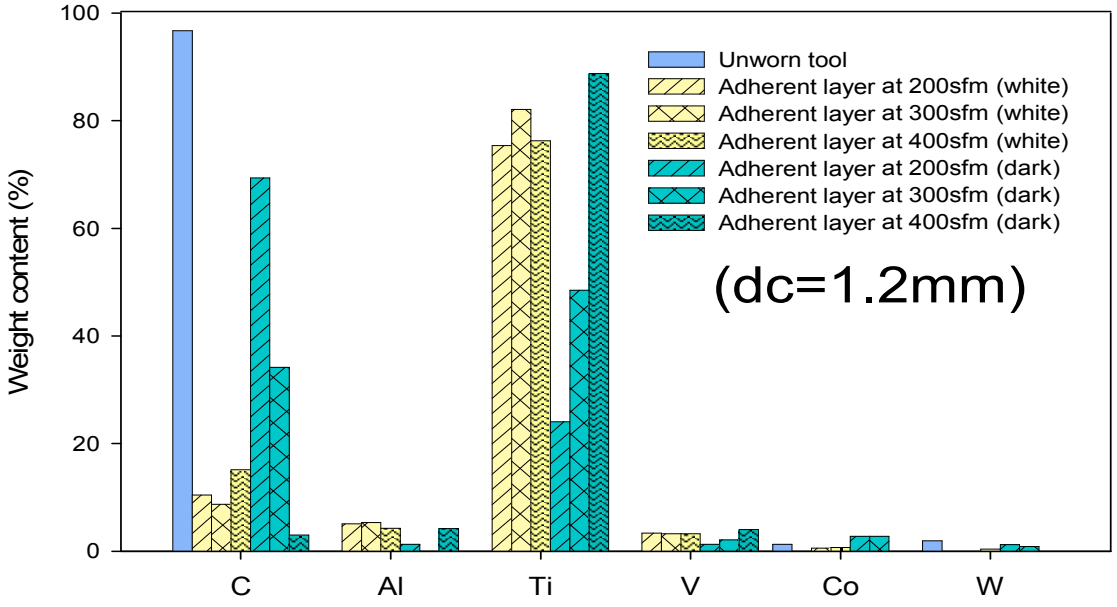

Figure 56: The elemental contents of adherent layers at white and dark area on PCD1510 inserts

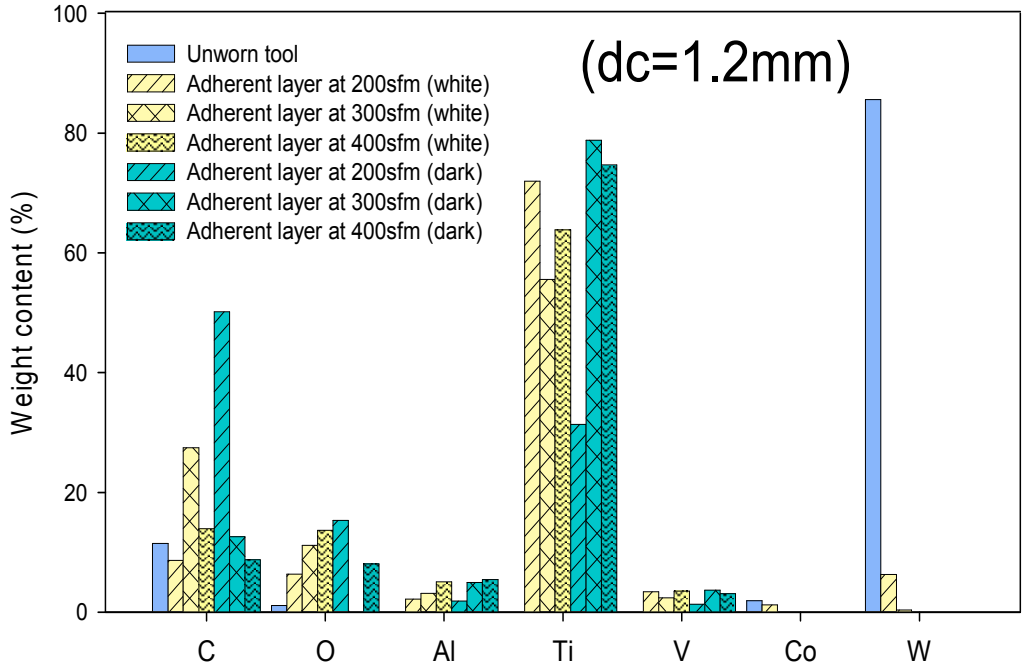

Figure 57: The elemental contents of adherent layers at white and dark area on carbide YD101 inserts

The SEM experiments were also conducted on the chips to determine if the tool material was dissolved into or attached to the chips. Figure 58 showed the SEM images of the tool-chip interface with the attached particles. The elemental mapping of the interface shown in Figure 59 indicates no traces of tool constituents (W, Co). To be more certain, the elemental mapping was performed on those particles (see Figure 60) to find high carbon and oxygen contents as shown in the element mapping of Figure 61. This indicates that those particles were the carbon contaminations, not the tool material.

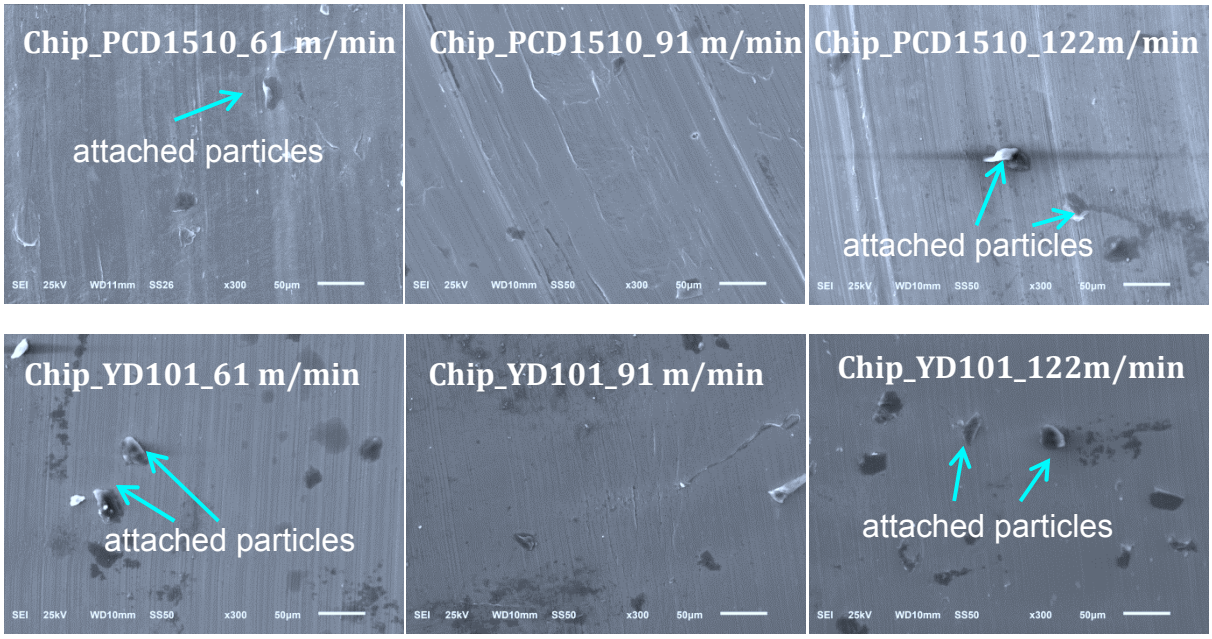

Figure 58: The SEM images of chip-tool interface of chips generated with carbide and PCD1510 inserts.

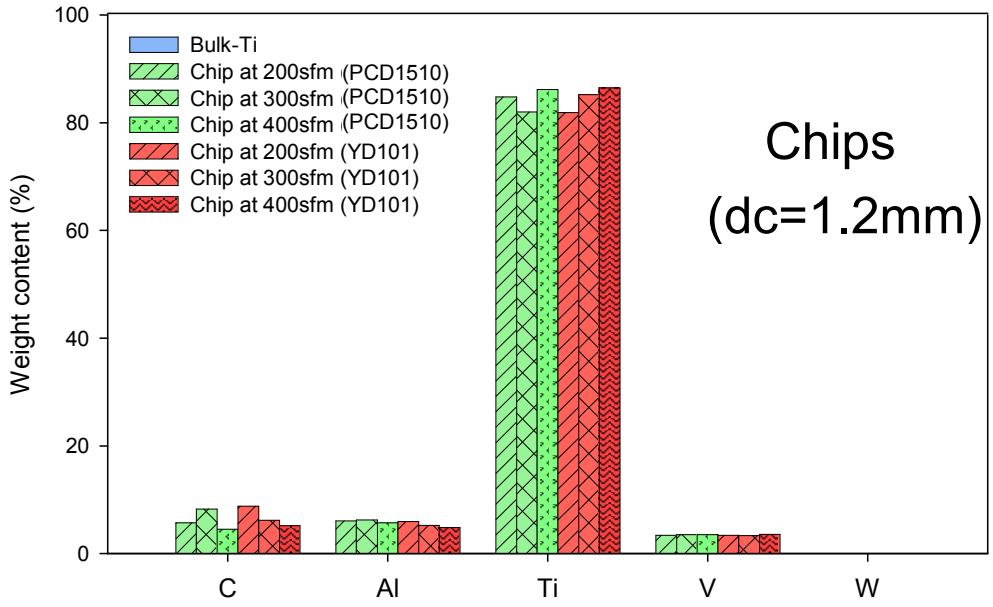

Figure 59: Elemental content of chips with carbide and PCD1510 inserts for three cutting speeds

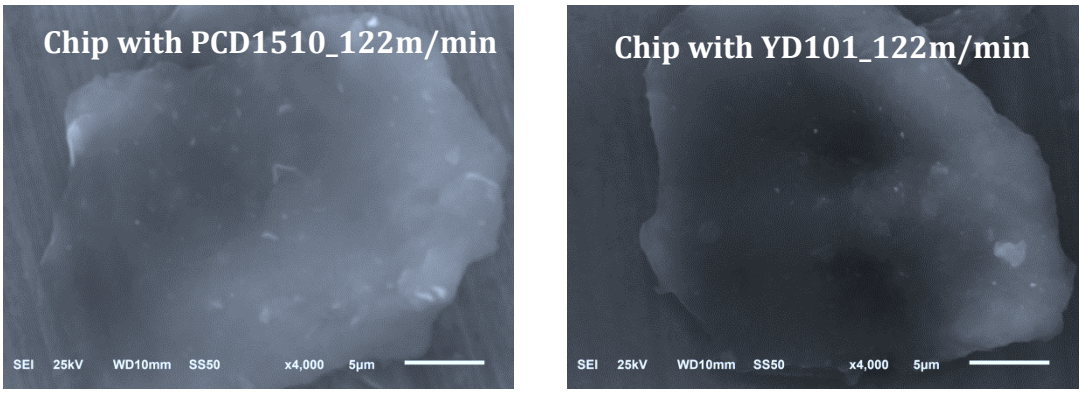

Figure 60: The SEM images of adhered particles on the chips.

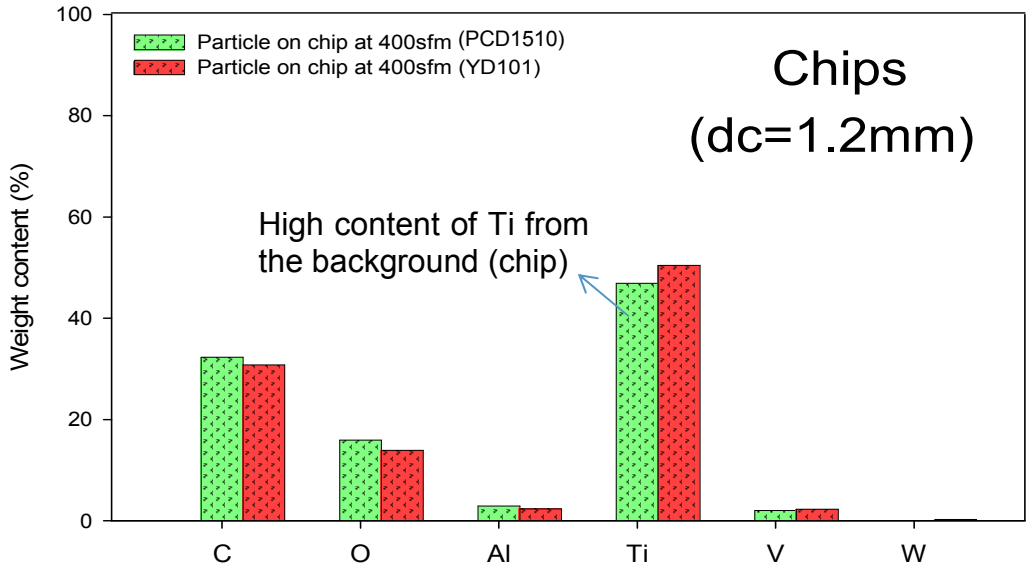

Figure 61: Elemental content of adherent particles on the chips.

I.3.4 Chip morphology

Figure 62 presents SEM image of chip morphology with the carbide and PCD1510 inserts at three cutting speeds. The segmented chips were observed in all cutting conditions with both carbide and PCD1510 inserts. Figure 63 presents five parameters (height of peak, height of valleys, spacing of peaks, spacing of valleys, and spacing of peak-to-valley) represented for chip morphology. The morphology of

chip generated with carbide and PCD1510 inserts was shown Figure 64. Statistical analysis for height of peaks and valleys were presented in Figure 65 and Figure 66. The higher height of peaks and valleys were found at the high cutting speed for both carbide and PCD1510 inserts. The comparative data for chip morphology between carbide and PCD1510 inserts was summarized in Figure 67. The carbide tool insert showed segmented chips with higher peaks and shorter spacing of peaks as well as spacing valleys (lower serrated frequency).

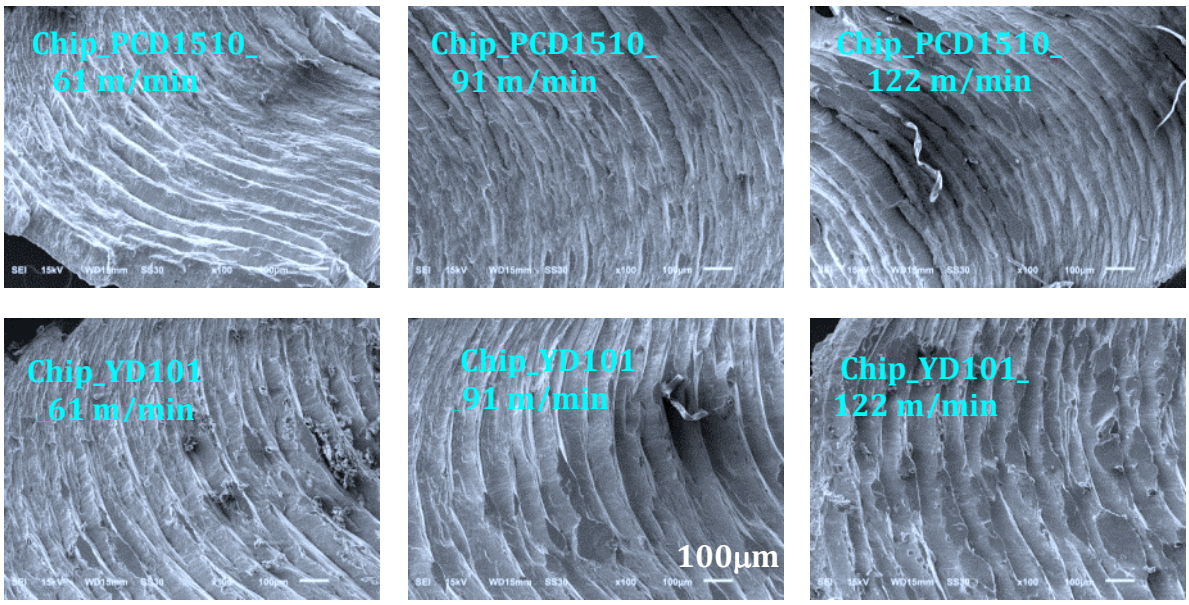

Figure 62: The chip morphology (top view).

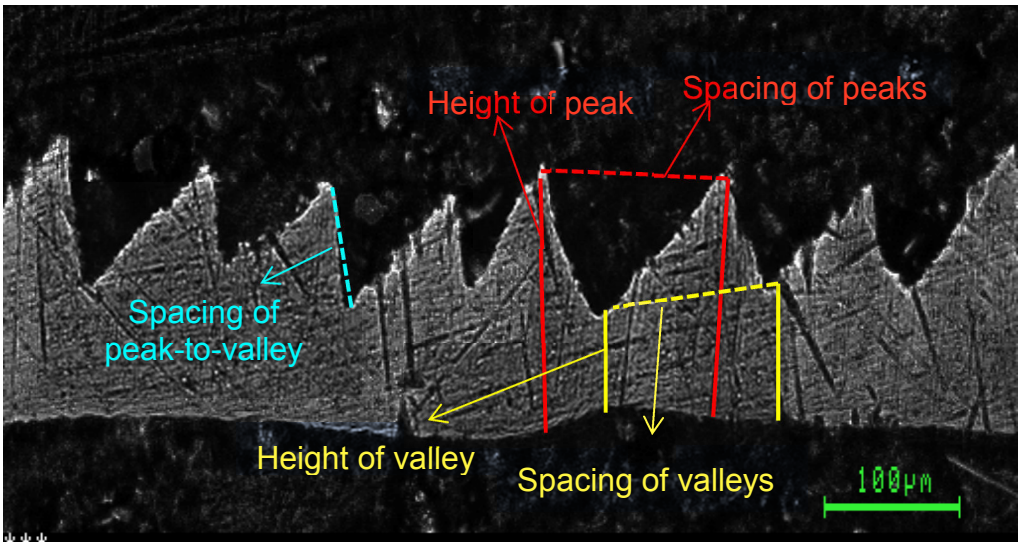

Figure 63: Five parameters represented for chip morphology (side view)

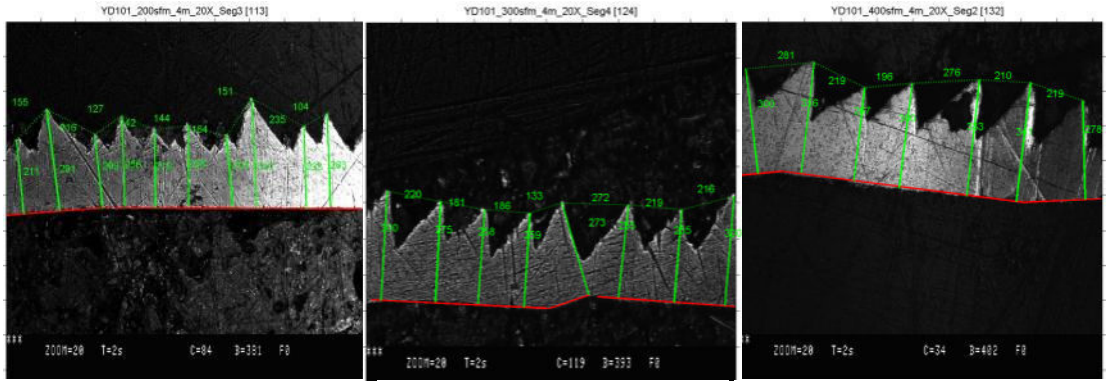

a) YD100 at 61 m/min b) YD100 at 91 m/min c) YD100 at 122 m/min

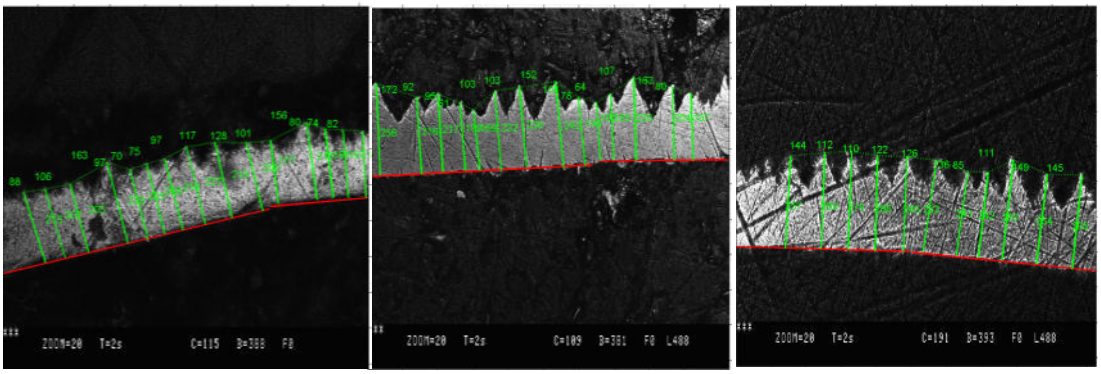

d) PCD1510 at 61 m/min e) PCD1510 at 91 m/min f) PCD1510 at 122 m/min

Figure 64: Chip morphology with carbide and PCD1510 inserts at all cutting speeds

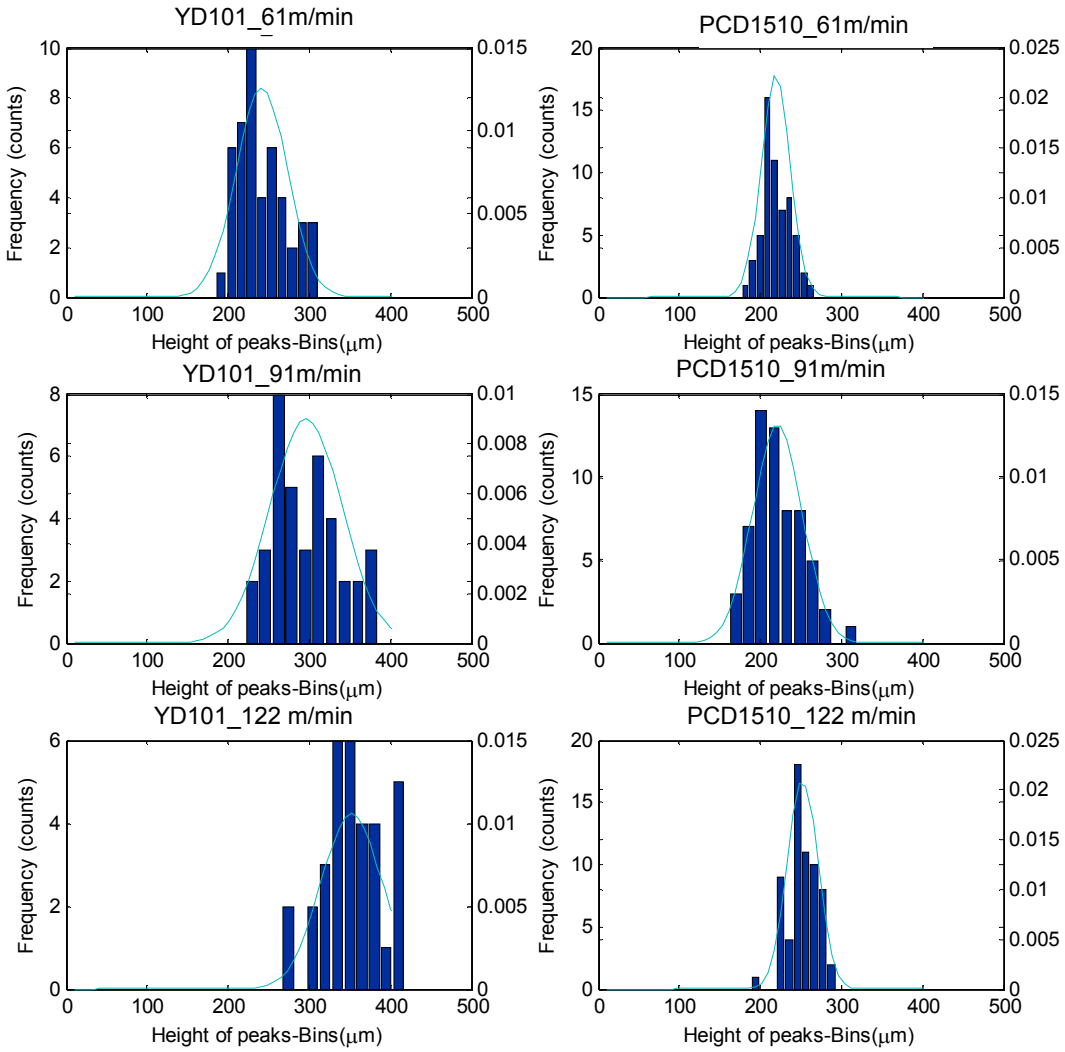

Figure 65: Statistical data for height of peaks.

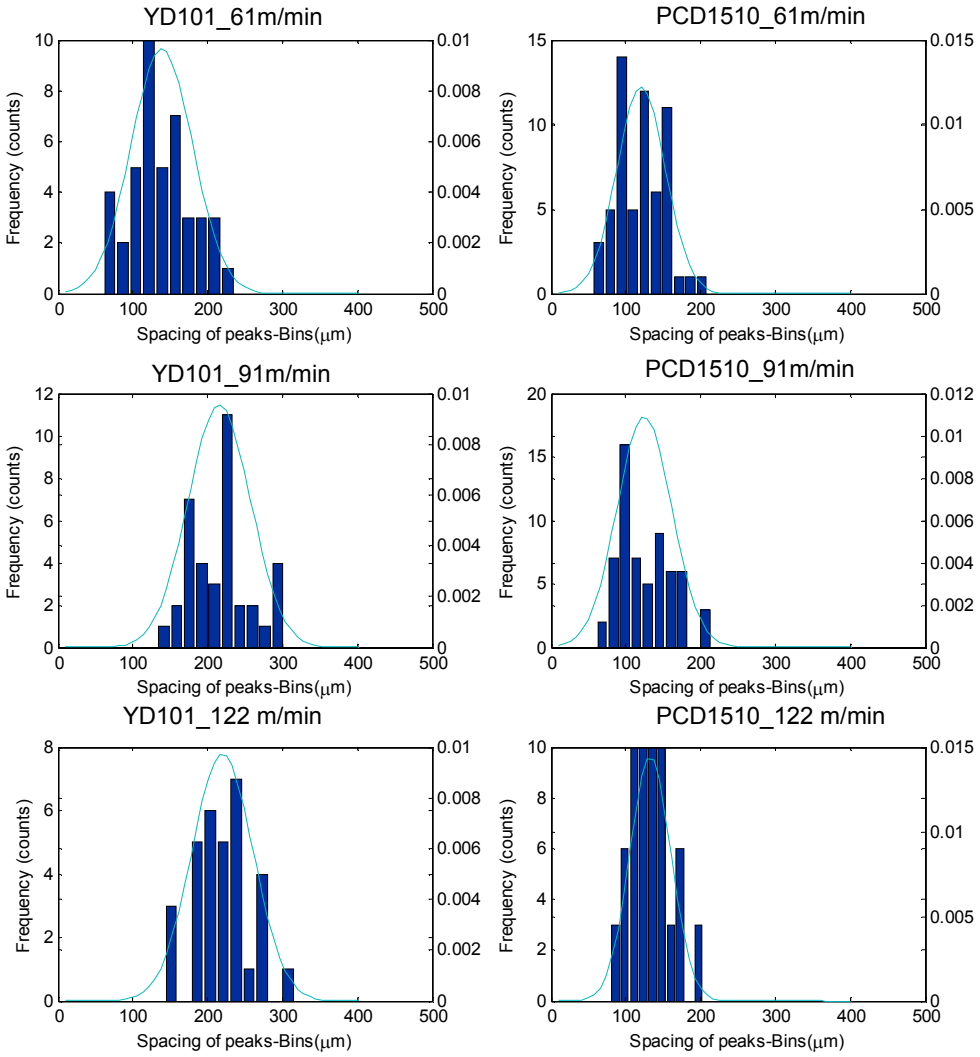

Figure 66: Statistical data for height of valleys.

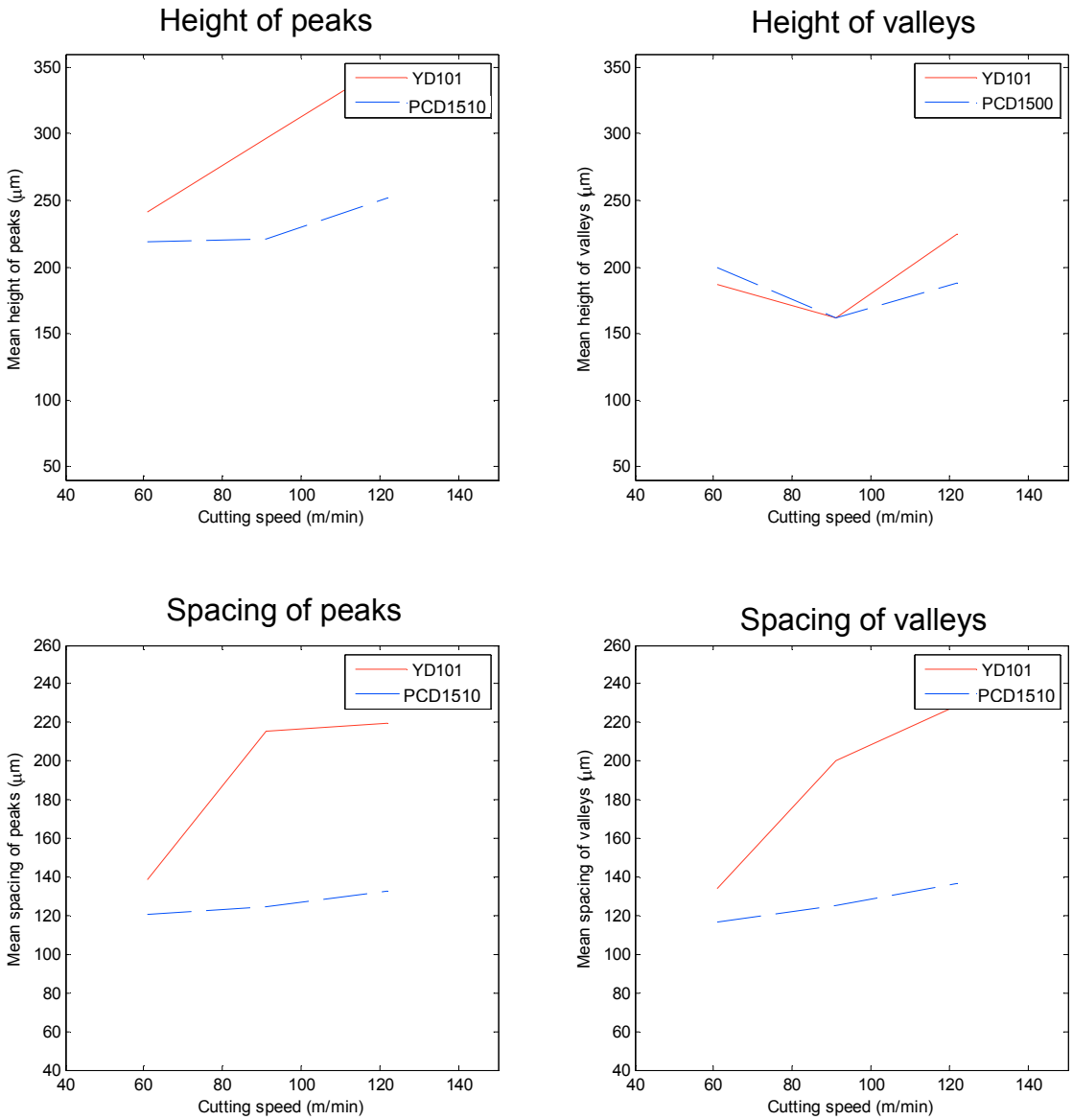

Figure 67: The comparison on chip morphology between carbide and PCD1510 inserts

I.4 CUTTING TEMPERATURE PROFILES WITH FEM SIMULATION

I.4.3 2D-FEM with the Johnson-Cook (JC) model

The cutting temperature played a very important role in identifying the main wear mechanisms involved in the cutting process. Both mechanical and thermochemical wear (dissolution and diffusion) are functions of temperature which were discussed in detail in Chapter 4. Thus, the temperature profiles along the chip thickness and rake and flank faces on the workpiece needed to be determined. In spite of the development of experimental techniques (thermocouple, infrared camera, temperature indicating liquid, etc.), these techniques only measure in-situ local temperatures. However, this study requires the estimation of temperature profiles on both the tool and the workpiece. Therefore, Finite Element Analysis (FEA) software was utilized. Many researchers have been using FEA simulation of cutting process to predict the temperature distribution. This study also used 2D-FEM with the Johnson-Cook (JC) model and Arbitrary Lagrangian-Eulerian (ALE) formulation to obtain the temperature profile. The simulations were run with few sets of JC coefficients of the Ti64 for comparison as shown in Table 6. However, the difference in the predicted temperatures was minute. The developed model only simulated the case of continuous chip as only rough estimation of the temperature profiles on tool and work materials was required. The flow stress equation for the Johnson-Cook model is given below.

$$\sigma\left(\bar{\varepsilon},\dot{\bar{\varepsilon}},T\right)=\left[A+B\left(\bar{\varepsilon}\right)^{n}\right]\left[1+C\ln\left(\frac{\dot{\bar{\varepsilon}}}{\dot{\varepsilon}_{0}}\right)\right]\left[1-\left(\frac{T-T_{0}}{T_{m}-T_{0}}\right)^{m}\right] \qquad (0.1)$$

where:

ε : the plastic strain

$\dot{\bar{\varepsilon}}$: the strain rate $\left(s^{-1}\right)$

$\dot{\bar{\varepsilon}}$: the reference plastic strain rate $\left(s^{-1}\right)$,

T : the temperature of the work material $\left(°\mathrm{C}\right)$,

T_m : the melting temperature of the work material $\left(1399\ °\mathrm{C}\right)$

T_0 : the room temperature $\left(20\ °\mathrm{C}\right)$

and the Johnson-Cook coefficients:

A : the initial yield strength (MPa)

B : the hardening modulus (MPa)

C : the strain rate sensitivity coefficient

n : the hardening coefficient

m : the thermal softening coefficient.

Note $\sigma\left(\bar{\varepsilon},\dot{\bar{\varepsilon}},T_m\right)=0\rightarrow$ there is no temperature effect to flow stress at melting temperature.

Table 6: Johnson-Cooks coefficients for Ti-6Al-4V

Tm (°C)	A (Mpa)	B (Mpa)	C	n	m	References
1650	880	695	0.04	0.36	0.8	This study [Meyer, 1998]
1650	870	990	0.028	0.25	0.8	Shivpuri et. al. [2002]
1630	783	498.4	0.028	0.28	1.03	Ozel et. al. [2004]
1600	870	990	0.008	1	1.4	Umbrello et. al. [2007]
1656	863	656	0.013	0.5	0.8	Meijer et. al. [2001]

I.4.4 2D-FEM JC model with heat transfer

The heat transfer simulation requires all three modes of heat transfer, conduction, convection and radiation, which were investigated in order to improve the accuracy in obtaining the temperature profile. The convection and radiation heat transfer was set up at the exposed surfaces of chip (top, chip flow and chip-tool contact surfaces). The surrounding was the air at room temperature with the appropriate properties shown in Table 7. Based on this, the convection had an important effect on the temperature profiles. Figure 68 shows the 2D simulation models with flat PCD and 10° positive rake angle PCD inserts. The model with the flat carbide insert was also developed.

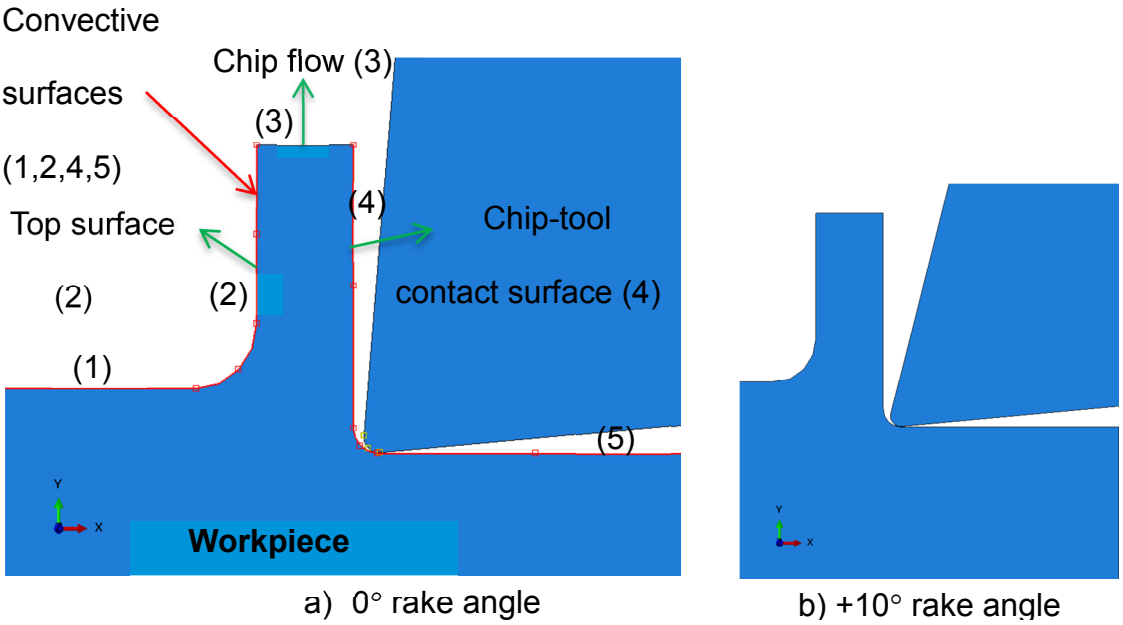

Figure 68: 2D orthogonal cutting FEM with heat transfer

Table 7: The parameters of air at 20°C and 1atm

Temperature	Density	Specific heat capacity		Kinematic viscosity	Thermal conductivity	
T (K)	ρ (kg/m^3)	Cp (kJ/kg.K)	$\mu.10^7$ (Ns/m^3)	$\nu.10^6$ (m^2/s)	$k.10^3$ (W/m.K)	$\alpha.10^6$ (m^2/s)
293.5 K	1.1614	1.0007	184.6	15.89	26.3	22.5

The heat transfer coefficient for free convection to the air was 5–25 (W/m^{2}K) while the value for forced convection was 10-200 (W/m^{2}K). In this simulation, the forced convection was appropriate because of the chip travels up to 2.03 m/sec approximated by the cutting speed. Table 8 reports the value for heat transfer coefficients for each cutting speed calculated based on Reynolds, Nusselt, Pardtl number, and chip flow using the equations (1.2) to (1.7).

Local heat flux :

$$q'' = h(T_s - T_\infty) \qquad \left[W / m^2\right] \tag{0.2}$$

Total heat rate :

$$q = \int_{A_s} q'' dA_s = (T_s - T_\infty)\int_{A_s} h dA_s \qquad [W]$$

or

$$q = \overline{h} A_s (T_s - T_\infty) \ ; \tag{0.3}$$

The average heat transfer coefficient :

$$\overline{h} = \frac{1}{A_s}\int_{A_s} h dA_s \tag{0.4}$$

The average heat transfer coefficient:

$$h = \frac{Nu_L \cdot k}{L} \tag{0.5}$$

Reynolds number:

$$\mathrm{Re}_L = \frac{u_\infty L}{\nu} = \frac{\rho u_\infty L}{\mu} \tag{0.6}$$

Nusselt number:

$$Nu_L = 0.664 \cdot \left(\mathrm{Re}_L\right)^{1/2} \left(\mathrm{Pr}\right)^{1/3} \tag{0.7}$$

Table 8: Reynolds, Nusselt number, and heat transfer coefficients for three cutting speeds

Chip flow (m/min)	Chip flow (m/sec)	Chip's Length (m)	Reynolds number	Nusselt number	h_avg
61	1.02 m/sec	0.0010	64.0	4.7	124.4
91.00	1.52 m/sec	0.0010	95.4	5.8	152.0
122.00	2.03 m/sec	0.0010	128.0	6.7	176.0

Although the majority of the heat generated during the process was from plastic deformation, the simulation results showed that the friction has some influence on the temperature profile. The comparison of chip-tool contact length between experiment data and those of the simulation model was made to determine a reasonable friction coefficient to be used in this model.

I.4.5 Cutting temperature profiles with 2D-FEM simulation

The temperature profiles on the chip along the rake face and through the thickness of the chip were the main interest. Figure 69 plots the temperature profile along the

rake face starting at the end-point of the round corner (see Figure 69) with the friction coefficient set at 0.8. The simulation results were adequate with the high temperature profile for the high cutting speed. The maximum temperatures did not happen at the cutting edge. The effects of heat transfer are reported in Figures 70-72 which show a significant reduction of temperature. The maximum temperature from the simulations without the heat transfer was along rake face while the simulations with the heat transfer showed the maximum temperature close to the shear bands presented in other publications [Sima, 2010; Y. C. Zhang, 2011; X. Zhang, 2011] with segmented chips.

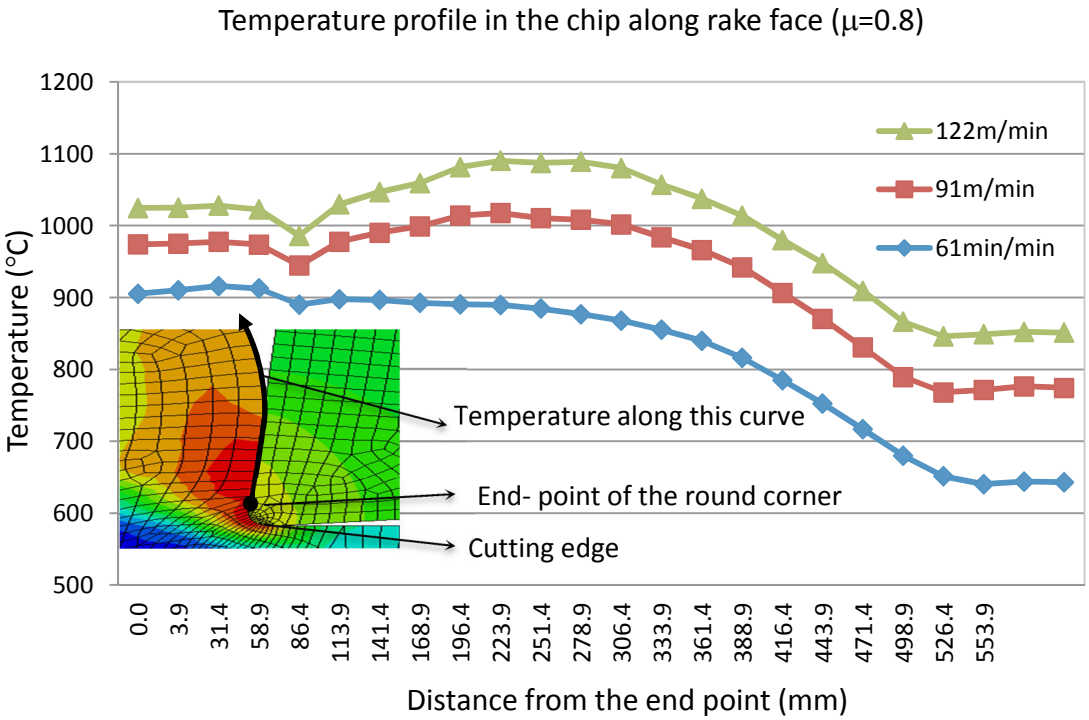

Figure 69: Temperature profiles on the chip along tool-chip interface with PCD

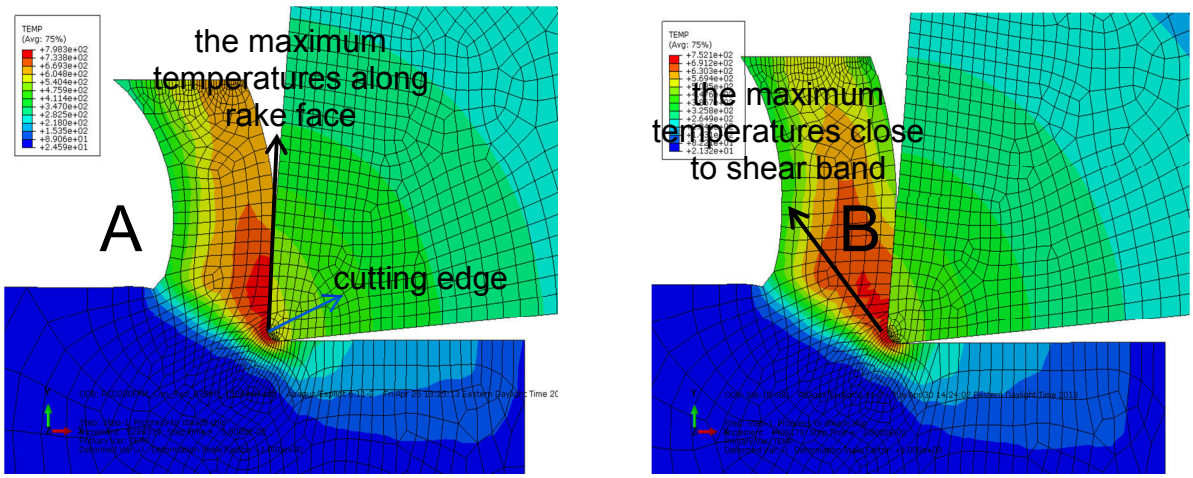

Figure 70: The temperature in Ti- turning with PCD rake angle: (A) Without heat transfer, (B) with heat transfer (friction μ=0.35)

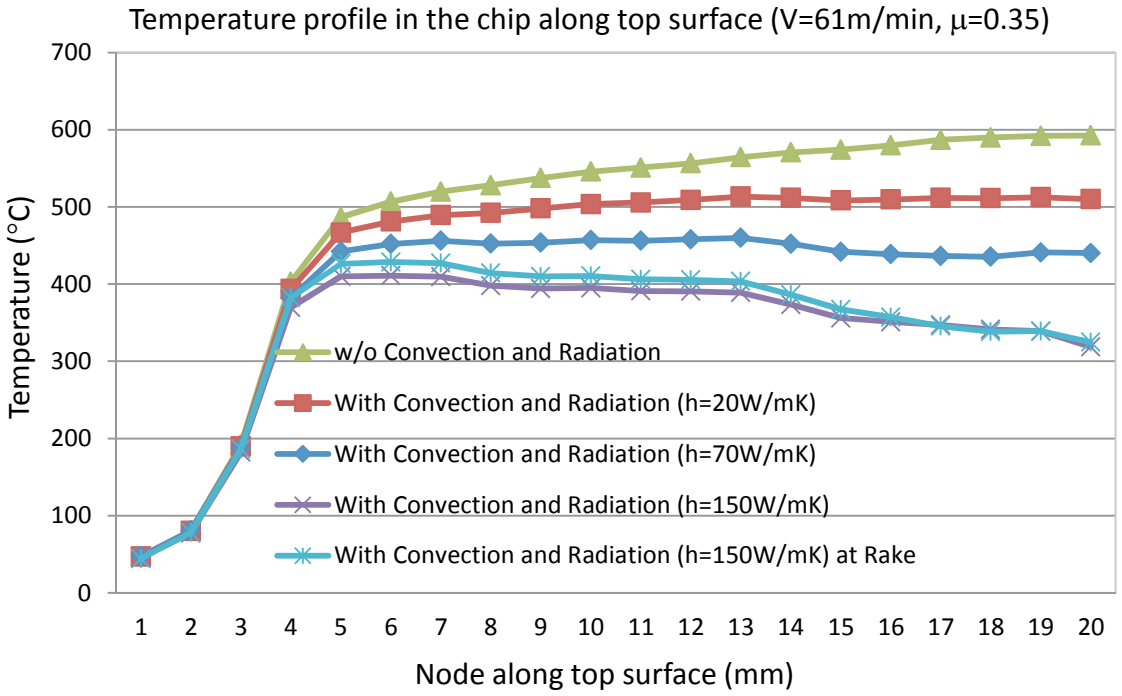

Figure 71: Effect of heat transfer to temperature profiles along the top surface of the chip with PCD

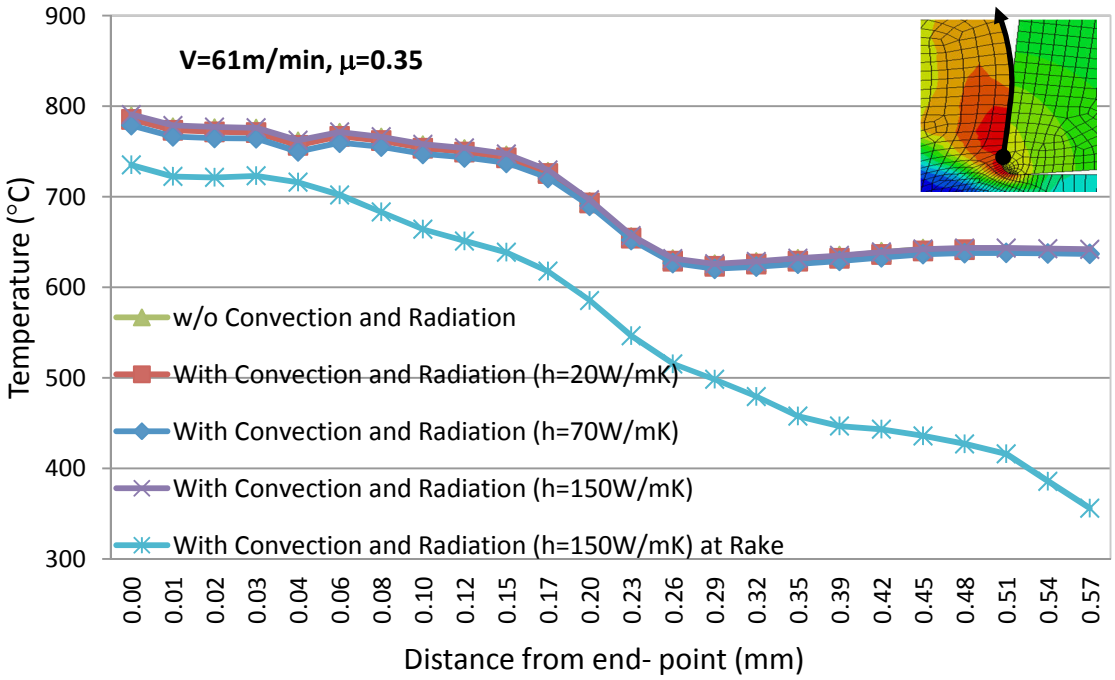

Figure 72: Temperature profiles on the chip along tool-chip interface with PCD with and without heat transfer

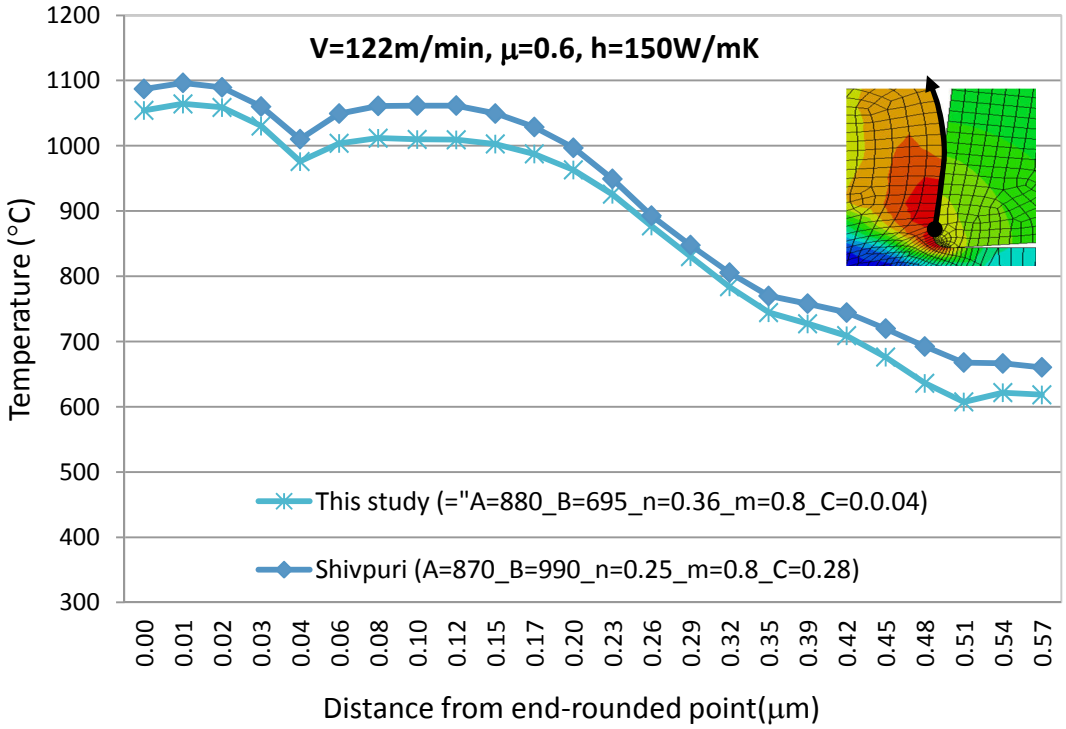

Figure 73: Effect of JC parameter to temperature profiles on the chip along tool-chip interface with PCD.

Figure 74 represents the significant effects of the friction coefficient in FE simulation on the temperature profile along the rake face. To estimate the reasonable friction coefficients for FEM simulation, the chip-tool contact lengths between simulation results and experiments were compared. These values of experiment were approximated by the maximum width of crater wear on the rake face of inserts. The simulated results shown in Figure 75 also indicate that the chip-tool contact length depended strongly on the friction coefficient. There was a small difference in the length among three cutting speeds. As shown in Figure 75, the chip-tool contact length of PCD and PCD+10° in the turning test was most likely close to those of the simulation model with the friction coefficients of 0.6. For the simplicity, 0.6 was used as friction coefficients for both PCD. The simulated temperature for all cutting speed with friction coefficient of 0.6 was shown in Figure 76. The temperatures at tool-chip interface were above transus temperature at medium and high cutting speed. The maximum cutting temperatures of 2D FEM simulation with carbide insert were reported at least 100 °C higher than those PCD at all cutting speeds [Schrock, 2012]. This thesis accepted that results although the FEM model was simulated without heat transfer.

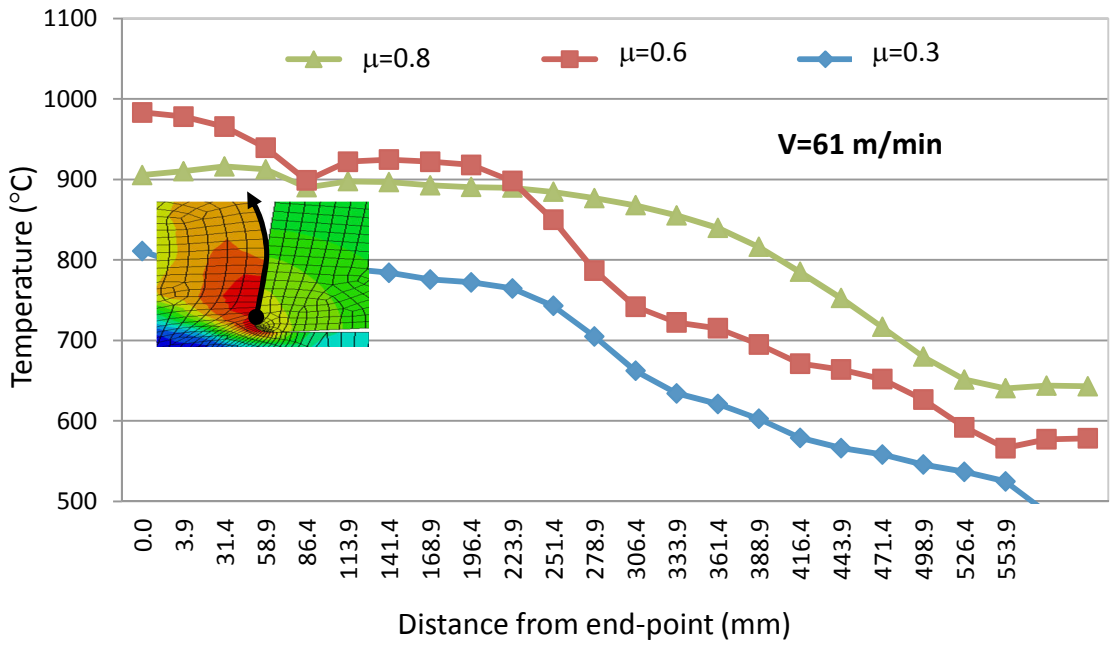

Figure 74: Temperature profiles on the chip along tool-chip interface with PCD at various friction coefficients

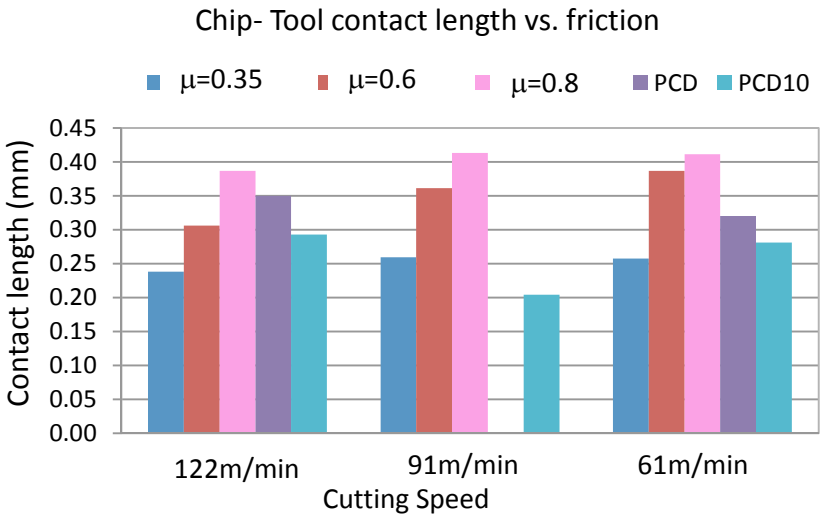

Figure 75: The chip contact length from experiment and simulation of PCD at various friction values

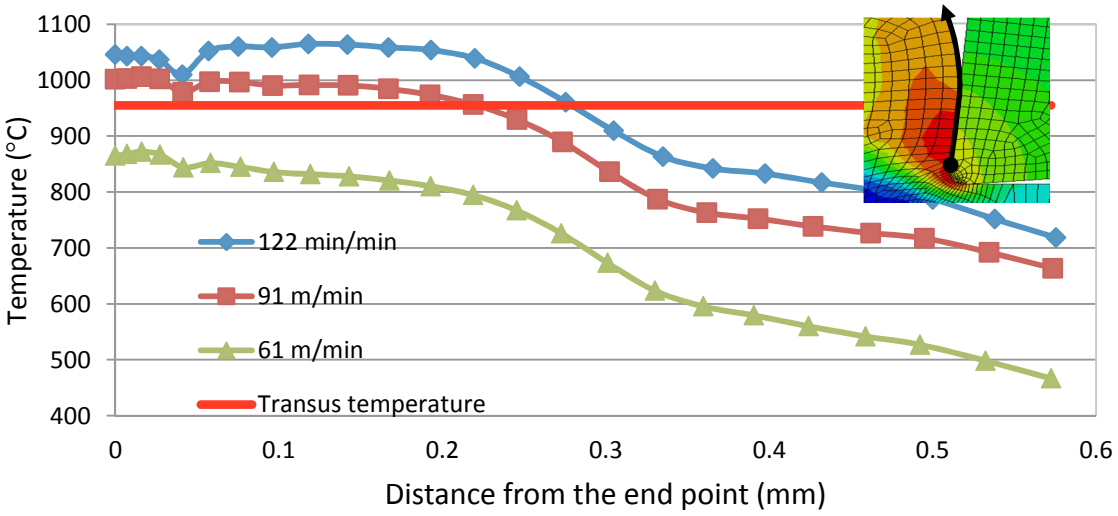

a) Temperature profile in the chip along tool-chip interface with PCD (μ=0.6)

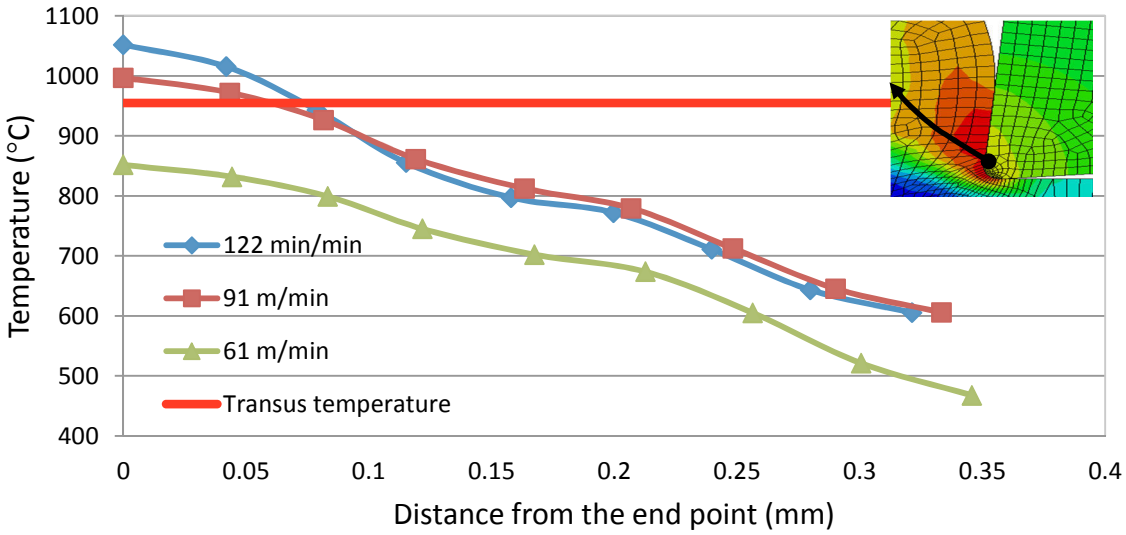

b) Temperature profile in the chip along shear band with PCD (μ=0.6)

Figure 76: Temperature profiles on the chip with PCD inserts and μ=0.6 at various cutting speeds.

Chapter 2: Evidence of phase change and root causes flank wear and scoring marks with orientation imaging microscopy (OIM)

II.1 OIM SETUP FOR CRYSTAL ORIENTATION IN TI64 ALLOY AND CHIPS

To explain the wear mechanism on both rake and flank face, the microstructure of Ti workpiece (before machining, to be called Bulk-Ti) and after machining (chip) was investigated with Orientation Imaging Microscopy (OIM) based upon electron-backscattered diffraction (EBSD). Two samples (Sample A and Sample B) were cut out from the Bulk-Ti to study the microstructure before machining in DOC and feed rate directions as shown in Figure 77a. The microstructure in the YZ plane is noted to be Sample A (in Feed direction) while that in the XY plane is Sample B (in DOC direction). To accurately obtain the original structure of the work material and limit effects deformation and heat-affected zones and heat of the cutting process, Wire Electron Discharge Machining (EDM) was applied to cut off these samples from the round bar of Ti workpiece. With Wire-EDM cutting, the heat-affected zones from the process can be easily removed [Hasçalık, 2007]. After polishing, EBSD scans were conducted at various locations on both samples. With the Bulk-Ti samples, the EBSD was scanned on the region of 800μmx800 μm, step size 2 μm, exposed time of 0.13sec. To have the reliable data, EBDS was conducted at various regions (named A1, A2, A3, B1, B2, B3) on both samples as showed in Figure 77a.

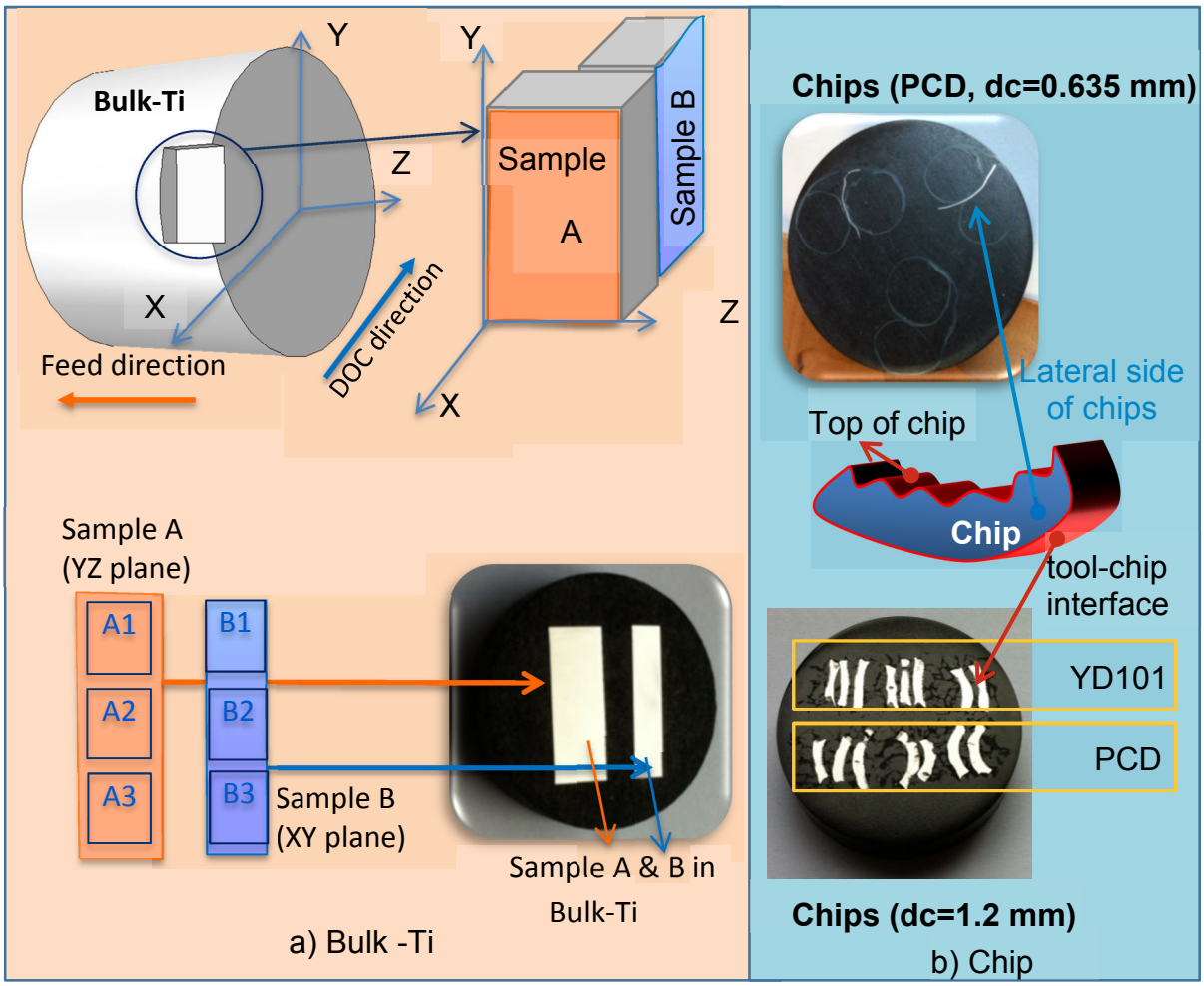

Figure 77: Samples for EBSD of material before (Bulk-Ti) and after (Chip) machining

The microstructures of chips generated with carbide and PCD inserts at all speeds were investigated to compare with those of bulk-Ti as shown in Figure 77b. The difference in the microstructures between bulk-Ti and chip contains the information about cutting temperature, stress, plastic deformation, phase change, etc. The scanned regions of 200μm x 200μm were taken on the chips with step size 1μm and exposed time of 0.13sec.

The EBSD studies shown in Figure 78 were carried out using a CamScan 44 FE scanning electron microscope, with a field emission gun operated at 20 kV using

TSL/Link OIM TM system. The working distance of 33 mm was used, and the exposure time for each Kikuchi pattern was 0.08 s. The TSL data collection software was connected with the EBSD camera to instantaneously convert the acquired Kikuchi patterns into crystal orientations. Each crystal orientation thus obtained was recorded as three Euler angles. The step size used for each scan varied and was indicated in the result session. Two clean-up steps were performed on all the EBSD datasets. The first step was to conduct a neighboring confidence index (CI) correlation procedure, where a data point with a CI smaller than 0.07 (user defined) is reassigned the orientation and CI of its neighbor with the highest CI.

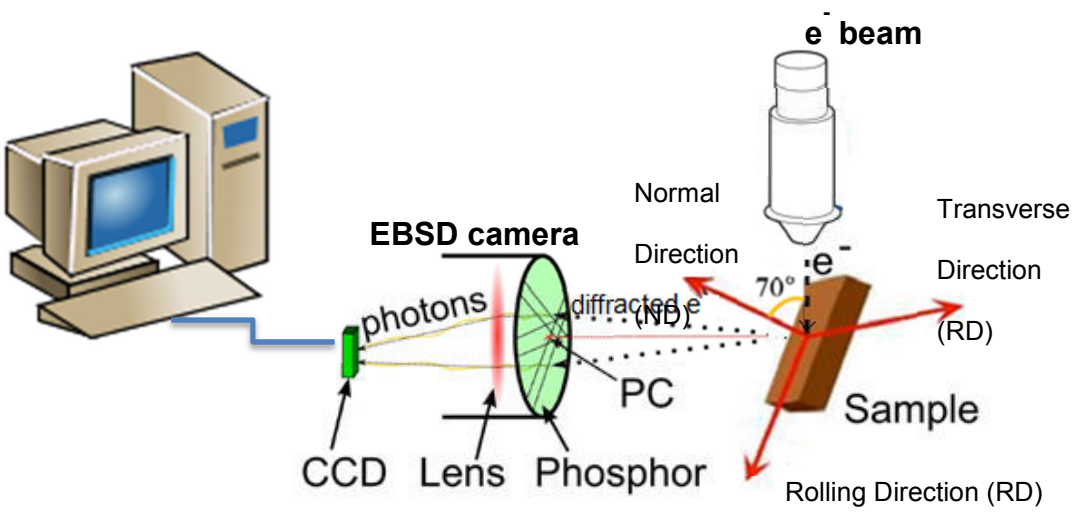

Figure 78: EBSD configuration

II.2 OIM RESULTS AND DISCUSSION

II.2.1 Evidence of phase change (α →β) in machining of Ti64

The OIM scan of the microstructure is very important to indicate the indirect evidence of phase change of titanium in the cutting process. Based on the average results of six scan areas (A1, A2, A3, B1, B1, B2, B3) on the Bulk-Ti sample as shown in Figure 79, the microstructure before machining was mostly the alpha phase accounting for up to 99% of area fraction with the rest being the β-phase as summarized in Table 9. The distribution of α-grain size in samples A and B was plotted in Figure 80. It should be emphasized that that the average grain sizes of α-phase and β-phase in the Bulk-Ti samples were 6.78 μm and 3.89μm, respectively. However, the grain size in chips was much smaller, as shown in Figure 81. This was likely the result of high deformation and recrystallization near the cutting zone on the chips. The lateral side (see Figure 77b) of the chip recrystallized more than the chip-tool interface as evident by the much smaller grain size on the side of chips. Only small differences in the average grain size in relation to the cutting speeds and tool materials were evident.

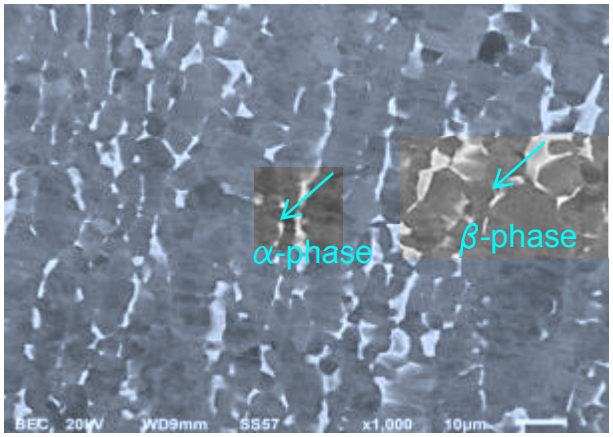

Figure 79: Microstructure of Ti64 alloy used in turning tests

Table 9: The area fraction of α-phase and the grain sizes of each phase in Bulk-Ti

Area	Area fraction of α-Ti	Grain size of α-Ti (μm)	Grain size of β-Ti (μm)
A1	99.6%	6.93	3.99
A2	99.6%	6.86	3.54
A3	97.3%	6.52	3.61
B1	99.5%	6.74	3.45
B2	99.4%	6.68	4.74
B3	98.9%	6.95	4.46
Average	**99.1%**	**6.78**	**3.97**

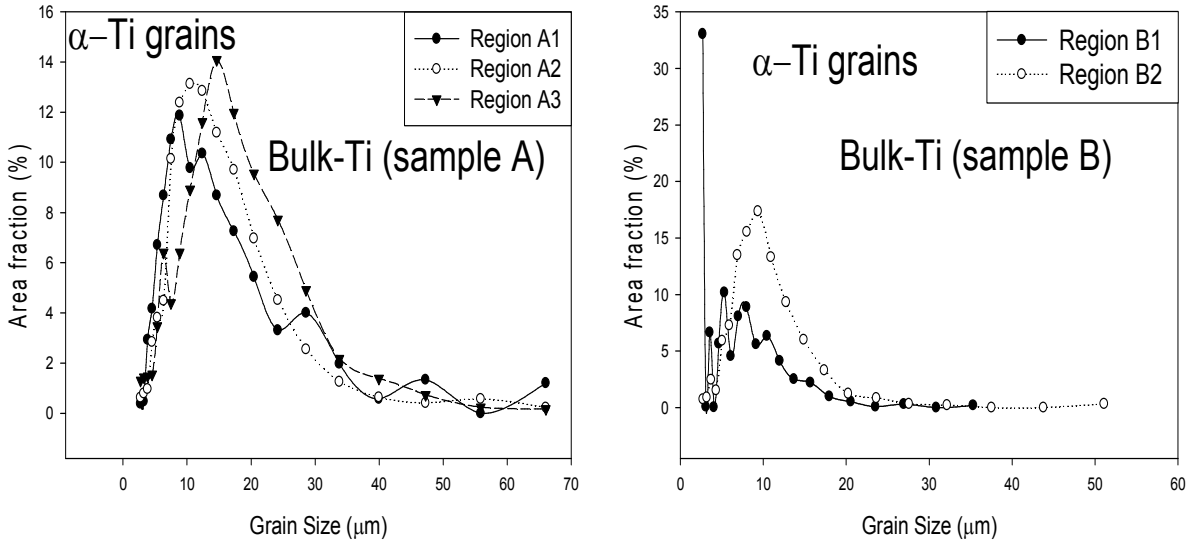

Figure 80: Grain size distribution of α-Ti in un-deformed work material (Bulk-Ti)

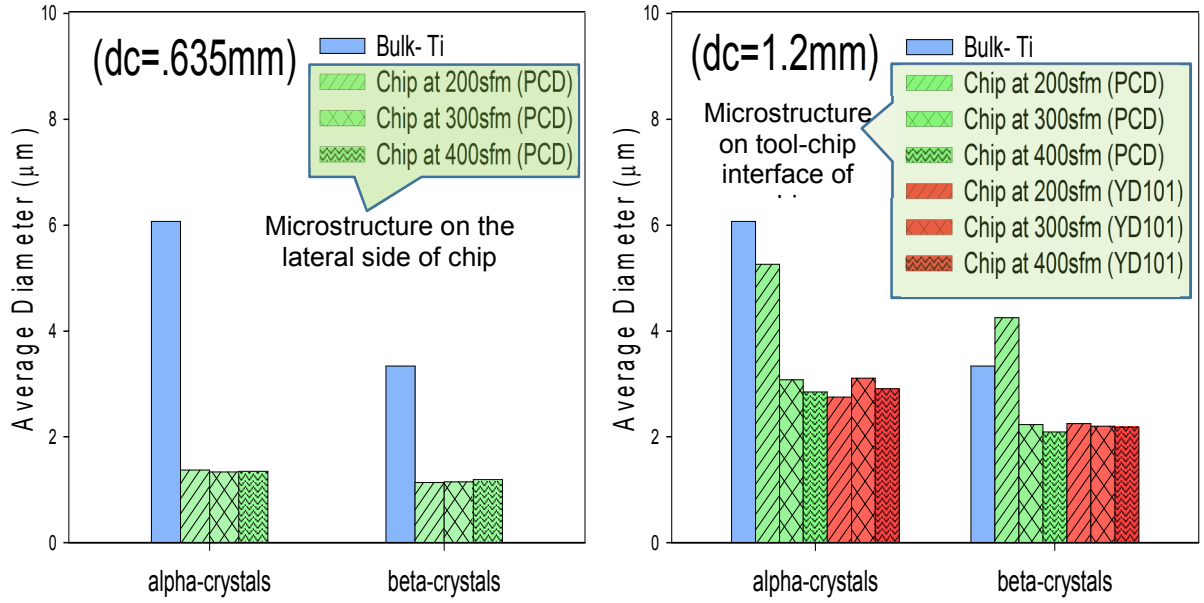

Figure 81: The comparison of average diameter of grains in the bulk-Ti and in the deformed material (chips).

In Ti machining, the evidence of phase change is not easy to prove. Due to the low thermal conductivity, the temperatures of chip are expected to be higher than the transus temperature (T_s) at which the phase transformation (α to β) occurs. At

atmospheric pressure, the α-phase in Ti64 transformed to the β-phase when the temperature increased above T_s = 995°C. The β-phase transformed back to the α-phase when the temperature was cooled to below T_s. However, due to the low thermal conductivities, the chips cooled slowly. This process helped the most of β-phase to have enough time to transform back to the α-phase. Therefore, the amount of β-phase formed during the cutting process cannot be determined directly. Because the $\beta \rightarrow \alpha$ transformation has a well-defined interphase misorientation relationship, it is possible to see evidence of $\alpha \rightarrow \beta$ phase by determining the misorientations in the α phase.

In a polycrystalline material, the misorientation is defined as the difference in crystallographic orientation between two adjacent crystals. When Ti64 is slowly cooled below the beta transus temperature, α-plates form with their base planes parallel to the transformation planes (110) of the β-phase as shown in Figure 82. The α-plates grow relatively slowly in perpendicular direction to the planes and much faster along the planes making acicular (plate-like) structures (see Figure 83). Because of the symmetry of the β-phase, the transformation planes are oriented 60° & 90° to each other resulting in alpha grains with precisely 60° & 90° misorientation as shown in Figure 82. A high fraction of boundary in the α-phase with 60° & 90° misorientations indicates proof of the phase change roughly.

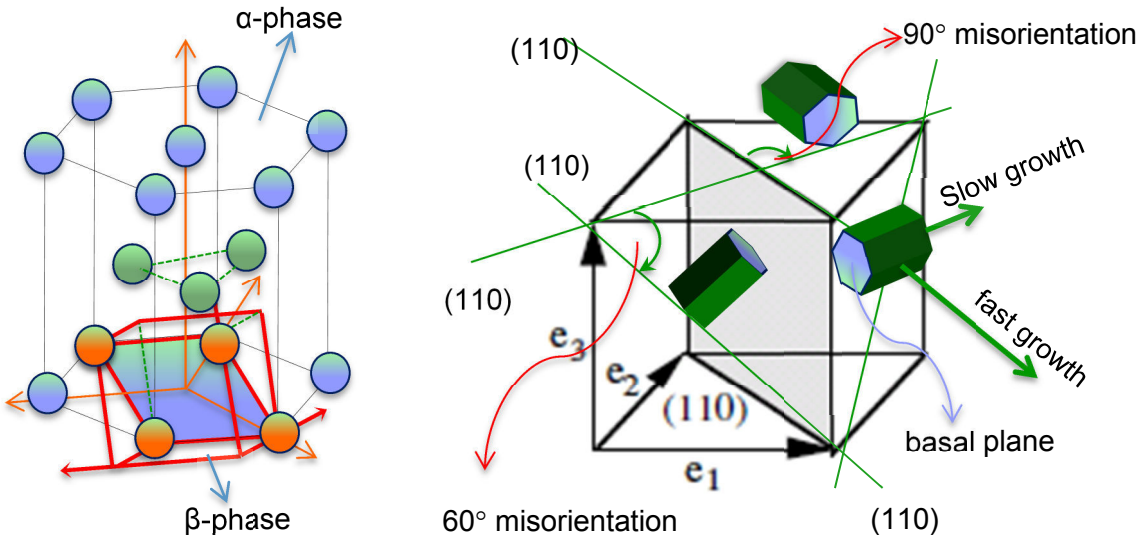

Figure 82: Burgers' orientation relationship in β → α transformation

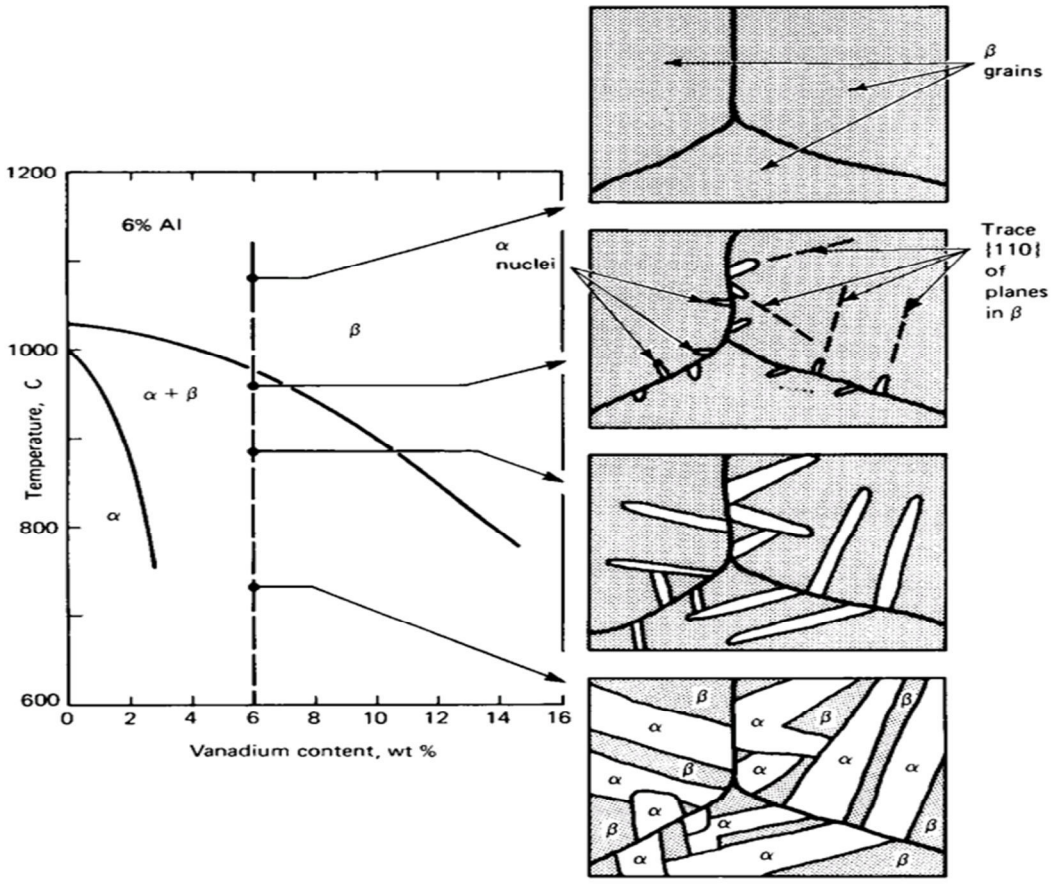

Figure 83: Microstructures achieved at various intermediate temperatures by slowly cooling from above the β transus

Figure 84 shows the higher peak of 60° and 90° misorientations in the chips than those in un-deformed work material. In addition, the portions of the β-phase in the chips were greater than those in Bulk-Ti as presented in Figure 85. This evidence provides a strong indication of the phase change during cutting process. It should be noted that the determination of the phase change is valuable in predicting the diffusion/dissolution wear. In observing the chips between low and high DOCs, a higher fraction of the β-phase and the higher peak of 60° and 90° misorientations with low DOC were observed. However, OIM scans were conducted on the side and tool-chip interface of chips for low and high DOC, respectively. One possible explanation is the higher and more uniform temperatures at the chip-tool interface while the temperatures on the side were closer to the transus temperature and the temperature gradients were greater due to the faster cooling on this side. The fast cooling process retains more β-phase in the chip. 3D FEM simulation which was not presented in this thesis may reveal the difference in terms of temperatures with two DOCs in order to have a more convincing explanation. Figure 86 shows the distribution of the β-phase among the α-phase in the underside of the chip at high DOC for both carbide and PCD inserts for three cutting speeds. It was interesting to see that, at high DOC, the β-phase crystals were distributed mostly at shear band where the temperature was reported highest in most FEM simulation with serrated chips.

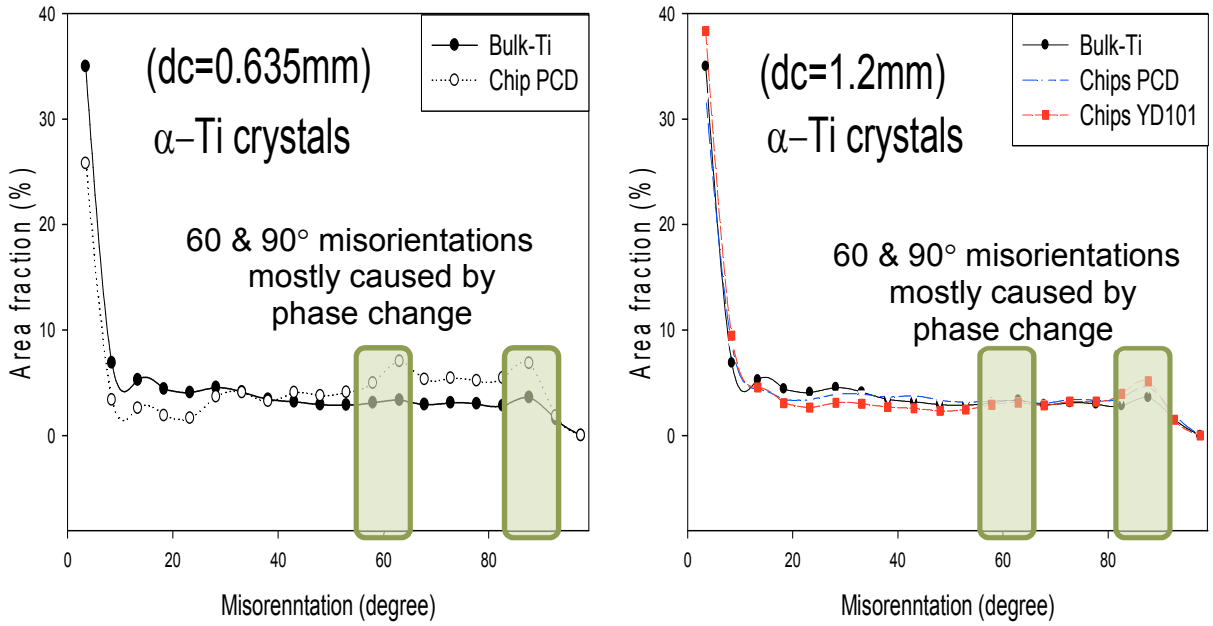

Figure 84: The comparison of misorientation in α-Ti crystals in un-deformed (bulk-Ti) and deformed (chips) work material at low and high DOC

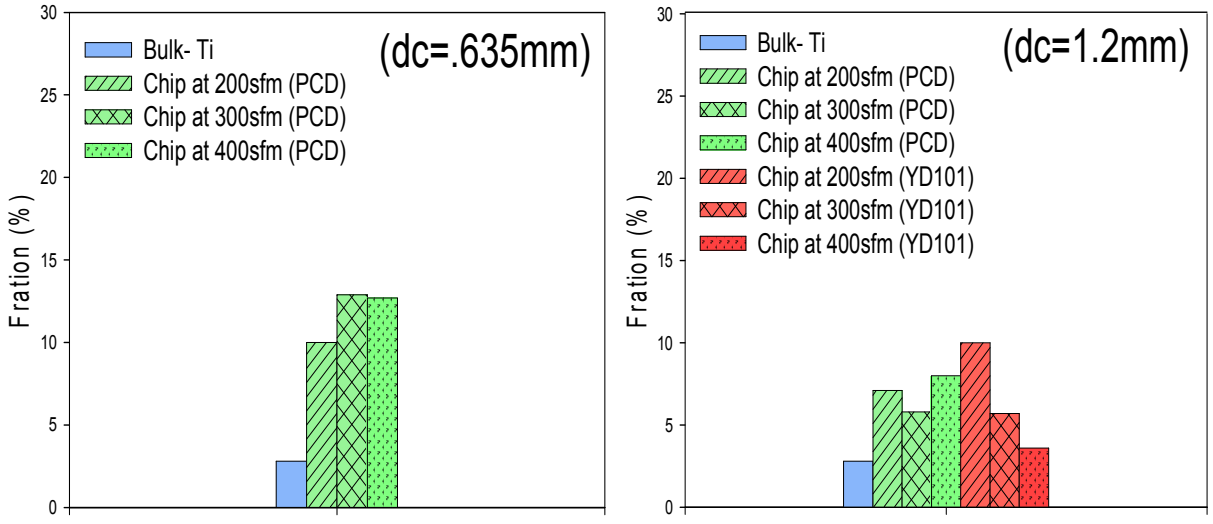

Figure 85: The comparison area fraction of β-Ti crystals in un-deformed (bulk-Ti) and deformed (chips) materials.

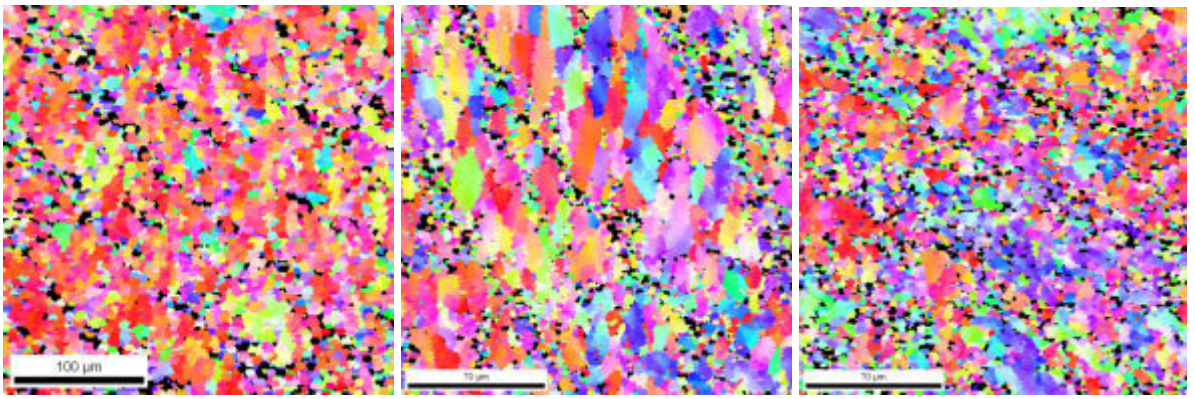

PCD1510 at 61 m/min PCD1510 at 91 m/min PCD1510 at 122m/min

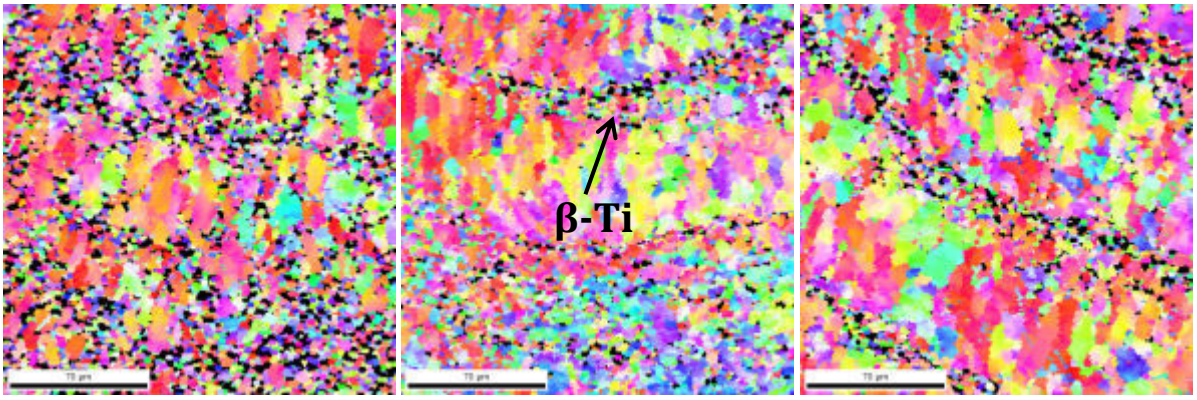

YD101 at 61 m/min YD101 at 91 m/min YD101 at 122m/min

Figure 86: The distribution of the β-Ti (dark) and the α-Ti (colored) in the chips at high DOC.

II.2.2 Root causes flank wear and scoring marks in Ti alloys machining

Scoring marks were typically found on the flank wear in machining of Ti alloys [Bermingham, 2011; Dearnley, 1986; Hughes, 2004; Narutaki, 1983; Venugopal, 2007; Wright, 1981] as shown in Figure 87. This section mainly focuses on the microstructure of a work material in an attempt to determine the root cause for flank wear and scoring marks on flank face.

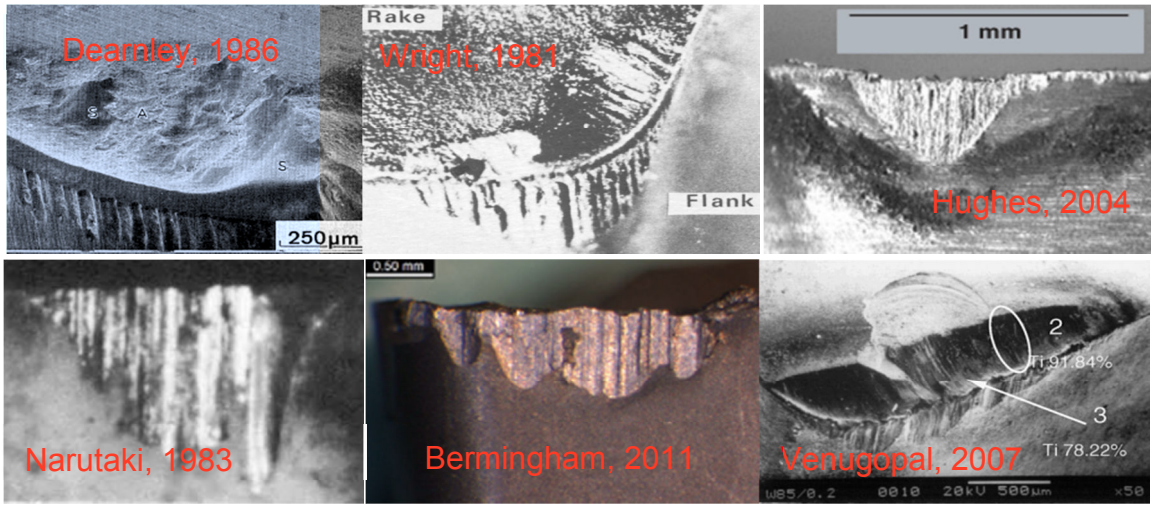

Figure 87: Scoring marks on flank face of inserts in machining of Ti alloys

The α-Ti has the characteristic anisotropy in mechanical properties. The hardness of α-Ti in the c-direction (0001) was reported to be much harder (~1.5 time) than any other directions [Britton, 2009; Kwon, 2013]. Figure 6 shows the anisotropy in hardness. Based on these data, the α-Ti with the c-axis within ±20° interacting with the wear land of the inserts was chosen as the grains with 'hard' orientations or the 'hard' α-grains respect to the inserts. During machining, the tool will be worn or damaged when the 'hard' α-grains interacts with the tool surfaces.

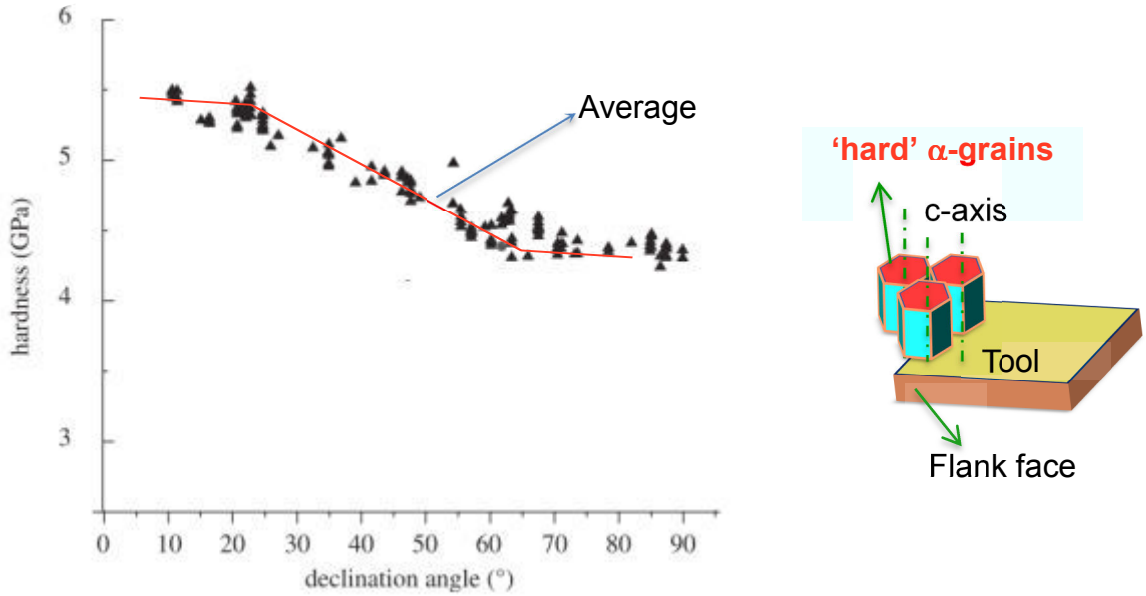

Figure 88: Hardness of α-Ti as a function of the declination angles between c-axis to vertical line [after Britton, 2009] and the 'hard' α-grains respect to flank face.

The results of EBSD scan showed that Bulk-Ti consists mostly of the α-Ti. Therefore, the anisotropy in hardness of α-grain had significant effect to wear. As shown in Figure 89, Sample A shows the distribution of the hard-orientation grains considering the hard orientation within 90±20° to the rake face. It shows that the clusters of hard α-grains in the Y-Z plane (the declination angle within ±20°) are distributed in the direction of Z. Sample B has the hard-orientation grains agglomerate more less at the 30° from the negative Y axis as shown in Figure 89.

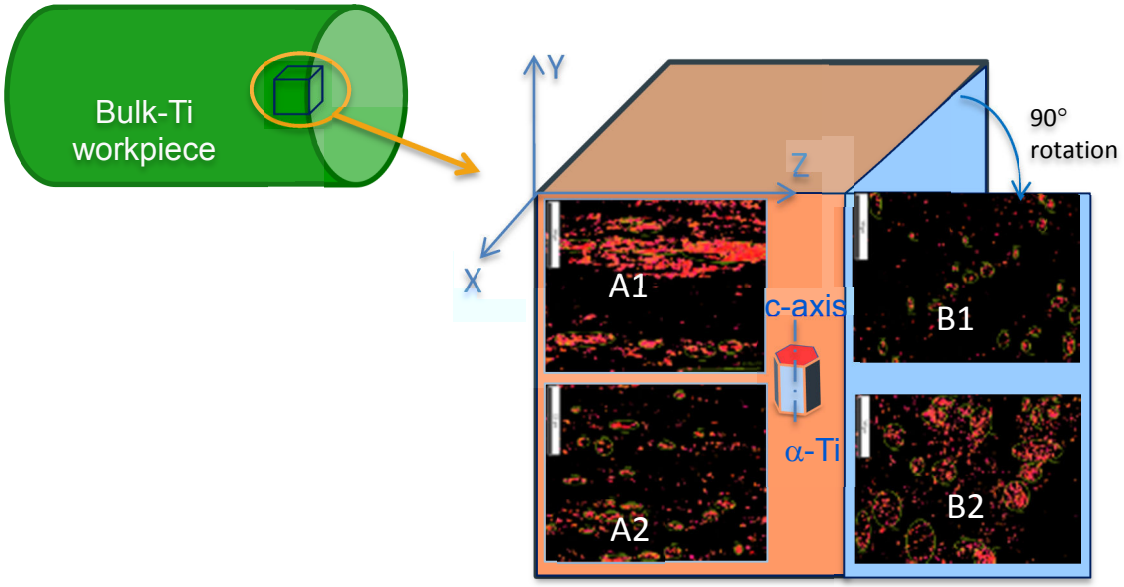

Figure 89: The distribution of α-crystal in hard orientation (red color) in Bulk-Ti sample respected to flank face of tool along feed direction

The interaction with the tool in the hard α-grains can cause the abrasion, chipping and the fracture. The size of the fracture may depend on the size of α-clusters in the Bulk-Ti as well as the detailed interaction conditions (e.g. impact angle and orientation). Table 10 summarizes the average dimensions of the 'hard' α-clusters based on the microstructures in both XY and YZ faces. Based on these OIM measurements, the size of the 'hard' α-clusters is roughly estimated and represented in Figure 90. In this particular microstructure, the 'hard' α-cluster can be easily approximated into an ellipsoid. Figure 91 shows how an ellipsoidal hard α-cluster interacts with the flank surface, generating the flank wear. In addition, the 'hard' clusters happen to be in a certain plane, horizontally on the YZ face and on the 30°-orientation on the XY face. Machining the same 'hard' α-cluster range in the Bulk-Ti, however, the much harder PCD insert has much better wear resistance, resulting in

smaller and shallower scoring marks on flank wear compared to the carbide insert as shown in Figure 92.

Table 10: The dimensions of the 'hard' α-cluster with Bulk-Ti

Sample	Minimum width (μm)	Maximum width (μm)	Average width (μm)
Sample A (YZ plane)	25.78	301.56	**87.49**
Sample B (XY plane)	16.41	89.06	**54.49**

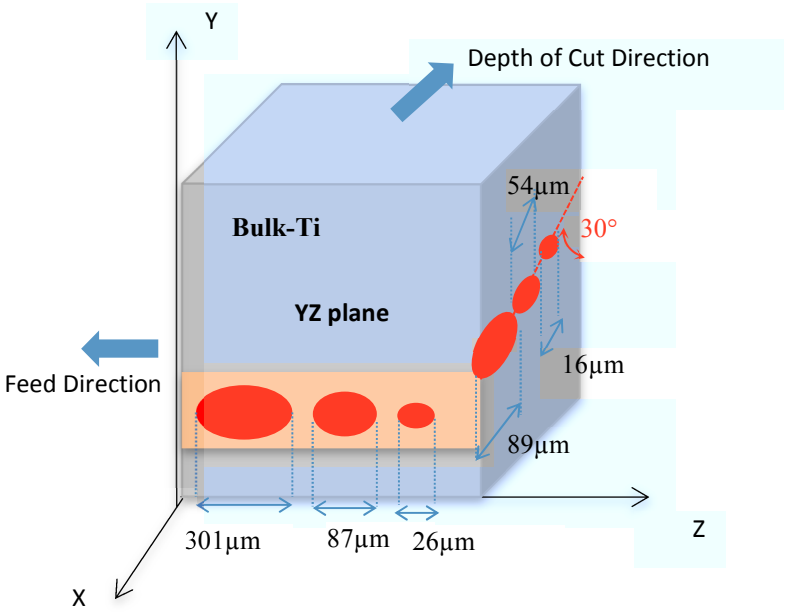

Figure 90: The size of 'hard' α cluster in Bulk-Ti.

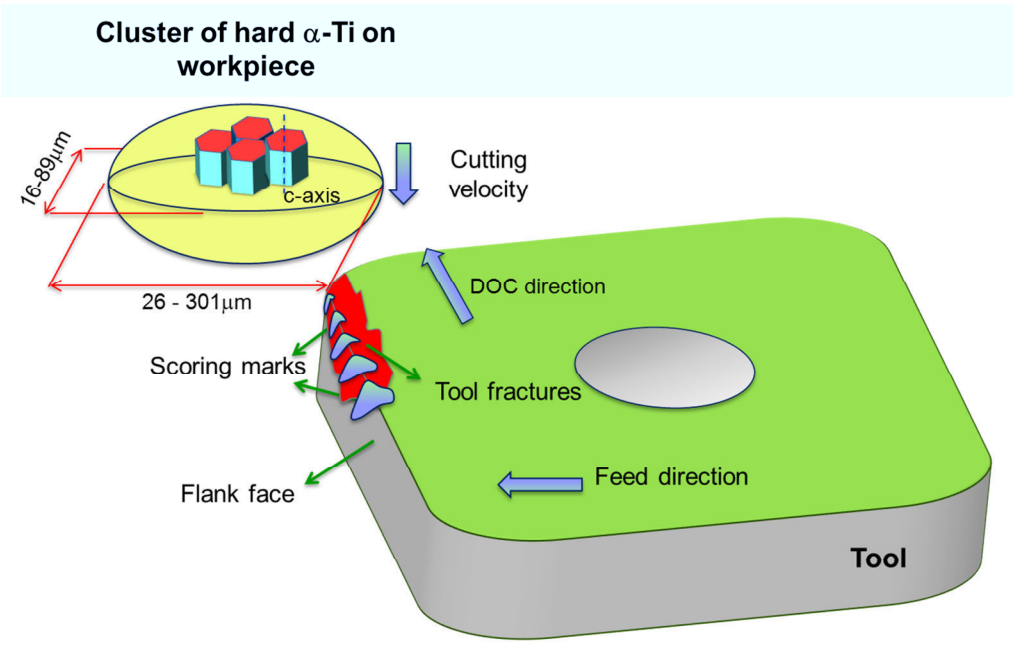

Figure 91: Interaction of the 'hard' α-cluster and the inserts.

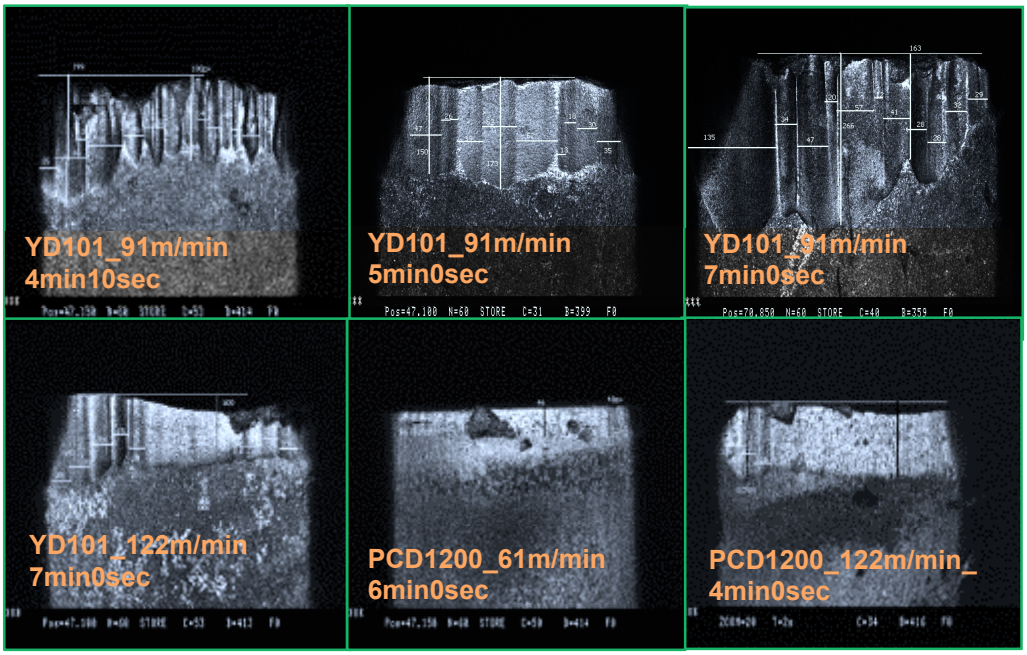

Figure 92: The scoring marks on the carbides and PCD inserts at low DOC

Obviously, because of the flank temperature being much lower than the crater temperature and the 'rough' wear surface, the dissolution and diffusion rate is not significant for the flank wear. Discounting the macro-fractures which may be more

related to the microstructural variations, two distinct types of steady-state wear patterns were identified, (a) micro-fracture at the cutting edge and (b) scoring marks. Both types of damage can be caused by the “hard” α-phase grains and clusters. However, micro-fracture can be affected by additional mechanisms, the adhesion and detachment of the work material. These two patterns on the flank face manifest themselves into four main types of observed damage presented in Table 11. Type I is the micro-fracture which occurs near the cutting edge most likely as a result of the impact with the ‘hard’ grain or cluster, which are observed only on the PCD inserts. Type II occurred near the cutting edge in both carbide and PCD. The distinction between Type I and II is the inverted shape of the fracture.

Both Types I and II are expected to be caused by the larger ‘hard’ α-clusters in a work material. Because the incidences of Type I damage are much rare and only occurred to the PCD inserts in our experiment, more detailed interaction conditions must be explained with the adhesion layer. Many researchers [Dhar, 2002; Ezugwu, 1997; Hartung, 1982; Rahman, 2003] reported that Ti adheres to a tool material, which leads to the chipping when detached. Our observations indicated that not only was the adhesion on carbide inserts substantially more extensive than PCD inserts but the adhesion layers were also mostly located on the crater surface as shown in Figure 93. Consequently, the cutting edge of the carbide inserts was more extensively damaged while the edge of the PCD inserts remained sharper. The difference in the adhesion layer between carbide and PCD inserts enabled Type I to cause damage on PCD inserts. With Type II, additional damage may occur as the loose fragments can further damage the surface evident by the damage at the trailing

end of the fracture. Type III was the scoring marks abraded by the 'hard' α-grains or cluster. Type IV was the combination of the first and third types of damage. Besides of Type III, the more common damage on PCD inserts were Type I and II while those of carbides were Type II and IV.

Table 11: Typical damage on the flank face

Typical damage		Explanation
Type I	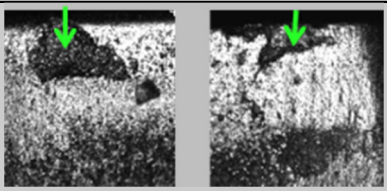	Micro-fracture by the Impact of the hard α-cluster only on PCD
Type II	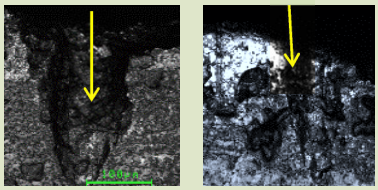	Micro-fractures by the Impact of the hard α-cluster
Type III	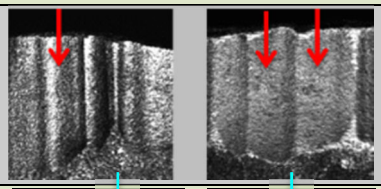	Scoring marks caused by the 'hard' α-crystal or cluster.
Type IV	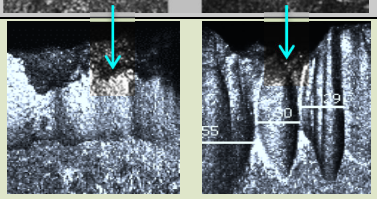	The Combination of Type I and Type III

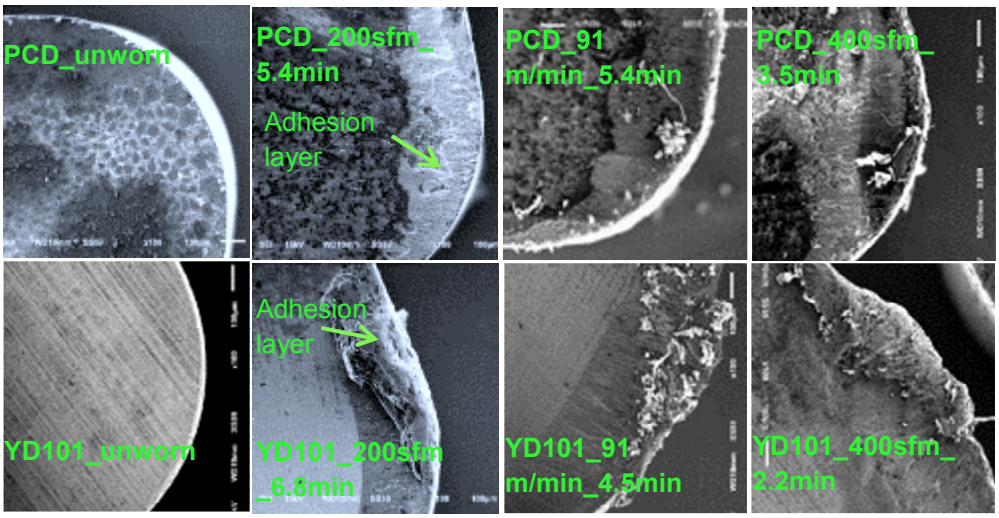

Figure 93. Adhesion layer on the rake face of carbide and PCD inserts

The scoring marks, Type II damage, were much more prevalent than any other types on both carbide and PCD inserts. However, the scoring marks on the carbides were not as distinct as those of PCD. Our hypothesis is that all four types of damage were caused by the 'hard' α-crystals and the adhesion may enhance Type I and II damage. To substantiate this claim, the widths were measured for at least ten scoring marks on both carbide and PCD inserts at various cutting lengths as shown in Figure 94. The distribution of width was presented using a 'box and whisker' plot with the minimum, maximum and average width as shown in Figure 95 for low DOC and Figure 96 for high DOC. These data were compared to the size range of the 'hard' α-clusters obtained in Sample B (mostly close to tool flank face) shown in the light gray boxes in Figures 95 and 96. Notice that the widths of the damage were substantially smaller as only a smaller part of each ellipsoidal cluster interacts with the tool during the abrasion process. The width of the scoring marks was larger with longer cutting distance for both carbide and PCD tool as demonstrated in Figures 95 and 96 as the probability of encountering larger clusters increases. Typically wider scoring marks

were observed at high cutting speed except the cutting speed of 122 m/min for carbide inserts. This may happen because the tool material becomes much softer at the high cutting temperature. The scoring marks on the carbide YD101 inserts were smooth and consistent in the width of each scoring mark as shown in Figure 97. For low DOC, with comparative grain size among carbide and PCD1200 and PCD1210 grades, grooves were smaller and less on PCD inserts than those on carbide inserts for all cutting speeds. For high DOC, the sizes of grooves on PCD1510 inserts were comparative to those on carbide inserts. As discussion early, diamond grains pulled out grains was main wear mechanisms on both rake and flank faces of PCD inserts. The scoring marks were produced from impact of hard α-clusters and flank face. The size of scoring marks was equivalent to the size of one or two diamond grains fractured out (much larger grain size of PCD1510 inserts).

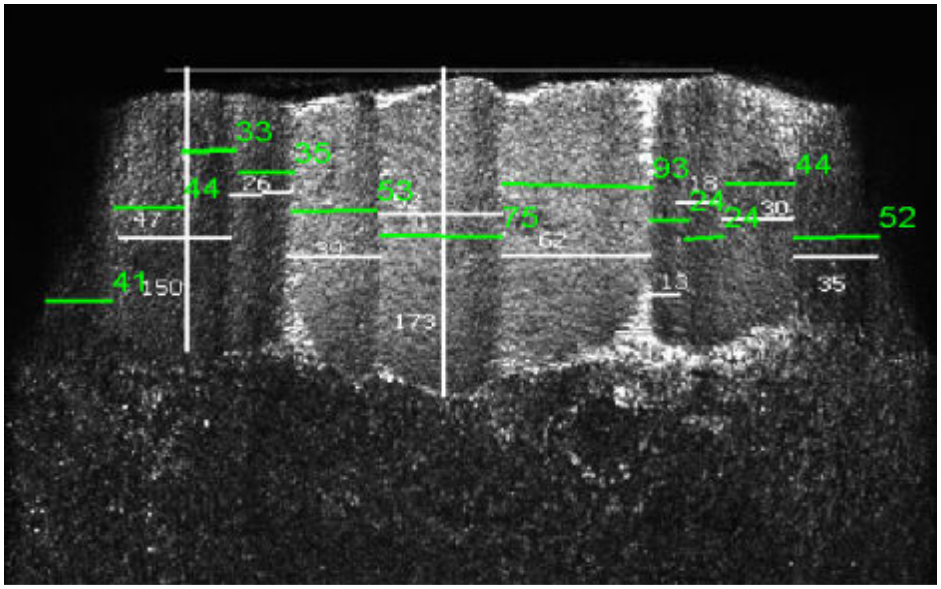

Figure 94: Width (μm) of ten scoring marks on YD101

With similar phenomena, the comparable grain size among PCD1200, PCD1210 and carbide YD101, YD201 inserts, the scoring marks were narrower and less in

number for PCD inserts than those for carbide insert for all cutting speeds due to the superior hardness of the PCD. For PCD inserts, the width of scoring marks was more independent of cutting speed. PCD inserts have much higher hardness than the carbide inserts and the 'hard' α-grain (6000kgf/mm^2 for PCD, 1800kgf/mm^2 for carbides [Groover, 2007] and 550kgf/mm^2 for α-grain in hard orientations [Britton, 2009] at room temperature) while their transverse rupture strength and fracture toughness of PCD (1550MPa and 6.86MPa·m$^{1/2}$ [Lammer, 1988]) were lower than those of carbide insert (3133MPa and 10.18MPa·m$^{1/2}$ [Fang, 2005]). Most of scoring marks on PCD were rough with uneven width (and depth) as the pulled-out diamond grains can abrade the tool surface, as shown in Figure 98. In addition, PCD inserts were more prone to micro-fracture than the carbide inserts, an indication of lower fracture toughness of PCD. The similar phenomenon was observed on the rake face reported in [Schrock, 2014]. At high cutting speed, the micro-fractures are more frequent and larger to suppress the appearances of the scoring marks on flank wear. There is no difference between flat and positive tool in term of scoring marks due to the end relief angle is the same for both inserts.

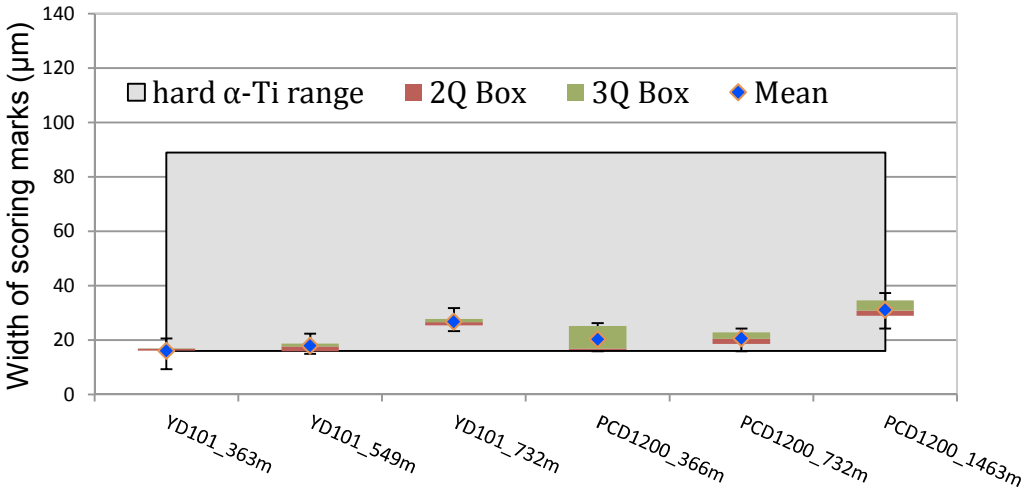

a) Vc = 61m/min, DOC = 0.635 mm

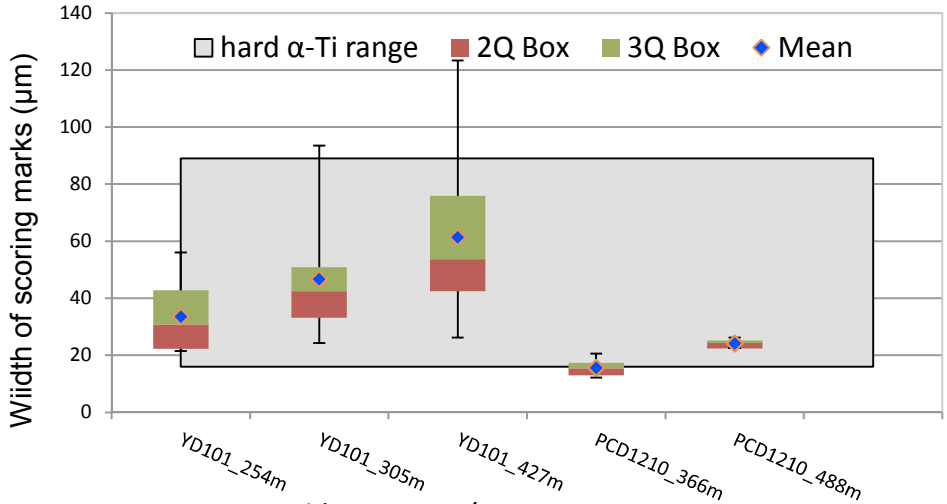

b) Vc = 91 m/min, DOC = 0.635 mm

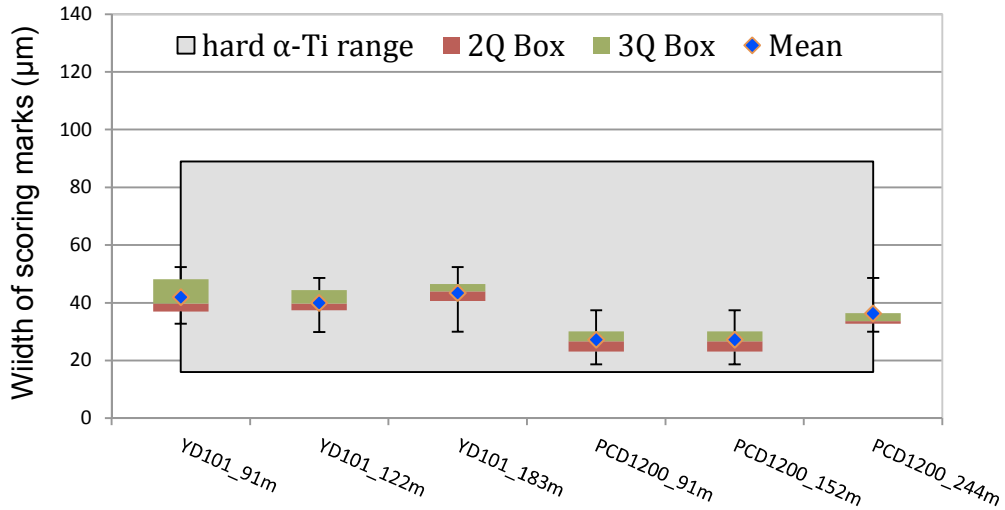

c) Vc = 122m/min, DOC = 0.635 mm

Figure 95: Range and distribution of width of scoring marks of nose at low DOC respect to 'hard' α-cluster size

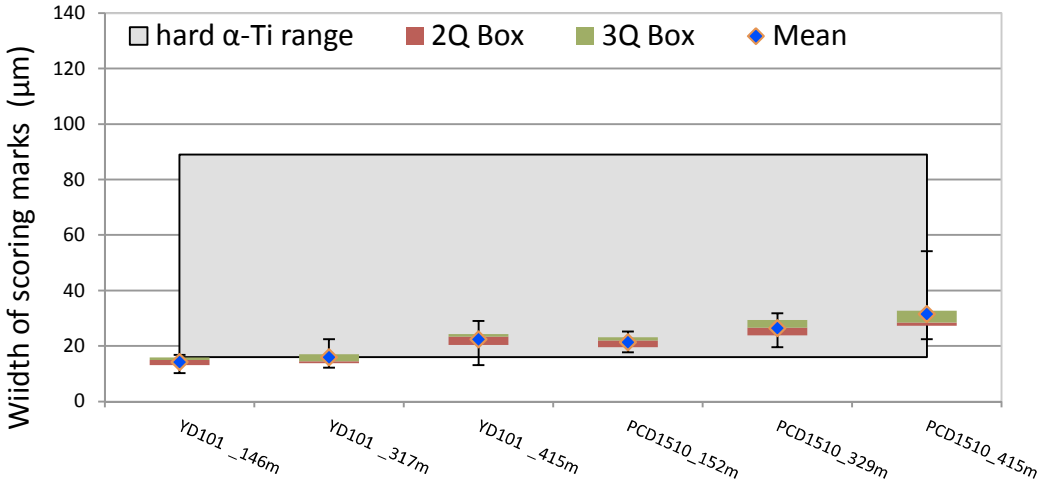

a) Vc =61m/min, DOC = 1.2 mm

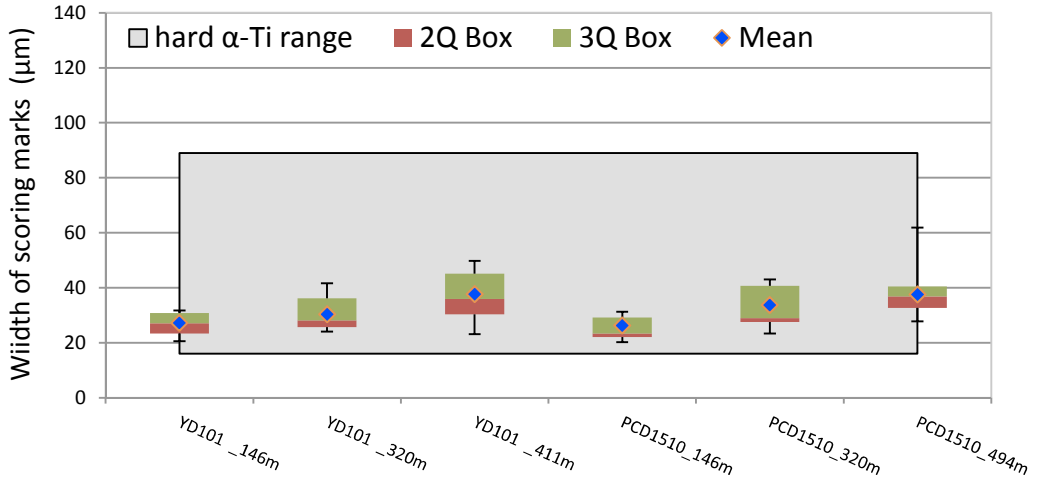

b) Vc =91m/min, DOC = 1.2 mm

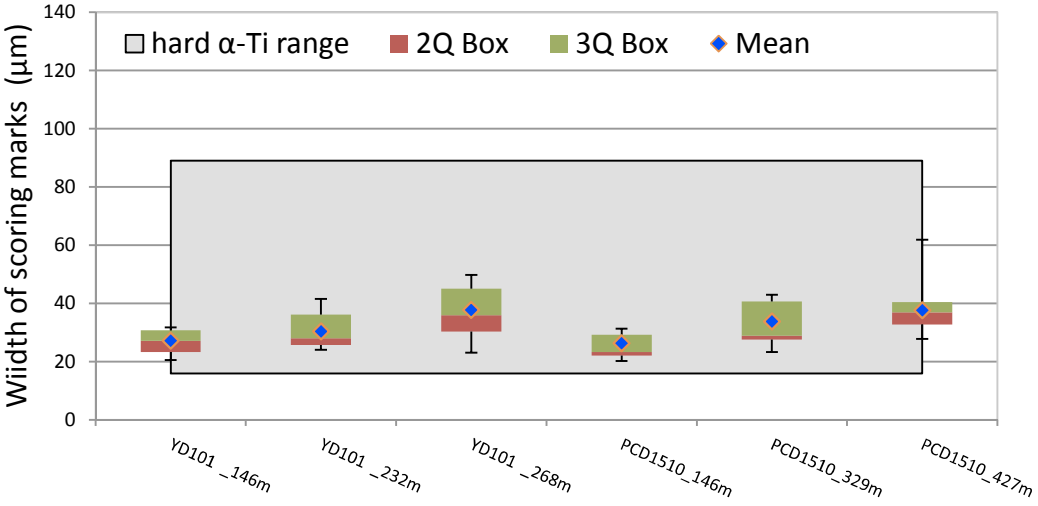

c) Vc =122m/min, DOC = 1.2 mm

Figure 96: Range and distribution of width of scoring marks on flank face at high DOC respect to 'hard' α-cluster size

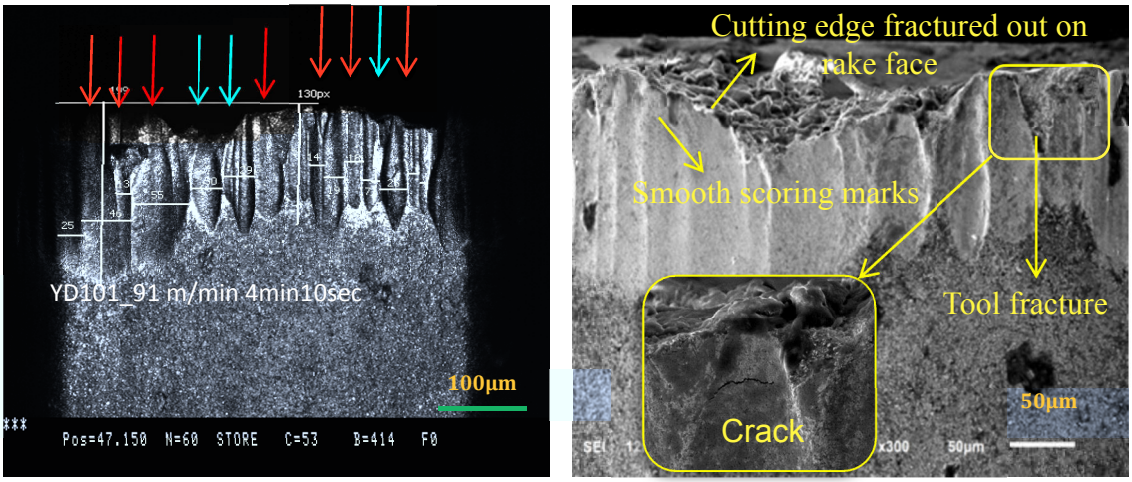

Figure 97: Classifying of scoring marks on YD101 (Left: confocal image, Right: SEM image)

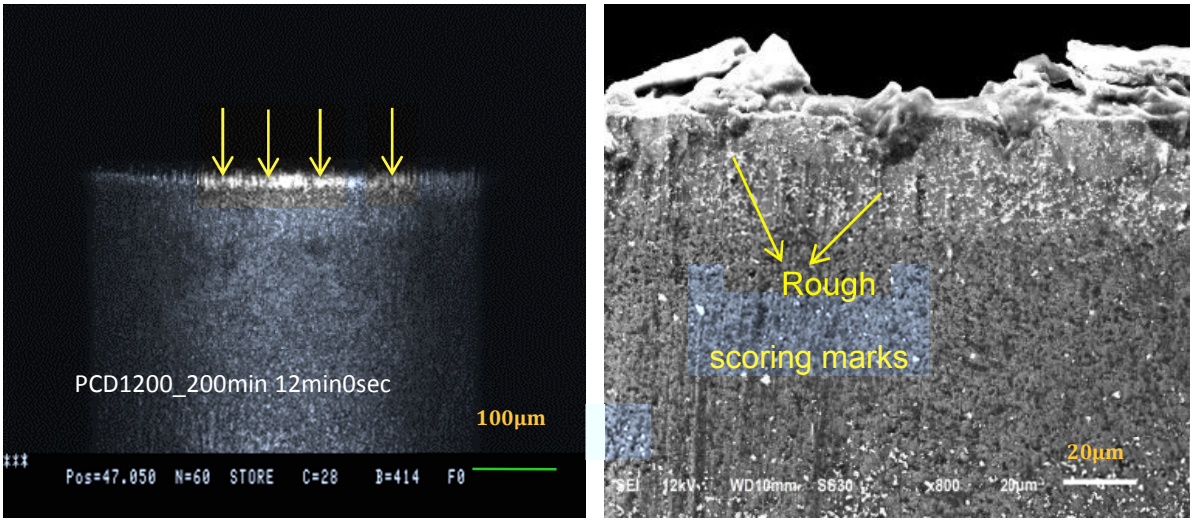

Figure 98: Classifying of scoring marks on PCD1200 (Left: confocal image, Right: SEM image

For both carbide and PCD inserts, the flank wear is directly related to the cutting speed. The thermal conductivity and the hardness of PCD are much higher compared to those of the carbide inserts, resulting in lower cutting temperatures and superior resistance to abrasion wear. Therefore, the flank wear rates of PCD inserts were much smaller than those of carbide inserts. The tool fracture started at 91m/min for both PCD and carbide inserts. These fractures are caused by the large 'hard' α-

cluster and the detachment of the adhesion layer. The fractured fragments of the inserts can also abrade the tool evident by the groove marking emanating from the fracture area. On PCD inserts, the tool wear including crater wear did not progress as rapidly as those of the carbide inserts and more importantly the cutting edge remained sharp and stable throughout the cutting process. In other words, the edges of PCD inserts were preserved while those of carbide inserts were destroyed. Consequently, the fracture on the PCD inserts was less frequent than that of the carbide inserts. This is an important factor to reduce cutting force and temperature in machining of Ti alloys [Hosseini, 2014].

Chapter 3: Driven process of thermochemical wear in Ti alloys machining

In thermochemical wear, beside the temperature, the wear rate of a tool material is controlled by both the solubility and the diffusivity of a tool material into a particular phase of a work material. The dominant wear mechanism may exist under a given machining condition to determine if a process is limited by dissolution or diffusion. Once determined, this information will help to design/select effective tool materials or coating materials for machining Ti alloys. According to Olortegui-Yume and Kwon [2007], the dissolution wear must take place prior to the diffusion wear. In ferrous machining, the dissolution of a tool material is much lower than the diffusion and the wear process is dominated by the dissolution. This has not been corroborated in machining Ti alloys. This section focused the thermochemical wear process involved in machining Ti alloys in order to determine which wear mechanism dominates the wear process.

I.1 BACKGROUND ON WEAR MECHANISMS

In general, the comprehensive wear model was considered as a combination of mechanical wear and thermochemical wear as:

$$W = \eta \cdot W_m + \zeta \cdot W_c \tag{3.1}$$

where W_m and W_c are mechanical and thermochemical wear rates and η and ζ are the weight factors for mechanical and thermochemical wear rates, respectively. The weight factors, η and ζ must be determined from experimental data.

I.1.1 Mechanical wear

The abrasion wear is one of the primary mode of mechanical wear model for flank wear in machining Ti alloys if harder inclusions are present. However, Ti alloys do not have hard inclusions like cementite (Fe_3C) in ferrous alloys. As shown in previous chapters, the hard inclusions in Ti alloys are the α-grains or clusters in the hard orientation. Depending on the general morphology of the hard α-phases, they can exhibit both 2-body and 3-body abrasion. The 2- body abrasion model presented in Rabinowicz et al. [1961] can be expressed as:

$$V_{2B}^{m} = \frac{F \tan\theta}{\pi P_t} x \tag{3.2}$$

where

V_{2B}^{m} : wear volume ; F: load between interacting surface

x : silding distance ; θ : roughness angle of abrasive

P_t : the hardness of abraded surface (work material)

Although F and x is depended on the cutting condition, θ is influenced by the roughness characteristics of the abrasives. They can be assumed to be the same for given cutting condition and work material. Consequently, the relative abrasive wear volume, RW_m, can be expressed as a function of ratio of the hardness of a tool material (2) and the reference tool material (1).

$$RW_m = \frac{V_{2B}^{m1}}{V_{2B}^{m2}} = \frac{P_t^2}{P_t^1} \tag{3.3}$$

If the hard inclusions are not constrained within the Ti matrix, an empirical quantitative 3-body wear model abrasion introduced by Rabinowicz [1977] can be used. In this model, hard particles can roll as well as slide between two surfaces. The model indicates the strong dependency on the hardness ratio of abrasive and tool material.

$$V_{3B}^{m} = \begin{cases} \dfrac{L\tan\theta}{3P_t}x & \text{if} \quad \dfrac{P_t}{P_a} < 0.8 \\ \dfrac{L\tan\theta}{5.3P_t}x\left(\dfrac{P_t}{P_a}\right)^{-5/2} & \text{if} \quad 0.8 < \dfrac{P_t}{P_a} < 1.25 \\ \dfrac{L\tan\theta}{2.43P_t}x\left(\dfrac{P_t}{P_a}\right)^{-6} & \text{if} \quad \dfrac{P_t}{P_a} > 1.25 \end{cases} \tag{3.4}$$

where V_{3B}^{m} is the wear volume and P_a is hardness of the abrasives.

While the 2-body model is more relevant for large hard clusters of grains or the hard particles with complex morphologies, the 3-body is expected to be more relevant with small isolated grains in the regions experiencing high deformation and recrystallizations. The α-phase has the hard orientation when the c-axis happens to be perpendicular to the rake face. The hardness in the c-direction was reported to be much harder (~1.5 time) than any other directions [Britton, 2009; Kwon, 2013]. To compare tool materials at the same cutting condition, the parameters, x and θ, for the hard clusters can be assumed to be the same. Therefore, the hardness ratio determines the relative abrasive wear rate of a tool material. In addition, due to the effects of thermal softening, the hardness of the tool and work materials were given

as a function of temperatures, so called 'hot hardness', which are needed to predict the relative abrasion wear rate. The hot hardness was introduced by the exponential function of temperature.

$$P = P_o e^{-\alpha T} \tag{3.5}$$

where P_o is hardness at 0°C, α is thermal softening factor, T is temperature. The cutting tool temperature is much higher compared to the temperature of the hard clusters as the workpiece undergoes a thermal transient condition.

Table 12: The hardness data of tool materials

Material	P_o (Kg/mm^2)	α x10^4 (/°C)	Temperature range(°C)	Softening temperature (°C)	References
WC	2350 7260	2.87 18.11	0 – 740 740 - 900	1100	Kwon et al. (1985)
pCBN	3500	7.56	0 - 1000	1500	Almond et al. (1982)
PCD	5500	8.12	0 -1000	1500	Almond et al. (1982)
Al2O3	2300	3.89	0 - 1000	1500	Kwon et al. (1985)
Ti64	255	29.3	0 - 800	NA	Bilous et al. (2005)

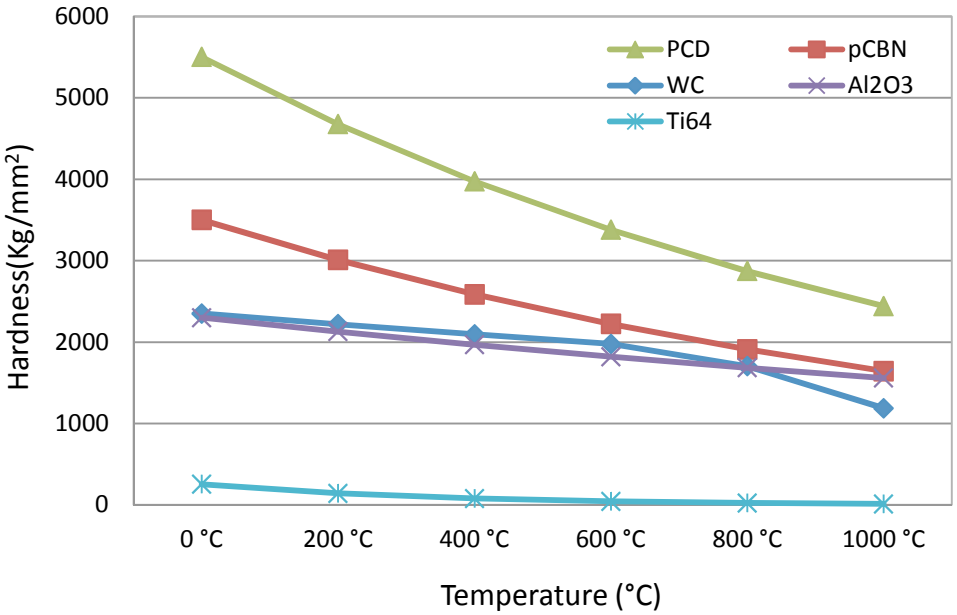

Figure 99: The hot hardness of Ti64 and typical tool materials

I.1.2 Independent of dissolution and diffusion wear model by Kramer

The thermochemical wear includes chemical reaction, dissolution and diffusion. The thermochemical wear occurs most likely on the rake face in the form of crater wear. A quantitative dissolution wear model was first proposed by Kramer [1979]. The model was proved to be effective to predict the crater wear in machining ferrous materials [Kramer, 1986; Wong, 2004].

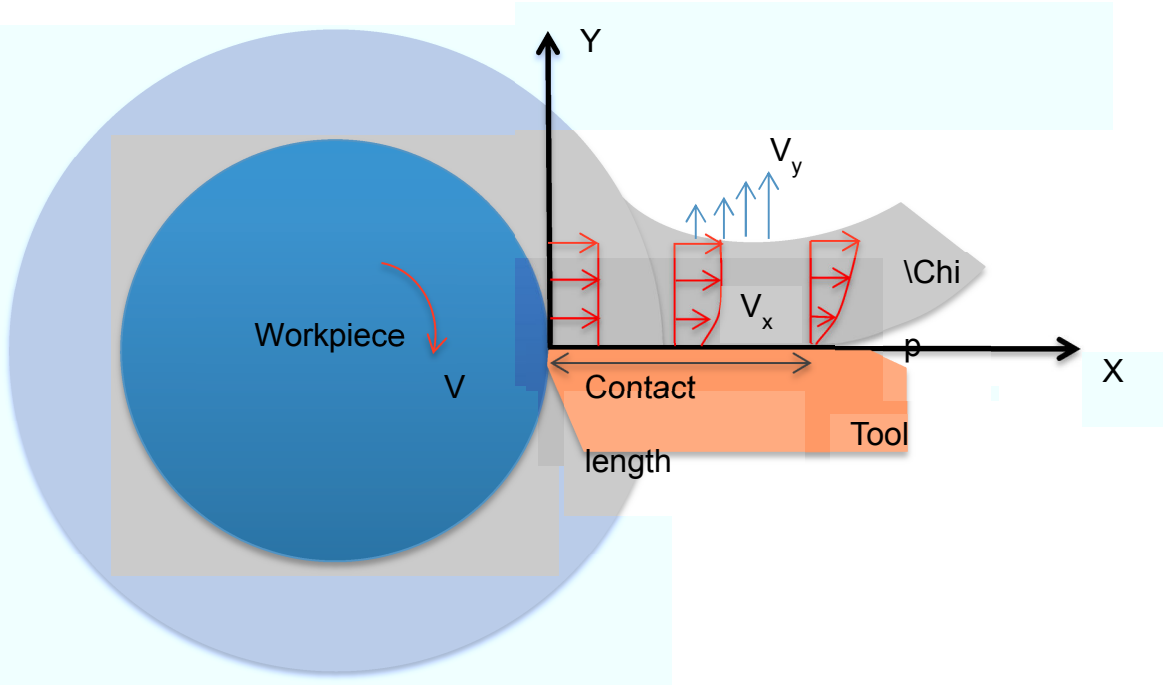

Figure 100: Distribution of velocity components of the chip in turning

Suh [1986] stated that thermochemical wear is a combination of dissolution and diffusion wear:

$$W_c = W^{dif} + W^{dis} = K \cdot S\left(-D\frac{\partial c}{\partial y} + V_y\right)_{y=0} \tag{3.6}$$

where :

$W_c\,[cm/\sec]$: thermochemical wear rate of the tool material

W^{dif} : diffusion wear rate of the tool material

W^{dis} : dissolution wear rate of the tool material

K : ratio of molar volumes of the tool material and the chip material

$D\left[cm^2/\sec\right]$: diffusion coefficient of the slowest diffusing tool constituent in the chip

$c\left[at\%\right]$: concentration of the tool material in the chip

$S\left[at\%\right]$: equilibrium concentration (solubility) of the tool material in the chip

$V_y\left[cm/\sec\right]$: bulk velocity of chip material at the tool-chip interface perpendiclar to the interface

The first term represents diffusion wear, which is strongly influenced by the concentration gradient and the diffusivity of the slowest diffusing tool constituents. The second term is dissolution wear which depends on the solubility of a tool material. At the present time, neither dissolution nor diffusion wear model has been applied successfully in predicting tool wear in machining Ti alloys. In particular, Hartung and Kramer [1982] showed the dissolution/diffusion wear model did not correctly predict the crater wear in machining Ti alloys.

I.1.2.1 Dissolution wear

In the dissolution wear model, the tool material dissolves into the chips and its solubility influenced by the cutting temperature affects the wear rate. The dissolution wear becomes more dominant with higher cutting temperatures. The dissolution wear is influenced by the bulk velocity term, V_y which cannot be easily determined. For the simplicity, V_y is considered as constant for each combination of cutting condition and tool material. Thus, the relative wear rate of two tool materials (1, 2) can be expressed as:

$$RW^{dis} = \frac{\mathrm{W}_1^{dis}}{\mathrm{W}_2^{dis}} = \frac{M_1 S_1}{M_2 S_2}$$
$$M = \frac{GMW}{\rho} \tag{3.7}$$

where *M*, *GMW* and ρ are the molar volume, the gram molecular weight and the density of a tool material, respectively.

Assuming the tertiary compounds as a tool material, $A_xB_yC_z$ has three constituents, A, B and C while x, y and z are their stoichiometric ratios, respectively. The free energy of formation per mole of a tool material can be calculated as:

$$\Delta G_{A_xB_yC_z} = x\,\Delta\overline{G}_A^M + y\Delta\overline{G}_B^M + z\Delta\overline{G}_C^M \tag{3.8}$$

where $\Delta\overline{G}_i^M$: relative partial molar energy of component i

The relative partial molar energy can be determined from excess Gibbs free energy, ΔG_i^{xs}, and the solubility, S_i, of component *i* in work material.

$$\Delta\overline{G}_i^M = \Delta G_i^{xs} + RT\ln S_i \tag{3.9}$$

At the equilibrium state the solubility of tool constituents is given by

$$S_A = x \cdot S_{A_xB_yC_z} \quad , \quad S_B = y \cdot S_{A_xB_yC_z} \quad , \quad S_C = z \cdot S_{A_xB_yC_z} \tag{3.10}$$

Substitute in Eq. (3.8)

$$\Delta G_{A_xB_yC_z} = x\,\Delta G_A^{xs} + y\Delta G_B^{xs} + z\Delta G_C^{xs} + RT(x\ln x + y\ln y + z\ln z) + (x+y+z)RT\ln S_{A_xB_yC_z} \quad (3.11)$$

Then the solubility tool material $A_xB_yC_z$ in work material is calculated:

$$\boxed{S_{A_xB_yC_z} = \exp\left[\frac{\Delta G_{A_xB_yC_z} - x\Delta G_A^{xs} - y\Delta G_B^{xs} - z\Delta G_C^{xs} - RT(x\ln x + y\ln y + z\ln z)}{(x+y+z)RT}\right]} \quad (3.12)$$

To determine the solubility of a tool material, $A_xB_yC_z$, into a particular phase (α or β) of a work material, the values of $\Delta G_{A_xB_yC_z}$, ΔG_A^{xs}, ΔG_B^{xs}, and ΔG_C^{xs} for the phase are needed. The free energy of formation is only dependent on the tool material, not the phase of work material while the excess Gibbs free energy is influenced by the phase of the work material as the solubility of a tool material was strongly affected by the phases (α, γ) of a ferrous material [Wong, 2004] as well.

The free energy of formation of tool material can be expressed as a function of temperature as below:

$$\Delta G_{A_xB_yC_z} = K_1 + K_2 \cdot T\log T + K_3 \cdot T \quad (3.13)$$

where T is the temperature and K_1, K_2 and K_3 are the curve-fit coefficients.

It is worth noting that that the solubility of tool material cannot be greater than the solubility of tool constituents over their stoichiometric ratios.

$$\begin{cases} S_{A_xB_yC_z} \le S_A/x \\ S_{A_xB_yC_z} \le S_B/y \\ S_{A_xB_yC_z} \le S_C/z \end{cases} \quad (3.14)$$

Hence, the solubility of tool material was determined by following procedure:

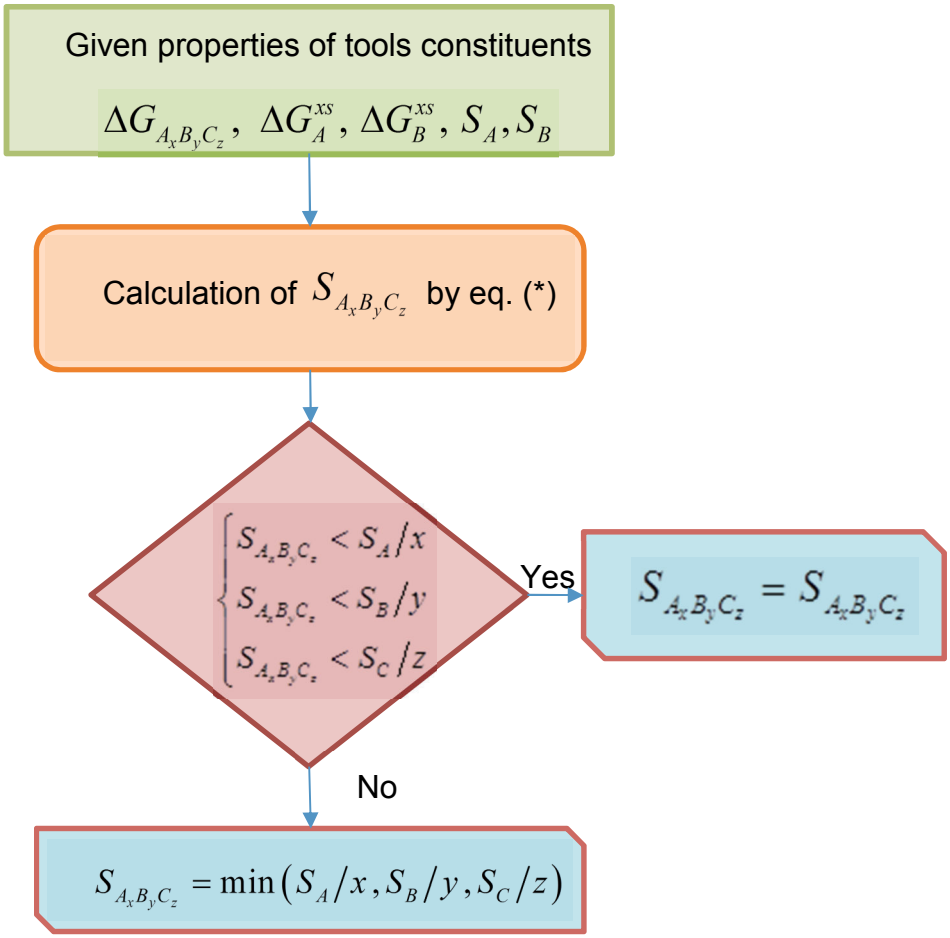

Figure 101: Flow chart for calculation of solubility of tool material

The solubility of a tool material into a work material strongly depends on the cutting temperature and the phase of a work material. As the cutting temperature increases, the hardness decreases and the solubility increases, accelerating tool wear. For example, Figure 102 presents the temperature dependence of hardness

and solubility of hafnium carbide (HfC) into α-grain. However, these properties of only few tool materials in α- and β- phases of titanium were available, which were used for the calculation in this thesis as shown in Table 13..

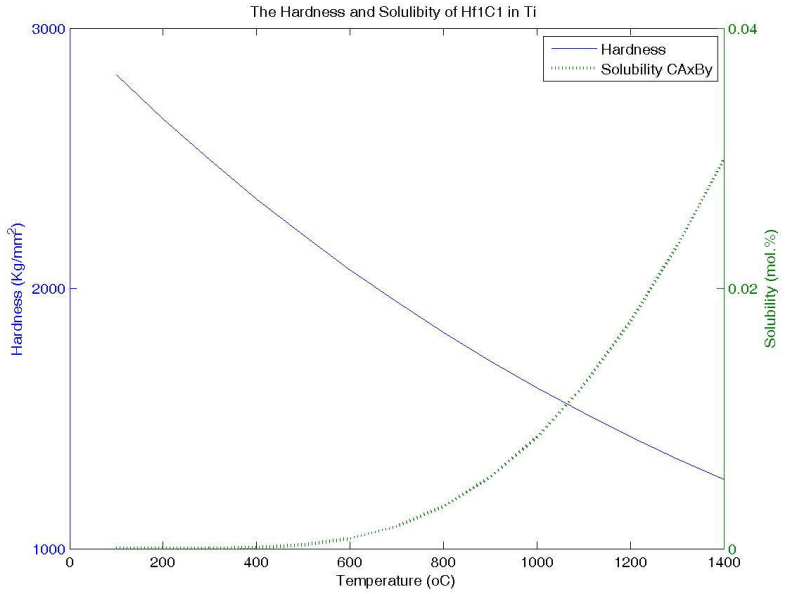

Figure 102: Temperature dependence of the hardness and solubility of HfC tool

Table 13: Estimated solubility of tool materials in α-Ti (at 800°C) and β-Ti (at 1000°C)

Tool (AxByCz)	S_A in α-Ti (at 800°C)	S_A in β-Ti (at 1000°C)	S_B in α-Ti (at 800°C)	S_B in β-Ti (at 1000°C)	S_C in α-Ti (at 800°C)	S_C in β-Ti (at 1000°C)	S_{AxByCy} in α-Ti (at 800°C)	S_{AxByCy} in β-Ti (at 1000°C)	S_{tool} in α-Ti (at 800°C)	S_{tool} in β-Ti (at 1000°C)
TiN	100.0	100.0	11.2 [1]	1.1 [1]			1.02E-04	2.49E-03	**1.02E-04**	**2.49E-03**
TiAlN	100.0	100.0	15.3 [2]	8.4 [2]	11.2 [1]	1.1 [1]			**1.12E+01**	**1.10E+00**
TiCN	100.0	100.0	0.9 [3]	0.6 [3]	11.2 [1]	1.1 [1]			**9.00E-01**	**6.00E-01**
cBN	0.1 [4]	0.3 [4]	11.2 [1]	1.1 [1]			7.69E+07 *	9.86E+07 *	**1.00E-01**	**3.00E-01**
Al_2O_3	15.3 [2]	8.4 [2]	15.3 [2]	8.4 [2]			1.04E+03 *	2.17E+03 *	**5.10E+00**	**2.80E+00**
WC	0.2 [5]	16.5 [5]	0.9 [3]	0.6 [3]			2.51E+04 *	1.07E+04 *	**2.00E-01**	**6.00E-01**

Ref: [1] Murray (1987) ; [2] CALPHAD ; [3] Bandyopadhyay (2000) ;[4] Rahaei ; [5] Murray (1981)
* solubility >100 (mol%) w as replaced by a modified solubility

I.1.2.2 Diffusion wear

The diffusion takes place as the atom moves from the regions of high concentration to low concentration as shown in Figure 103. The diffusion is possible only if the contact interface reaches high enough temperature for an adequate amount of time. In high speed turning, the condition is favorable for the diffusion of tool material into the chip [Trent, 1991]. Besides the temperature, the diffusivity of a tool element is affected by the particular phase present in a work material during machining. The diffusivities into the β-phase are reported two or three orders of magnitude higher than those into the α-phase as shown in Figure 104 for some selected tool materials. The diffusivity data of tool constituents in the α-phase at 800°C and the β-phase at 1000°C was represented in Table 14. The diffusion of tool constituents in the β-phase is much faster than that into the α-phase leading to a higher diffusion wear rate with the β-phase.

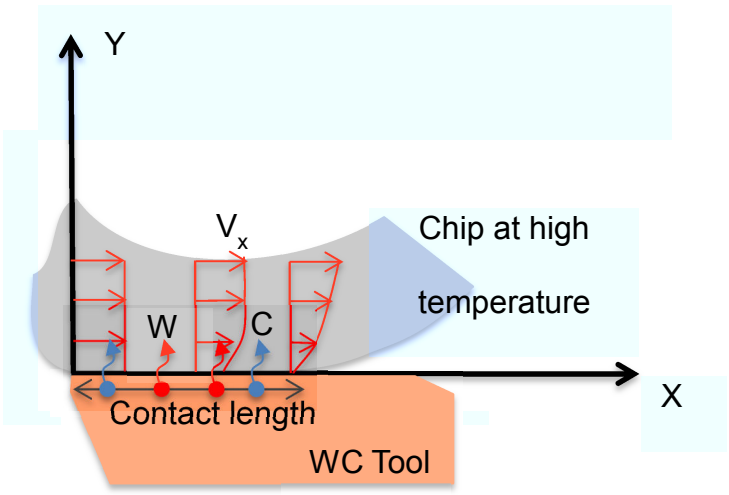

Figure 103: Dissolution of carbide tool into chip

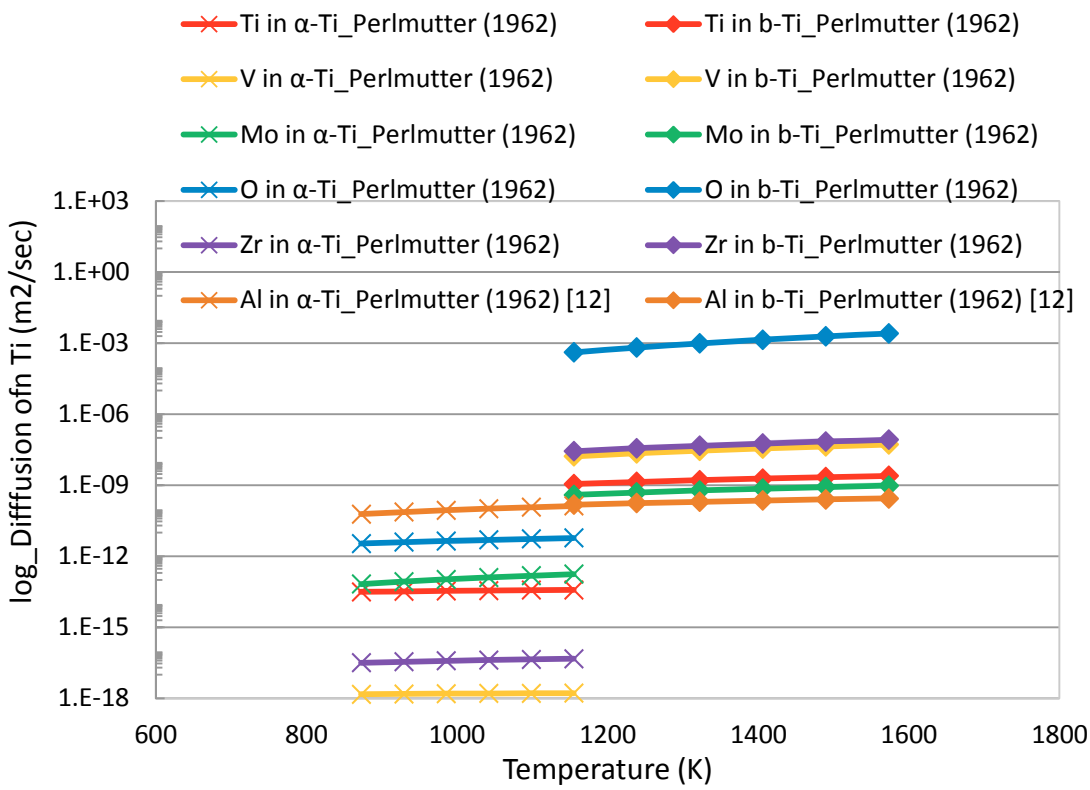

Figure 104: Diffusion of elements into α-Ti and into β-Ti.

Table 14: Diffusivity (m^2/sec) of tool components in α-Ti and into β-Ti

Tool (AxByCz)	D_A in α-Ti (at 800°C)	D_A in β-Ti (at 1000°C)	D_B in α-Ti (at 800°C)	D_B in β-Ti (at 1000°C)	D_C in α-Ti (at 800°C)	D_C in β-Ti (at 1000°C)
TiN	3.69E-14 [1]	1.51E-09 [1]	2.06E-15 [2]	1.18E-12 [2]		
TiAlN	3.69E-14 [1]	1.51E-09 [1]	1.13E-10 [1]	1.89E-10 [1]	2.06E-15 [2]	1.18E-12 [2]
TiCN	3.69E-14 [1]	1.51E-09 [1]	6.57E-13 [3]	2.11E-12 [3]	2.06E-15 [2]	1.18E-12 [2]
cBN	1.33E-11 [4]	NA	2.06E-15 [2]	1.18E-12 [2]		
Al_2O_3	1.13E-10 [5]	1.89E-10 [5]	5.29E-12 [1]	7.84E-04 [1]		
WC	NA	9.80E-15 [6]	6.57E-13 [3]	2.11E-12 [3]		

Refs. : [1] Perlmutter (1962); [2] Bellot (1996) ; [3] Bucur (1954); [4] Divinski (2008); [5] Perlmutter (1962) [12] ; [6] Hartung (1981) [71]

More importantly, the reaction layer formed at the interface also affects the diffusion process. As mentioned in the previous chapter, the TiC layer was most likely formed in the adherent layer at the low cutting speed. The presence of TiC layer

substantially reduces the diffusion of tool constituents into the work material. Figure 105 shows the significant reduction of carbon diffusing into the TiC layer. The adhesion layers (consisting of Ti and TiC) covered most of the contact zone on the rake face of PCD inserts in all cutting speeds while the carbide inserts had fewer localized areas covered by the adhesion layer. However, as discussed in pervious section, the dominant wear mechanism with the carbide insert was dissolution and diffusion while that for the PCD inserts is grain-pulled out. Hence, the diffusion wear is mostly relevant to the carbide inserts.

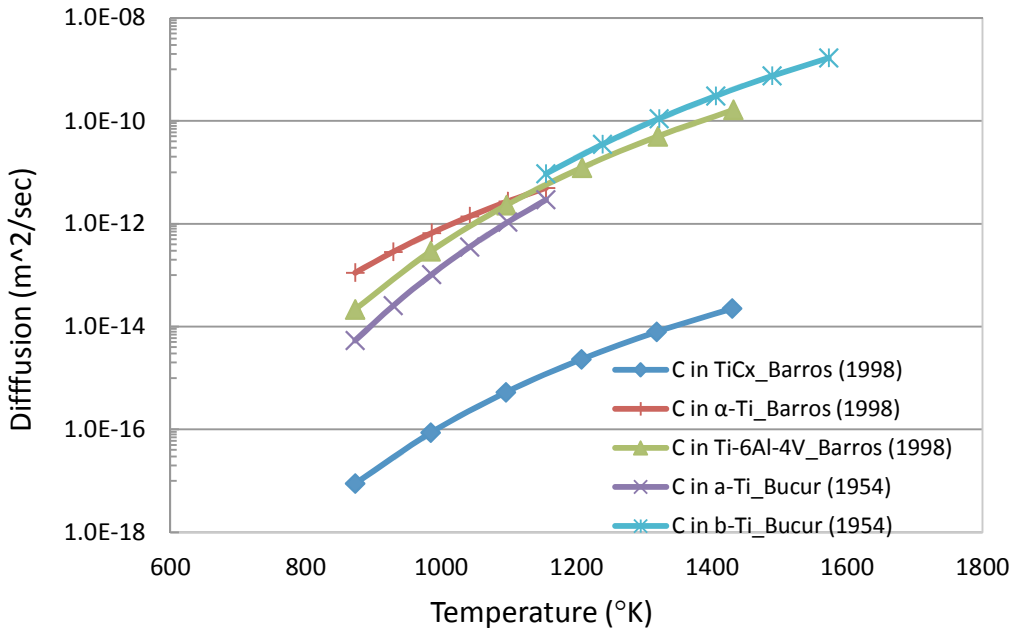

Figure 105: The diffusivity of carbon in α-Ti, β-Ti, Ti64 and TiCx

The diffusion wear was influenced by the concentration gradient in y direction, $\frac{\partial c}{\partial y}$ in Equation (3.6), of tool constituents in the chip, which cannot be accurately determined. Therefore, the upper bound diffusion wear model was adopted by

Hartung and Kramer [1982] to simply predict the relative diffusion wear rate of tool materials into titanium.

I.1.3 Upper bound of diffusion wear model

The upper bound calculation of diffusion wear model was introduced by Cook and Nayak [1986] to predict the maximum diffusion wear rate with the assumption of no chip deformation as it traverses across tool chip interface

$$V_{wear} = -K \cdot S\left(D / \pi t\right)^{0.5} \tag{3.15}$$

where:

K : ratio of molar volumes of the tool material and the chip material

$D\left[cm^2 / \sec\right]$: diffusion coefficient of the slowest diffusing tool constituent in the chip

$S\left[at\%\right]$: equilibrium concentration of the tool material in the chip

$t\left[\sec\right]$: travelling time, taken for the chip to move from the edge of the tool to the center of the crater

The accuracy of this model depends on the diffusivity and solubility of tool constituents used in the model. As the cutting time increases, the size of crater wear grows. Hence, the distance from the cutting edge to the center of the crater wear increases with cutting time for a given cutting speed. Then, the respective traveling times can be calculated. Table 15 lists the traveling times after cutting for certain amounts of times in all cutting speeds of carbide inserts. In fact, the difference in the travelling times among various cutting times is relatively small. In this thesis, the average value at 91m/min was used as the travel time for each cutting speed.

Table 15: The distance from cutting edge to crater's center and traveling time with carbide inserts

Cutting speed	Cutting time (min)	Distance to center of crater (μm)	Time to travel (sec)	Average time (sec)
61 m/min	2.4	130	6.40E-05	7.71E-05
	5.2	150	7.38E-05	
	6.8	190	9.35E-05	
91 m/min	1.6	150	9.84E-05	1.14E-04
	3.5	180	1.18E-04	
	4.5	190	1.25E-04	
122 m/min	0.6	150	1.48E-04	1.48E-04
	1.1	150	1.48E-04	
	2.2	150	1.48E-04	

Table 16 shows the upper bounds of diffusion wear for a tool material used in Hartung and Kramer (1982). The results were calculated with the diffusivity of the slowest diffusing tool constituent, the solubility of the slowest dissolving tool constituent and the same travelling time, $t=1.14x10^{-4}$sec (see Table 15), at the cutting speed of 91 m/min. For instance, the diffusivity of W and solubility of C were used to calculate the diffusion wear rate of carbide. The results of predicted diffusion wear did not agree with experiment data. For example, for turning Ti alloy with a high DOC, carbide inserts showed that the crater wear rate was 20.6 μm/min at the cutting speed of 91 m/min (see Figure 42), much higher than the predicted value. Furthermore, the predicted wear rate of the carbide tool was much lower than those of diamond tool. The experiment showed the opposite fact. It is worth stressing that the wear mechanism (diffusion or dissolution) has not been well defined for titanium machining. In general, the diffusion is known to be slower than the dissolution in Ti alloys.

Table 16: Predicted upper bound of diffusion wear at cutting speed of 91 m/min

Tool at 300sfm	Ratio molar volumes (K)	Diffusion coeff. D(cm2/sec) of			Solubility C(at%) of constituents			wear rate (um/min)
		least constituent	D (cm^2/sec)	REF	least constituent	C (at%)	REF	with t=1e-4 (sec)
Diamond	0.321	C	2.28E-06	Hartung [11,12]	C	0.6		98.44
NbC	1.266	Nb	3.66E-09	Hartung [11,12]	C	0.6		15.56
TiC	1.147	Ti	4.82E-09	Hartung [11,12]	C	0.6		16.17
VC	1.025	V	2.92E-09	Hartung [11,12]	C	0.6		11.25
ZrC	1.472	Zr	1.40E-08	Hartung [11,12]	C	0.6		35.37
TiN	1.082	Ti	4.82E-09	Hartung [11,12]	Ni	23.5		597.54
ZrO2	2.068	Zr	1.40E-08	Hartung [11,12]	O	17		1408.03
TiB2	1.492	Ti	4.82E-09	Hartung [11,12]	B	0.5		17.53
WC	1.165	W	1.05E-10	Hartung [11,12]	C	0.6		2.42

Diffusivity of the slowest diffusing tool constituent

Solubility of the slowest dissolving tool constituent

- **The effects of reaction layer TiC to diffusion wear rate**

In the case of the carbide insert, the diffusivity of tungsten is two or three orders of magnitude lower than that of carbon into titanium [need reference]. Although the diffusivity of Co is comparable to that of carbon, the amount of Co is very small in comparison with W and C. In addition, tungsten, which was used as the wear

controlling constituent in Hartung and Kramer [1982], diffuses slower than C in titanium. However, the diffusivity data of tungsten and cobalt in α-Ti, β-Ti, Ti64 and TiC is scarce. Thus, carbon was assumed to be the wear controlling constituent for calculation of the upper bound diffusion wear of carbide tool to study the effect of TiC reaction layer. Table 17 represents the upper bound of diffusion wear rate of carbide tools in α-Ti at 1000°K, β-Ti at 1400°K, Ti64 and TiC at 1200°K for three cutting speeds based on the diffusivity and solubility data of carbon in α-Ti, β-Ti, Ti64 and TiC collected from few publications. The effect of the TiC reaction layer is significant in controlling the wear rate of the carbide tool.

Table 17: Predicted diffusion wear of carbide tool in which carbon is control elements.

Diffusion coeff. D(cm^2/sec) of constituents			Solubility C(at%) of constituents			wear rate (μm/min)		
least constituent	D (cm^2/sec)	REF	least constituent	C (at%)	REF	200sfm	300sfm	400sfm
C	8.02E-09	C in α-Ti_Barros (1998)		0.6		17.44	19.87	24.13
C	1.10E-07	C in Ti64_Barros (1998)		0.6		64.63	73.63	89.43
C	1.72E-10	C in TiCx_Barros (1998)		0.6		2.55	2.91	3.53
C	1.42E-09	C in α-Ti_Bucur (1954)		0.6		7.34	8.36	10.15
C	2.85E-06	C in β-Ti_Bucur (1954)		0.6		328.74	374.55	454.91

The experimental results from the high DOC showed the crater wear rates of carbide inserts at 7.2, 20.6 and 43.7 μm/min (see Figure 42) for cutting speeds of 61 m/min, 91 m/min, and 122 m/min, respectively. In comparison with the predicted diffusion wear of the carbide insert shown in Table 17, the diffusion wear observed in the experiments behave similar to the diffusion prediction of the carbide into the TiC

reaction layers at the low cutting speed, into both Ti64 and the TiC reaction layers at the medium cutting speed, and into Ti64 at the high cutting speed as the formation of TiC reaction layer is deterred at higher cutting speeds.

I.2 DRIVEN PROCESS OF GENERALIZED THERMOCHEMICAL WEAR

Olortegui-Yume and Kwon [2007] have introduced a generalized thermochemical wear where the tool constituent undergoes as a sequence of dissociation, chemical reaction if possible, dissolution, and diffusion.

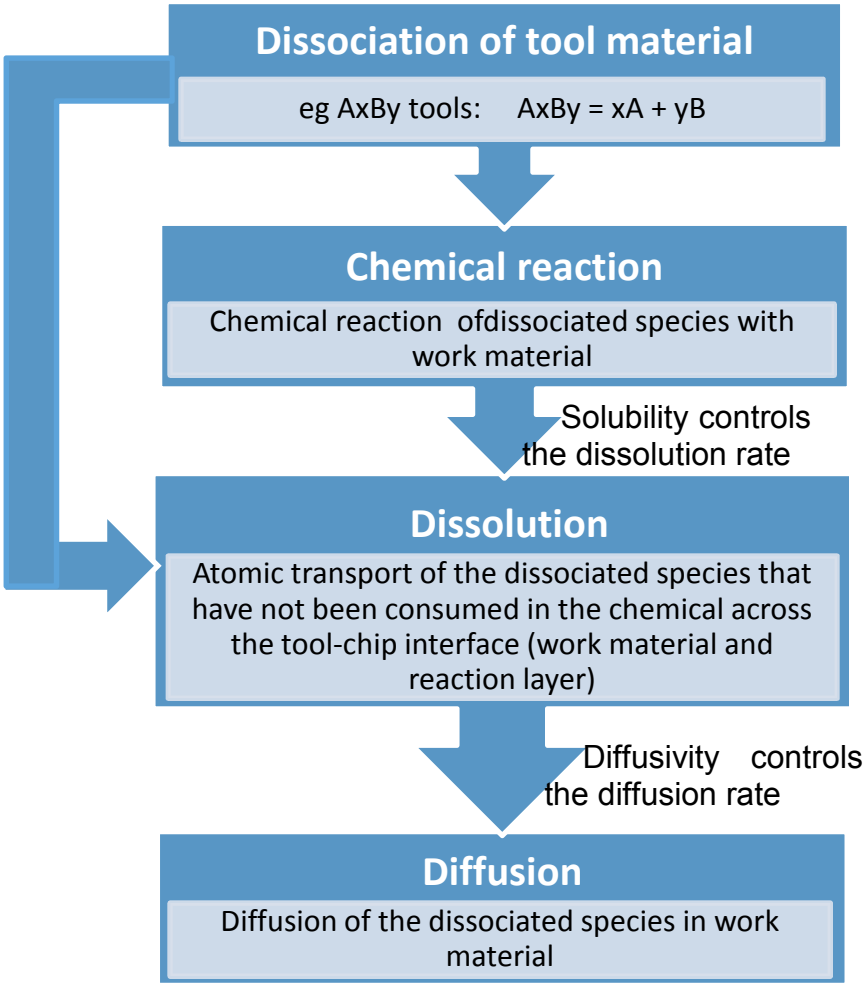

Figure 106: Generalized thermochemical wear [after Olortegui-Yume, 2007]

Assuming that the tool material, so called AxBy, dissociates into species, xA and yB at the early stage of thermochemical wear process.

$$A_x B_y = xA + yB \tag{3.16}$$

Then, the dissolution of tool constituents into a work material or the reaction layer happened. The dissolution is controlled by the solubility (mol% or at%) of tool material in work material. Therefore, at one instance of time, the specific mole of A and B atoms in tool-chip interface, so called "dissolution mole limit", n_{dis}^{i}, i is A, B, are present.

Considering a volume of chip, V_{dis}, in the dissolution zone as shown in Figure 107, the mole of Ti can be calculated as:

$$n^{\mathrm{Ti}} = \frac{V_{dis}}{\rho^{\mathrm{Ti}} \cdot M^{\mathrm{Ti}}} \quad [mol] \tag{3.17}$$

where $\rho^{\mathrm{Ti}}\left[g/cm^3\right]$: density; $M^{\mathrm{Ti}}\left[g/mol\right]$: molar mass

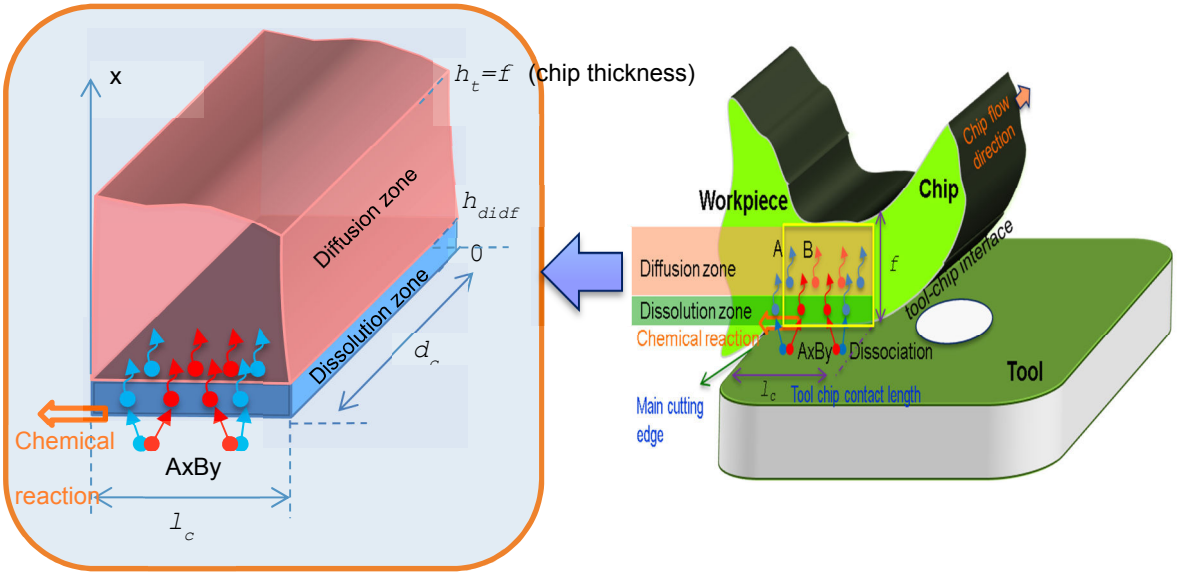

Figure 107: Tool constituents diffused into chip

The solubility (mol%) of tool component ***i*** (A or B) in tool-chip interface is defined as:

$$S^{\mathrm{i}}\left[mol\%\right]=\frac{n_{dis}^{i}}{n_{dis}^{i}+n^{\mathrm{Ti}}} \tag{3.18}$$

The mole of component ***i*** dissolved in dissolution zone of chip is calculated as:

$$\boxed{n_{dis}^{i}=\frac{S^{\mathrm{i}}}{1-S^{\mathrm{i}}}\cdot\frac{V_{dis}}{\rho^{\mathrm{Ti}}\cdot M^{\mathrm{Ti}}}\qquad\left[mol\right]\rightarrow\text{called as "solubility mole limit"}} \tag{3.19}$$

Concentration of tool component ***i*** (A or B) in dissolution zone is obtained as:

$$c_s^i\left[mol/cm^3\right]=\frac{n_{dis}^{i}}{V_{dis}}=\frac{S^{\mathrm{i}}}{1-S^{\mathrm{i}}}\cdot\frac{1}{\rho^{\mathrm{Ti}}\cdot M^{\mathrm{Ti}}}\qquad\rightarrow\text{called as "solubility concentration limit"} \tag{3.20}$$

The solubility concentration limit is also the fixed surface concentration at the boundary of dissolution and diffusion zone.

Subsequently, the diffusion process takes place. Depending on how fast A and B atoms diffuse in the work material, the numbers of A and B atoms at the tool-chip interface are determined. Let, n_{diff}^{A} and n_{diff}^{B} are the moles of A and B's diffused into the work material in time ***t*** (sec). These numbers are functions of diffusivity and temperature.

The net flux of atom passing through the unit area per unit time along x direction is (Fick's first law of diffusion):

$$J = -D\frac{dc(x)}{dx} \quad \left[\frac{mol}{cm^2 \cdot \sec}\right]; \quad \text{where} \quad D\left[\frac{cm^2}{\sec}\right] \text{is diffusivity} \tag{3.21}$$

The Fick's second law of diffusion:

$$\frac{\partial c(x,t)}{\partial t} = \frac{\partial^2 c(x,t)}{\partial^2 x} \tag{3.22}$$

with a boundary condition of $c(0,t) = c_s^i = const$ and initial condition of $c(x,0) = 0$

$$\text{B.C: } c(0,t) = c_s^i = \frac{S^{\text{i}}}{1 - S^{\text{i}}} \cdot \frac{1}{\rho^{\text{Ti}} \cdot M^{\text{Ti}}} \left[mol/cm^3\right] = const; \quad \text{I.C: } c(x,0) = 0$$

Hence, the diffusion concentration of component ***i*** (A or B) in diffusion zone at time *t* and location *x* can be determined as:

$$c^i(x,t) = c_s^i\left[1 - erf\left(\frac{x}{2\sqrt{D_i t}}\right)\right] \Rightarrow \underbrace{\frac{dc^i(x,t)}{dx}}_{conc.gradient} = c_s^i \frac{dz}{dx}\frac{d}{dz} erf(z) = \frac{c_s^i}{\sqrt{\pi D_i t}} \exp\left[-\left(\frac{x}{2\sqrt{D_i t}}\right)^2\right] \tag{3.23}$$

where $a = 2\sqrt{D_i t}$ is characteristic distance for diffusion.

$$\text{erf}(z) = \frac{2}{\sqrt{\pi}} \int_0^z e^{-\zeta^2} d\zeta \; ; \;\; \text{erfc}(z) = 1 - \text{erfc}(z) \text{ is Gauss Error function}$$

$$\text{erf}(0) = 1; \;\; \text{erf}(\infty) = 1; \;\; \frac{d}{dz} \text{erf}(z) = \frac{2}{\sqrt{\pi}} e^{-z^2}$$

The diffused mole of component ***i*** passed through cross-section, A_c, at location x of diffusion zone at time ***t*** (sec) is:

$$n^i(x,t)\left[mol\right] = c(x,t) \cdot A_c \cdot dx \quad ; \quad A_c = d_c \cdot l_c \; ; \tag{3.24}$$

where l_c is chip-tool contact length, d_c is depth of cut, dx is thickness of a cross-section

Hence, the total mole of the tool component ***i*** diffused in chip can be calculated as:

$$\begin{aligned} n^i_{diff}(t) &= \lim_{h_{diff} \to 0} \int_{h_{diff}}^{h_t} n^i(x,t) dx = A_c \cdot c^i_s \lim_{h_{diff} \to 0} \int_{h_{diff}}^{h_t} \left[1 - \text{erf}\left(\frac{x}{a}\right)\right] dx \\ &= A_c \cdot c^i_s \cdot a \lim_{h_{diff} \to 0} \int_{h_{diff}/a}^{h_t/a} \left[1 - \text{erf}\left(\frac{x}{a}\right)\right] d\frac{x}{a} = A_c \cdot c^i_s \cdot a \int_0^{z=h_t/a} \text{erfc}(z) dz \end{aligned} \tag{3.25}$$

$$\text{where} \int_0^{z=h_t/a} \text{erfc}(z) dz = \left[z \cdot \text{erfc}(z) + \frac{1 - e^{-z^2}}{\sqrt{\pi}} \right]_{z=h_t/a} = \frac{h_t}{a} \cdot \text{erf}\left(\frac{h_t}{a}\right) + \frac{1 - e^{-\left(\frac{h_t}{a}\right)^2}}{\sqrt{\pi}}$$

$$\boxed{n^i_{diff}(t)\left[mol\right] = A_c \cdot c^i_s \cdot a \left[\frac{h_t}{a} \cdot \text{erfc}\left(\frac{h_t}{a}\right) + \frac{1 - e^{-\left(\frac{h_t}{a}\right)^2}}{\sqrt{\pi}} \right] \rightarrow \text{called as "diffusion mole limit"}} \tag{3.26}$$

The average of diffusion rate limit the tool component ***i*** in chip at time t is defined as:

$$WR_{diff}^{i}\left[\frac{mol}{cm^3\cdot\sec}\right]=\frac{n_{diff}^{i}(t)}{V_{diff}\cdot t}=\frac{A_c\cdot c_s^i}{A_c\cdot f\cdot t}\left[h_t-h_t\cdot\mathrm{erf}\left(\frac{h_t}{a}\right)+a\frac{1-e^{-\left(\frac{h_t}{a}\right)^2}}{\sqrt{\pi}}\right]\propto t \qquad (3.27)$$

whereas the dissolution rate limit the tool component ***i*** at time t is calculated as :

$$WR_{dis}^{i}\left[\frac{mol}{cm^3\cdot\sec}\right]=\frac{n_{dis}^{i}}{V_{dis}}=c_{dis}^{i}=\frac{S^{\mathrm{i}}}{1-S^{\mathrm{i}}}\cdot\frac{1}{\rho^{\mathrm{Ti}}\cdot M^{\mathrm{Ti}}}\not{\propto}t \quad \text{but} \propto S_{A_xB_y} \qquad (3.28)$$

The process that controls the thermochemical wear was determined by comparing the diffusion rate limit, WR_{diff}^{i} , and the dissolution rate limit, WR_{dis}^{i} . The process with a smaller rate limit controls the thermochemical wear of tool constituents. Figures 108 - 111 compared the dissolution and diffusion wear rates of the constituents of WC, TiN and cBN tool material into α-phase and β-phase using the data of solubility of tool material, $S_{A_xB_yC_z}$, in Table 13 and diffusivity tool constituents in Table 14. At the very beginning stage (less than 1E-04 sec), the thermochemical wear is dominated by the dissolution mechanism. Then, for most tool components such as W, C, Ti, B (exclude N into β-phase at 1000°C), diffusion will control the thermochemical wear rate after that. To summarize, traffic jam analogy was used and demonstrated the difference in the thermochemical wear between ferrous and titanium alloys with the carbide tool on Figure 112. The dissolution controls the thermochemical wear in machining ferrous while thermochemical wear of mostly tool material in machining Ti will be restrained by the diffusion the fastest tool constituent. Thermochemical wear of carbide into β-Ti is an example of this. After dissociating from carbide tool, W and C dissolved and diffused independently into chip in which diffusion is driven process for both W and C

as shown in Figure 108. The diffusion of W and C is influenced by solubility of carbide which controls the dissociation of tool at tool-chip interface as the way how solubility of tool was calculated. To put it more simply, diffusion of W and C control both the dissociation of carbide and their dissolution. Therefore, thermochemical wear of carbide depends on how fast W or C diffused in the chip. This means that C with higher diffusion rate (see Figure 108) will control thermochemical wear of carbide tool. The slower diffusion rate, a part of W will diffuse in chip while the other left will be taken away with the chip flow. The relative thermochemical wear of tool 1 and tool 2 was determined by the chart shown in Figure 113.

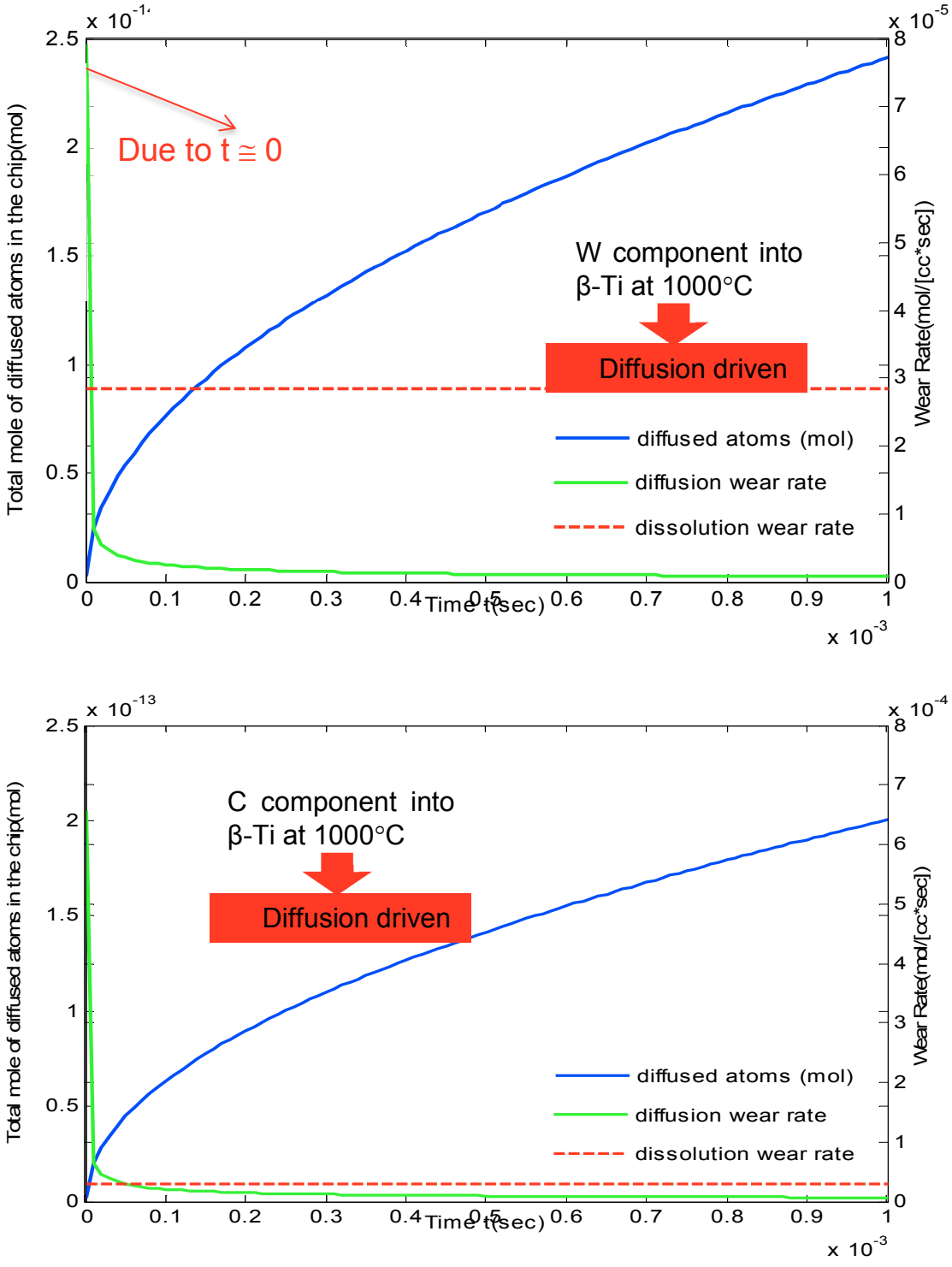

Figure 108 Dissolution and diffusion wear rate of carbide tool (WC) into β-Ti at 1000°C

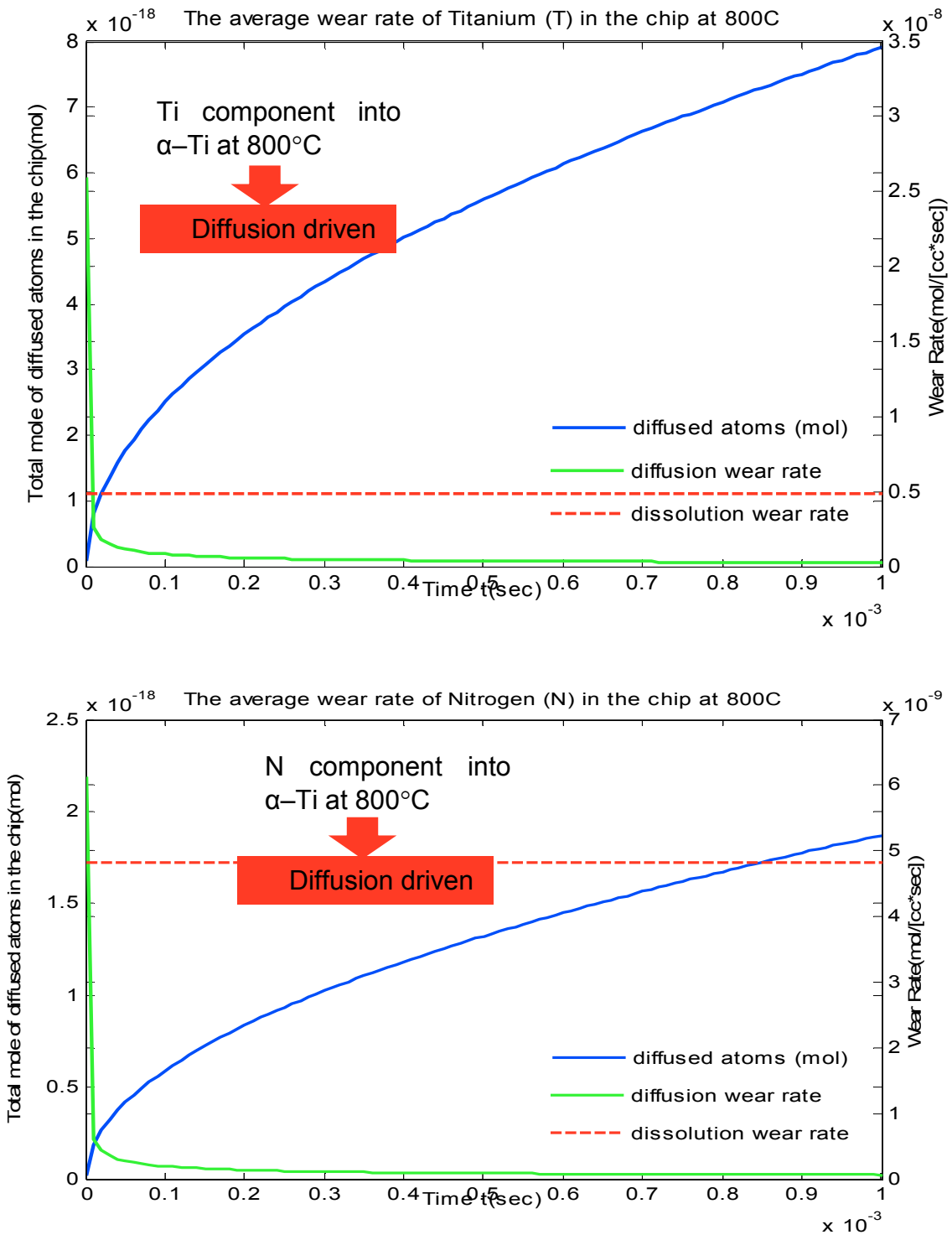

Figure 109: Dissolution and diffusion wear rate of TiN tool into α-Ti at 800°C

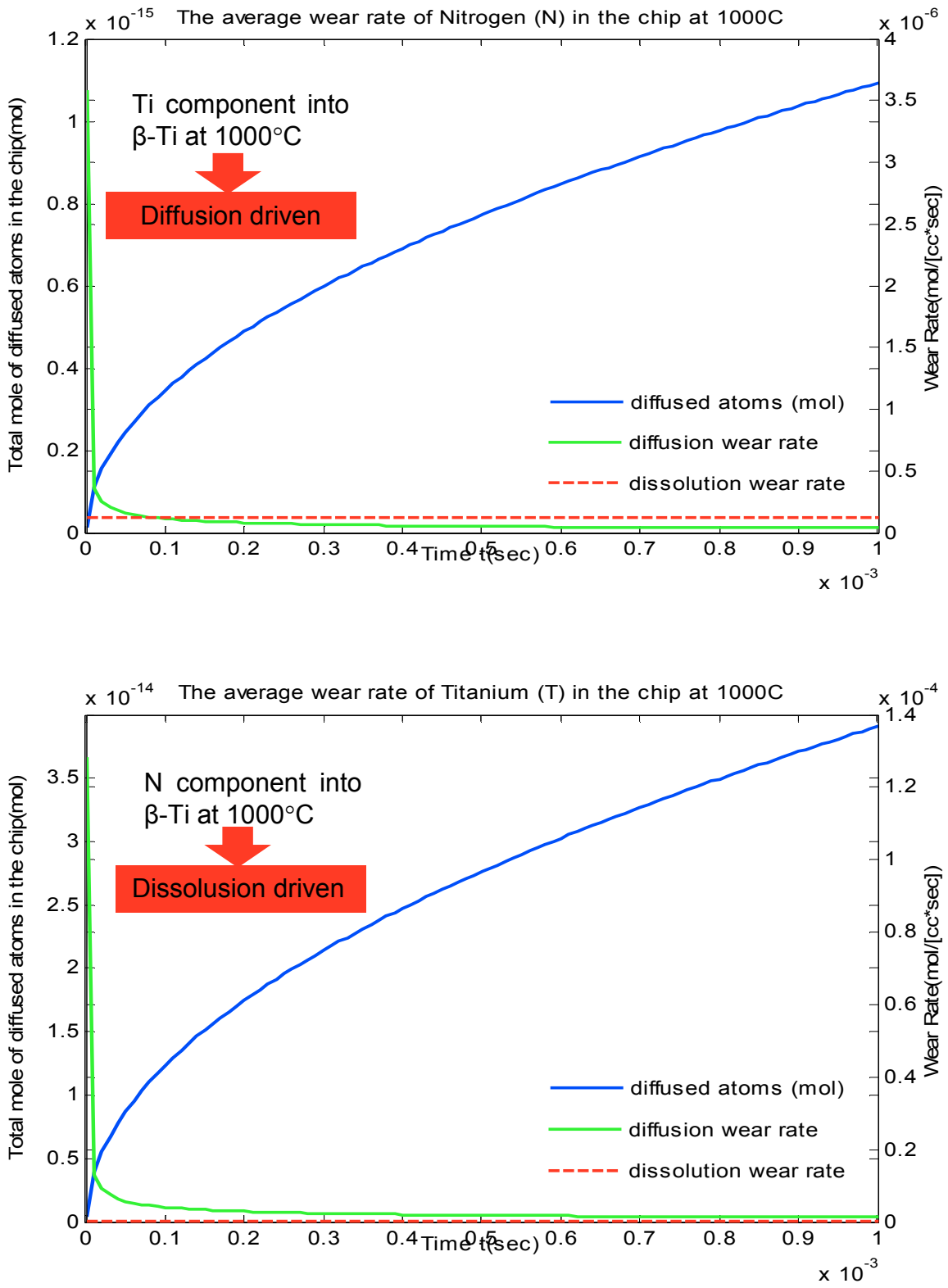

Figure 110: Dissolution and diffusion wear rate of TiN tool into β-Ti at 1000°C

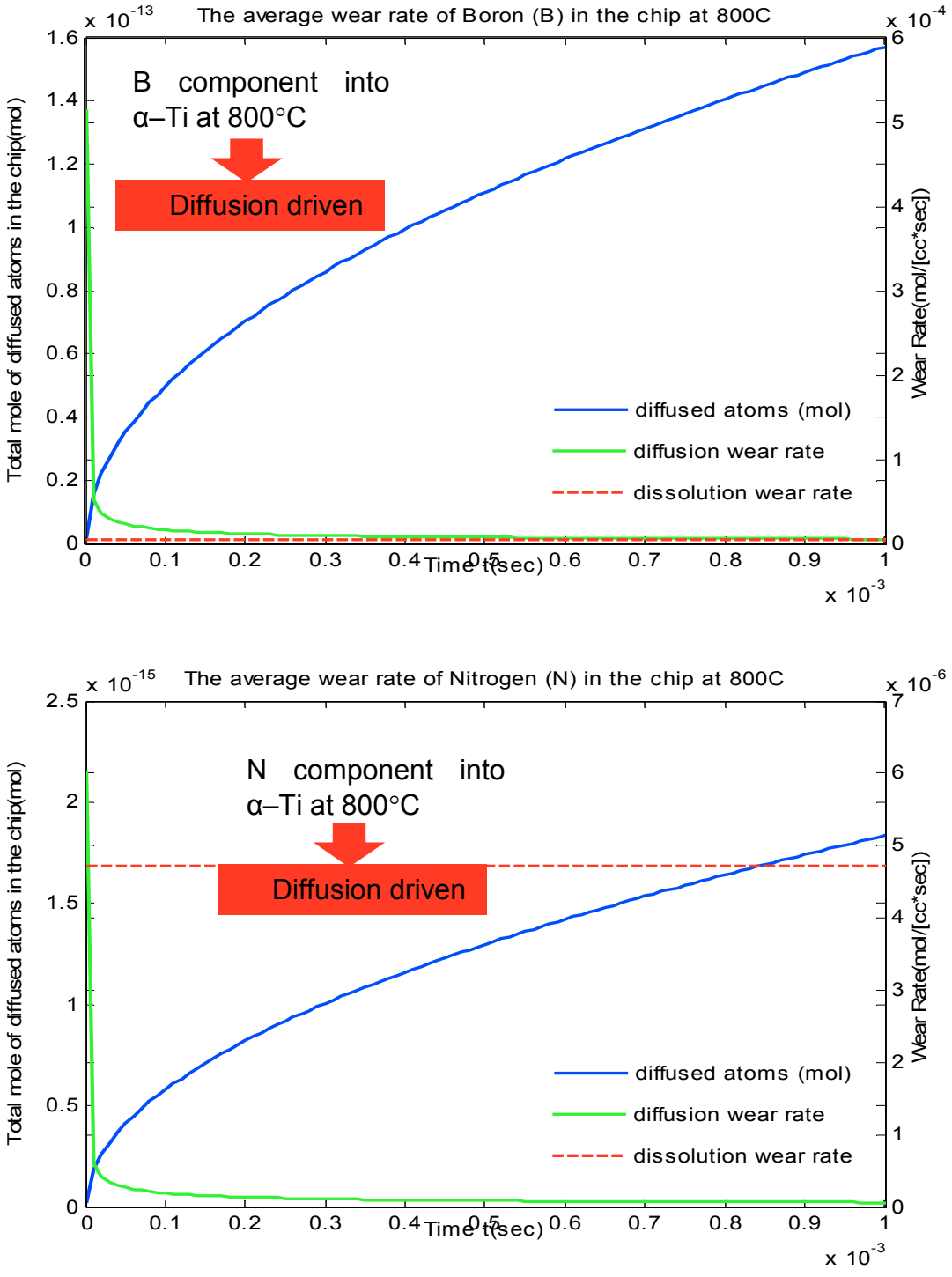

Figure 111: Dissolution and diffusion wear rate of cBN tool into α-Ti at 800°C

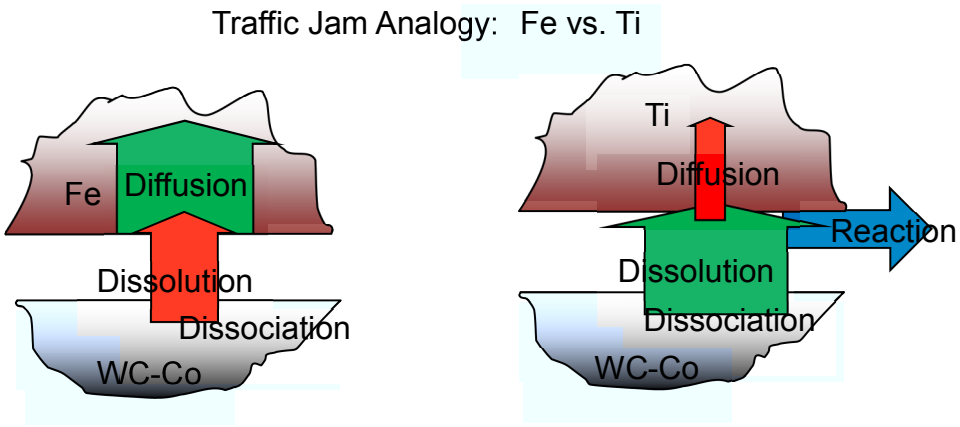

a) Dissolution controls in cutting steels

b) Diffusion controls in cutting titanium

Figure 112: Process (dissolution and diffusion) controls thermochemical wear for machining of ferrous and Titanium with carbide tool.

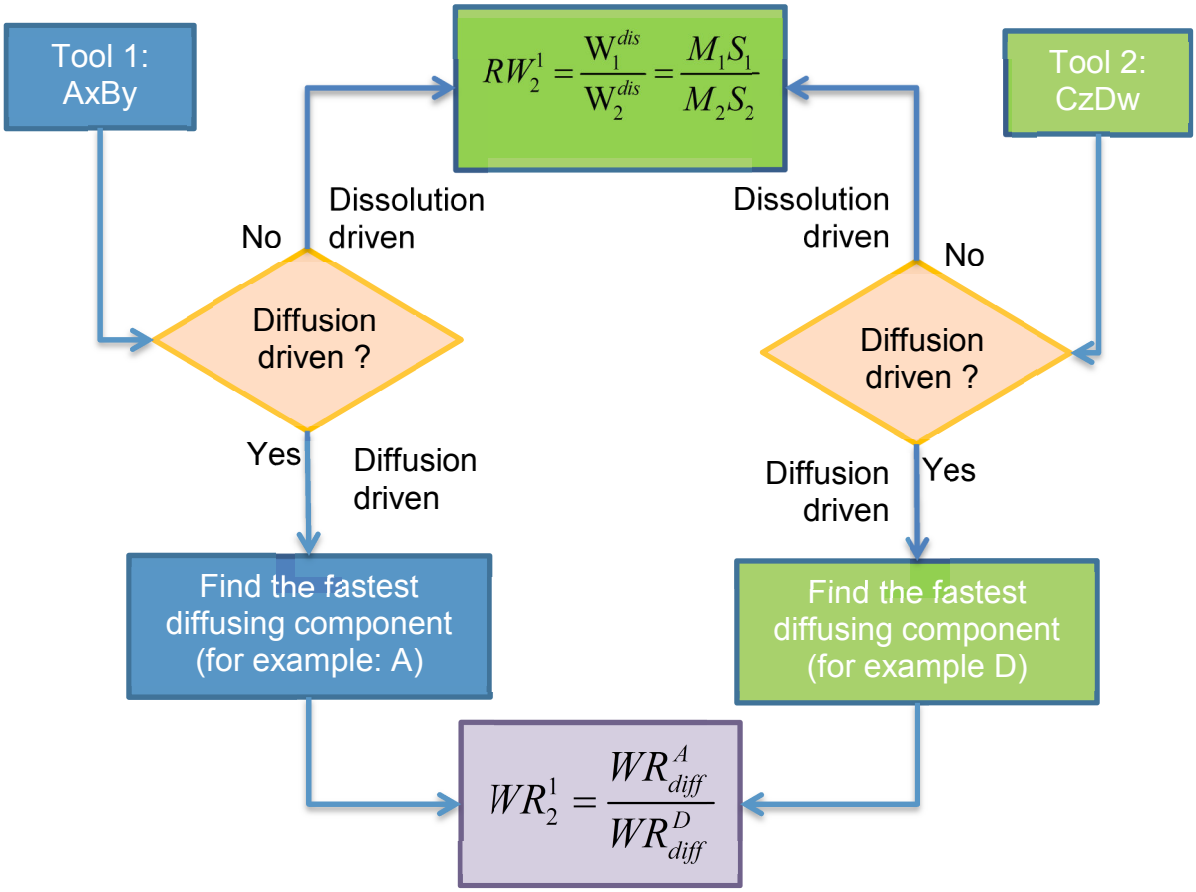

Figure 113: Flow chart for calculation of relative thermochemical wear rate.

According to the pervious chapters, the thermochemical (dissolution/diffusion) is proven to be the dominant wear mechanism of carbide tools in machining Ti64. The diffusion mechanism takes place by the diffusion action of W and C or Co from carbides into Ti alloys. However, the diffusion process is hampered due to the presence of TiC layer that forms by the reaction of Ti and C from carbides. The diffusivity of W and C in TiC is fairly lower than in titanium and Ti64. The reaction layer TiC formed at tool-chip interface helps to reduce wear rate. This can be proved with the nano-lubricants, which can provide the additional carbon from graphitic platelets. However, providing the nano-lubricants during turning is not always successful with MQL as the cutting tools is always engaged with the workpiece. Instead, the nano-graphitic platelets can provide additional lubricity at the tool-chip interface.

In next chapters, the study of tool wear improvement was conducted with MQL machining with micro and nano-platelets of graphite added in MQL oil. However, due to the difficulty in setting up MQL turning experiment, the ball mill was selected. The AISI 1045 steel was initially chosen for the workpiece to reduce the cost of the experiments. Based on the MQL ball-mill experiments with the steel, the investigation was carried out to find the effect of diameter and thickness of platelets and presented in in Chapter 4. Finally, the performance of MQL experiment with nano graphite platelets was evaluated with Ti64 in Chapter 5.

Chapter 4: Tool wear improvement in machining of Steel AISI 1045 with micro and nano-platelets enhanced MQL

IV.1 INTRODUCTION

Flood cooling has been the backbone of machining processes for manufacturing industries. The traditional flood cooling, which uses and discards a large amount of metal working fluid, is widely used in industrial machining operations. The primary purposes of metalworking fluid (MWF) are to rapidly dissipate heat, reduce friction between the tool and the chip and carry the chip away from the cutting zone. Consequently, the reduction in force and power consumption and the improvement in tool life and surface finish [1] are apparent. However, flood cooling has many disadvantages due to its associated maintenance and disposal cost (7-17%) [Kajdas, 2010] as well as occupational hazards and environmental impacts. According to the U.S. Occupational Safety and Health Administration (OSHA) [Aronson, 1995] and the U.S. National Institute for Occupational Safety and Health (NIOSH) [U.S. DHHS, 1998], the permissible exposure level (PEL) for metalworking fluid aerosol concentration is 5 mg/m^3 and 0.5 mg/m^3, respectively. The coolant mist level in U.S. automotive parts manufacturing facilities has been estimated to be on the order of 20-90 mg/m^3 with the use of traditional flood cooling and lubrication [Bennett & Bennett, 1985]. As a result, the need to reduce cutting fluid consumption is strong and the discrepancy in fluid aerosol concentration needs to be aggressively addressed. Dry machining has offered an alternative solution by completely eliminating cutting fluid. However, its applications are limited due to the poor surface quality, the accelerated tool wear and the high

concentration of airborne particles on the factory shop floor [R Khettabi, 2008; 2009]. Recently, Minimum Quantity Lubrication (MQL)-based machining has been introduced as an ideal alternative which provides a compromise between productivity and environmental concerns. MQL machining refers to a class of machining processes where the lubricant use is limited to only a extremely small amount – typically a flow rate of 2.5 to 500 ml/h [Gaitonde, 2008; Shen, 2008]. This amount of lubricant is about three to four orders of magnitude lower than the amount commonly used in flood cooling which dispenses up to 60 l/h [Srikant, 2009]. Thus, MQL offers many benefits such as the diminution of the environmental and occupational hazards and the reduction of maintenance and disposal cost. A general study on the efficiency of MQL to dry machining was introduced in Weinert et al. [2004]. In mild machining conditions, MQL provides a great substitute for flood cooling. However, MQL-based machining possesses have few major drawbacks such as chip disposal and limitation in machining conditions. Chip disposal can be somewhat remedied by adding compressed air. However, the lack of cooling capacity with MQL-based machining has been a major drawback preventing this technology to reach its full potential in industrial applications. To improve MQL performance and expand the range of MQL applications, many spray configurations and cutting parameters are proposed and investigated while others study to enhance the lubricity.

IV.1.1 Improved performance of MQL with alternative lubricants

Several works have been published to evaluate the characteristics of various lubricants for finding optimum lubricants in MQL machining. The most common

lubricants in MQL are mineral oil [Braga, 2002; Brandao, 2011; Brinksmeier, 1999; Shen, 2008; Varadarajan, 2002], emulsions (soluble or synthetic fluid) [Brinksmeier, 1999; Gaitonde, 2008; Wakabayashi, 2006], synthetic oils, esters [Brinksmeier, 1999; Wakabayashi, 2006], neat oil [Sarhan, 2012; Thepsonthi, 2009] and vegetable oil [Cetin, 2011; Ozcelik, 2011; Shen, 2008; Singh, 2013; Wakabayashi, 2006]. Some researchers used alcohol [Heinemann, 2006; Shen, 2008] and deionized water [Mao, 2012; Shen, 2008]. The mixture of water and oil-free synthetic lubricant provided longer tool life compared to both synthetic ester with and without alcohol in deep-hole drilling due to its high cooling ability and low viscosity of water [Heinemann et al., 2006]. A new approach to enhance the cooling effect with the MQL process, oil-on-water droplets produced through a new design nozzle system, reduced cutting forces in end milling [Itoigawa, 2006; Yoshimura, 2005]. Cutting performance in the tapping test as well as secondary factors (biodegradability, oxidation, and storage stability) for synthetic polyor esters were superior to vegetable oil [Wakabayashi, 2006; Suda, 2002].

In general, vegetable oil is favorable in MQL machining due to reduction in cutting force [Sadeghi, 2008], better surface finish [Emami, 2014; Singh, 2013; Tai, 2011] and improvement in tool life [Nguyen, 2012; Park, 2011] in comparison with MQL with other lubricants. More importantly, the biodegradability makes it safe for the workers in the environment. Thus, MQL offers many benefits such as the diminution of the environmental and occupational hazards and the reduction of maintenance and disposal costs. However, MQL lacks the ample cooling offered by flood cooling. Due to the extremely small amount of a liquid lubricant, MQL mainly provides essential lubricant function, which makes effective to only mild cutting conditions.

IV.1.2 Improved performance of MQL by adding solid lubricants

Solid lubricants have been used either to eliminate the use of cutting fluids or to mix with cutting fluid to enhance its lubricity. Many of them have lamellar or layered crystal structures where each layer readily slides against adjacent layers to provide lubricity. Some examples of such solids include soft metals, graphite, hexagonal boron nitride, boric acid, and the transition-metals dichalcogenides MX_2 (M is molybdenum, tungsten or niobium and X is sulfur, selenium or tellurium), such as MoS_2 and monochalcogenides (e.g., GaSe and GaS) [Erdemir, 2001]. However, no single solid lubricant can provide the lubricity over a wide range of cutting conditions (different tool and work materials). For example, molybdenum sulfide (MoS_2) works well in vacuum or dry conditions but degrades quickly in moist and oxidizing environments [Wiener, 1967]. Most transition metal dichalcogenides tend to oxidize at elevated temperatures, and thus lose their lubricity. MoS_2 can provide lubrication up to 350°C while WS_2 endures up to 500°C [Sliney, 1982]. In general, those with higher oxidation resistance or chemical/structural stability perform the best at elevated temperatures. Oxide and fluoride-based solid lubricants (e.g., CaF_2, BaF_2, PbO, and B_2O_3) [Sliney, 1993] as well as some soft metals (e.g., Ag, Au) function quite well at elevated temperatures [Erdemir, 1990; Erdemir and Erck, 1996; Maillat, 1993), but all fail to provide low friction at room or lower ambient temperatures. The lubricity of these solids at elevated temperatures is largely controlled by their ability to soften and resist oxidation. Solid lubricants such as molybdenum disulfide (MoS_2), tungsten disulfide (WS_2) graphite, hexagonal boron nitride (hBN) and polytetrafluoroethylene (PTFE) have been used as dry powders or coating materials [Donnet, 2004]. The effectiveness of the solid lubricant was

demonstrated in some publications. For example, the recent developments and future trends of well-known solid lubricants were summarized at Donnet et al. [2004]. Yukhno et al. [2001] reviewed the frictional behavior and wear resistance of solid lubricant coatings at low temperatures. Prasad et al. [2010, 2005] inspected the effects of some solid lubricants such as graphite, talc, MoS_2, and lead suspended in oil on the wear performance of cast iron and zinc–aluminum alloy. Hsu et al. [2004] discussed the important characteristics of nano-lubricants such as being non-volatile, oxidation and thermal decomposition resistant, and self-repairing as well as having a more effective film organization of nano-lubricant compared to conventional lubrications. The effect of the concentration of solid lubricants (MoS_2 and graphite) were studied and the "optimal concentrations" were found to be 3wt.% and 10wt.% for MoS_2 and graphite, respectively [Bartz, 1971]. Below the critical concentrations of MoS_2 and graphite, they did not effectively protect the surfaces against wear.

The main advantage of solid lubricants is the preservation of lubricity even under extreme pressure and temperature. Thus, by mixing the solid lubricants into a MQL lubricant, MQL-based machining can be enhanced for more aggressive conditions. Several works were published to evaluate the effectiveness of MQL applications at elevated temperatures by adding small amounts of solid lubricant to MQL oils. However, to be effective in general machining applications, solid lubricants should provide lubricity in a broader range of temperatures.

Molybdenum sulfide (MoS_2)

Shen et al. [2008] used MoS_2 to enhance grinding processes. By mixing MoS_2 nano-particles into MQL grinding fluid, the MQL-grinding process showed excellent performance on cutting forces. However, its effectiveness, especially in traditional machining applications, is questionable due to the low dissociation temperature of MoS_2 (350°C in oxidizing environments). Kalita et al. [2012] added 2 and 8 wt.% of MoS_2 nano-particles (40-70 μm) and micro-particles (3–5 μm) into paraffin and soybean oils used in MQL grinding tests of cast iron and EN 24 steel. He concluded that the grinding process was improved with MQL oil with added MoS_2 (both nano- and micro- particles) to flood cooling and MQL with pure oil. Furthermore, the nanoparticles less than 100nm exhibited superior performance to micro-particles (3-5 μm), resulting in up to 30% and 50% reduction in the friction coefficient and grinding ratio, respectively. The increase in the nano-particle content reduced the friction, energy consumption and cutting forces. In milling tests of AL6061-T6 alloy, Rahmati [2013] used the MQL mixture with MoS_2 nanoparticles (20–60 nm) added in ECOCUT HSG 905S neat cutting oil at various concentrations. The machining experiment with the presence of MoS_2 nanoparticles in the MQL oil showed outstanding performance compared to pure MQL oil in term of cutting force, temperature and surface finish. He claimed that optimum concentrations for minimizing cutting force and temperature were 1 wt.% and 0.5 wt.%, respectively. The surface roughness was minimized by applying the MQL oil mixed with 0.5 wt.% of MoS_2 nanoparticles.

Graphite (C)

The main advantage of graphite over MoS_2 is that the dissociation of graphite is much higher than that of MoS_2. The graphite was found to start decomposing at moderately high temperatures (e.g.: 500°C in oxidizing environments [Zhu, 1998]). The nano-graphene platelet enhanced lubricants were studied under various conditions. Lee et al. [2009] studied nano lubricants by mixing graphite nanoparticle additives (at 0.1 vol% and 0.5 vol%) with industrial gear oil to improve the lubrication properties in the disk-on-disk tribo-test between two sliding grey cast iron plates which showed superior performance in reducing the friction coefficient, sliding temperature, and surface roughness. Huang et al. [2006] compared the performance of pure paraffin oil to mixtures of paraffin oil with flake graphite (particle size: 48 μm) and with graphite nano-sheets (average diameter: 500nm, thickness: 10-20nm) in pin-on-disk tests using steel balls. He pointed out that the mixture with graphite nano-sheets formed a film on the rubbing surface that not only improved the friction coefficient but also reduced the wear. The pure graphite powder was used as solid lubricant to prolong the tool life and improve the cutting force and surface quality in milling AISI 1045 [Reddy, 2006]. Amrita et al. [2013] studied MQL turning of AISI 1040 steel using varying concentrations of graphite nano-particles (particle size < 100nm) suspended in water soluble oil (20:1). The cutting temperature, flanks wear and cutting force were significantly reduced compared to those of dry, flood and pure MQL oil machining. Among the concentrations of 0.1%, 0.3%, and 0.5 wt%, the higher content showed more improvement in the cutting performance. In turning of hardened AISI 4340 steel with a MQL mixture of 10%

graphite added in semi-solid lubricant (composed of calcium and a sodium soap base emulsified with mineral oil) [Paul, 2013], the machining process presented better cutting performance (e.g. tool wear, cutting force and temperature, surface finish) compared to dry machining and turning with pure MQL. In the MQL grinding process of a hardened tool steel, Alberts et al. [2009] found that the mixture of exfoliated Graphite nano-Platelet (xGnP) at 1wt% dispersed in isopropyl alcohol (IPA) was the optimal concentration to reduce cutting forces, specific energy and surface roughness. Park et al. [2011] showed that by using a very small amount (0.1wt%) of exfoliated graphite nano-platelets (xGnP) added in MQL Unist Coolube® 2210 vegetable oil, the tool wear was reduced by up to 50% in MQL ball milling of 1045 steel.

Boric acid (H_3BO_3)

Boric acid is a popular alternative solid lubricant added to MQL oils which have been evaluated in a few publications. Rao et al. [2008] investigated turning of EN 28 steel using compressed air and solid lubricant powders (graphite and boric acid) at different particle sizes of 50, 100, 150 and 200μm . The reduction of cutting force and flank wear was found when using solid lubricants compared to dry and wet conditions. He claimed that a particle size of 50μm would be most effective for both graphite and boric acid. Krishna [2012] examined the performance of boric acid nano-particle (100um) suspensions at various concentrations (0.25, 0.5, 0.75, and 1.0 wt%) in coconut oil with MQL turning AISI 1040 steel. In comparison to dry conditions, the turning process with MQL oil showed significant reduction in cutting temperature, surface finish and tool flank wear due to slight improvements in thermal conductivity and the heat transfer

coefficient. Among them, the 0.5wt% mixture showed the best cutting performance. Using the same approach, Ramana [2011] studied MQL mixtures of boric acid particles (50 nm, 60nm, 80nm and 0.5um) in canola oil in turning tests of AISI 1040 hardened steel. Surprisingly, the experimental results revealed that MQL oil with boric acid showed higher cutting force and tool temperature compared to dry and flood cooling with pure canola oil. Furthermore, the smaller particles showed worse performance in terms of cutting force, tool wear and surface quality of the machined surface.

IV.1.3 Improved performance of MQL by varying spray configuration

The effectiveness of MQL is directly dependent on the application angle of the nozzle. Figure 114 depicts the illustration of spray angles (yaw and pitch angle) of an external MQL nozzle in a ball-milling experiment. The experiment is set for the rotating mill to travel along the Y axis. In this setup, the pitch angle is the angle between the Y axis and nozzle spray while yaw angle is the angle between the table feed direction and nozzle spray. Table 18 summarizes the findings from other works in determining the optimal spray angles and other spray parameters for external MQL systems with respect to the definitions of yaw and pitch angle in Figure 114.

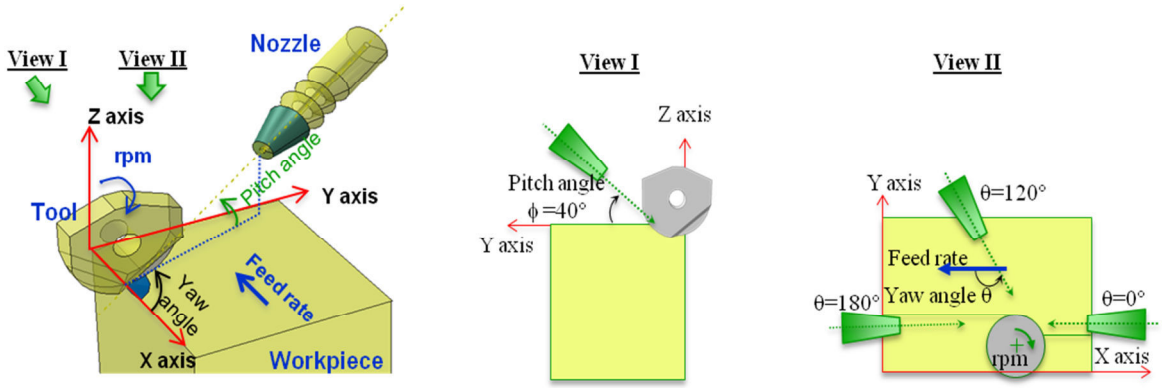

Figure 114: Pitch and Yaw angle of the nozzle in End-ball milling

Table 18: Publication on optimal spray conditions in MQL machining with definition of Yaw and Pitch angle as shown in Figure 114

Ref.	Machining Process	Cutting fluid	Additive	Nozzle distance	Flow rate	Yaw angle	Pitch angle	Improvement
Mao et al. [2012]	Grinding of AISI 52100	Deionized water	0.75wt% Al_2O_3particles (60nm)	20mm	60 ml/h	180°	15°	50% in surface roughness, 20% in grinding temperature
Yan et al. []	Milling of forged steel	Esters	--	20mm	43.8 ml/h	60°	60°	10% in Flank wear and surface roughness to other yaw and pitch angles
Lacalle et al. [2006]	Milling of Aluminum 5083-H112	Biodegradable oil	--	--	0.06ml/min	45°	--	30% in flank wear to flood coolant with emulsion 95% of water
Liu et al. [2011]	Milling Ti6Al4V	Vegetable oil	--	25mm	10 ml/h	45°	--	Little lower cutting force and temperature to others
Ueda et al. [2006]	Turning and Milling of AISI 1045	Vegetable oil	--		40 ml/h	45°	45°	10% in temperature
Tawakoli et al. [2010]	Grinding of hardened steel 100Cr6	Syntilo XPS Castrol 5%	--	40	100 ml/h	180°	10-12°	Slightly improvement in grinding force and surface finish to other positions and depend on material of wheel
Park et al. [2011]	Milling of AISI 1045 steel	Vegetable oil	xGnP	50-70 mm	1 ml/min	--	10°	40-50% in Flank improvements of xGnP mixture in comparison to pure oil.

IV.2 BACKGROUND

Lamellar-type solid lubricants are readily available in the form of platelets. The diameter and thickness of these platelets are typically to the scale of tens of microns and only a few microns, respectively, which are classified in this thesis as micro-platelets. Some of these platelets are also available as nano-platelets whose thickness is well below a micron (even to a few nanometers). Clearly, the micro-platelets are not as inexpensive. However, the mixtures with micro-platelets are not as stable as those with nano-platelets. Another aspect of nano-particles is the worldwide excitement of nanotechnology research. Many research findings are reporting on new processing

techniques, which will eventually make them cheaper and available for wide varieties of applications. In this study, these micro- & nano-particles and platelets are used to reduce friction and/or wear. It is also important to recognize that a wide variety of shape and size distributions of these particles are now available.

In this chapter, we will explore the use of micro and nano platelets of graphite and hBN mixed in the vegetable oil, Unist Coolube 2210 obtained from Unist, Inc. (Grand Rapid, Michigan) in tribometer tests and MQL ball-milling tests. This study defines 'nano-platelets' to have a thickness of less than 0.1μm and 'micro-platelets' to have a thickness of more than 0.1μm. The hBN phase is similar to graphite but quite different from its related compound, cubic boron nitride (cBN). Like graphite, the hBN phase has a layered structure where each layer is weakly bonded with adjacent layers. With the application of a shear load, each layer can easily slide against other layers providing lubricity. Both graphite and hBN can provide the lubricity desperately needed in more severe machining conditions, even when the oil droplets can dissociate. The dissociation temperature of hBN is even higher than that of the graphite. The main advantage of the nano-platelet form of solid lubricants (hBN and graphite) is the aspect ratio of diameter to thickness. When applied, the larger surface of the nano-platelets will land on the tool surfaces and additional lubricity from these nano-platelets can be provided in the MQL-machining. The nano-platelets have the thickness in nano-scale and the diameter in micro-scale, which offers a unique advantage of being filtered by nose hair and not being absorbed through human skin. This thesis intends to find the effect of thickness and diameter on these platelets in MQL machining of AISI 1045 steel and Ti64.

IV.2.1 Micro and nano-platelet characterizations

In the periodic table of elements, boron and nitrogen are the neighbors of carbon (C). Boron Nitride (BN) was first founded in early 19th century. The compound has the same number of outer shell electrons as graphite and diamond. BN has very similar properties as carbon with both hexagonal and cubic crystal structures [Haubner, 2002]. Figure 115 illustrates the similarity in the hexagonal structure of graphite and hBN. While both forms of carbon exist as graphite and diamond in nature, both forms of BN are synthetic and exist as cubic boron nitride (cBN) and hexagonal boron nitride (hBN). The hBN phase is more similar to graphite but quite different from its related compound, cubic boron nitride (cBN). The electrical properties are recognized as the prominent differences between carbon and BN. Due to its high electrical resistivity, BN is well-known as dielectric and thermally conductive whereas carbon is electrically and thermally conductive. The main difference in appearance is that hBN is white while graphite is black. Like graphite, the hBN phase has a layered structure where each layer is weakly bonded with adjacent layers. With the application of a shear load, each layer can easily slide against other layers providing lubricity. hBN is expected to have the similar lubricant properties to graphite. The main advantage of the mixtures of graphite/oil and hBN/oil is that they can provide lubricity even if the oil droplets dissociate due to a high cutting temperature. The hBN is stable up to 1000°C [Haubner, 2002], while graphite was known to start decomposing at moderately high temperatures (500°C) [Zhu, 1998]. The hBN has good chemical inertness and is not wetted by most molten metals [Haubner, 2002]. These advantages of hBN compared to graphite make

hBN a more promising solid lubricant in MQL processes where the cutting temperature is expected to be very high.

Several research investigations on the lubricity of BN for various applications were published. The early research on tribological properties of cubic, amorphous and hexagonal boron nitride films by Watanabe et al. [1991] showed that BN films helped to decrease the friction force and the friction coefficient as a function of normal load. The curious behavior of hBN was discovered with a ring-on-roller tribometer when added to lubricating oil as well as the effect of hBN concentration on friction and wear in Kimura et al. [1999]. The sliding experiment of bearing steel vs. itself showed that the addition of BN at as little as 1 wt% resulted in the reduction of wear. The wear was reduced as concentrations of BN increased, although the friction coefficient was slightly increased. Based on these investigations, BN was considered as a potential additive for the lubricants.

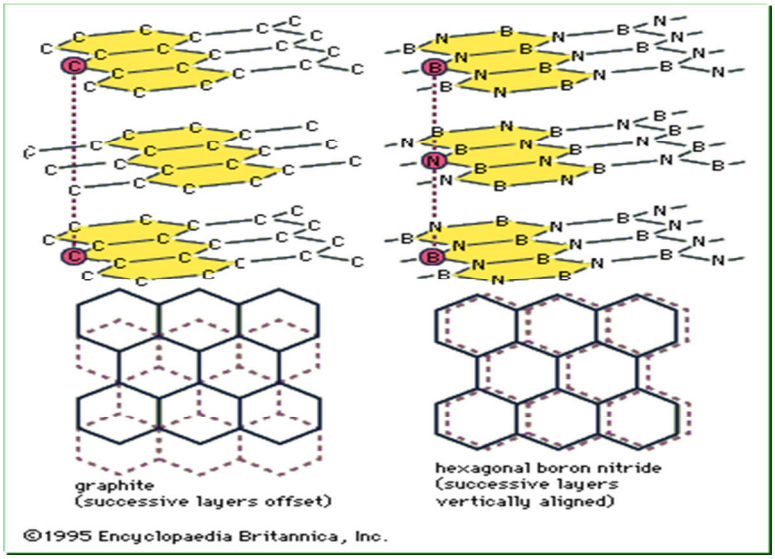

Figure 115: An illustration of hexagonal crystalline structures of ghraphite and hBN [Encyclopedia Britannica, Inc., 1995]

Table 19: Properties of graphite and hBN

Formula	BN	Graphite (C)
Molecular mass	24.82 g/mol	12.01 g/mol
Density (hexagonal)	2.27 g/cm^3	2.23g/cm^3
Density (cubic)	3.48 g/cm^3	3.51 g/cm^3
Melting range	2700-3000°C	3652 - 3697°C
Mohs hardness	1-2	1-2
Youngs Modulus (MPa)	20-102	8-15
Coefficient of Friction	0.15 to 0.70	0.2 to 0.6
Thermal conductivity	34	25-470
Temperature Stability	1000°C	500°C

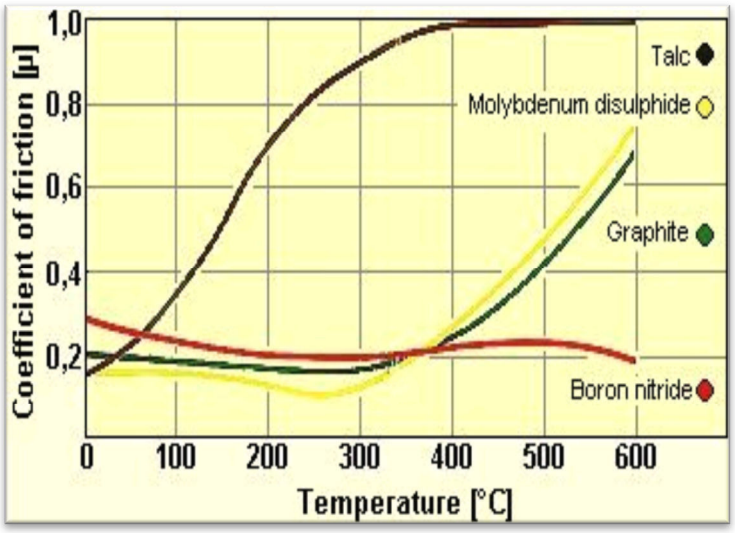

Figure 116: Temperature range for lubrication of different solid lubricants [Chen N., 2004]

The solid lubricant platelets examined in this study include micro-platelets (graphite and hBN) and nano-platelets (xGnP and exfoliated hBN). The graphite micro-platelets were obtained from Alfa Aesar Com., USA while the micro-platelets of hBN5 were obtained from Changsung Corp. (South Korea). Four nano-platelets designated as

xGnP M5, xGnP M15, xGnP C300, xGnP C750 and one exfoliated hBN300 were provided by XG Science, Inc., (Lansing, Michigan, USA) using their cost-effective exfoliation process after being downsized by the pulverization process [Fukushima, 2003]. Among xGnP platelets, the Grade M5 and M15 have the same thickness with distinct diameters while C300 and C750 have the same diameter with distinct thicknesses. Table 20 summarizes the diameters and thicknesses of each platelet. Some of these data have been interpreted based on surface area measurements or based on SEM images. As presented in Table 20, a typical, commercially available hBN powder has a surface area of around 2 m^2/g while the surface area of XGS® hBN is 246 m^2/g. The surface area of hBN is quite larger than that of xGnP grade M5 (~120-150 m^2/g) but is smaller than that of xGnP grade C (300 and 750 m^2/g for C300 and C750, respectively).

Table 20: The diameters and thicknesses of various platelets

	Platelets	Diameter	Thickness	Aspect ratio	$S_{BET}(m^2/g)$	Company
Micro-platelets	Graphite	7μm	200 nm+	35	4.8**	Alfa Aesar
	hBN5	5μm	1-2μm+	3	1.27**	Changsung
Nano-platelets	xGnP M5	5μm	6-8 nm	714	~120-150	XG Sciences
	xGnP M15	15μm	6-8 nm	2143	~120-150	XG Sciences
	xGnP C300	2μm	3 nm*	667	300	XG Sciences
	xGnP C750	2μm	1.2 nm*	1667	750	XG Sciences
	hBN300	11 nm*	8.24 nm	1	246	XG Sciences

+ A estimation based on SEM image (See Figures 5 and 6)

* A calculated value based on the surface area BET (Brunauer–Emmett–Teller theory) data

** The calculated surface area based on diameter and thickness

The patent by Kwon and Drazl [2010] has been issued using xGnP platelets to enhance the effectiveness of MQL machining. A wide variety of graphite platelets varying in diameter and thickness are now produced by XG Science, Inc.. The main advantage of xGnP over MoS_2 is that the dissociation of graphite is much higher than that of MoS_2. In the paper by Park et al. [2011], the oil and the nano-platelets have been mixed in a high-speed mixer to produce stable solutions, which have been substituted for vegetable MQL oil in the MQL-based ball-milling experiments. The diameter and thickness of the graphite platelets were approximately 1μm and 10nm in average, respectively. The results were very encouraging in the reduction of tool wear.

Figure 5 presents the micrographs of some of the platelets at 1000x magnification. Figure 6 shows the thickness of xGnP and graphite micro-platelets at 30,000x magnification. Although both platelets have a similar particle diameter, the thicknesses of xGnP and hBN are much smaller than those of micro-platelets. We expect that the nano-platelets can facilitate a better lubricity and reduce wear even at the same concentration levels in oil. Figure 119 presents the diameter versus thickness and the aspect ratio for graphite platelets.

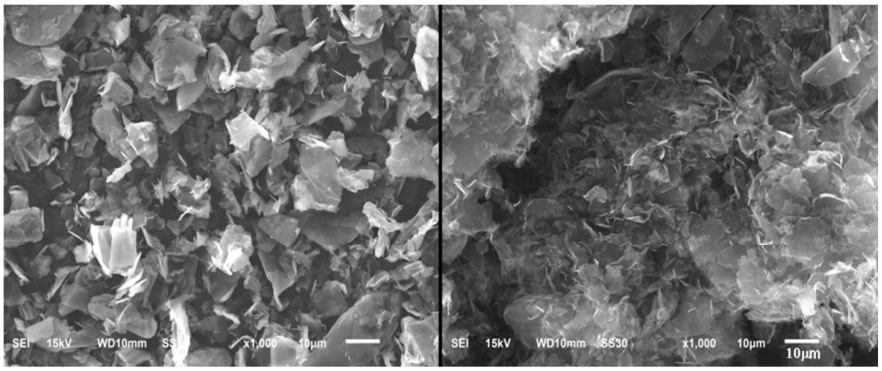

a) micro-platelet graphite b) nano-platelet xGnP (M5)

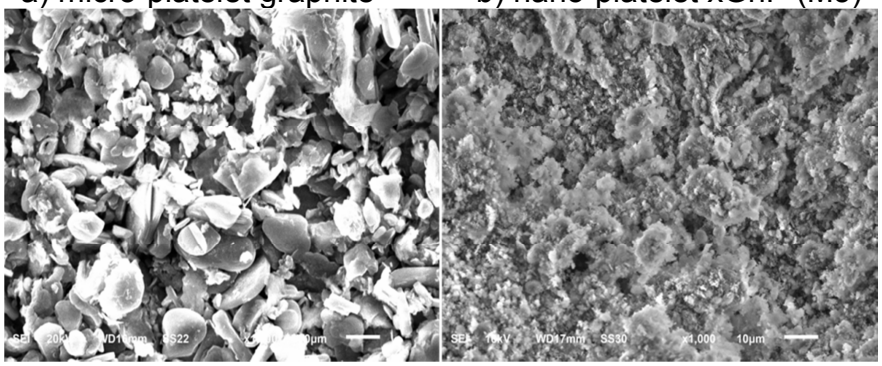

c) micro-platelet hBN5 d) nano-platelet hBN300

Figure 117: SEM analysis

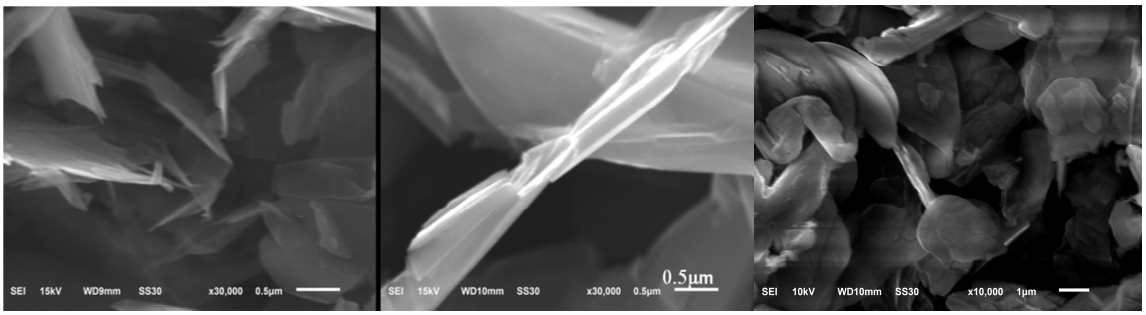

a) xGnP M5 b) micro-platelet graphite c) hBN5

Figure 118: SEM images micro- and nano-platelets

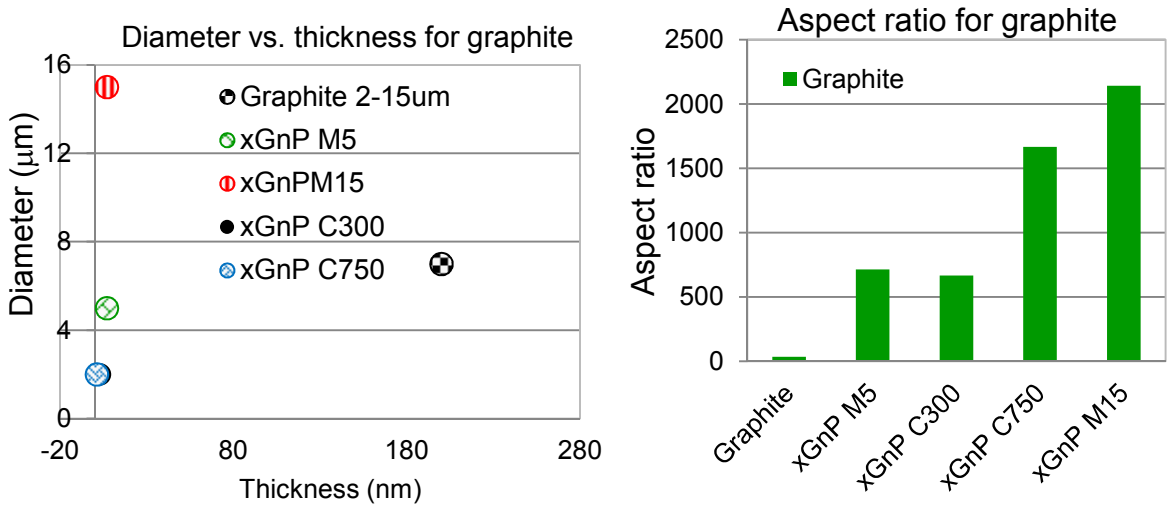

Figure 119: Diameter, thickness and aspect ratio of graphite platelets.

IV.2.2 Vegetable oil Unist Coolube 2210

The vegetable oil, Unist Coolube® 2210, has the flash point ~200° C from Unist, Inc., (Grand Rapid, Michigan, US) and was selected as the lubricant It is not hazardous to the workers. More importantly, it is formulated from renewable plant-based oils, which is biodegradable, making it friendly to the environment. With very small amounts of oil used in MQL machining, its main purpose is a “lubricant”, not a “coolant”. As a lubricant, it reduces friction between tool and work material, thus decreasing heat generation. Unlike flood cooling, it does not provide cooling. As shown in Park et al. [2011], the Unist oil showed the smallest wetting angle among various lubricants tested. The lubricant with the smallest wetting angle will spread out on the machined surface easily, covering a larger area by a thin, low friction lubricant between the cutting tool and work piece. Henceforth, wetting angle was measured on various mixtures of graphite, xGnP and hBN platelets with vegetable oil. The mixtures were tested in a pin-on-disc type tribometer with reciprocating motion to study the performance of lubricity and wear

resistance. The ball-mill experiment is chosen to evaluate the applicability of the nano-platelet enhanced MQL lubricant as the cutting edges of the tools are exposed each revolution.

IV.3 EXPERIMENTAL SETUP AND PROCEDURES

IV.3.1 Suspension Stability of Mixtures

In practice, the stability of MQL mixtures – the segregation of particulates in a mixture - is important. With the unstable mixture, the addition of solid lubricants will not provide the intended function. The suspension stability is influenced by diameter, thickness of platelets and mixing conditions such as mixing speed and mixing time. The suspension stability test was conducted with the mixtures made with both micro- and nano-platelets of graphite and hBN with vegetable oil. The mixtures were prepared on a high-speed mixer DAC 150FVZ-K from FlackTek (Landrum, SC) as shown in Figure 120. The mixing conditions were set at a speed of 2300rpm and durations of 4, 6 and 8 minutes as the stabilities of the mixtures were achieved.

Figure 120: High-speed mixer DAC 150FVZ-K

IV.3.2 Wetting angle measurement

The wetting angle is one of the significant parameters determining lubricity of the MQL lubricant. As the MQL droplets are applied to the spinning tool, the wetting angle indicates how well the droplets will stick to the tool surface. A lubricant with a small wetting angle shows good wettability on the surface. The wetting angle tests were conducted with both micro- and nano-platelets of graphite and hBN platelet-mixtures at various concentrations on the TiAlN-coated WC ball insert to be used in the ball-milling tests. The mixtures include vegetable oil mixed with 0.1 and 0.5wt% of hBN300 and 0.1 wt% and 1.0 wt% of xGnP grade M5 and xGnP C300 and C750 grades. Figure 121 shows the equipment and setup for the wetting angle measurement. To generate consistent amounts of droplets, the motorized syringe assembly (from AST Product, Inc.) was used to dispense a droplet of 0.5, 1, or 2.0 μl on the tool surface. The CCD camera was used to capture the image of the droplet produced by the LED black light. The droplet image was processed to obtain the wetting angles based on the boundaries of the droplet and the tool surface.

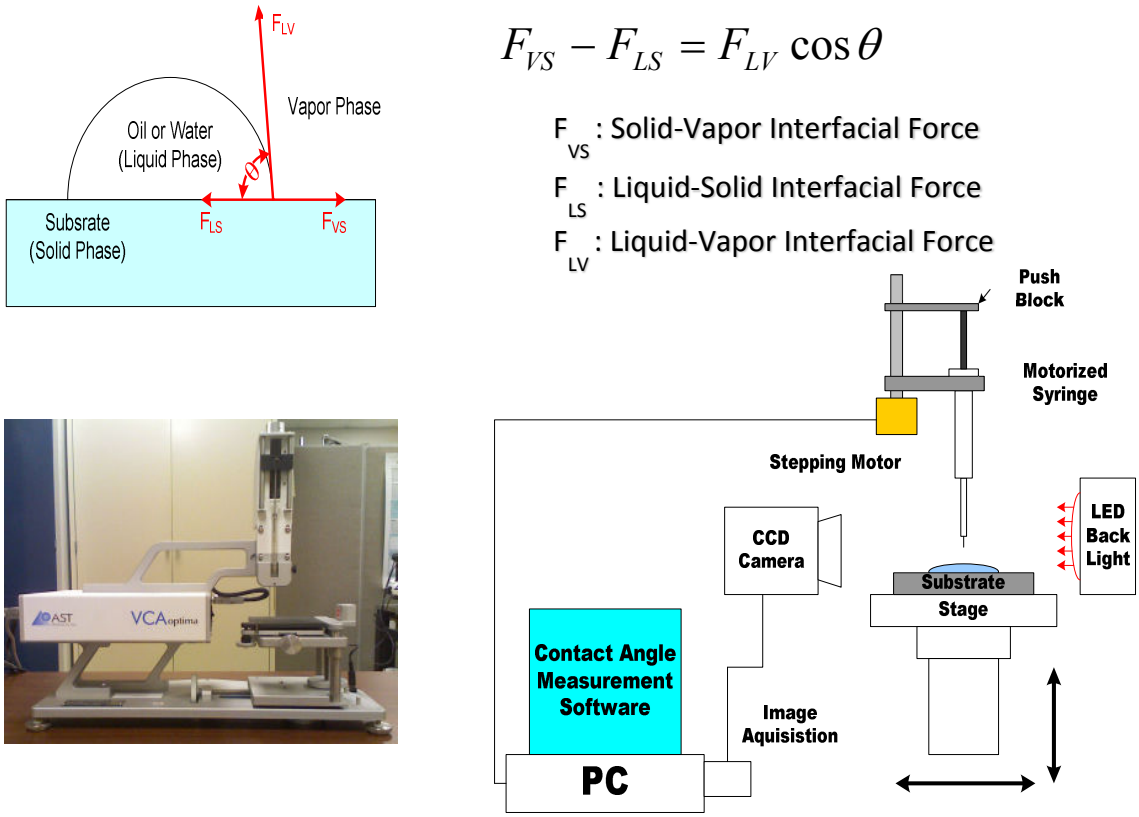

Figure 121: Wetting Measurement system [Park, 2011]

IV.3.3 Surface characterization of two coated inserts using in tribotest and end-ball milling experiment

In the MQL milling experiments, two different types (denoted as A and B) of ball nose end mill TiAlN-coated carbide inserts from two manufactures were used. To study the effect of tool surface quality on the performance of solid lubricant platelet-enhanced MQL mixtures, the topography of the surface of each tool was investigated. The surface appearance and profile of these tool inserts were investigated by SEM images. The roughness parameters such as the ten-point height mean roughness (Rz) and mean spacing between peaks (Sm) were also measured with the Dektak 6M stylus surface profilometer with the point-to-point resolution of 1 angstrom as shown in Figure 121.

These data were attained at a horizontal resolution of 0.067μm/sample over the average value of 30,000 data points on the 2mm evaluation length scan in the parallel and perpendicular directions of the grinding marks on the tool inserts.

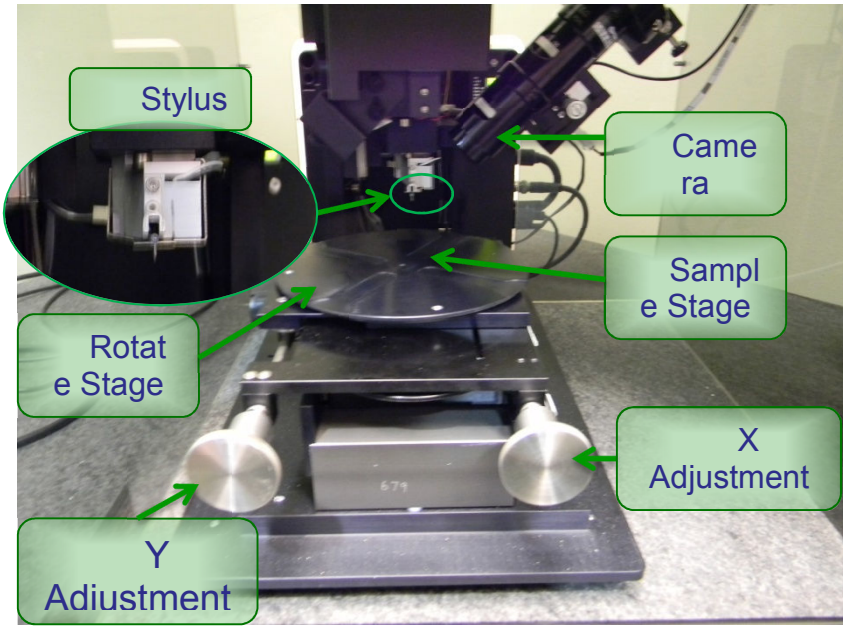

Figure 122: Veeco Dektak 6M Surface Profiler

IV.3.4 Tribometer Tests

The friction measurements on the mixtures were attained with the tribometer test. The tests were performed with a linear ball-on-disc type tribometer (CSM Instruments) as shown in Figure 123 where a steel 440c ball, with 6.35 mm in diameter, oscillated on TiAlN-coated carbide flat and rough surfaces (tool A and B) to evaluate frictional characteristics under various lubrication conditions. The software calculates the coefficient of friction between two sliding objects at a given normal load. All the tests were set at a track length of 6mm (with an amplitude of 3mm) while carrying a load of 1, 5 and 10N with a sliding speed of 1.0, 2.5 and 4.0 cm/s at room temperature as summarized in Table 4. The lubrication conditions include dry, pure vegetable oil and

mixtures of vegetable oil with 0.1, 1.0wt% of graphite and xGnP (M5); 0.1, 0.5wt% of hBN300 and hBN5.

The wear characteristics under each lubricant condition were measured with a WC ball instead of the 440C steel ball used in the friction tests in order to accelerate the wear on the surfaces. The wear tests were conducted on both tool A and B, on which depth and width measurements of the wear tracks were measured after 25,000, 35,000 and 50,000 cycles. However, since it is not possible to continue the wear test on the exactly the same location, each wear cycle started from scratch. The average depth and width on the wear tracks were measured on three cross-sections along a wear track length of 6mm. Wear rate and volume of the wear track were calculated based on the measurements from Dektak 6M Stylus Surface Profilometer. Figure 124 presents the profile of a cross-section of the wear tracks using a Dektak 6M Surface Profiler which the wear depth and width were measured.

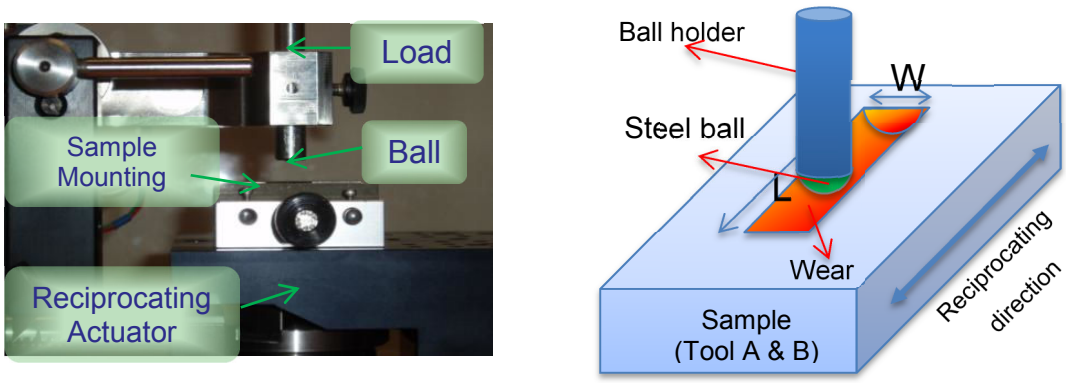

Figure 123: Linear ball-on-disc type tribometer

Table 21: Parameter for Tribometer tests

Tool	Ball-nose TiAlN-coated carbide inserts Tool A and tool B (diameter of 25mm from two manufacturers)
Ball	Steel (in friction test) & WC (in wear resistance test), diameter of 6.35mm(1/4")
Speed	0.25cm/sec, 1.0cm/sec, 2.5cm/sec, 4.0cm/sec
Normal load	1N, 5N, 10N
Length of track	L=6mm
Running time	• 3333cycles (14m with amplitude of 3mm) for friction tests • 25000 and 50000 cycles for wear tests

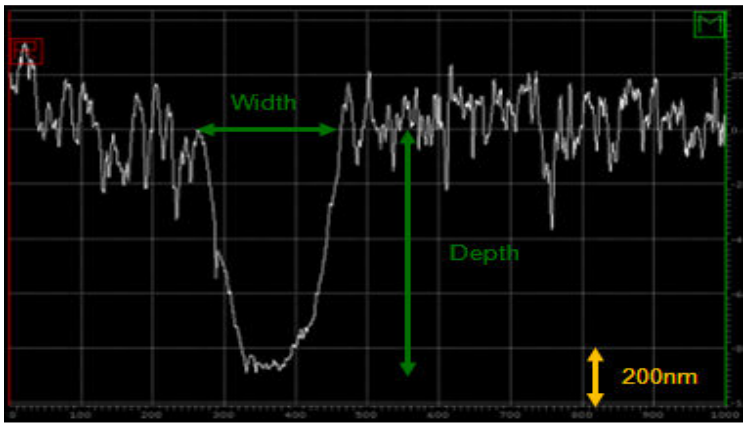

Figure 124: Profile of a cross-section of wear track.

IV.3.5 Ball Milling Experiments with steel AISI 1045

The MQL dispensing device (Uni-MAX) provided by Unist, Inc. (Grand Rapid, Michigan) was used for MQL process providing the mist to the cutting area in the ball milling experiments. The device sprays the vegetable oil through an external co-axial nozzle. The definitions of the pitch and yaw angles for MQL nozzle was presented in Figure 114. Pitch angle is the nozzle angle respected to XY plane. Yaw angle is

defined by the angle between nozzle and X axis in the XY plane. The nozzle outlet pressure and flow rate can be adjusted with the air metering screw and pulse duration/frequency in the control panel, respectively. According to the previous work [Park, 2010], the optimum MQL condition was determined to be 8 psi and 1.5ml/min for outlet pressure and flow rate, respectively. The ball-mill experiments under various MQL conditions were performed on the 3-axis vertical milling center (Sharnoa CNC mill) as shown in Figure 125. The 25mm diameter end ball-nose TiAlN coated carbide inserts (Tool A and B) were used for tool materials. AISI 1045 steel (203.2 mm×127 mm×203.2 mm) was used for work materials. In the experiment, the feed rate and cutting speeds were kept constant at 2500mm/min and 3500 rpm, respectively. The depth of cut (DOC) and radial depth of cut (ROC) were 1 mm and 0.6mm, respectively. The machining conditions are summarized in

Table 22. The cutting started at one corner of the work material in the direction of 203.2mm and continued line by line to finish one layer. A layer is removed when all the passes are completed at the same vertical height. In each layer (203.2 mm×127 mm), the tool cuts the total of 212 lines. The tool wear was also measured after cutting each layer to record the progress of tool wear. Due to the limited supply of work materials, the maximum of cutting layer was set at 8 layers. The milling was conducted at different lubrication conditions: dry condition and MQLs (pure MQL oil and nano-platelets enhanced MQL oil). This study mainly focuses on the steady stated wear. To minimize the effect of chipping and fracture in our analysis, the insert was considered broken if the chipping and fracture were larger than twice of the average of flank wear width.

Table 22: Machining conditions for steel AISI 1045

Tool	Ball-nose TiAlN-coated carbide inserts Tool A and Tool B (diameter of 25mm)
Feed Rate	2500 mm/min
Axial DOC	1 mm
Radial DOC	0.6 mm
Cutting Speed	3500rpm (108 m/min)
Lubricants	Dry, MQL oil Nano-platelets xGnP enhanced MQL oil at 0.1, 1, and 5 wt%
MQL spray parameter	Pitch angle: 15° Yaw angle: -30, 60, 120 and 180° Outlet pressure: 8 psi Flow rate: 1.5ml/min

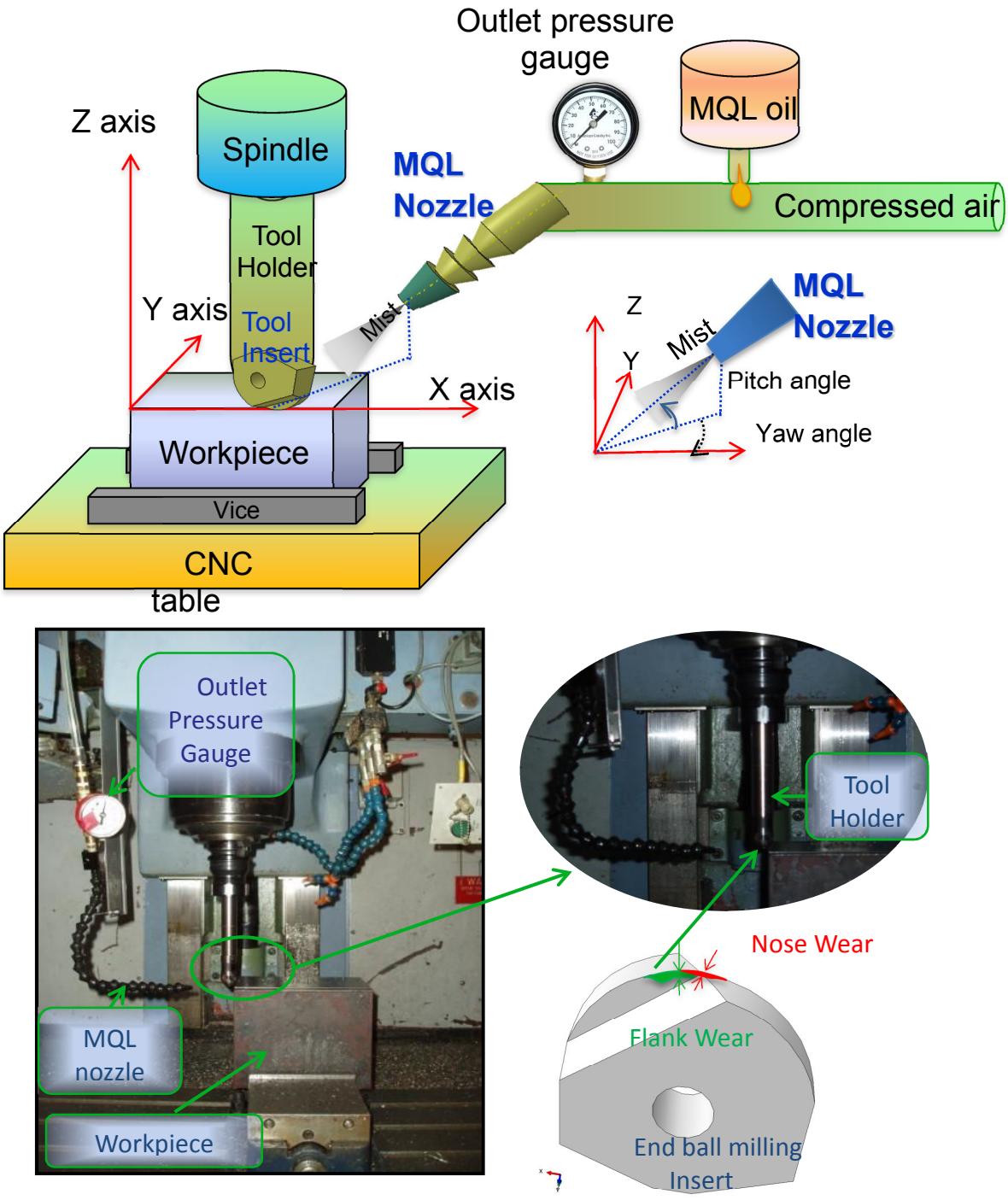

Figure 125: Experimental Set up for MQL ball milling

IV.4 EXPERIMENTAL RESULTS AND DISCUSSION

IV.4.1 Stability of Mixtures

The tests showed that the graphite mixtures were stable less than one day after mixing in comparison to more than 3 days for the xGnP mixtures. The results also showed that the stability of the mixtures was improved with a longer mixing time for both micro- and nano-platelets. Park et al. [2011] showed that the larger diameter platelets were segregated quicker than the smaller diameter platelets with the same thickness. Based on the stability tests with graphite, xGnP M5 and xGnP M15, it was determined that the thickness of the platelets influenced the stability of the mixtures more than the diameter. For example, the graphite micro-platelets with thickness of 200nm and average diameter 7μm were segregated much faster than both xGnP M5 and M15 nano-platelets (with the same thickness of 6-8nm), which have the diameter of 5μm and 15μm, respectively. The stability of the mixtures with 0.1wt% platelets after mixing for 3 days are shown in Figure 126, of which xGnP C750 provided the most stable mixture because of the smaller thickness and diameter.

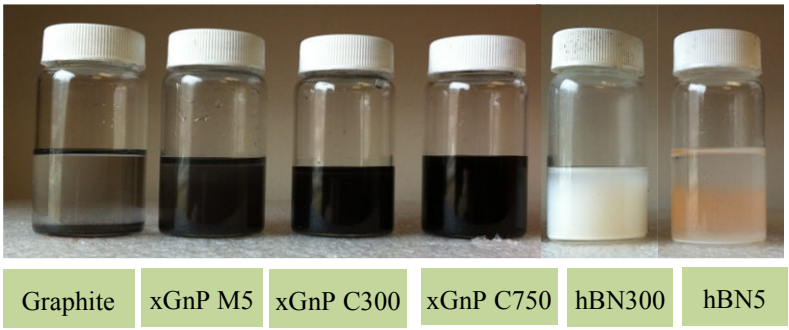

Figure 126: The stability of the mixtures with 0.1wt% micro- and nano platelets after 3 days

IV.4.2 Wetting angle measurement

Figure 127 compares the wetting angles of water, water mixed with mineral oil produced by NRG Resources (NRG oil), pure unist oil and mixtures of unist oil with micro and nano-platelets for droplets of 0.5 μm. It can be seen not only that the introduction of nano-platelets decreases the wetting angle but also that the wetting angle of hBN is slightly smaller but comparable to those of the xGnP mixtures. In the later section, the result from our tribometer test revealing the preponderant wear resistance of hBN to xGnP will be shown.

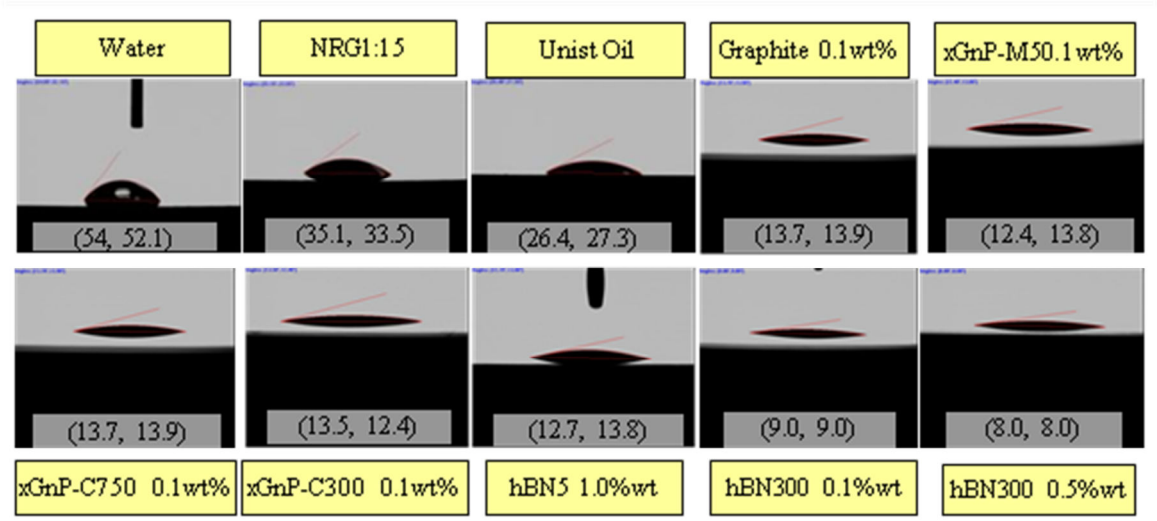

Figure 127: Wetting angle of MQL lubricants on the surface of TiAlN coated carbide inserts (left angle, right angle)

IV.4.3 Surface characterization of two coated inserts

Figure 128 presents the SEM micrographs of both (Tool A and B) tool surfaces at 1000x and 5000x magnifications. Figure 129 presents R_z and S_m for measurements over the length of 200 um which were along and perpendicular to the grinding marks of the tools. Despite the similar spacing parameters, the roughness of tool B is around 1.6

μm while the roughness of tool A is 0.6 μm. Thus, tool A has a smoother surface, which we expected to yield a better sliding contact with less wear.

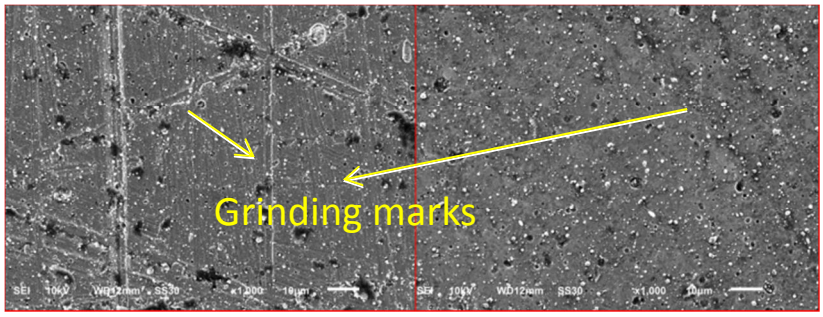

a) Tool A at 1000x b) Tool B at 1000x

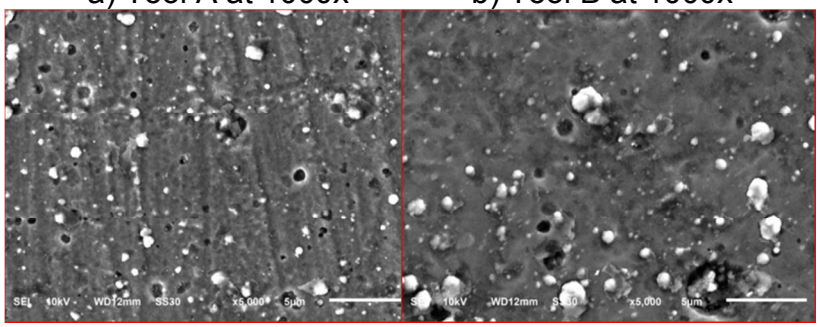

c) Tool A at 5000x d) Tool B at 5000x.

Figure 128: SEM surface images of tool surfaces

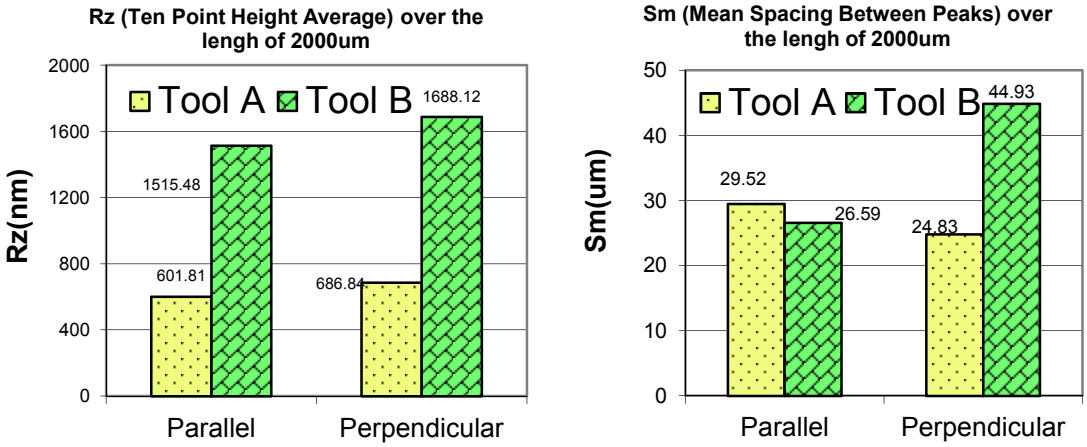

Figure 129: Roughness (R_z) and spacing parameters (S_m)

IV.4.4 Tribometer Tests

Because of the space limitations, only a few selected results are presented in this thesis to convey the effectiveness of this technology. Figure 130 depicts the friction coefficients at sliding speeds of 2 and 4 cm/sec under various loads. The friction results show that the oil in these mixtures primarily controls the friction behavior as the friction coefficients with oil and oil mixtures do not vary much. Also, no significant change in the frictional behavior can be found between nano-platelet-enhanced and micro-platelet-enhanced lubricants. As noted in Park et al. [2011], the friction behavior of the xGnP(M5)/oil mixtures did not differ much with that of the hBN/oil mixtures and did not change much compared to pure oil. With the increase in load, the friction increased slightly as shown in Figure 131. At elevated temperatures, solid lubricants are expected to provide a better lubricant performance [Allam, 1991] as expected in MQL machining.

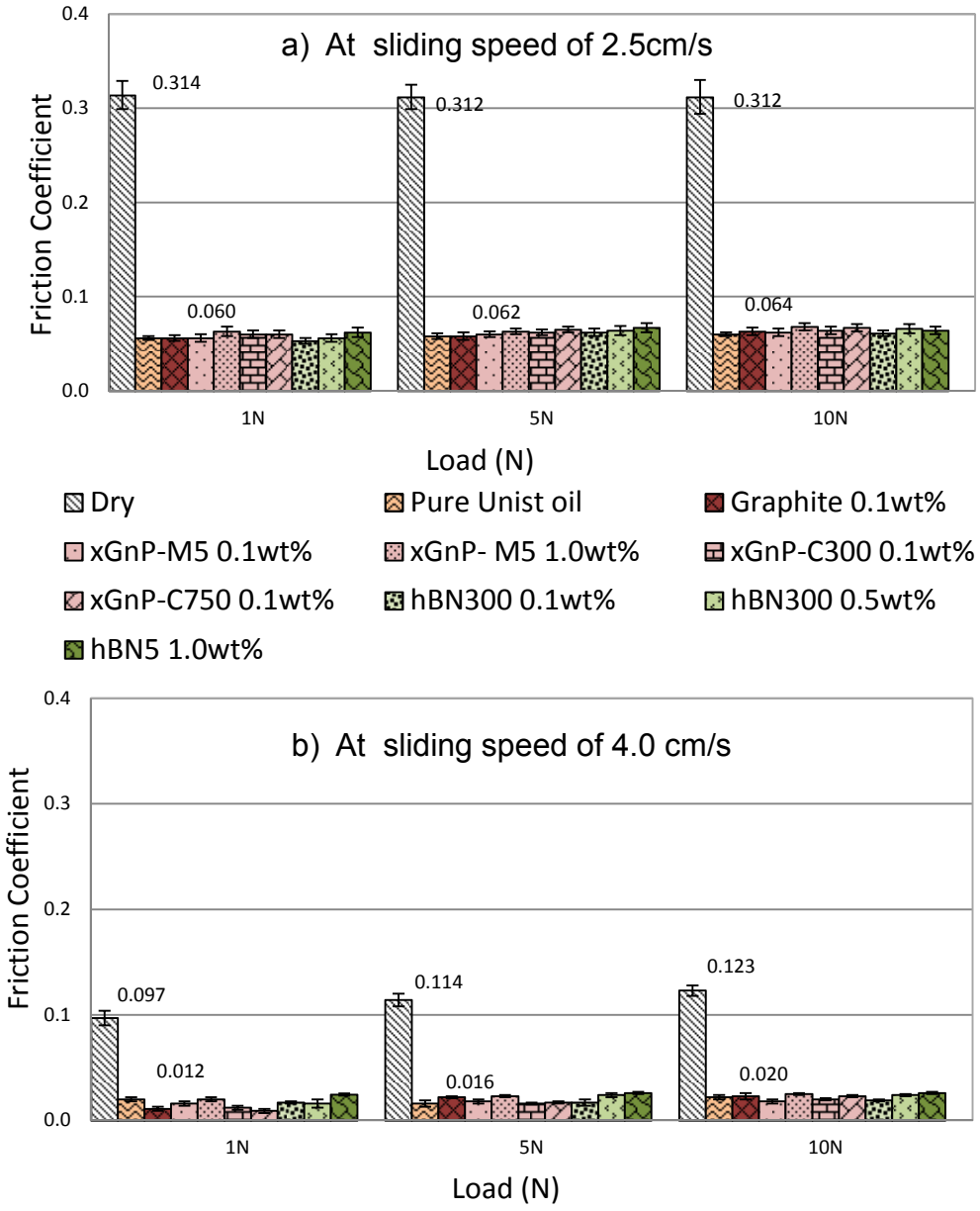

Figure 130: Friction coefficients of various mixtures on tool A

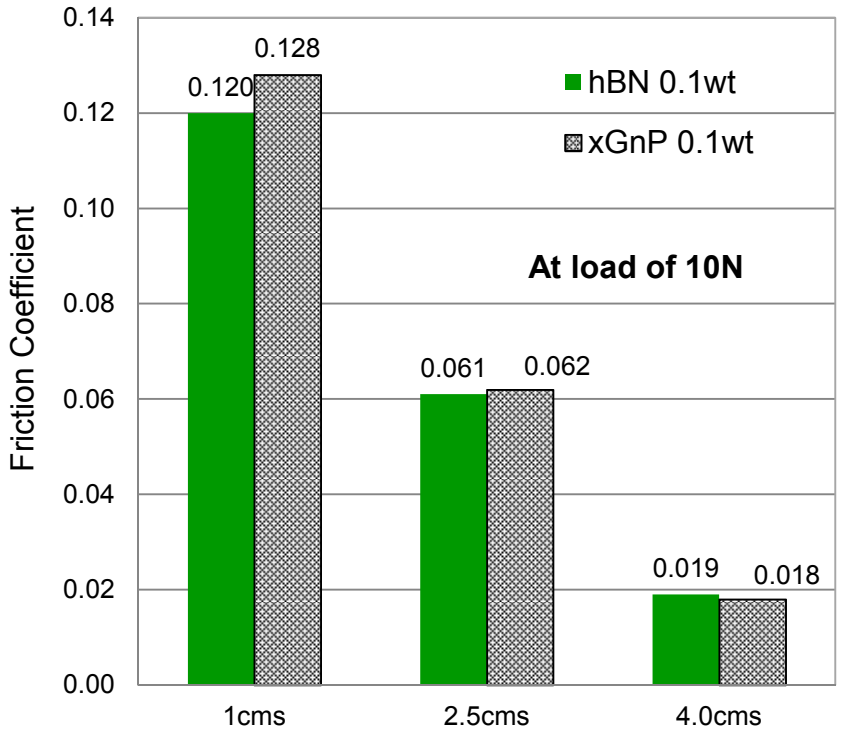

Figure 131: Friction coefficients of mixtures with xGnP (M5) and hBN300 as function of sliding speeds.

Despite the similar friction behaviors of xGnP (M5) and hBN300 enhanced lubricants, the wear behavior has been substantially improved with the hBN300 enhanced lubricants. Figure 132 shows the comparison in appearance of wear tracks between micro- and nano-platelet/oil mixtures. The comparative results in wear resistance performance between micro and nano-platelet/oil mixtures were summarized in Figures 133 - 134 where the wear depth and width were presented. The wear tracks generated with the nano-platelets mixture were smaller than those with the micro-platelets mixture in terms of both depth and width on Tool A. Among three grades of xGnP, M5, C300 and C750, the best result was obtained with C750 grade with its thickness of 1.2nm, which indicates that the thickness is an important factor. The effect is much more

pronounced on the track depth than on the track width. Because of the thickness of the nano-platelets, they can effectively cover the large area of the tool surface, which facilitate sliding in their shear planar direction between the WC ball and tool surface. On the other hand, due to its larger thickness and the associated low coverage area, the micro-platelets did not perform as well. The wear track data on Tool B showed slight improvement in wear resistance using nano-platelet mixtures compared to micro-platelet mixtures as shown in Figure 133. One common lubrication condition between Figures 133 and 134 is a mixture with nano-platelets of hBN300 at 0.5wt%. The wear depth of Tool A is one fourth that of tool B, which cannot be completely explained by the difference in surface roughness. This may be possibly due to the coating quality.

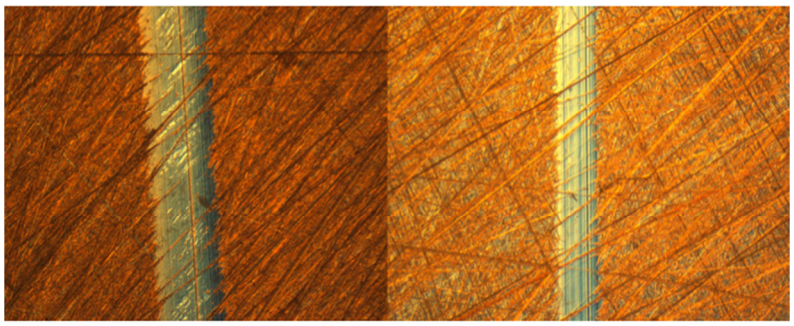

Figure 132: The wear track appearance with 0.1wt% of nano-platelets at a speed of 2.5cms and load of 10N after 35000cycles (Left: xGnP M5, Right: hBN300)

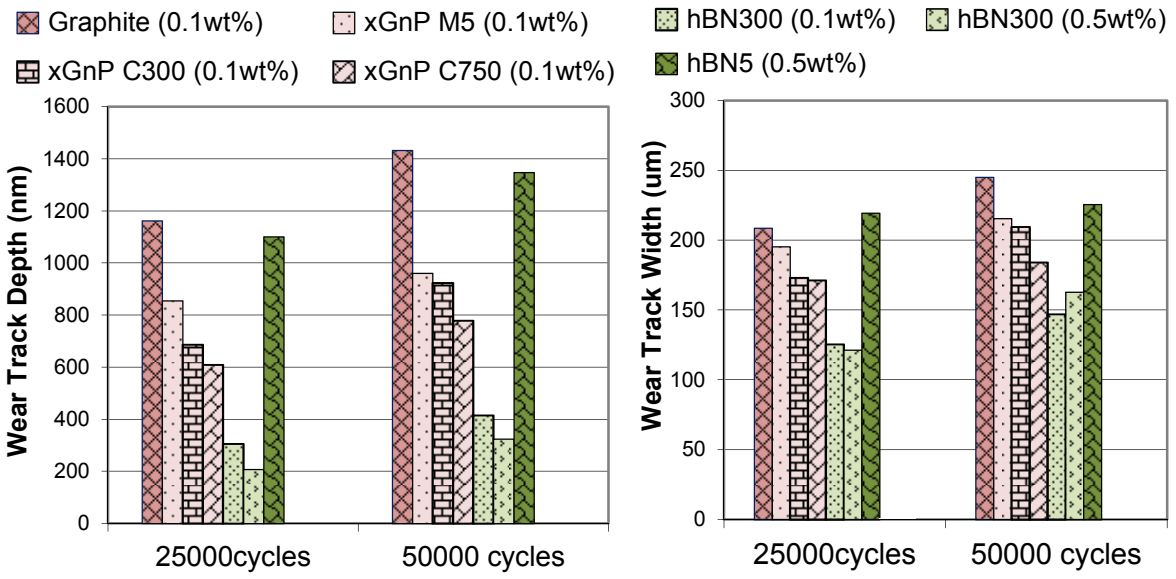

a) Depth of wear tracks b) Width of wear tracks

Figure 133: Depth and Width of wear track under various lubricant conditions on tool A (Normal load: 10N, Speed: 2.5cm/s)

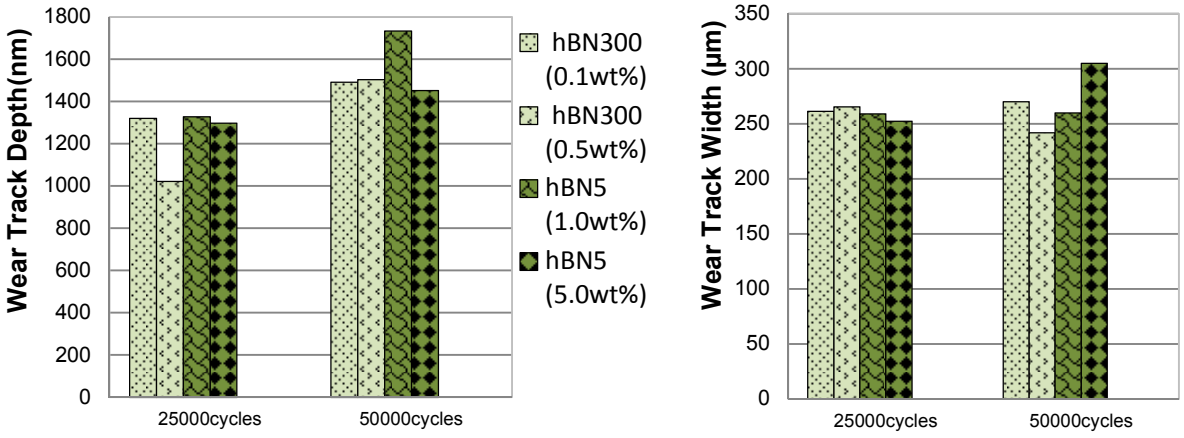

a) Depth of wear tracks b) Depth of wear tracks

Figure 134: Depth and Width of wear track under various lubricant conditions on tool B (Normal load: 10N, Speed: 2.5cm/s)

Figure 135 presents two platelets, hBN5 and xGnP M5 in relation to the surface characteristics of Tool A and B. The difference in the vertical and horizontal scales, especially for the hBN5 platelet, should be noted. The xGnP M5 is very thin compared to the surface characteristics of the tools. Only a few (1-2) hBN5 micro platelets filled in a valley on tool surface. The larger area coverage by the nano-platelets enables them to provide better lubricity and resistance to wear. Based on this primary finding, MQL ball mill tests were conducted with both Tool A and B to evaluate the performance of the nano- and micro-platelet lubricants in an experiment with MQL ball milling.

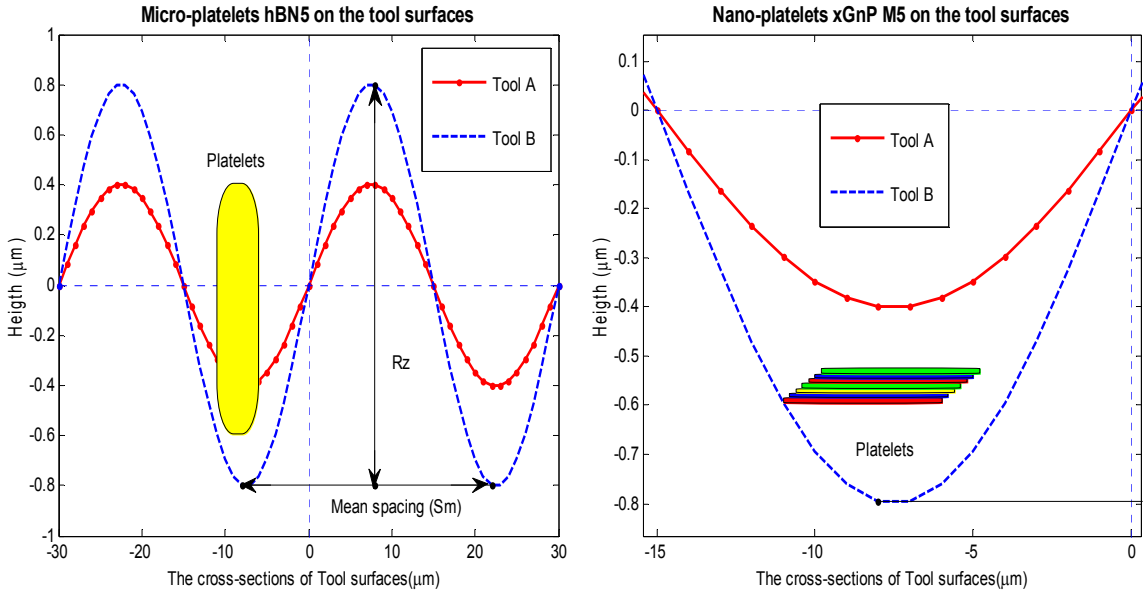

a) hBN 5 on tool b) xGnP M5 on tool surfaces

Figure 135: Geometric Relationships of micro and nano-platelets on the tool surfaces

IV.4.5 Tool Wear with Ball Milling Experiments

IV.4.5.1 Optimal MQL spray angles for ball milling

Based on the cutting geometry calculation with tool diameter and DOC, the pitch angle of 11° is the minimum angle that the oil-mist flow can access the full cutting zone

at any yaw angle as shown in Figure 136. Thus, the pitch angle was fixed at 15° and the MQL ball milling tests were conducted with Tool B to find the optimal yaw angle for our MQL experiments. The vegetable oil mixed with 1.0wt% of xGnP (M5) was used for these experiments. Various yaw angles, -30, 60, 120 and 180°, were chosen for the experiment. Figure 137 shows the resulting flank wear at various yaw angles which showed that the negative 30° yaw angle setup provided a relatively good lubrication conditions for the cutting region while the 120° yaw angle configuration showed the worst conditions. The results showed 180° is the optimal yaw angle contributing to adequate lubrication. This finding is corroborated by the geometry calculation from experiment setup with 30° and 120° yaw angle as shown in Figure 138. At 30°yaw angle, the rake face, flank face and nose were lubricated by the oil-mist during the MQL cutting process. In other words, the lubricant oil-mist was not blocked by tool as tool entered into the cutting region. Based on this finding, a pitch angle of 15° and a yaw angle of 180° were set for the MQL ball-mill tests.

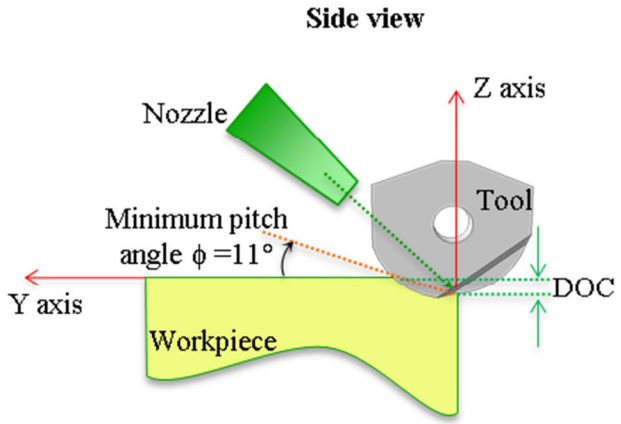

Figure 136: Minimum pitch angle of MQL nozzle for oil mist entering the cutting zone

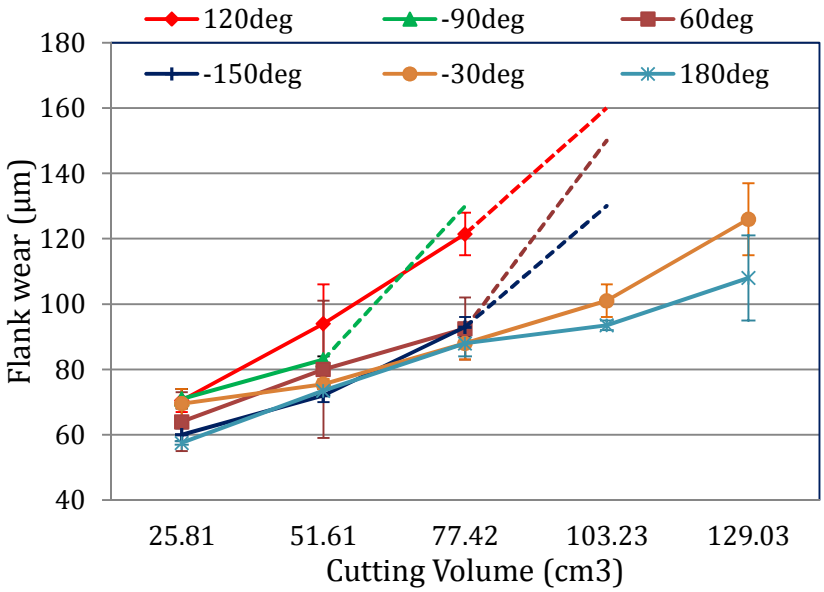

Figure 137: Flank wear at 15° pitch angle and various yaw angles with tool B (dash-line: Tool chipping)

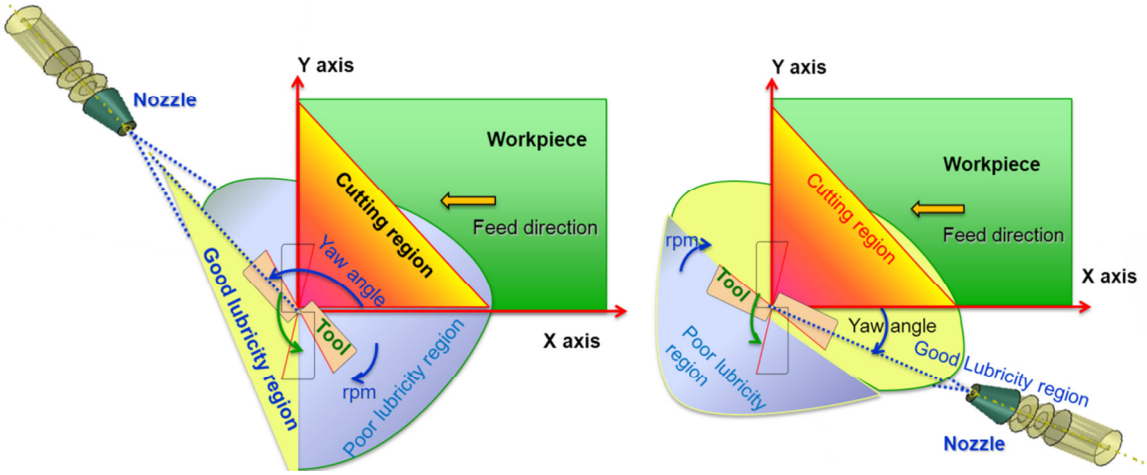

Figure 138: Top View of MQL Experiment: The distribution of lubricant at 120° and -30° yaw angle

IV.4.5.2 Effectiveness of thickness and diameter of platelets to tool wear

A series of MQL ball-milling tests was carried out on AISI 1045 steel with the vegetable oil mixed with nano- and micro-platelets to study the effects of the thickness on the wear performance. The lubrication conditions include pure vegetable oil, vegetable oil mixed with micro-platelet additives (0.1wt% of graphite, 0.5 and 5.0wt% of

hBN5) and vegetable oil mixed with nano-platelet additives (0.1 and 1.0 wt% of xGnP M5, xGnP C300 and xGnP C750 and 0.5wt% of hBN300) used with Tool A and B. Figures 139-140 showed nose wear and flank wear at various lubrication conditions. In appearances, the nose wear and flank wear with MQL mixtures were much lower than those of dry machining. Due to nose of the insert being in contact with the workpiece during the cutting process and not exposed to MQL oil mist, the improvement in nose wear of MQL mixtures with nano-platelets to MQL with pure oil was not significant and consistent as summarized in Figure 141. To help discussion on flank wear without too much information, Figure 142 for Tool A and Figure 143 for Tool B present some of the flank wear results.

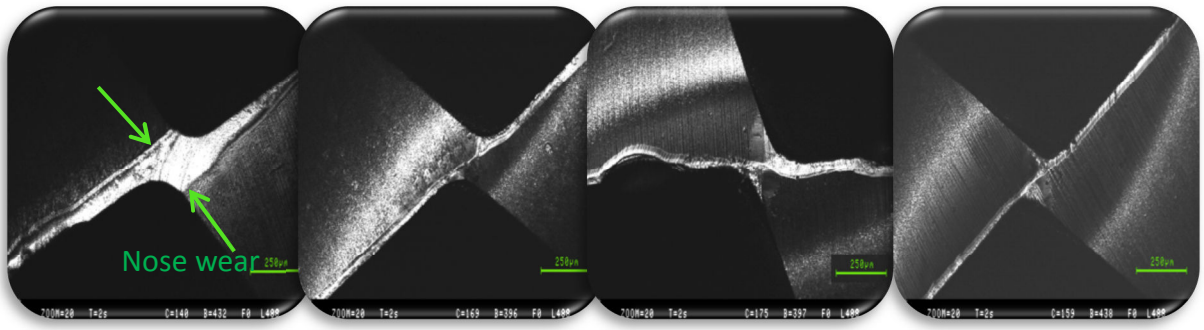

a) Dry b) 0.1wt% xGnP M5 c) 0.1 wt% hBN300 d) 0.5 wt% hBN300

Figure 139: Central wear with MQL nano-platelet enhanced mixtures after milling 3 layers

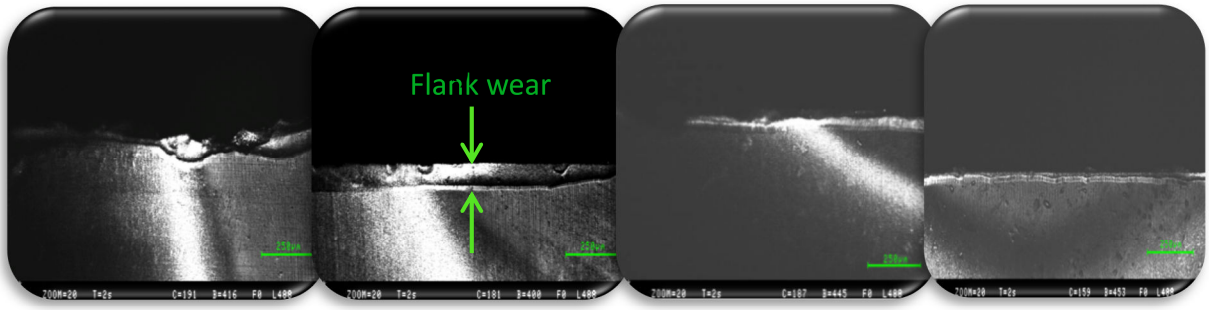

a) Dry b) 0.1wt% xGnP M5 c) 0.1 wt% hBN300 d) 0.5 wt% hBN300

Figure 140: Flank wear after milling 6 layers.

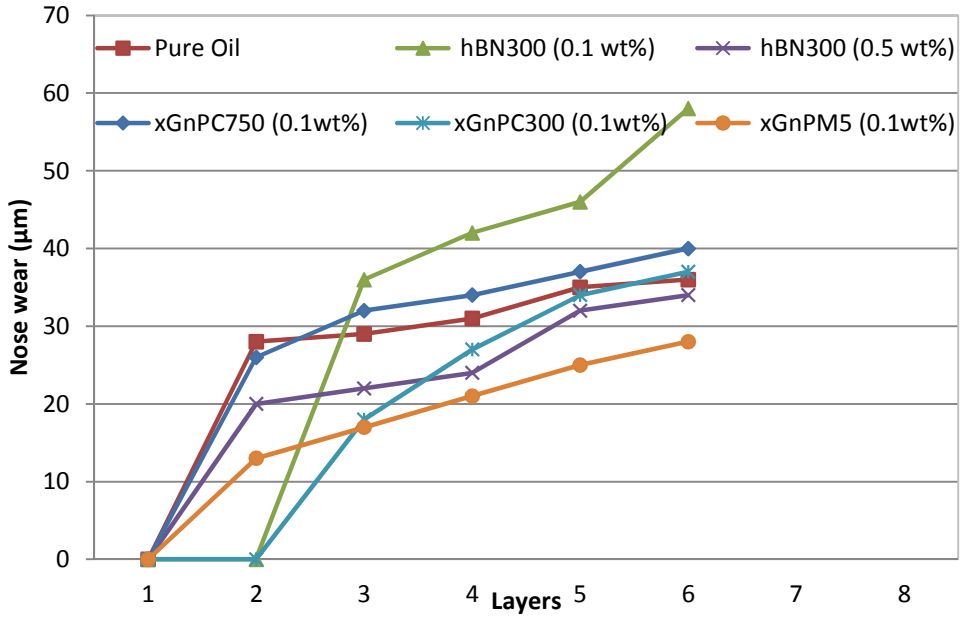

Figure 141: Nose wear at 3500 rpm after ball milling six layers with tool A

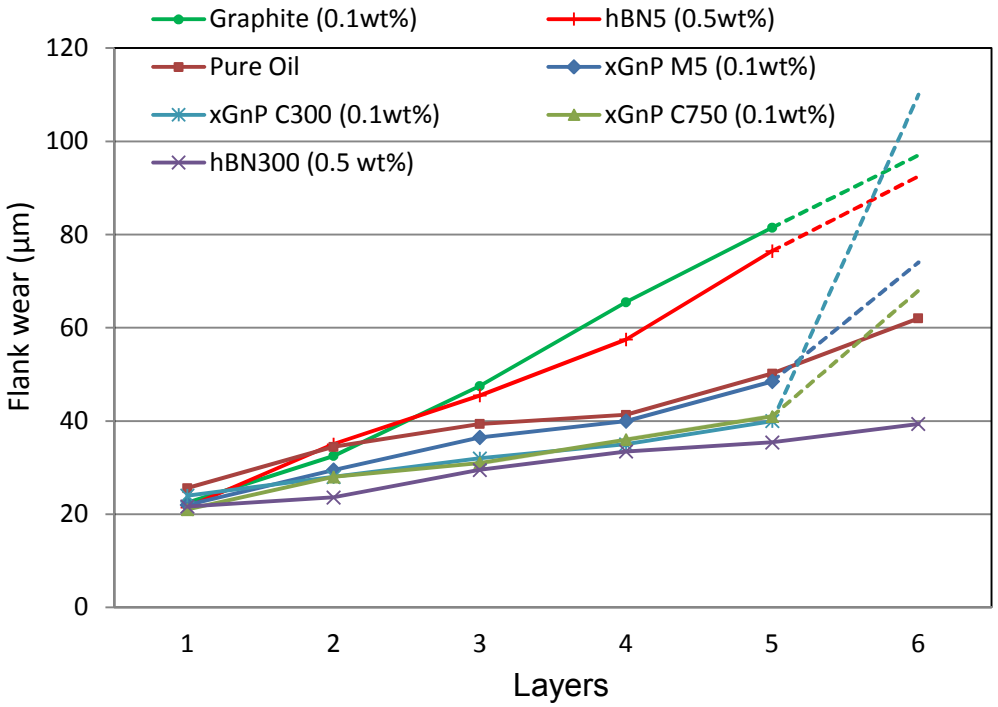

Figure 142: Flank Wear at 3500rpm after ball milling six layers with tool A (dash-line: Tool chipping)

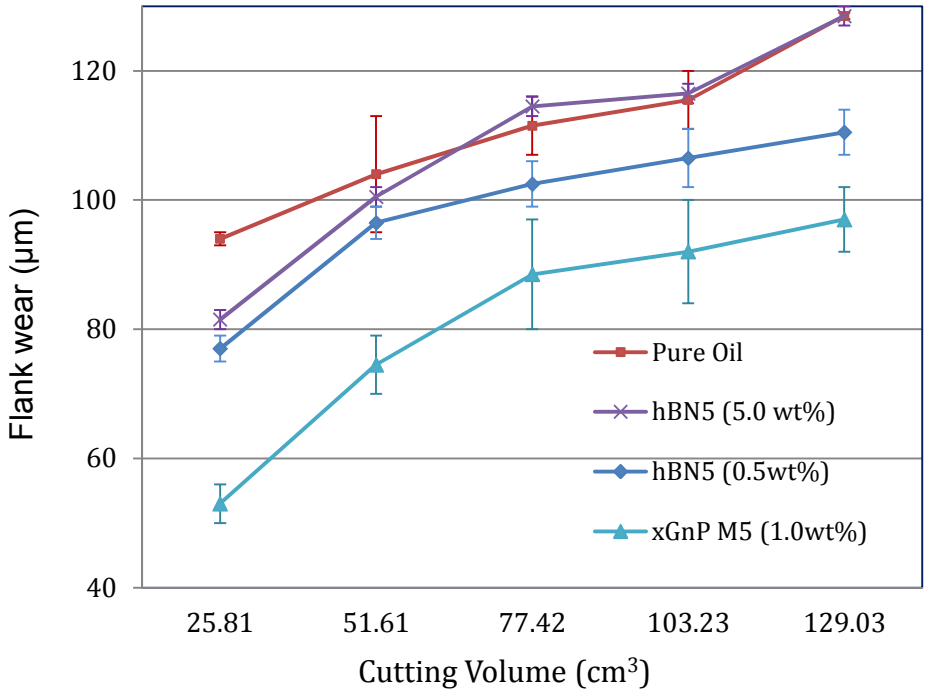

Figure 143: Flank Wear at 3500 rpm after ball milling six layers with tool B

The micro-platelet enhanced lubricants increased tool wear than pure oil lubricant (traditional MQL), exposing the ineffectiveness of the micro-platelets. Comparing three xGnP grades, M5, C300 and C750, The flank wear with both C300 and C750 grades, despite chipping after cutting 5 layers, was reduced much more than M5. The flank wear with M5 was at the level of pure oil. Similarly, the comparison between hBN5 (micro-platelet) and hBN300 (nano-platelet) also indicates the importance of the nano-scale thickness. The MQL-ball mill experiments with nano-platelet enhanced lubricants performed better than pure oil lubricants (traditional MQL).

Chapter 5: Tool wear improvement in machining of Ti64 with nano-platelets enhanced MQL

From the previous chapter (or Chapter 4), the thickness of both graphite and hBN need to be in nano scale in order to be effective in MQL. Obviously, the cutting conditions in machining Ti64 are more aggressive with higher cutting forces and temperatures than machining steel AISI1045. The nano-platelet enhanced lubricant found to be very effective in machining steel AISI1045 may not be effective. In this chapter, thus, the performance of MQL with xGnP C750, which performed the best among xGnP grade with steel AISI1045, was evaluated in machining Ti64. The performance of the lubricant mixed with nano xGnP C750 could be better for crater wear where TiC reaction layer act as a barrier to dissolution and diffusion of tool in the chip. These wear mechanisms may not be operating in flank wear, which is more critical in milling.

V.1 EXPERIMENTAL SETUP AND PROCEDURES

V.1.1 Ball Milling Experiments with Ti64

The MQL ball-milling setup with Ti64 was the same as that with AISI 1045 steel as shown in Figure 125. The 25mm diameter end ball-nose TiAlN coated carbide inserts (Tool B) were used for tool materials. The Ti workpiece was TIMETAL® Ti64 block (203.2mm×101.6mm×203.2mm) from Titanium Metals Corporation (Tomroto, OH), whose ingot chemical analysis of the Ti64 sample is shown in Table 23. In the experiment, the cutting speeds were set at 2500 rpm and 3500 rpm. The feed rate and the radial depth of cutting (ROC) were kept constant at 2500mm/min and 0.6mm,

respectively. Due to the poor machinability of Ti64, the depth of cut (DOC) was set at 0.5mm, which is a half of the DOC used in milling of AISI 1045 steel. The machining conditions for Ti64 are summarized in Table 24. The status of tool wear was captured after cutting each layer (203.2mm×101.6mm) (170 lines of cutting for each layer) to record the progress of tool wear. The maximum of cutting layer was set at 8 layers. The milling was conducted at different lubrication conditions: dry, pure MQL oil and MQL oil enhanced with nano-platelets xGnP C750. To study mainly the steady stated wear with minimized effect of chipping and fracture in our analysis, the insert was considered broken if the chipping and fracture were larger than twice of the average of flank wear width.

Table 23: Ingot chemical analysis of Ti64 work material

	Fe	V	Al	C	O	N	Y
Top	0.15	4.00	6.23	0.025	0.18	0.008	<0.0005
Bottom	0.16	3.89	6.19	0.026	0.19	0.008	<0.0005

Table 24: Machining conditions for Ti64

Tool	25mm diameter end ball-nose TiAlN coated carbide inserts (Tool B)
Feed Rate	2500 mm/min
Axial DOC	0.5mm
Radial DOC	0.6 mm
Cutting Speed	2500 rpm (55 m/min) 3500rpm (77m/min)
Lubricants	Dry, MQL oil Nano-platelets xGnP enhanced MQL oil at 0.1, 1, and 5wt%
MQL spray parameter	Pitch angle: 15° Yaw angle: 180° Outlet pressure: 8 psi Flow rate: 1.5ml/min

V.1.2 Tool wear measurements

Because chipping and tool fracture are common in machining of titanium alloys, flank wear is characterized by capturing four areas,VB_1, VB_2, VB_3, VB_4 of the cutting edges, as shown in Figure 144. Seven data points were taken for the flank wear width on each area as shown in Figure 145. The maximum and average values of the flank wear width (VB_{max}, VB_{avg}) are reported based on a total of 28 data points.

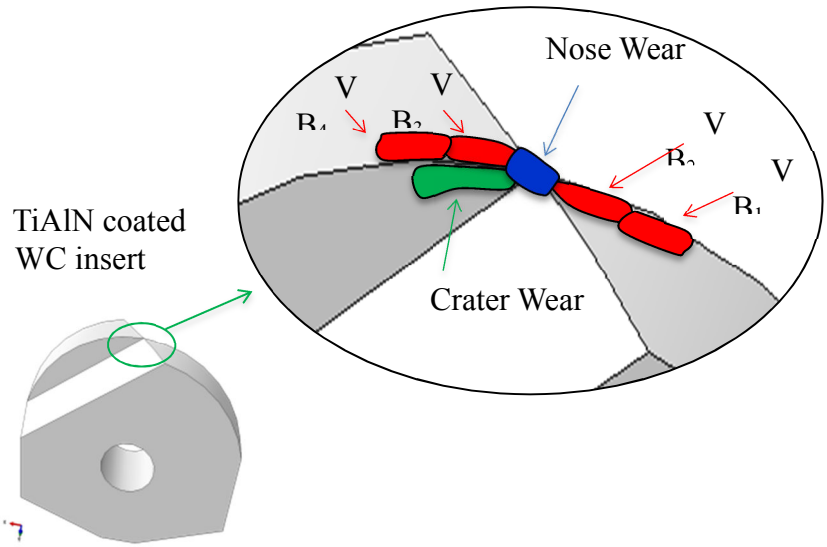

Figure 144: Types of tool wear were measured on end-ball nose inserts

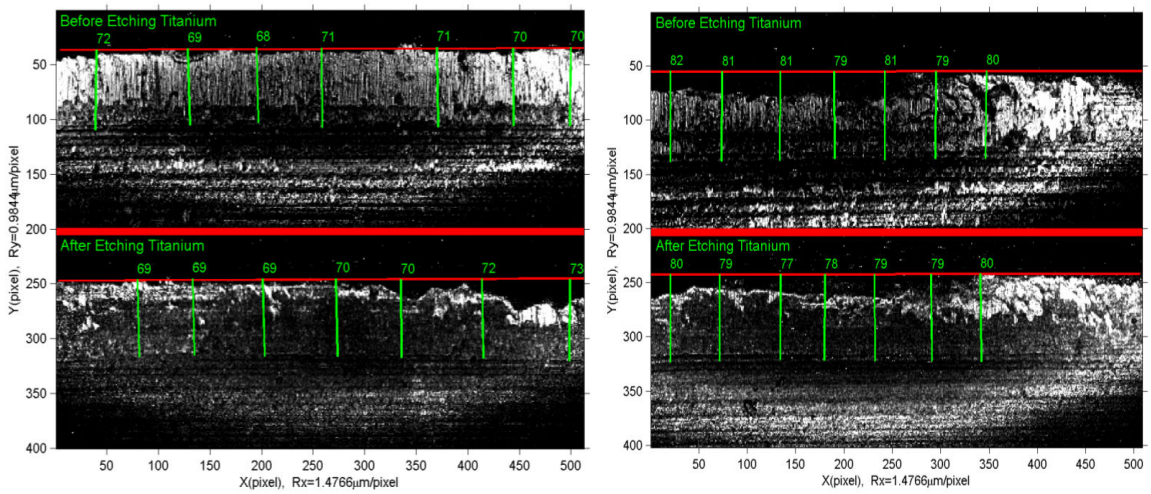

Figure 145: The flank wear measurement in a) VB_2 and b) VB_1 on the cutting edge before and after etching the adhesion layer of titanium.

V.2 EXPERIMENTAL RESULTS AND DISCUSSION

V.2.1 Flank wear and chipping on cutting edges

V.2.1.1 Flank wear at low cutting speed (2500rpm)

As expected, the milling inserts used in MQL conditions cut more layers than under dry conditions. Figures 146-149 presents the flank wear at VB_1 on the inserts after cutting the 1^{st} to 8^{th} layers under each lubrication condition at a cutting speed of 2500rpm. The maximum flank wear's width, VB_{max}, and the average values of the flank wear widths, VB_{avg} are summarized in Figures 150 and 151. The MQL mixture with 1wt% of xGnP C750 is the best followed by the mixture with 0.1wt% of xGnP C750. In the case of dry machining, the flank wear was not even due to the numerous chippings and tool fractures. Consequently, the insert was only able to cut 5 layers. The flank wear was more uniform when using the MQL mixture with 1wt% of xGnP C750. Only a few minor chippings at the cutting edge were present with pure oil and the mixture with 0.1wt% of xGnP C750. Therefore, a certain concentration of nano-platelets of xGnP are needed to substantially reduce both flank wear and chipping on the tool. In steady state wear (VB_{avg}), the mixture with 1wt% of xGnP C750 was most effective, which yielded 15% and 25% reduction in flank wear after cutting 5 layers. More importantly, machining was stopped before reaching the life of each insert.

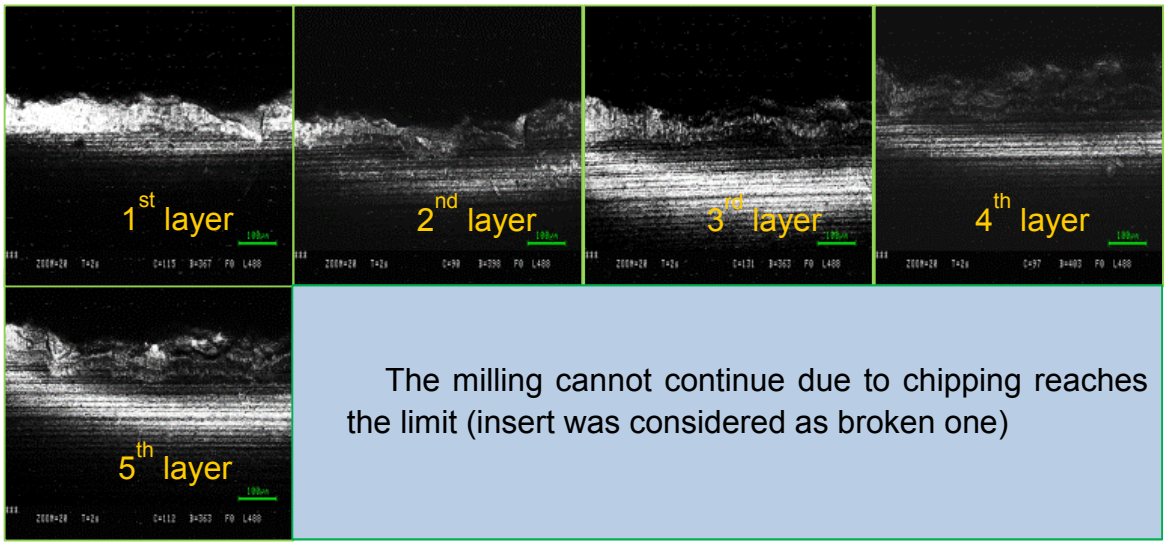

Figure 146: The flanks wear in VB_1 on insert with Dry at 2500rpm.

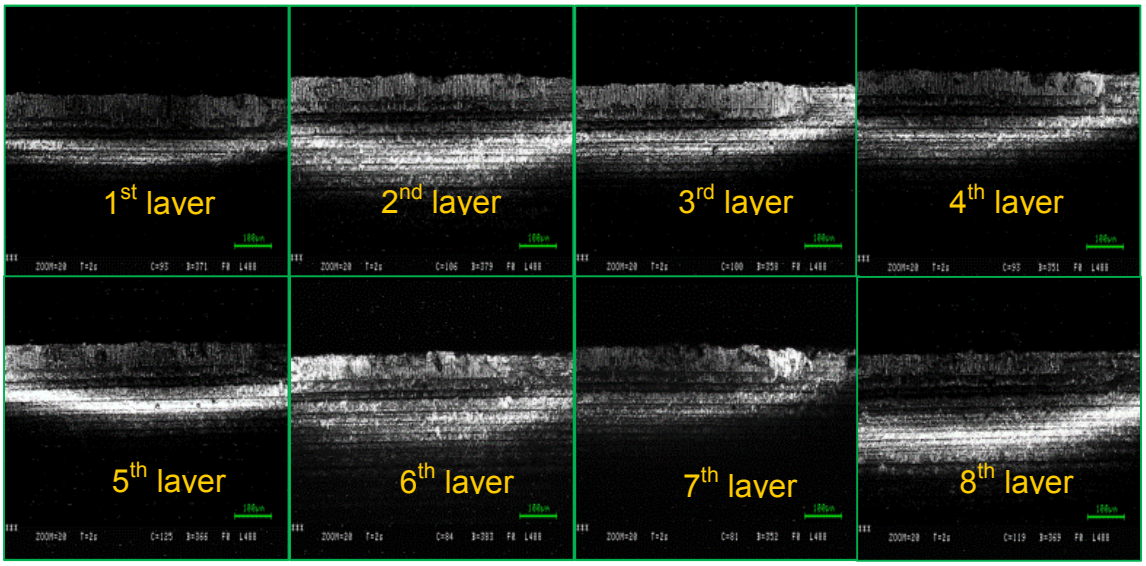

Figure 147: The flank wear in VB_1 on the insert with pure Unist oil at 2500rpm.

In [Park, 2011], the optimum concentration of xGnP platelets was 0.1wt% in machining of AISI 1045 steel. The higher concentration, 1wt%, did not perform as well as. In the machining experiment with Ti alloys, 1.0wt% is the optimum weight content for at a cutting speed of 2500rpm. The optimum concentration may be affected by the dimensions of xGnP platelets and the surface quality of the tool.

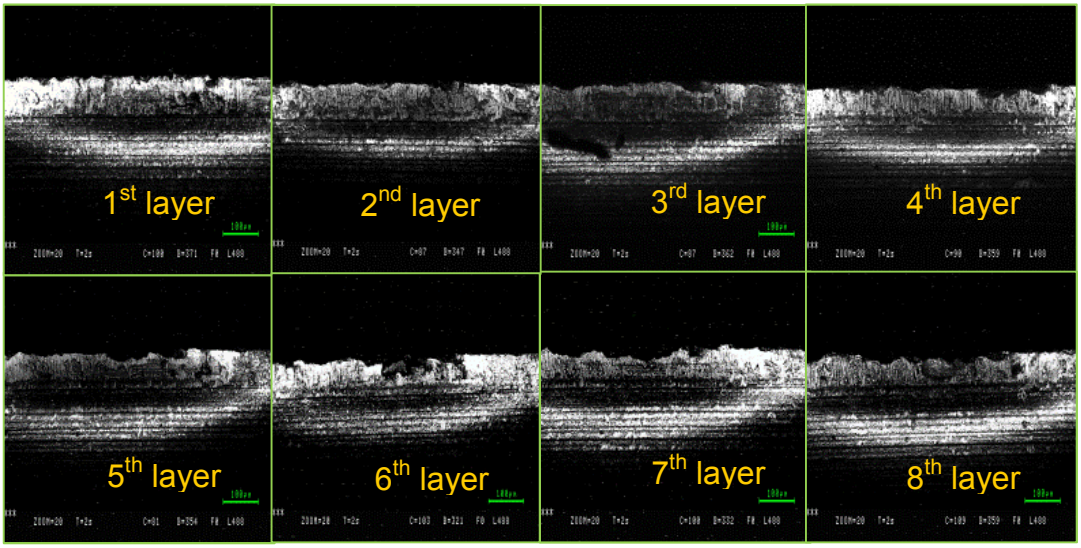

Figure 148: The flank wear in VB_1 on insert with xGnP C750 0.1wt% at 2500rpm.

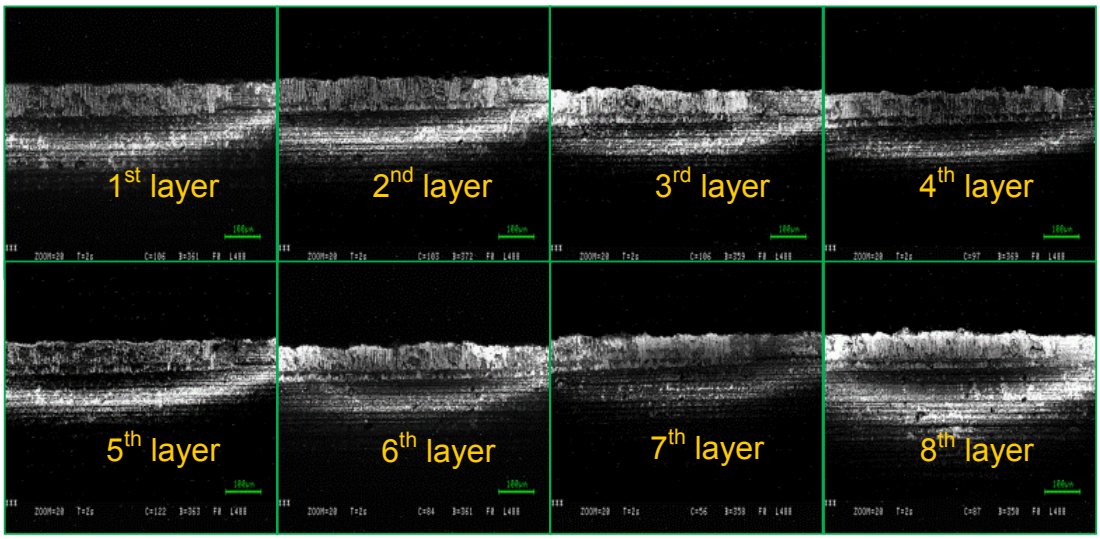

Figure 149: The flank wear in VB_1 on insert with xGnP C750 1wt% at 2500rpm.

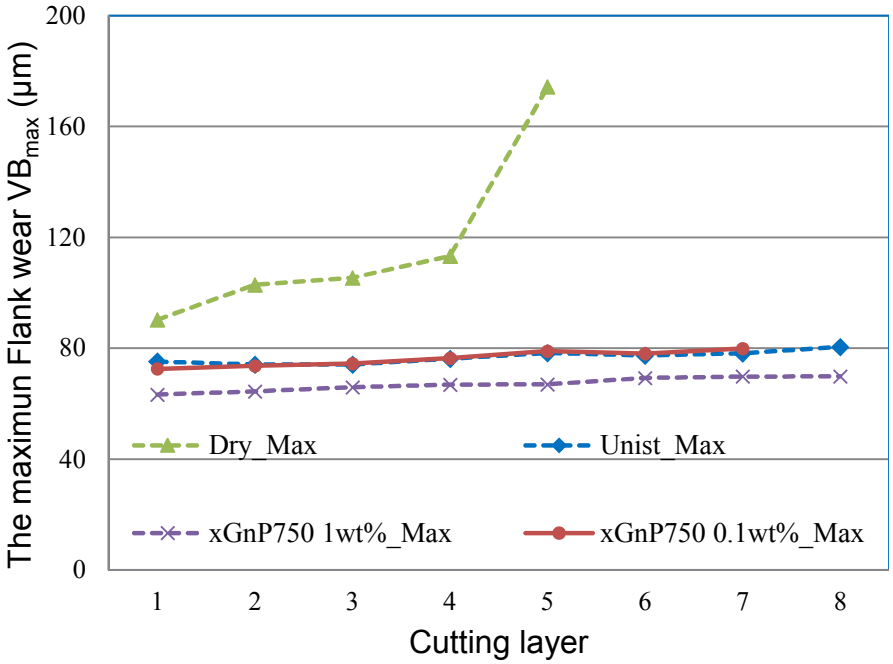

Figure 150: Maximum flank wear with (VB_{max}) at 2500rpm (after etching)

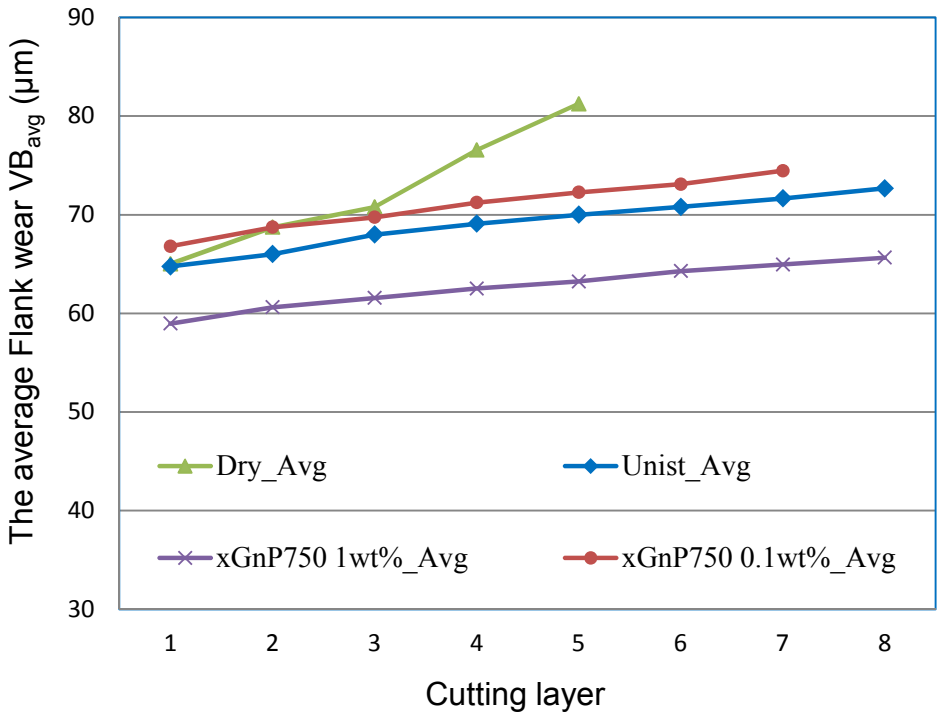

Figure 151: The average flank wear width (VB_{avg}) at 2500rpm (after etching)

V.2.1.2 Flank wear at high cutting speed (3500rpm)

As shown in Figures 152 and 153, the enhancement of MQL solution is not as pronounced because of the chipping under high impact conditions. It is important to note that chipping occurred substantially more when cutting of the first few layers. The higher concentration (5wt%) of xGnP nano-platelets was tested with an expectation of more lubricity and/or damping due to more xGnP platelets in the lubricant. However, the experimental results did not agree with the expectation. Among the MQL mixtures, the mixture with 1wt % of xGnP C750 is the best followed by dry, Unist oil and 5wt% as shown Figures 15 and 16. The reason why enhanced MQL solution at 5wt% did not perform well is not clear at this time. It could be the poor wettability with the tool surfaces or, the hindrance of the sliding actions at the high concentrations.

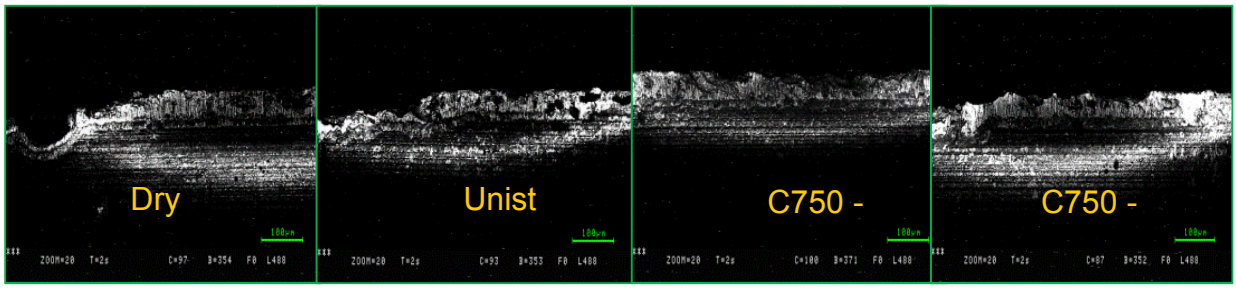

Figure 152: The flank wear in VB_1 after 1st layer with different lubrication conditions at 3500rpm.

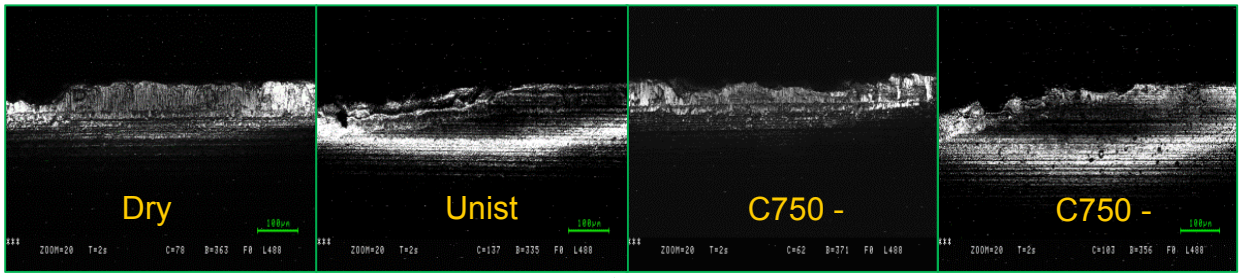

Figure 153: The flank wear in VB_1 after 2st layer with different lubrication conditions at 3500rpm.

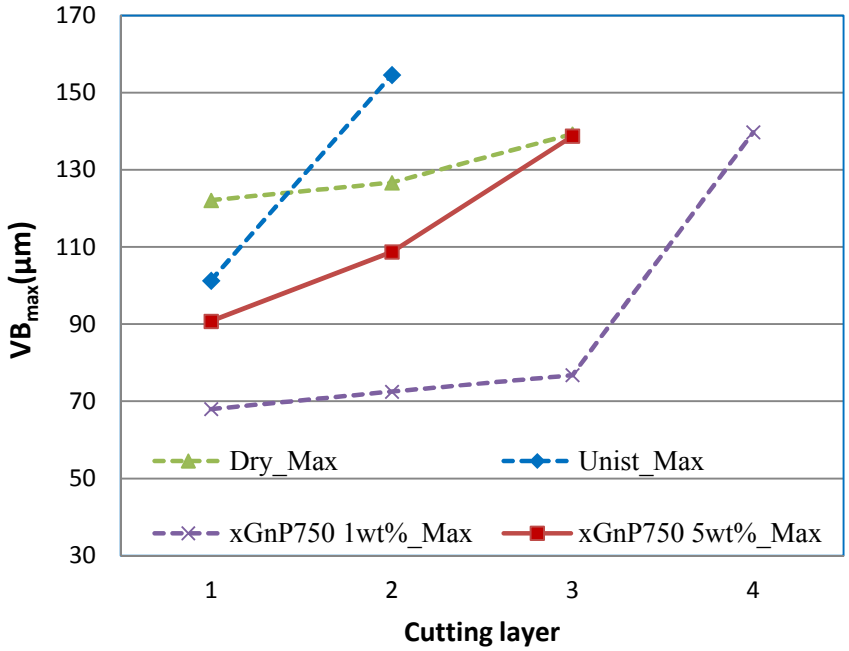

Figure 154: Maximum flank wear width (VB_{max}) at 3500rpm (after etching)

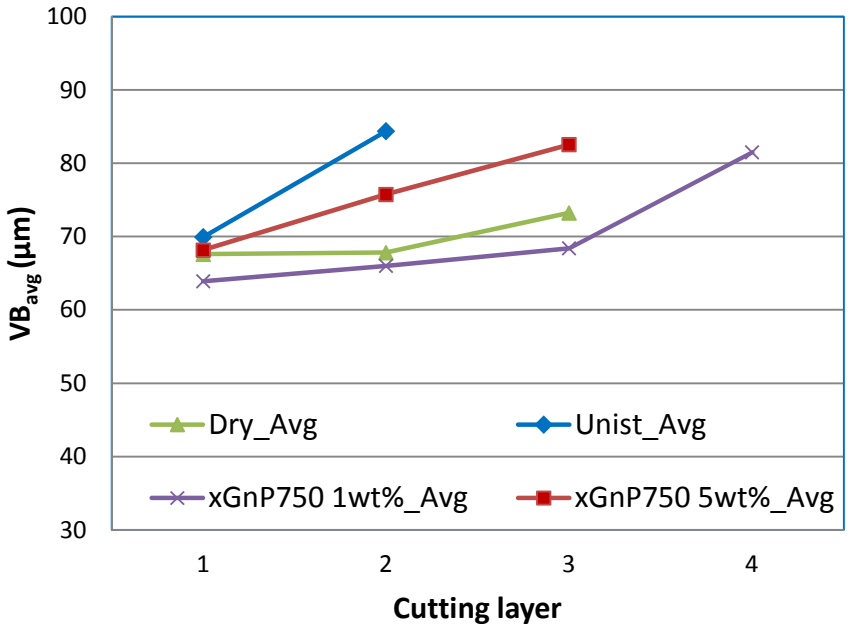

Figure 155: The average flank wear width (VB_{avg}) at 3500rpm (after etching)

V.2.1.3 Micro-chipping and tool fracture

Chipping and tool fracture are the common modes of tool damage in machining Ti alloys. Especially for the consistently interrupted cutting process of milling, the tool experiences high stress cycles and high impact leading to the cutting edges being chipped frequently. In this work, the tool damage were classified into two categories: micro-chipping and fracture, as shown in Figure 156. The elliptical shape represents micro-chipping while the rectangular shape represents fracture. They were distinguished based on the size; micro-chippings if the size was smaller than half of the average flank wear width and tool fractures otherwise. To be more confident, the type of chipping was evaluated based on the images from the flank face and the rake face. At the low cutting speed, the MQL solutions (pure oil and the mixture with nano-platelets) helped to reduce micro-chipping and prevent the propagation of micro-chipping into tool fractures. Figures 157 and 158 represent the cutting layer on which the first damage occurred at the cutting speeds of 2500rpm and 3550rpm, respectively, for various lubrication conditions. The largest damage on tools under various lubrications was presented in Figures 159 and 160 for cutting speeds of 2500rpm and 3550rpm respectively. At low cutting speed, the tool fractures occurred at the first cutting layer with dry milling while only micro-chippings were found with MQL mixtures even after cutting 8th layers. At the cutting speed of 3500rpm, due to the high impact condition, both micro-chippings and tool fractures occurred even with the MQL conditions. Tool fractures happened after cutting only one layer under dry condition were more severe than those under MQL mixtures which occurred after cutting 3-4 layers. The higher

concentration of nano-platelets did not help to reduce chipping. The concentration of 1wt% outperformed the others in preventing tool damage.

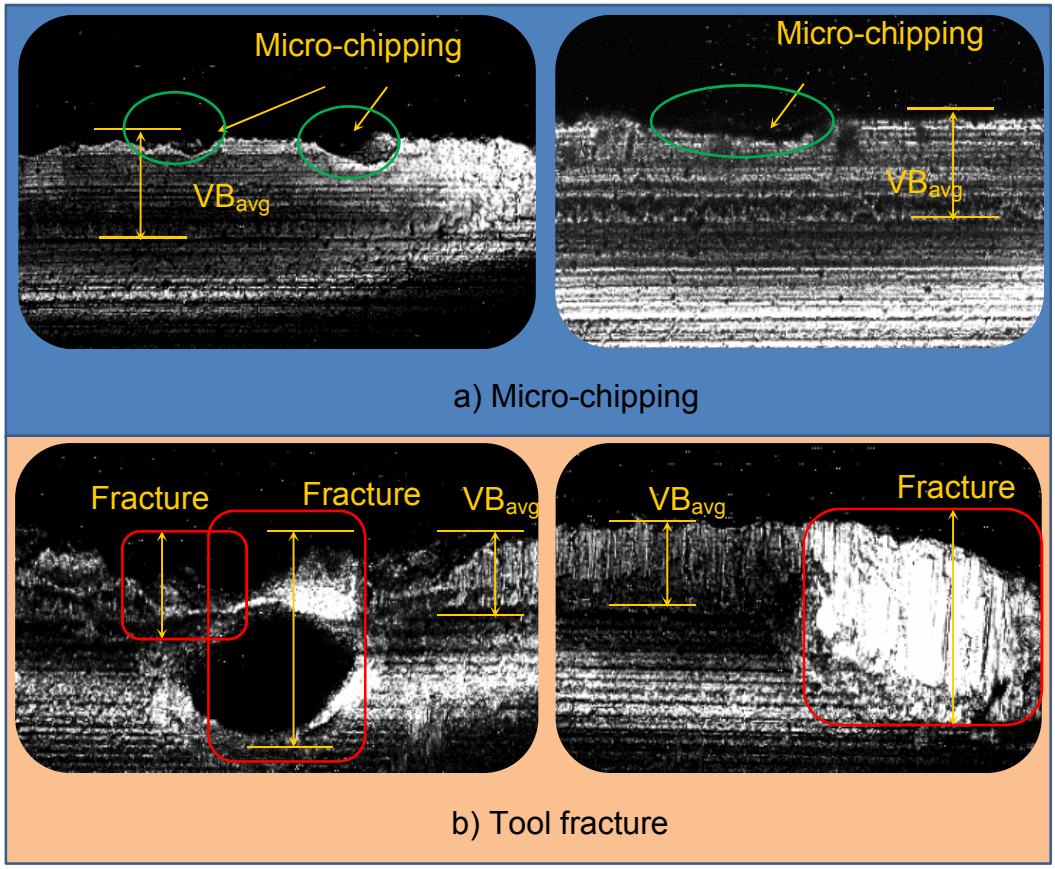

Figure 156: Types of tool damage on ball nose end mill insert.

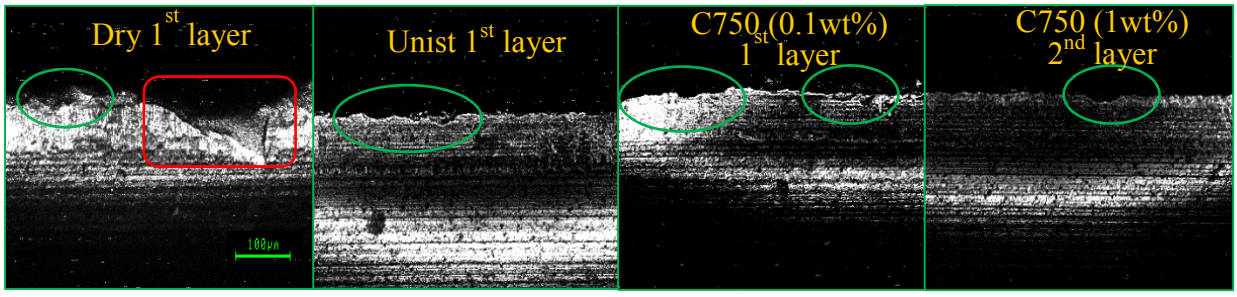

Figure 157: The first damage at the cutting edge with different lubrication conditions at 2500rpm.

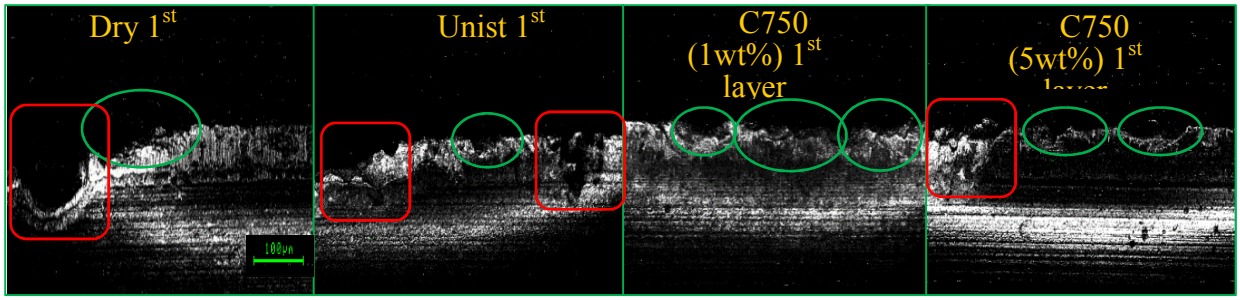

Figure 158: The first damage at the cutting edge under various lubrication conditions at 3500rpm.

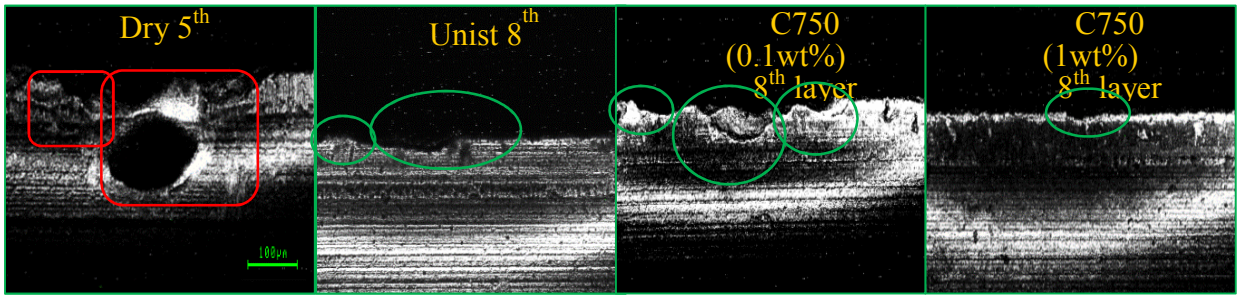

Figure 159: The largest damage at the cutting edge under various lubrication conditions at 2500rpm.

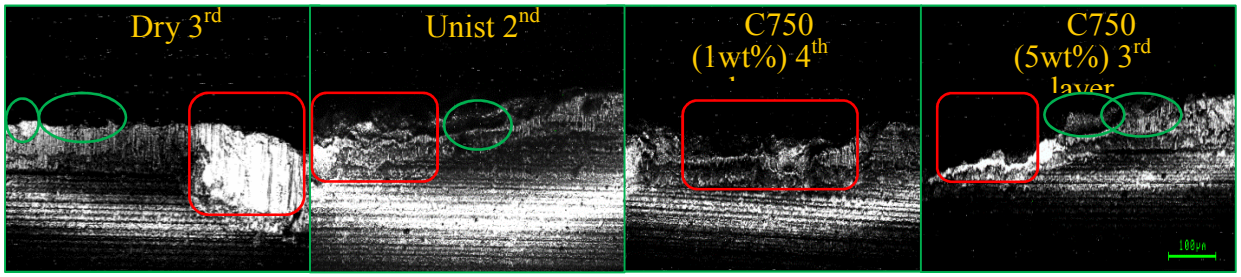

Figure 160: The largest damage at the cutting edge with different lubrication conditions at 3500rpm.

V.2.2 Nose wear of insert

The cutting speed at the nose of the insert is very low due to the small effective diameter (represented by De shown in Figure 161). Furthermore, the nose of the insert being in contact with the workpiece during the cutting process is the least lubricated region by the MQL oils in the contact zone. As expected, the effectiveness of MQL mixture on nose wear was not significant as on flank and rake face. Figure 162 and

Figure 163 present the center wear under certain lubrication conditions for low and high cutting speeds, respectively. At low cutting speed, the nose wear under dry cutting was higher than those MQL pure oil and MQL mixtures with xGnP C750. However, the outperformance of MQL lubrication conditions to dry was reduced as high cutting speeds increased.

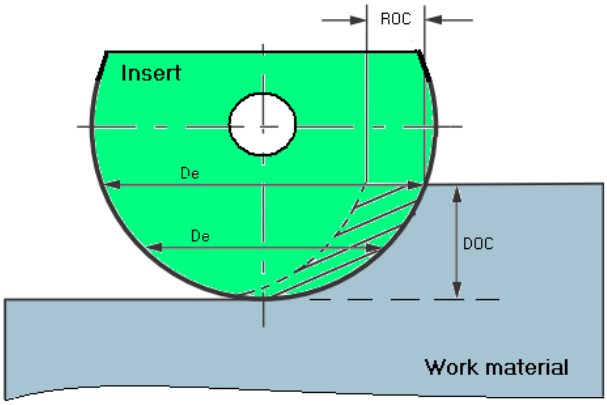

Figure 161: The effective diameter of the cut, De, for ball-nose end-mill insert

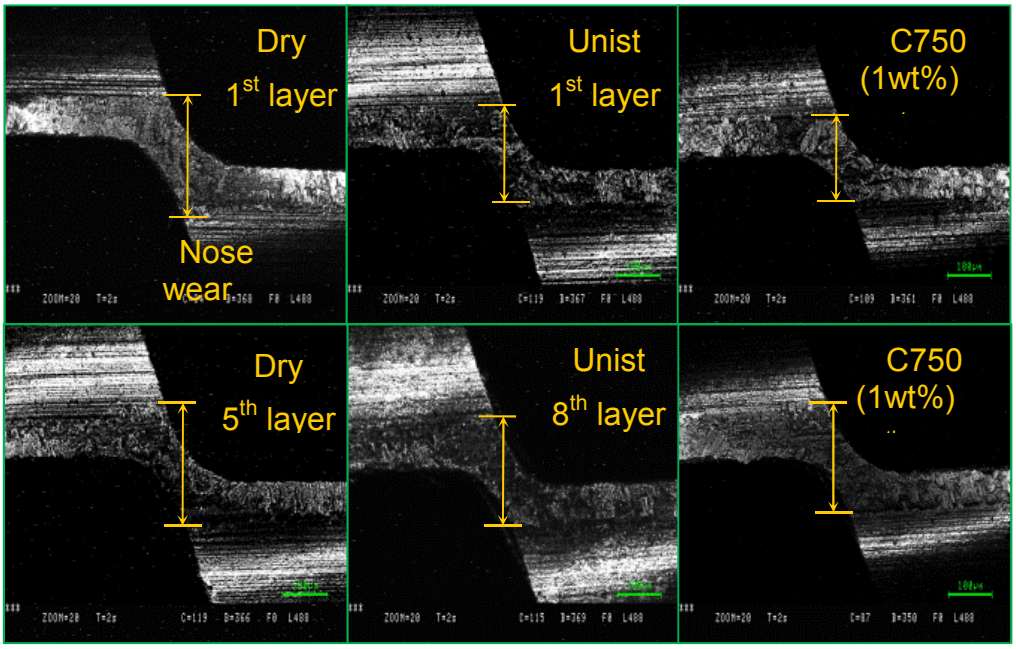

Figure 162: The nose wear at the first and the last cutting layer under different lubrication conditions at 2500rpm.

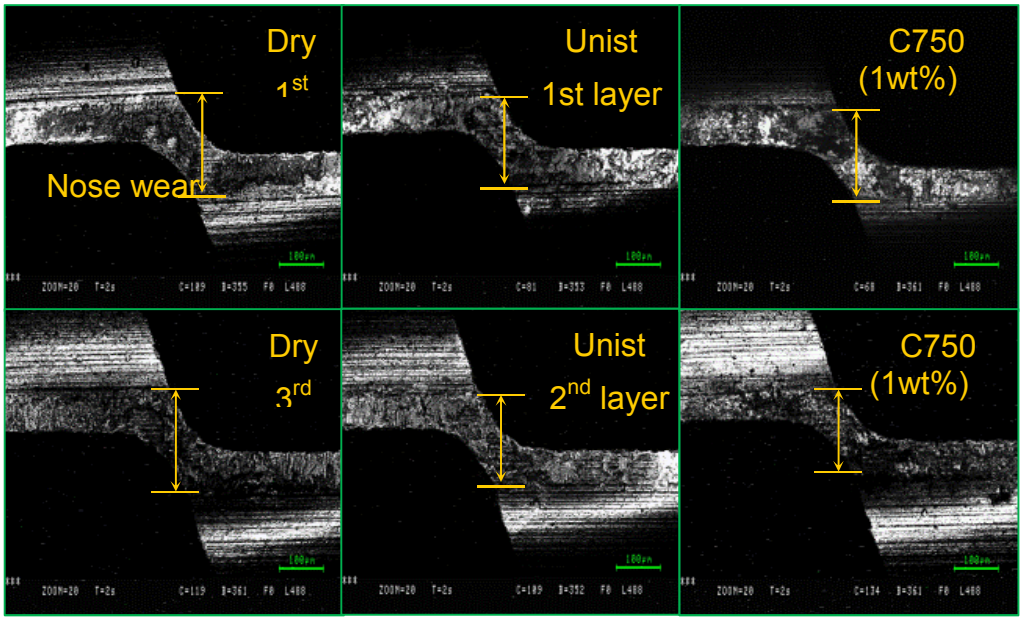

Figure 163: The nose wear at the first and the last cutting layer under different lubrication conditions at 3500rpm.

V.2.3 Crater wear

In the milling process, the rake face of the tools did not experience the dramatic wear unlike those in turning. In the milling experiment, only slight wear with a thin adhesion layer was observed in the rake face of the inserts under all lubrication conditions. Therefore, the MQL solution does not affect the rake face. The chipping at the cutting edge had a more significant impact on the rake face than on the crater wear as shown in Figures 164 and 165 for cutting speeds of 2500rpm and 3500rpm, respectively. Fracture at the cutting edge was more frequent and larger in dry condition than the MQL conditions at both low and high cutting speeds. Among MQL conditions, the lubricant enhanced by nano-platelets helps to reduce the chipping at the cutting edge. The low crater wear revealed the deformation of the tool is not as severe as in turning. A reason for low crater wear is the cutting temperatures in milling were fairly lower than those in

turning which limited dissolution/diffusion. The abrasion of chip to rake face was less compared with turning due to discontinuous chip in milling. In milling of Ti64 at low cutting speed, cooling is not as critical as lubrication, which enhances the effectiveness of MQL.

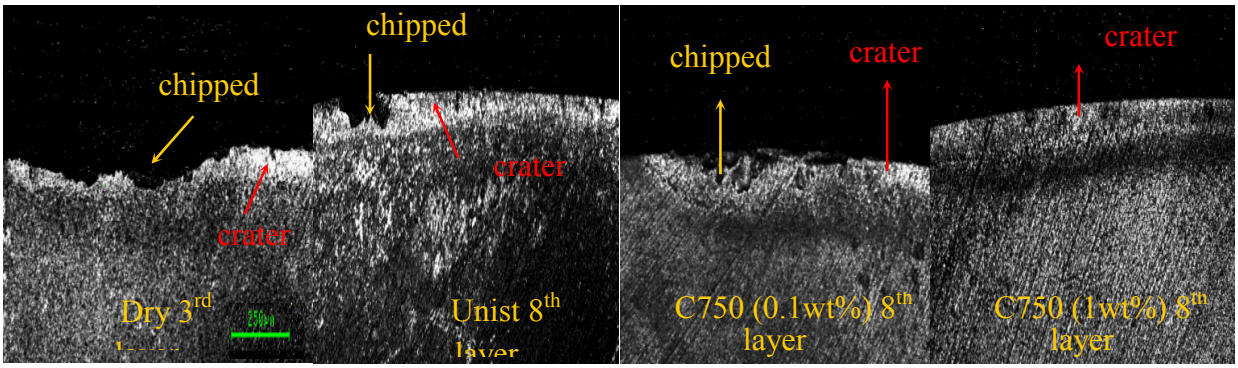

Figure 164: The crater wear and damage on the tool at the last cutting layer with different lubrication conditions at 2500rpm.

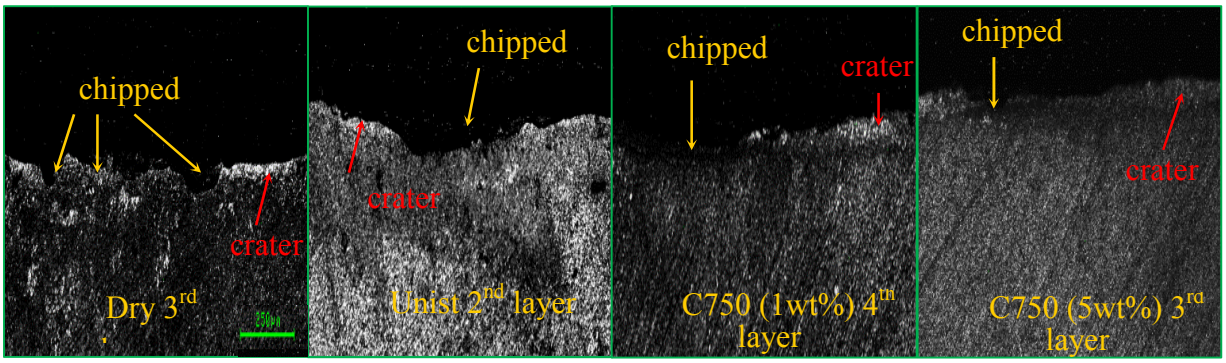

Figure 165: The crater wear and damage on the tool at the last cutting layer with different lubrication conditions at 3500rpm.

Chapter 6: Conclusions

In the turning experiment of Ti64 with carbide and PCD inserts, the dissolution/diffusion wear is the dominant wear mechanism on the rake face of carbide insert while grain-pulled out is the main mode of tool wear on rake face of PCD insert. These conclusions are corroborated by the smooth craters found on carbide inserts and the rough and uneven crater on PCD inserts. Because the crater wear started away from the cutting edge and progressed rapidly to cutting edge on carbide inserts, tool fracture on cutting edge was more excessive than the PCD inserts. The cutting edge on PCD inserts was intact, which enable them to have longer tool lives. Abrasion by the hard α-clusters and tool fractures were the main causes for flank wear on both carbide and PCD inserts. At the high cutting speed, PCD inserts were additionally damaged by notch wear. Obviously, for both carbide and PCD inserts, the wear in low cutting speeds is not as extensive as those from high cutting speeds. The thermal conductivity and hardness of PCD are much higher compared to those of the carbide inserts, resulting in lower cutting temperatures and superior resistance to abrasion wear. Therefore, the wear rates of PCD inserts were much smaller than those of carbide inserts at each cutting speed. PCD showed a better performance in resisting flank wear independent of cutting speed. However, the performance of PCD is even more superior at high cutting speed.

The OIM results of the microstructure analysis of work material and chip in the turning experiments of Ti64 proved the evident of phase change and root cause flank wear and scoring marks on flank face. The chips generated with carbides and PCD inserts contain the higher β-phase faction and higher peaks at 60° and 90°

misorientations compared to the original work material indicated that the phase change α→β happened during machining. This result agreed well with the FEM simulation, which showed the cutting temperature reaching beyond the transus temperature. The microstructure of the original work material revealed the heterogeneity in the microstructure coming from the presence of both α and β grains and the cluster of the α-grains in the hard orientations which abrade and fracture the tool surfaces,. In addition, when the adhesion layers are detached from the inserts, some grains are pulled out of the tool materials, further damaging the inserts. The hard α-clusters caused large, steady and smoother scoring marks on 'softer' carbide surface and sometime fracture with large 'hard' clusters. The hard α-clusters can damage the inserts in a more brittle manner and the detached tool fragments further damaged mainly evident by the surface patterns showing the grain fractured out from the flank surface with the scoring mark on PCD inserts.

To enhance the machinability, the ball milling experiment of 1045 steel and Ti64 was conducted with the MQL oil mixed with micro- and nano-platelets of graphite and hBN to compare with dry and regular MQL cutting. Despite the fact that the friction of these mixtures with micro and nano- platelets regardless of the thickness and concentrations did not change from that of pure oil, the tribo-test clearly showed the advantage of mixing nano-platelets of xGnP and hBN in reducing wear. These findings have been corroborated with the experimental results from the ball milling experiment with 1045 steels. The MQL mixtures with micro-platelets (Graphite and hBN5) did not present any advantage over the pure oil (traditional MQL) in reduction of flank wear while the mixtures with only a small amount (0.1w% for xGnP M5, xGnP C300, xGnP C750 and

0.5wt% for HBN300) of nano-platelets presented a significant improvement in wear performance. Among the xGnP grades, the thinner platelets showed better resisting wear performances in both tribotest and MQL-ball mill test. In the milling of Ti64, however, the content of nano-platelet C750 needed to be increased (up to 1wt%) to provide significant improvement. MQL with nano-lubricants substantially outperforms to dry and regular MQL machining by reducing flank wear and tool damage which consist of micro chippings and fractures. At the cutting speed of 2500rpm, the tool fractured in dry machining while only micro chippings occurred when the MQL mixtures were used. At given cutting speed, cutting condition is more aggressive in machining Ti64 than those in machining steel. As expected, the effectiveness of mixtures with nano-platelets in MQL machining Ti64 was less significant at cutting speed of 3500rpm while those mixtures showed outperformance at that cutting speed in machining 1045 steel. Machining of Ti64 at the lower cutting speed, the nano-platelets enhanced MQL presented much more effective. This nano-lubricant technology works because it provides the necessary lubricity even when the oil dissociate due to the high cutting temperature.

BIBLIOGRAPHY

BIBLIOGRAPHY

Alberts, M., Kalaitzidou, K., & Melkote, S. (2009). An investigation of graphite nanoplatelets as lubricant in grinding. International Journal of Machine Tools and Manufacture, 49(12-13), 966–970.

Allam, I. (1991). Solid lubricants for applications at elevated temperatures. Journal of Materials, 26(15), 3977–3984.

Amrita, M., Srikant, R., Sitaramaraju, a., Prasad, M., & Krishna, P. V. (2013). Experimental investigations on influence of mist cooling using nanofluids on machining parameters in turning AISI 1040 steel. Proceedings of the Institution of Mechanical Engineers, Part J: Journal of Engineering Tribology, 227(12), 1334–1346.

Andriya, N., Rao, P. V., & Ghosh, S. (2012). Dry Machining of Ti-6Al-4V using PVD Coated TiAlN Tools. Proceedings of the World Congress on Engineering, III, 2–7.

Arrazola, P.-J., Garay, a., Iriarte, L.-M., Armendia, M., Marya, S., & Le Maître, F. (2009). Machinability of titanium alloys (Ti6Al4V and Ti555.3). Journal of Materials Processing Technology, 209(5), 2223–2230.

Attanasio, A., Gelfi, M., Pola, A., Ceretti, E., & Giardini, C. (2013). Influence of Material Microstructures in Micromilling of Ti6Al4V Alloy. Materials, 6(9), 4268–4283.

Bartz, W. J. (1971). Solid lubricant additives - effect of concentration and other additives on anti-wear performance. Wear, 17(5-6), 421–432.

Bayoumi, a. E., & Xie, J. Q. (1995). Some metallurgical aspects of chip formation in cutting Ti-6wt.%Al-4wt.%V alloy. Materials Science and Engineering: A, 190(1-2), 173–180.

Bermingham, M. J., Kirsch, J., Sun, S., Palanisamy, S., & Dargusch, M. S. (2011). New observations on tool life, cutting forces and chip morphology in cryogenic machining Ti-6Al-4V. International Journal of Machine Tools and Manufacture, 51(6), 500–511.

Boothroyd, G. (1975). Fundamentals of Metal Machining and Machine Tools. Washington. DC: Scripta Book Company.

Boyer, R. R. (1996). An overview on the use of titanium in the aerospace industry. Materials Science and Engineering: A, 213(1-2), 103–114.

Braga, D. U., Diniz, A. E., Miranda, G. W. ., & Coppini, N. L. (2002). Using a minimum quantity of lubricant (MQL) and a diamond coated tool in the drilling of aluminum–silicon alloys. Journal of Materials Processing Technology, 122(1), 127–138.

Brandao, L. C., Coelho, R. T., & Lauro, C. H. (2011). Contribution to dynamic characteristics of the cutting temperature in the drilling process considering one dimension heat flow. Applied Thermal Engineering, 31(17-18), 3806–3813.

Brinksmeier, E., Diersen, P., Zillmer, A., & Janssen, R. (1999). Cooling Lubrication Reduction when Machining Advanced Materials. Aspects of Cooling Lubrication Reduction in Machining Advanced Materials, 213(08), 769–778.

Britton, T. B., Liang, H., Dunne, F. P. E., & Wilkinson, a. J. (2009). The effect of crystal orientation on the indentation response of commercially pure titanium: experiments and simulations. Proceedings of the Royal Society A: Mathematical, Physical and Engineering Sciences, 466(2115), 695–719.

Calamaz, M., Coupard, D., & Girot, F. (2008). A new material model for 2D numerical simulation of serrated chip formation when machining titanium alloy Ti–6Al–4V. International Journal of Machine Tools and Manufacture, 48(3-4), 275–288.

Cetin, M. H., Ozcelik, B., Kuram, E., & Demirbas, E. (2011). Evaluation of vegetable based cutting fluids with extreme pressure and cutting parameters in turning of AISI 304L by Taguchi method. Journal of Cleaner Production, 19(17-18), 2049–2056.

Chen N. (2004). Coefficients of Friction for Graphite.

Cook, N. H., & Nayak, P. N. (1986). The thermal mechanics of tool wear. Journal of Manufacturing Science and Engineering, 88(1), 93–100.

Corduan, N., Himbart, T., Poulachon, G., Dessoly, M., Lambertin, M., Vigneau, J., & Payoux, B. (2003). Wear Mechanisms of New Tool Materials for Ti-6Al-4V High Performance Machining. CIRP Annals - Manufacturing Technology, 52(1), 73–76.

Dearnley, P. A., & Grearson, A. N. (1986). P. A. Dearnley A. N. Grearson, 2(January), 47–58.

Dhar, Ahmed, M. T., & Islam, S. (2007). An experimental investigation on effect of minimum quantity lubrication in machining AISI 1040 steel. International Journal of Machine Tools and Manufacture, 47(5), 748–753.

Dhar, N. R., Paul, S., & Chattopadhyay, A. B. (2002). Machining of AISI 4140 steel under cryogenic coolingÐtool wear, surface roughness and dimensional deviation. Journal of Materials Processing Technology, 123(3), 483–489.

Donnet, C., & Erdemir, a. (2004). Solid Lubricant Coatings: Recent Developments and Future Trends. Tribology Letters, 17(3), 389–397.

Emami, M., Sadeghi, M. H., Sarhan, A. A. D., & Hasani, F. (2014). Investigating the Minimum Quantity Lubrication in grinding of Al2O3 engineering ceramic. Journal of Cleaner Production, 66, 632–643.

Ezugwu, E. O., & Wang, Z. M. (1997). Materials Titanium alloys and their machinability. Journal of Materials Processing Technology, 68, 262–274.

Fang, Z. Z. (2005). Correlation of transverse rupture strength of WC–Co with hardness. International Journal of Refractory Metals and Hard Materials, 23(2), 119–127.

Fukushima, H. (2003). Graphite Nano-reinforcements in polymer Nanocomposites. Ph.D. Thesis, Michigan State University, East Lansing, MI, USA.

Gabriel, S. B., de Almeida, L. H., Nunes, C. a, Dille, J., & Soares, G. a. (2013). Maximisation of the ratio of microhardness to the Young's modulus of Ti-12Mo-13Nb alloy through microstructure changes. Materials Science & Engineering. C, Materials for Biological Applications, 33(6), 3319–24.

Gaitonde, V. N., Karnik, S. R., & Davim, J. P. (2008). Selection of optimal MQL and cutting conditions for enhancing machinability in turning of brass. Journal of Materials Processing Technology, 204(1-3), 459–464.

Gente. (2001). Chip Formation in Machining_Ti64 (chip morphology vs CS).pdf. CIRP Annals - Manufacturing Technology, 50, 49–52.

Groover, M. P. (2007). Fundamentals of modern manufacturing: materials processes, and systems (3rd ed.). John Wiley & Sons.

Hartung, P. D., & Kramer, B. M. (1982). Tool Wear in Titanium Machining. Ann. CIRP, 31(1), 75–80.

Hasçalık, A., & Çaydaş, U. (2007). Optimization of turning parameters for surface roughness and tool life based on the Taguchi method. The International Journal of Advanced Manufacturing Technology, 38(9-10), 896–903.

Haubner, R., Wilhelm, M., Weissenbacher, R., & Lux, B. (2002). Boron Nitrides - Properties, Synthesis and Applications (Vol. 102, pp. 1–45). Springer Berlin Heidelberg.

Heinemann, R., Hinduja, S., Barrow, G., & Petuelli, G. (2006). Effect of MQL on the tool life of small twist drills in deep-hole drilling. International Journal of Machine Tools and Manufacture, 46(1), 1–6.

Hickman B.S. (1969). The Formation of Omega Phase in Titanium and Zirconium Alloys: A Review, 4, 554–563.

Hosseini, A., & Kishawy, H. A. (2014). Machining of Titanium Alloys. In J. P. Davim (Ed.), Machining of Titanium Alloys. Berlin, Heidelberg: Springer Berlin Heidelberg.

Hsu, H.-C., Wu, S.-C., Hsu, S.-K., Lin, T.-F., & Ho, W.-F. (2013). Structure and mechanical properties of as-cast Ti–5Nb–xCr alloys. Materials & Design, 51, 268–273.

Hsu, S. M. (2004). Nano-lubrication: concept and design. Tribology International, 37(7), 537–545.

Hua, J., & Shivpuri, R. (2005). A Cobalt Diffusion Based Model for Predicting Crater Wear of Carbide Tools in Machining Titanium Alloys. Journal of Engineering Materials and Technology, 127(1), 136.

Huang, H. D., Tu, J. P., Gan, L. P., & Li, C. Z. (2006). An investigation on tribological properties of graphite nanosheets as oil additive. Wear, 261(2), 140–144.

Hughes, J. I., Sharman, A. R. C., & Ridgway, K. (2004). The effect of tool edge preparation on tool life and workpiece surface integrity. Proc. IMechE Part B: J. Engineering Manufacture, 220, 1113–1123.

Ibrahim, G. A., CheHaron, C. H., & Ghani, J. A. (2009). Surface integrity of ti-6al-4v eli when machined using coated carbide tools under dry cutting condition. International Journal of Mechanical and Materials Engineering (IJMME), 4(2), 191–196.

Jaffery, S. I., & Mativenga, P. T. (2008). Assessment of the machinability of Ti-6Al-4V alloy using the wear map approach. The International Journal of Advanced Manufacturing Technology, 40(7-8), 687–696.

Jawaid, a, Che-Haron, C. ., & Abdullah, a. (1999). Tool wear characteristics in turning of titanium alloy Ti-6246. Journal of Materials Processing Technology, 92-93, 329–334.

Jon, M. C., Engineering, M., Science, M., & York, N. (1972). Omega-Phase Formation in Beta III Titanium Alloy, 150, 139–150.

Jones, N., Dashwood, R., Jackson, M., & Dye, D. (2009). Development of chevron-shaped α precipitates in Ti–5Al–5Mo–5V–3Cr. Scripta Materialia, 60(7), 571–573.

Joshi, S., Pawar, P., Tewari, A., & Joshi, S. S. (2014). Effect of β phase fraction in titanium alloys on chip segmentation in their orthogonal machining. CIRP Journal of Manufacturing Science and Technology, 7(3), 191–201.

Kajdas, C., Kanpsika, A., & Kulczycki, A. (2010). Chemistry and Technology of Lubricants. In R. M. Mortier, M. F. Fox, & S. T. Orszulik (Eds.), Chemistry and technology of lubricants (pp. 239–292). Dordrecht: Springer Netherlands.

Kalita, P., Malshe, A. P., Arun Kumar, S., Yoganath, V. G., & Gurumurthy, T. (2012). Study of specific energy and friction coefficient in minimum quantity lubrication grinding using oil-based nanolubricants. Journal of Manufacturing Processes, 14(2), 160–166.

Khettabi, R., Songmene, V., & Masounave, J. (2009). Effects of Speeds, Materials, and Tool Rake Angles on Metallic Particle Emission During Orthogonal Cutting. Journal of Materials Engineering and Performance, 19(6), 767–775.

Khettabi, R., Songmene, V., Masounave, J., & Zaghbani, I. (2008). Understanding the Formation of Nano and Micro Particles During Metal Cutting.pdf. International Journal of Signal System Control and Engineering, 1(3), 203–210.

Kimura, Y., Wakabayashi, T., Okada, K., Wada, T., & Nishikawa, H. (1999). Boron nitride as a lubricant additive. Wear, 232(2), 199–206.

Konig, W. (1979). Applied research on the machinability of titanium and its alloys. Proc. AGARD Conf. Advanced Fabrication Processes, Florence, Italy.

Kramer, B. M., & von Turkovich, B. F. (1986). A Comprehensive Tool Wear Model. CIRP Annals - Manufacturing Technology, 35(1), 67–70.

Kwon, J., Brandes, M. C., Sudharshan Phani, P., Pilchak, a. P., Gao, Y. F., George, E. P., … Mills, M. J. (2013). Characterization of deformation anisotropies in an α-Ti alloy by nanoindentation and electron microscopy. Acta Materialia, 61(13), 4743–4756.

Kwon, P., & Drzal, L. T. (2010). Nanoparticle graphite-based minimum quantity lubrication method and composition. US.

Lammer, A. (1988). Mechanical properties of polycrystalline diamonds. Materials Science and Technology, 4(November), 949–955.

Lee, C.-G., Hwang, Y.-J., Choi, Y.-M., Lee, J.-K., Choi, C., & Oh, J.-M. (2009). A study on the tribological characteristics of graphite nano lubricants. International Journal of Precision Engineering and Manufacturing, 10(1), 85–90.

List, G., Nouari, M., Géhin, D., Gomez, S., Manaud, J. P., Le Petitcorps, Y., & Girot, F. (2005). Wear behaviour of cemented carbide tools in dry machining of aluminium alloy. Wear, 259(7-12), 1177–1189.

Liu, Z. Q., Cai, X. J., Chen, M., & An, Q. L. (2011). Investigation of cutting force and temperature of end-milling Ti-6Al-4V with different minimum quantity lubrication (MQL) parameters. Proceedings of the Institution of Mechanical Engineers, Part B: Journal of Engineering Manufacture, 225(8), 1273–1279.

López de Lacalle, L. N., Angulo, C., Lamikiz, a., & Sánchez, J. a. (2006). Experimental and numerical investigation of the effect of spray cutting fluids in high speed milling. Journal of Materials Processing Technology, 172(1), 11–15.

Lütjering, G., & Williams, J. C. (2003). Titanium (2nd ed.). Berlin: Springer.

Machado, A. R., & Wallbank, J. (1990). Machining of titanium and its alloys-a. Proceedings of the Institution of Mechanical Engineers, Part B: Journal of Engineering Manufacture, 204(1), 53–60.

Machai, C., Iqbal, A., Biermann, D., Upmeier, T., & Schumann, S. (2013). On the effects of cutting speed and cooling methodologies in grooving operation of various tempers of β-titanium alloy. Journal of Materials Processing Technology, 213(7), 1027–1037.

Maciej Motyka, K. K. J. S. and W. Z. (2012). Titanium Alloys - Towards Achieving Enhanced Properties for Diversified Applications. (A. K. M. N. Amin, Ed.). InTech.

Mao, C., Tang, X., Zou, H., Huang, X., & Zhou, Z. (2012). Investigation of grinding characteristic using nanofluid minimum quantity lubrication. International Journal of Precision Engineering and Manufacturing, 13(10), 1745–1752.

Mao, C., Zou, H., Huang, X., Zhang, J., & Zhou, Z. (2012). The influence of spraying parameters on grinding performance for nanofluid minimum quantity lubrication. The International Journal of Advanced Manufacturing Technology, 64(9-12), 1791–1799.

Meyer, L. W., Krüger, L., Sommer, K., Halle, T., & Hockauf, M. (2008). Dynamic strength and failure behavior of titanium alloy Ti-6Al-4V for a variation of heat treatments. Mechanics of Time-Dependent Materials, 12(3), 237–247.

Molinari, a, Musquar, C., & Sutter, G. (2002). Adiabatic shear banding in high speed machining of Ti–6Al–4V: experiments and modeling. International Journal of Plasticity, 18(4), 443–459.

Motonishi, S., Isoda, S., Itoh, H., Tsumori, Y., & Terada, Y. (1987). Study on Machining of Titanium and Its Alloys. Kobelto Technology Review, 2, 28–31.

Nabhani, F. (2001). Machining of aerospace titanium alloys. Robotics and Computer-Integrated Manufacturing, 17(1-2), 99–106.

Nageswara Rao, D., & Vamsi Krishna, P. (2008). The influence of solid lubricant particle size on machining parameters in turning. International Journal of Machine Tools and Manufacture, 48(1), 107–111.

Nandy, a. K., & Paul, S. (2008). Effect of coolant pressure, nozzle diameter, impingement angle and spot distance in high pressure cooling with neat oil in turning Ti-6Al-4V. Machining Science and Technology, 12(4), 445–473.

Narutaki, N., Murakoshi, A., Motonishi, S., & Takeyama, H. (1983). Study on Machining of Titanium Alloys. CIRP Annals - Manufacturing Technology, 32(1), 65–69.

Narutaki, N., Murakoshi, A., Motonishi, S., & Takeyama, H. (1983). Study on Machining of Titanium Alloys. CIRP Annals - Manufacturing Technology, 32(1), 65–69.

Nguyen, T. K., Do, I., & Kwon, P. (2012). A tribological study of vegetable oil enhanced by nano-platelets and implication in MQL machining. International Journal of Precision Engineering and Manufacturing, 13(7), 1077–1083.

Olortegui-Yume, J. A., & Kwon, P. Y. (2007). Tool wear mechanisms in machining. Nternational Journal of Machining and Machinability of Materials, 2(3), 316–334.

Olortegui-Yume, J. a., & Kwon, P. Y. (2010). Crater wear patterns analysis on multi-layer coated carbides using the wavelet transform. Wear, 268(3-4), 493–504.

Oosthuizen, G. A., Akdogan, G., Dimitrov, D., & Treurnich, N. F. (2010). A Review of the Machinability of Titanium Alloys. R & D Journal of the South African Institution of Mechanical Engineering, 26(September), 43–52.

Ozcelik, B., Kuram, E., Huseyin Cetin, M., & Demirbas, E. (2011). Experimental investigations of vegetable based cutting fluids with extreme pressure during turning of AISI 304L. Tribology International, 44(12), 1864–1871.

Park, K.-H., & Kwon, P. Y. (2011). Flank wear of multi-layer coated tool. Wear, 270(11-12), 771–780.

Park, K.-H., Ewald, B., & Kwon, P. Y. (2011). Effect of Nano-Enhanced Lubricant in Minimum Quantity Lubrication Balling Milling. Journal of Tribology, 133(3), 031803.

Paul, P. S., & Varadarajan, a. (2013). Performance evaluation of hard turning of AISI 4340 steel with minimal fluid application in the presence of semi-solid lubricants. Proceedings of the Institution of Mechanical Engineers, Part J: Journal of Engineering Tribology, 227(7), 738–748.

Prasad, B. K. (2005). Effectiveness of an externally added solid lubricant on the sliding wear response of a zinc?aluminium alloy, its composite and cast iron. Tribology Letters, 18(2), 135–143.

Prasad, B. K., Rathod, S., Yadav, M. S., & Modi, O. P. (2010). Effects of Some Solid Lubricants Suspended in Oil Toward Controlling the Wear Performance of a Cast Iron. Journal of Tribology, 132(4), 041602.

Rabinowic, E., L.A., D., & Russell, P. G. (1961). A study of abrasive wear under three-body conditions. Wear, 4(5), 345–355.

Rabinowicz, E. (1977). Abrasive wear resistance as a materials test. Lubr. Eng., 33(7), 378–381.

Rahim, E. A., Kamdani, K., & Sharif, S. (2008). Performance Evaluation of Uncoated Carbide Tool in High Speed Drilling of Ti6Al4V. Journal of Advanced Mechanical Design, Systems, and Manufacturing, 2(4), 522–531.

Rahman, M., Wong, Y. S., & Zareena, A. R. (2003). Machinability of titanium alloys. JSME International Journal Series C, 46, 107–115.

Rahman, M., Wong, Y. S., & Zareena, A. R. (2003). Machinability of titanium alloys. JSME International Journal Series C, 46, 107–115.

Rahmati, B., Sarhan, A. a. D., & Sayuti, M. (2013). Investigating the optimum molybdenum disulfide (MoS2) nanolubrication parameters in CNC milling of AL6061-T6 alloy. The International Journal of Advanced Manufacturing Technology, 70(5-8), 1143–1155.

Ramesh, S., Karunamoorthy, L., & Palanikumar, K. (2008). Fuzzy Modeling and Analysis of Machining Parameters in Machining Titanium Alloy. Materials and Manufacturing Processes, 23(4), 439–447.

Reddy, N. S. K., & Rao, P. W. (2006). Experimental investigation to study the effect of solid lubricants on cutting forces and surface quality in end milling. International Journal of Machine Tools and Manufacture, 46(2), 189–198.

Rioul, O., & Vetterli, M. (1991). No Title. IEEE Signal Processing Magazine, 8, 14–38.

Sadeghi, M. H., Haddad, M. J., Tawakoli, T., & Emami, M. (2008). Minimal quantity lubrication-MQL in grinding of Ti–6Al–4V titanium alloy. The International Journal of Advanced Manufacturing Technology, 44(5-6), 487–500.

Sarhan, A. a. D., Sayuti, M., & Hamdi, M. (2012). Reduction of power and lubricant oil consumption in milling process using a new SiO2 nanolubrication system. The International Journal of Advanced Manufacturing Technology, 63(5-8), 505–512.

Schrock, D. J., & Kwon, P. (2012). Evidence of Phase Dependent Tool Wear in Ti-6Al-4V Turning Experiments Using PCD and Carbide Inserts. In ASME 2012 International Manufacturing Science and Engineering Conference (p. 371). ASME.

Schrock, D. J., Kang, D., Bieler, T. R., & Kwon, P. (2014). Phase Dependent Tool Wear in Turning Ti-6Al-4V Using Polycrystalline Diamond and Carbide Inserts. Journal of Manufacturing Science and Engineering, 136(4), 041018.

Semiatin, S. L., Seetharaman, V., & Weiss, I. (1996). The Thermomechanical Processing of Alpha/Beta Titanium Alloys. JOM, 49(6), 33–40.

Shahan, A. R., & Taheri, A. K. (1993). Adiabatic shear bands in titanium and titanium alloys: a critical review. Materials & Design, 14(4), 243–250.

Shen, B., Malshe, A. P., & Shih, A. J. (2008). Performance of novel mos 2 nanoparticles based grinding fluids in minimum quantity lubrication grinding. Transaxtions of NAMRI/SME, 36, 357–364.

Shen, B., Shih, A. J., & Tung, S. C. (2008). Application of Nanofluids in Minimum Quantity Lubrication Grinding. Tribology Transactions, 51(6), 730–737.

Sima, M., & Özel, T. (2010). Modified material constitutive models for serrated chip formation simulations and experimental validation in machining of titanium alloy Ti–6Al–4V. International Journal of Machine Tools and Manufacture, 50(11), 943–960.

Singh, G., Singh, S., Singh, M., & Kumar, A. (2013). Experimental investigations of vegetable & mineral oil performance during machining of en-31 steel with minimum quantity lubrication. International Journal of Research in Engineering and Technology, 02(06), 1030–1037.

Srikant, R. R., Rao, D. N., Subrahmanyam, M. S., & Vamsi Krishna, P. (2009). Applicability of cutting fluids with nanoparticle inclusion as coolants in machining. Proceedings of the Institution of Mechanical Engineers, Part J: Journal of Engineering Tribology, 223(2), 221–225.

Suh, N. P. (1986). Tribophysics. (Pretice-Hall, Ed.).

Tai, B. L., Dasch, J. M., & Shih, A. J. (2011). Evaluation and Comparison of Lubricant Properties in Minimum Quantity Lubrication Machining. Machining Science and Technology, 15(4), 376–391.

Tawakoli, T., Hadad, M. J., & Sadeghi, M. H. (2010). Influence of oil mist parameters on minimum quantity lubrication–MQL grinding process. International Journal of Machine Tools and Manufacture 50, 50(06), 521–531.

Thepsonthi, T., Hamdi, M., & Mitsui, K. (2009). Investigation into minimal-cutting-fluid application in high-speed milling of hardened steel using carbide mills. International Journal of Machine Tools and Manufacture, 49(2), 156–162.

Toh, C. K., & Kanno, S. (2004). Surface integrity effects on turned 6061 and 6061-T6 aluminum alloys. Proc. IMechE,Vol. 225, Part N: J. of Nano Engineering and Nano Systems, 225(1), 3–16.

Trent, E. M. (1991). Metal cutting. Butterworth-Heinemann Ltd, Oxford.

Ueda, T., Hosokawa, A., & Yamada, K. (2006). Effect of Oil Mist on Tool Temperature in Cutting. Journal of Manufacturing Science and Engineering, 128(1), 130.

Varadarajan, a. S., Philip, P. K., & Ramamoorthy, B. (2002). Investigations on hard turning with minimal cutting fluid application (HTMF) and its comparison with dry and wet turning. International Journal of Machine Tools and Manufacture, 42(2), 193–200.

Venugopal, K. a., Paul, S., & Chattopadhyay, a. B. (2007). Growth of tool wear in turning of Ti-6Al-4V alloy under cryogenic cooling. Wear, 262(9-10), 1071–1078.

Wakabayashi, T., Inasaki, I., & Suda, S. (2006). Tribological Action and Optimal Performance: Research Activities Regarding Mql Machining Fluids. Machining Science and Technology, 10(1), 59–85.

Watanabe, S., Miyake, S., & Murakawa, M. (1991). Tribological properties of cubic, amorphous and hexagonal boron nitride films. Surface and Coatings Technology, 49(1-3), 406–410.

Weinert, K., Inasaki, I., Sutherland, J. W., & Wakabayashi, T. (2004). Dry Machining and Minimum Quantity Lubrication. CIRP Annals - Manufacturing Technology, 53(2), 511–537.

Wong, T., Kim, W., & Kwon, P. (2004). Experimental support for a model-based prediction of tool wear. Wear, 257(7-8), 790–798.

Wright, P. K., & Bagchi, a. (1981). Wear mechanisms that dominate tool-life in machining. Journal of Applied Metalworking, 1(4), 15–23.

Yang, X., Liu, C. R., & Lafayette, W. (1999). Machining titanium and its alloys. Machining Science and Technology, 3(1), 107–139.

Yukhno, T. ., Vvedensky, Y. ., & Sentyurikhina, L. . (2001). Low temperature investigations on frictional behaviour and wear resistance of solid lubricant coatings. Tribology International, 34(4), 293–298.

Zhang, X. P., Shivpuri, R., & Srivastava, a. K. (2014). Role of phase transformation in chip segmentation during high speed machining of dual phase titanium alloys. Journal of Materials Processing Technology, 214(12), 3048–3066.

Zhang, X., Wu, S., Wang, H., & Liu, C. R. (2011). Predicting the Effects of Cutting Parameters and Tool Geometry on Hard Turning Process Using Finite Element Method. Journal of Manufacturing Science and Engineering, 133(4), 041010.

Zhang, Y. C., Mabrouki, T., Nelias, D., & Gong, Y. D. (2011). Chip formation in orthogonal cutting considering interface limiting shear stress and damage evolution based on fracture energy approach. Finite Elements in Analysis and Design, 47(7), 850–863.

Zhu, Q., Qiu, X., & Ma, C. (1998). The oxidation resistance improvement of matrix graphite of spherical fuel elements by slip-gelation process. Journal of Nuclear Materials, 254(2-3), 221–225.